Universität Hamburg
DER FORSCHUNG | DER LEHRE | DER BILDUNG

Test Beam Studies of Prototype Module and Test Measurements of MaPSA for The CMS Outer Tracker Phase-2 Upgrade

Dissertation

zur Erlangung des Doktorgrades an der Fakultät

für Mathematik, Informatik und Naturwissenschaften

Fachbereich Physik
der Universität Hamburg

vorgelegt von

CHUN CHENG

Hamburg

2025

Declaration on oath

I hereby declare and affirm that this doctoral dissertation is my own work and that I have not used any aids and sources other than those indicated.

If electronic resources based on generative artificial intelligence (gAI) were used in the course of writing this dissertation, I confirm that my own work was the main and value-adding contribution and that complete documentation of all resources used is available in accordance with good scientific practice. I am responsible for any erroneous or distorted content, incorrect references, violations of data protection and copyright law or plagiarism that may have been generated by the gAI.

Hamburg
09.01.2025
Date

Chun Cheng
Signature of doctoral candidate

Gutachter der Dissertation:	Dr. Doris Eckstein
	Prof. Dr. Elisabetta Gallo
Zusammensetzung der Prüfungskommission:	Prof. Dr. Günter H. W. Sigl
	Prof. Dr. Elisabetta Gallo
	Prof. Dr. Erika Garutti
	Prof. Dr. Johannes Haller
	Dr. Doris Eckstein
Vorsitzender der Prüfungskommission:	Prof. Dr. Günter H. W. Sigl
Datum der Disputation:	29.01.2025
Vorsitzender des Fach-Promotionsausschusses Physik:	Prof. Dr. Wolfgang J. Parak
Leiter des Fachbereichs Physik:	Prof. Dr. Markus Drescher
Dekan der Fakultät MIN:	Prof. Dr.-Ing. Norbert Ritter

Abstract

The High-Luminosity Large Hadron Collider (HL-LHC) represents a significant leap in the pursuit of fundamental physics. Scheduled to operate at a center-of-mass energy of 14 TeV and a peak instantaneous luminosity up to $7.5 \times 10^{34}\,\mathrm{cm^{-2}s^{-1}}$, it aims to deliver up to $3000\,\mathrm{fb^{-1}}$ of integrated luminosity by the late 2030s. To meet the unprecedented challenges of the HL-LHC environment, the Compact Muon Solenoid (CMS) experiment is undergoing comprehensive upgrades. The silicon tracker will be completely replaced with a more robust design to withstand higher radiation doses and handle significantly increased data rates. The Outer Tracker introduces an innovative p_T-module concept that enables transverse momentum discrimination by correlating hits from closely spaced silicon sensors. This functionality reduces the data volume processed by the Level-1 trigger by filtering low-p_T candidates, ensuring that only high-p_T tracks, which are more relevant for physics analysis, contribute to the Level-1 trigger decision.

This thesis presents contributions to key aspects of the Outer Tracker upgrade, including both 2S and PS module development. The first part focuses on the assembly and characterization of prototype 2S modules, with a sensor thickness of 240 µm. The 2S prototype module demonstrated excellent performance, as validated through electrical and beam tests conducted at DESY, achieving a particle detection efficiency above 99.9% and a stub detection efficiency exceeding 99.7%. Beam tests also confirmed the design concept for discriminating low transverse momentum tracks, showing agreement with expectations.

The second part focuses on the development of a test stand for the quality assurance of the Macro Pixel Sub-Assembly (MaPSA), a main component of the PS module. Established to support the production of over 1250 PS modules at DESY, the test stand facilitates the testing and grading of MaPSAs. A comprehensive electrical testing workflow was implemented, including current measurements, pixel functionality tests, bump bonding evaluations, and threshold equalization. The threshold equalization procedure was optimized to achieve precise alignment of pixel responses, minimizing the risk of misclassifying untrimmable pixels. Through successful evaluations of prototype MaPSAs, the test stand has demonstrated its reliability and readiness for the production phase.

Zusammenfassung

Der Large Hadron Collider (HL-LHC) in der Hochluminisitätsphase stellt einen bedeutenden Fortschritt bei der Erforschung der Grundlagenphysik dar. Er soll bei einer Schwerpunktsenergie von 14 TeV und einer instantanen Luminosität von bis zu $7,5 \times 10^{34}\,\mathrm{cm}^{-2}\mathrm{s}^{-1}$ betrieben werden und in den späten 2030er Jahren eine integrierte Luminosität von bis zu $3000\mathrm{fb}^{-1}$ erreichen. Um den beispiellosen Herausforderungen der HL-LHC Umgebung gerecht zu werden, wird das Compact Muon Solenoid (CMS)-Experiment einer umfassenden Erneuerung unterzogen. Der Silizium-Tracker wird vollständig durch eine robustere Konstruktion ersetzt, die höheren Strahlungsdosen standhält und deutlich höhere Datenraten verarbeiten kann. Mit dem Outer Tracker wird ein innovatives p_T-Modulkonzept eingeführt, das die Diskriminierung von Transversalimpulsen durch Korrelation von Treffern aus eng beieinander liegenden Siliziumsensoren ermöglicht. Diese Funktion reduziert die vom Level-1-Trigger verarbeitete Datenmenge, indem sie Treffer von Teilchen mit niedrigem Transversalimpuls herausfiltert und sicherstellt, dass nur Treffer von Teilchen mit hohem Transversalimpuls, die für die physikalische Analyse relevanter sind, zur Level-1-Trigger-Entscheidung beitragen.

In dieser Arbeit werden Beiträge zu Schlüsselaspekten des Outer-Tracker Erneuerung vorgestellt, einschließlich der Entwicklung von 2S- und PS-Modulen. Der erste Teil konzentriert sich auf den Zusammenbau und die Charakterisierung von 2S-Prototypmodulen mit einer Sensordicke von 240 µm. Das 2S-Prototypmodul zeigte eine hervorragende Leistung, die durch elektrische und Strahltests bei DESY bestätigt wurde. Es erreichte eine Teilchennachweis-effizienz von über $99,9\%$ und eine Nachweiseffizienz für Stubs von über $99,7\%$. Die Strahltests bestätigten auch das Konzept zur Unterscheidung von Spuren mit niedrigem und hohem Transversalimpuls und zeigten eine Übereinstimmung mit den Erwartungen.

Der zweite Teil konzentriert sich auf die Entwicklung eines Prüfstands für die Qualitätssicherung der Makro-Pixel-Sensoreinheit (MaPSA), einer Hauptkomponente des PS-Moduls. Der Teststand, der zur Unterstützung der Produktion von über 1250 PS-Modulen bei DESY eingerichtet wurde, erleichtert die Prüfung der MaPSAs. Es wurde ein umfassender elektrischer Prüfablauf implementiert, der Strommessungen, Pixelfunktionstests, Bump-Bonding-Bewertungen und Schwellenwertausgleich umfasst. Das Verfahren zur Schwellwertangleichung wurde optimiert, um eine präzise Ausrichtung der Pixelantworten zu erreichen und so das Risiko der Fehlklassifizierung von nicht trimmbaren Pixeln zu minimieren. Durch die erfolgreiche Evaluierung von MaPSA-Prototypen hat der Prüfstand seine Zuverlässigkeit und Bereitschaft für die Produktionsphase bewiesen.

For my beloved granny,
whose faith in me was abiding and true.
Though you left before this journey's end,
your love lights every step I take.
This achievement is as much yours as it is mine.

Acknowledgements

First and foremost, I would like to express my deepest gratitude to all my friends and family who have supported me emotionally and morally throughout the challenges and triumphs of my doctoral journey. Their unwavering belief in me kept me grounded and motivated during the most challenging moments.

I am profoundly thankful to Dr. Doris Eckstein and Dr. Andreas Mussgiller for giving me the incredible opportunity to join the group and conduct my doctoral research at DESY. Their trust in my abilities provided the foundation for my growth as a researcher and as a scientist.

To my supervisor, Dr. Doris Eckstein, words cannot fully capture my appreciation. Her unwavering support, encouragement for my ideas, and guidance during both my brightest and darkest moments have been the cornerstone of my journey. Her consistent belief in me allowed me to confidently pursue my research goals and overcome countless obstacles along the way

I also owe gratitude to my supervisor, Prof. Dr. Elisabetta Gallo, for equipping me with the theoretical expertise that underpinned my research. Her guidance and insightful advice were instrumental in shaping this thesis.

My sincere gratitude goes to Dr. Andreas Nürnberg, whose expertise in detector physics and technical knowledge played a pivotal role in my research. His patience, willingness to engage in scientific discussions, and invaluable support during equipment debugging made a significant impact. I am especially thankful for his detailed proofreading of this thesis, which greatly enhanced its quality.

I extend my warmest thanks to Dr. Simon Spannagel, Dr. Paul Schütze, and Dr. Daniel Pitzl for guiding me through test beam studies during the early stages of my doctoral research. Their mentorship not only helped me gain a deeper understanding of test beam analysis but also laid the groundwork for the work presented in this thesis.

To Dr. Doug Berry and Dr. Jennet Dickinson, thank you for your dedication in helping me establish the MaPSA test stand and for your continued support in refining the testing software. I am also grateful to Dr. Sumera Kousar for sharing her expertise on hybrid bump bonds, which greatly enriched my understanding of detector technologies.

I am fortunate to have collaborated with incredible researchers during this journey. Dr. Younes Otarid, Dr. Ali Harb, Dr. Roland Koppenhöfer, Dr. Florian Wittig, Dr. Christian Dziwok, Dr. Nicolas Röwert, and Dr. Tim Ziemons: thank you for your teamwork and for sharing your experience during module assembly, test beam experiments, and the night shifts. Working alongside you not only made the projects successful but also created some of the most memorable moments of my PhD journey.

I am deeply appreciative of Dr. Moritz Guthoff, Dr. Anastasiia Velyka, Dr. Mykyta Haranko, and Mr. Carsten Muhl for the stimulating discussions that broadened my perspective and inspired new ideas for my research.

The measurements leading to the results of this thesis were made possible by the outstanding facilities at the Test Beam Facility at DESY Hamburg (Germany), a member of the Helmholtz Association (HGF). I am grateful for their resources and support, which were integral to the success of my work.

I am equally thankful to the DESY secretarial staff for their administrative support, which ensured the smooth progress of my research. Their assistance was invaluable in navigating the logistical challenges of this journey.

Special thanks to my former and current colleagues and friends: Ana Ventura Barroso, Daniil Rastorguev, Leonie Sommer, Aenne Abel, Andrea Cardini, Soham Bhattacharya, and Oskar Reichelt. Your companionship and encouragement made my time at DESY truly unforgettable. The vibrant and supportive atmosphere you created has been a source of inspiration and joy.

Finally, to all the people I have worked with at DESY and beyond, your collaboration, advice, and encouragement have left an indelible mark on my journey. This thesis is as much a product of your support as it is of my efforts. Thank you for everything you have done to help me grow, both professionally and personally.

Contents

Chapter 1

Introduction

The Large Hadron Collider (LHC) at the European Organization for Nuclear Research (CERN) is the largest and most powerful particle accelerator. It accelerates protons and heavy ions to nearly the speed of light, allowing them to collide at unprecedented high energies to study fundamental particles and forces of nature. To explore rare processes and uncover potential physics beyond the Standard Model, the LHC will be upgraded to its high-luminosity phase (HL-LHC) in the coming years. During this phase, the instantaneous luminosity is expected to increase up to $7.5 \times 10^{34}\,\mathrm{cm}^{-2}\mathrm{s}^{-1}$, with proton-proton collisions occurring at a center-of-mass energy of 14 TeV. Over the anticipated ten years of HL-LHC operation, this upgrade is projected to deliver an integrated luminosity of 3000 to $4000\,\mathrm{fb}^{-1}$. The significantly increased amount of data at the HL-LHC will allow precise measurements of known phenomena and provide greater sensitivity to new physics.

The Compact Muon Solenoid (CMS) detector is one of the primary experiments at the LHC, designed to investigate a wide range of physics phenomena. The CMS detector comprises a silicon tracker, electromagnetic and hadronic calorimeters, a superconducting solenoid generating a 3.8 T magnetic field, and muon chambers. The strong magnetic field bends the trajectories of charged particles, allowing for precise momentum measurements and efficient particle identification.

As the LHC transitions to its High-Luminosity phase (HL-LHC), the increased instantaneous luminosity will result in significantly higher radiation levels and up to 200 proton-proton collisions per bunch crossing. The current CMS detector lacks the radiation tolerance and granularity required to handle these conditions, resulting in reduced detection efficiency, higher noise levels, and challenges in isolating individual collision events. To address these issues, the Phase-2 upgrade introduces advanced technologies that improve granularity, radiation resistance, data acquisition capabilities, and pseudorapidity coverage. Notably, the tracker will provide track information directly to the Level-1 trigger for the first time, enabling more efficient event selection by identifying high-momentum tracks in real-time. A detailed overview of the physics motivation and detector upgrades is presented in Chapter 2.

This thesis focuses on the Phase-2 Outer Tracker upgrade for the CMS experiment, which uses silicon as its detection material. Chapter 3 covers the fundamentals of charged particle interactions with matter, the principles of silicon sensors, and their application in silicon trackers, laying the groundwork for the experimental studies in later chapters.

The significant increase in data rates makes it impossible for the Level-1 trigger system to process all the data within the given timescale, making event selection at the module level essential. The Phase-2 Outer Tracker upgrade introduces a novel p_T module concept that enables on-module selection of high transverse momentum tracks. This functionality is achieved by placing two parallel sensors closely separated by a few millimeters, with both sensors read out by the same set of ASICs. The p_T of the charged particles relates to spatial displacement of the detection position on the two sensors due to the effect of the magnetic field. High p_T particles exhibit low curvature in their trajectory; thus, the detected position on the two sensors will be close to each other. By defining a programmable search window on the sensor placed farther away from the interaction point, the p_T module can identify and generate trigger primitives for the Level-1 trigger decision. This capability significantly reduces the data rate to the trigger by ensuring that only relevant information is transmitted. The upgraded tracker features two types of modules: Strip-Strip (2S) modules and Pixel-Strip (PS) modules. The details of the p_T module concept and the structure of these two module types are discussed in Chapter 4.

My contributions to the Phase-2 Outer Tracker upgrade span the validation of the module concept and the development of a test system, which ensures the reliable production and integration of detector components for the HL-LHC era.

As part of the CMS Phase-2 Outer Tracker collaboration, a 2S module was assembled at Deutsches Elektronen-Synchrotron (DESY) in the course of this thesis. This effort aimed to verify the assembly techniques for future large-scale production and the performance study of a prototype 2S module. The assembled module underwent multiple electric tests in the cleanroom and beam testing at the DESY II facility to study its electrical properties, noise performance, particle hit detection, and p_T-discrimination logic performance. I contributed to all stages of this project, including the assembly of the module, its electrical testing, and the execution of testbeam campaigns. The offline analysis was performed using the Corryvreckan testbeam analysis software. In addition to conducting the full analysis, I contributed to the software by extending its analysis packages to incorporate CMS-specific features, such as coordinate system transformations, stub performance calculations, and adjustments to accommodate the CMS testbeam setup. These contributions were essential for tailoring the software to meet the requirements of CMS applications. The details of this work, including the experimental setup, results, and implications, are discussed in Chapter 5.

DESY is one of the PS module assembly sites for the production. To ensure their quality and functionality, the components need to be tested beforehand, as any defective parts could compromise the detector's performance. In the scope of this thesis, I developed a test stand on a probe station to evaluate the Macro Pixel Sub-Assembly (MaPSA), a component of the PS module. The primary objective is to ensure the functionality and quality of the MaPSA by identifying defects such as dead pixels, noisy pixels, or defective bump bonding connections. Additionally, the manufacturing process of the readout chip can introduce variations in the baseline of the amplifier output among pixels, and affect the effective threshold of the pixel comparators, leading to non-uniform pixel responses. To address this, threshold equalization was implemented to mitigate such mismatches. I established the testing procedure at DESY and implemented an optimized threshold equalization algorithm for the working group. Chapter 6 provides a detailed discussion on the quality assurance procedures for MaPSAs, the setup and software of the probing system, and the results obtained from probe testing, including IV measurements, single pixel qualification, and trimming optimization.

Chapter 2

Particle Physics Exploration

Contents

2.1 Particle Physics at the Large Hadron Collider

2.1.1 The Standard Model of particle physics

The field of particle physics explores the formation of the universe. The Standard Model (SM) of particle physics is the best theory that summarizes the current understanding of fundamental elements of matter and the force interactions among them.

The origins of the Standard Model can be traced back to the late 19th and early 20th centuries. During this time, subatomic particles were being discovered, and the atomic nucleus was being revealed [1]. Moreover, the theoretical foundation established in the first half of the 20th century – Quantum Electrodynamics (QED), describes the electromagnetic interactions between charged particles. In the 1970s, a theory called the electroweak theory was proposed to unify the electromagnetic and weak forces. Later, the discovery of the W and Z bosons at CERN in 1983 validated this theory experimentally [2].

Simultaneously, the study of strong forces is regulated by Quantum Chromodynamics (QCD), which has contributed to our understanding of quark interactions. The mediator of the strong force, the gluon, was discovered at DESY in 1979. The concept of asymptotic freedom [3], a fundamental feature of QCD, was experimentally confirmed [4], revealing the behavior of quarks within protons, neutrons, and other hadrons.

The Higgs mechanism, which finalized the current Standard Model, was proposed in the 1960s. It explains the process by which particles acquire mass. This fundamental theory was initially proposed during the 1960s, and its validation came in 2012 with the detection of the Higgs boson at CERN [5].

The Standard Model is illustrated in Figure 2.1. This figure provides a comprehensive overview of the fundamental particles and the mediators responsible for the electromagnetic, weak, and strong forces. Elementary particles are classified into two distinct categories, namely, *fermions* and *bosons*, based on their spin values. Fermions, characterized by having half-integer spin value, follow Fermi-Dirac statistics and are the building blocks of matter. They are further divided into *quarks* and *leptons*. The quarks possess a unique property called color charge, which makes them subject to strong interactions. Bosons have an integer-value spin, following the Bose–Einstein statistics. One class of bosons acts as the mediator of the forces described by gauge theory, with a spin value of 1. In contrast, the Higgs boson interacts with fundamental particles, enabling them to acquire mass. It is the only scalar (spin=0) particle present in the Standard Model.

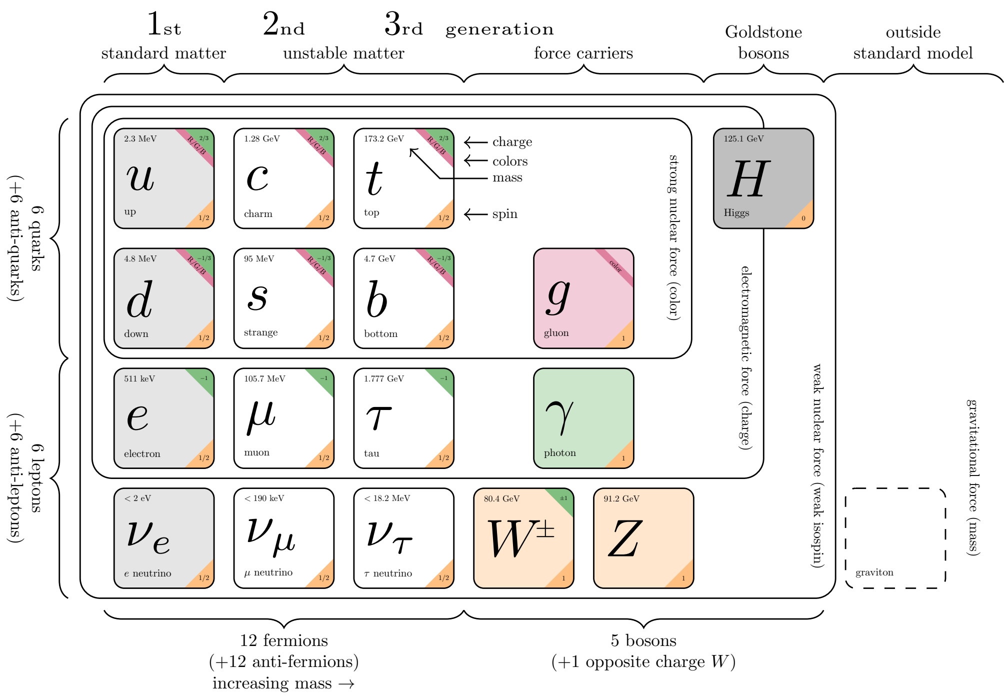

FIGURE 2.1: The Standard Model Table includes the elementary particles and the mediators of the fundamental forces. The first three columns indicate the three generations of the *fermions*, which are the known constituents of the matter. The fourth column consists of the force mediators, namely, *gauge bosons*. The fifth column covers the Higgs bosons. It should be noted, however, that the proposed mediator of the gravitational force, the graviton, remains a hypothesis and has yet to be described by the Standard Model. The figure is taken from [6].

While the Standard Model provides a comprehensive framework for understanding the formation of the universe and the existence of the particles has been successfully validated through experiments, it has unsolved questions as listed below:

1. **Carrier of gravity**: The Standard Model does not incorporate one of the four fundamental forces—gravity. While gravity has been described by the theory of General Relativity, the hypothesized carrier particle, the graviton, is not consistent with the mathematics of the Standard Model.
2. **Dark matter and energy**: Dark matter and dark energy constitute approximately 95 % of the total mass-energy content of the universe. However, dark matter does not interact with any of the fields that are addressed in the Standard Model. Dark energy, which is responsible for the expansion of the universe, was indirectly observed by the Hubble Space Telescope, and yet it is not described in the Standard Model.
3. **Mass of the neutrino**: While the Standard Model assumes that neutrinos are massless, neutrino oscillation experiments have revealed that neutrino has a non-zero mass [7]. However, the mass and the mechanism by which they gain mass remain unknown.
4. **Baryon Asymmetry**: The observed asymmetry in the abundance of the matter and antimatter cannot be explained by the Standard Model.
5. **Hierarchy Problem**: There is a vast gap between the electroweak scale (approximately 246 GeV) and the Planck scale (around 10^{19} GeV), where gravitational effects become significant. The physical mass of the Higgs boson should include an enormous quantum correction from interactions with high-energy particles up to the Planck scale, which would drive its mass to be near the Planck scale, rather than at the electroweak scale. The apparent fine-tuning needed to cancel out these large corrections and yield a relatively low mass for the Higgs boson is seen as unnatural. More details are explained in [8].

The existence of many unsolved questions that the Standard Model does not address motivates the development of additional theories and experiments. A well-recognized extension of the Standard Model, the Supersymmetry (SUSY) [9], resolves the Hierarchy Problem by introducing a partner particle with a half-integer spin difference to each particle in the Standard Model. The predictions made by SUSY and various other theories beyond the Standard Model have not been observed in experiments, prompting the upgrade of current experimental setups, including the Large Hadron Collider.

2.1.2 The Large Hadron Collider

Since the discovery of the nucleus and atoms, scattering experiments have stood out as one of the methods to investigate matter at the smallest scale. With higher collision energies, there is an increased likelihood of producing unknown collision products that could be the fundamental elements of the universe. The Large Hadron Collider (LHC), the current largest and highest-energy particle accelerator and collider, was designed for this purpose. Constructed at the European Organization for Nuclear Research (CERN) from 1998 to 2008, it resides at a mean depth of 100 m beneath the France–Switzerland border, near Geneva [10]. The LHC features a circular storage ring with a 27 km circumference, comprising two parallel beam pipes. It is primarily designed for colliding proton-proton beams but is also capable of other collisions such as proton-ion or ion-ion.

Figure 2.2 provides a schematic drawing of the CERN accelerator complex, depicting the beam path from creation to collision. In the case of LHC proton-proton collision, the proton beam originates from a linear accelerator (LINAC4) [11] where the hydrogen anions are accelerated to the energy of 160 MeV. Subsequently, the electrons are stripped away from the anions, leaving only the protons to be injected into the Proton Synchrotron Booster (BOOSTER). The BOOSTER accelerates and propels protons even further, sending them to the Proton Synchrotron (PS) with an energy of 1.4 GeV. Their energy is subsequently raised to 25 GeV within the PS, and these protons are directed to the Super Proton Synchrotron (SPS), where the particles are furthermore accelerated to an energy of 450 GeV [12] before injected into the LHC storage ring. Finally, the proton beam is guided into two beam pipes circulating the ring in opposite directions, containing a nominal of up to 2808 bunches of protons (approximately 10^{11} protons per bunch) and 25 ns bunch spacing [10].

Inside the LHC storage ring, numerous superconducting dipole and quadrupole magnets along the path maintain the beams in orbit and focused. Proton beams are accelerated to a maximum of 7 TeV, under the influence of 16 superconducting radio frequency cavities. The operating temperature of the LHC is at 1.9K, using a superfluid helium cooling system to maintain the superconductivity of the magnets. This creates a high magnetic field, keeping the circulated beams at their nominal trajectories. With two beams circulating in opposite directions, they collide at four dedicated interaction points where detection and measurements of the products take place.

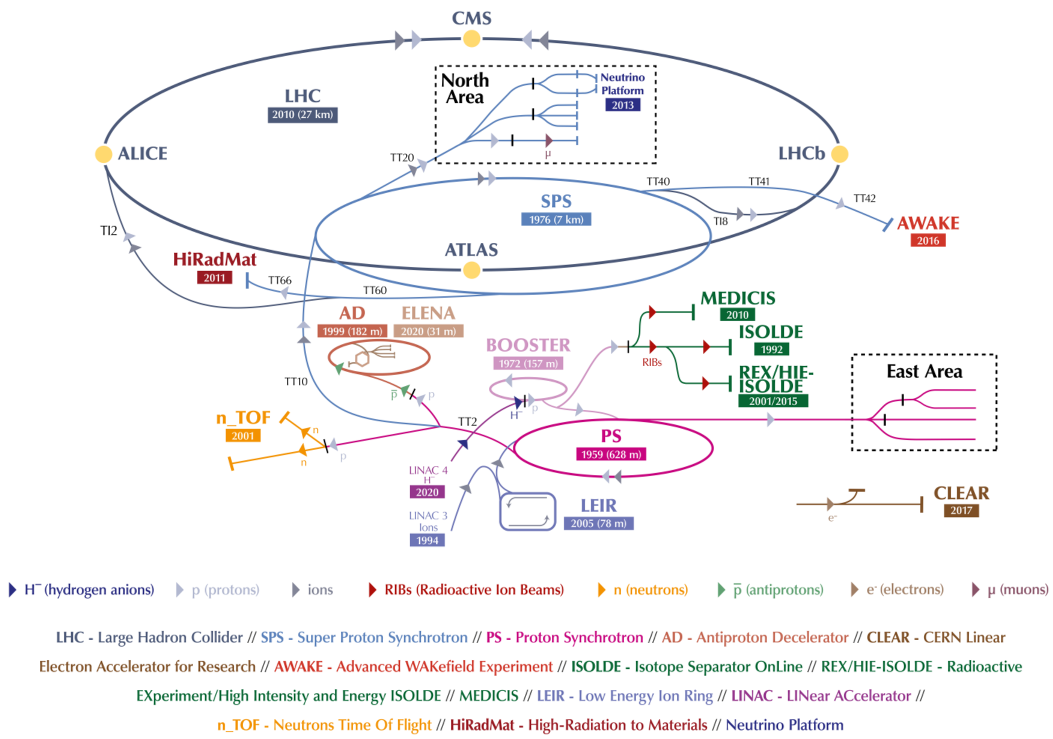

FIGURE 2.2: The CERN accelerator complex, layout in 2022. The particle beam undergoes a series of acceleration processes. Proton beams, initially generated by LINAC4, progress through sequential accelerations in BOOSTER, PS, and SPS. Eventually, they reach the LHC storage ring, where they undergo further acceleration to reach their designated energy levels and collide at the four interaction points. [13]

The interaction point of the two beams hosts four major experimental apparatuses: CMS (Compact Muon Solenoid), ATLAS (A Toroidal LHC Apparatus), ALICE (A Large Ion Collider Experiment), and LHCb (Large Hadron Collider beauty). Each apparatus detects secondary particles emerging from the collisions of primary particles to explore various physics objectives. The CMS and ATLAS experiments serve multiple purposes, including the search for the Higgs boson, investigations of the top quark, and exploration beyond the Standard Model. The ALICE experiment is specifically designed to study strongly interacting matter at extreme energy densities, where a phase of matter called quark-gluon plasma forms. The LHCb experiment focuses on understanding matter-antimatter asymmetry in the universe through the study of B-mesons physics. In the ongoing operation, a center-of-mass energy of 13.6 TeV is achieved, potentially resulting in the production of new particles that can be observed by the four experiments.

In the detection of collision production for new physics, high energy is not the only crucial factor; the number of useful interactions is important as well. The quantity that measures the ability to produce the amount of interactions is called the luminosity ($\mathcal{L}$). The instantaneous luminosity is defined as the proportionality factor between the number of events per second $\mathrm{d}N_i/\mathrm{d}t$ and the cross-section σ_i for a specific process i [14],

$$\mathcal{L} \cdot \sigma_i = \frac{\mathrm{d}N_i}{\mathrm{d}t}\,. \tag{2.1}$$

By measuring the event rate of a process with a known cross-section, luminosity can be calculated. The instantaneous luminosity of the two colliding proton beams can be written as:

$$\mathcal{L} = \frac{N_b N_p^2 f}{A}\,, \tag{2.2}$$

where N_b is the number of bunches, N_p represents the number of protons per bunch, f indicates the revolution frequency around the ring, and A denotes the effective cross-section of the two beams at the interaction point.

The LHC is designed to operate at an instantaneous luminosity of $\mathcal{L} = 10^{34}\,\mathrm{cm}^{-2}\,\mathrm{s}^{-1}$ with a nominal filling of $N_p = 1.15 \times 10^{11}$ protons per bunch. The goal of achieving the desired instantaneous luminosity can be realized by modifying the operating parameters such as minimizing the cross-section. As of 2017, the recorded value has exceeded the nominal value by a factor of 2 [15].

The total number of observable events (N_i) is proportional to the integrated luminosity ($\mathcal{L}_{int}$), which is the luminosity integrated over time T:

$$N_i = \sigma_i \cdot \int_0^T \mathcal{L}(t)\,\mathrm{d}t = \sigma_i \cdot \mathcal{L}_{int}\,. \tag{2.3}$$

The integrated luminosity $\mathcal{L}_{int}$ is generally expressed in inverse femtobarn (fb^{-1}), where $1\,\mathrm{b} = 1 \times 10^{-24}\,\mathrm{cm}^2$. Figure 2.3 displays the integrated luminosity delivered by the LHC up until the year 2023, alongside the recorded values by the CMS experiment. As of 2023, the LHC has generated data equivalent to $266\,\mathrm{fb}^{-1}$ from proton collisions, and the CMS experiment has recorded $246\,\mathrm{fb}^{-1}$.

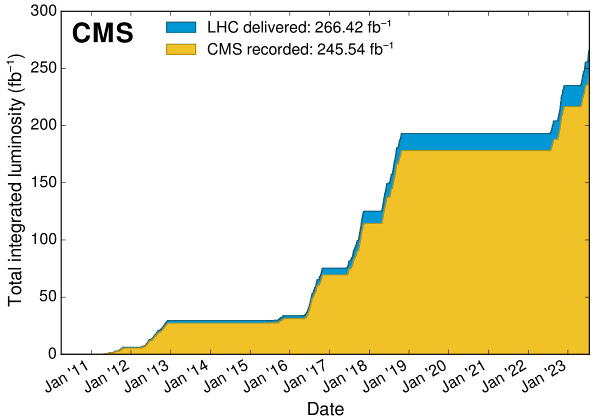

FIGURE 2.3: Evolution of the integrated luminosity throughout the operating years from 2011 to 2023. Blue indicates the luminosity delivered by the LHC and orange shows the value recorded by the CMS experiment. [16]

2.2 The Compact Muon Solenoid Experiment

The total proton-proton cross-section for $\sqrt{s} = 14\,\mathrm{TeV}$ collisions at the LHC is approximately 110 mb. At the design luminosity of $\mathcal{L} = 10^{34}\,\mathrm{cm}^{-2}\mathrm{s}^{-1}$, this corresponds to an inelastic event rate on the order of 10^9 events per second. With a bunch crossing frequency of 40 MHz, this results in an average pile-up of approximately 25 proton-proton interactions per bunch crossing. *Pile-up* refers to the simultaneous occurrence of particle products from multiple proton-proton interactions in a single bunch crossing. To mitigate the effects of pile-up, detectors require fast electronics along with precise tracking and trigger systems, which will be introduced later in this section. Additional advanced algorithms used in offline data analysis, such as pile-up per particle identification (PUPPI) [17], have been developed to mitigate the impact of pile-up on physics observables by using local event properties and tracking information.

In addition to addressing the technical obstacles that a detector has to overcome, the Compact Muon Solenoid (CMS) experiment is designed to investigate a variety of physics phenomena. This includes the detailed study of the Higgs boson [18], measurement of its properties, exploration of the electroweak sector and vector boson scattering, precision measurement of the Standard Model particles, investigations in flavor physics, heavy-ion physics, and the search for new physics such as SUSY. Therefore, the detector requirements for CMS to meet the above studies are stated in [19] as follows:

1. Good muon identification and momentum resolution over a wide range of momenta and angles, good dimuon mass resolution (with approximately 1 % at 100 GeV)), and the ability to determine unambiguously the charge of muons with $p < 1\,\mathrm{TeV}$.

2. Good charged-particle momentum resolution and reconstruction efficiency in the tracking detector. Efficient triggering and offline tagging of τ and b-jets, requiring pixel detectors close to the interaction region.

3. Good electromagnetic energy resolution, good diphoton and dielectron mass resolution (with approximately 1 % at 100 GeV), wide geometric coverage, π^0

rejection, and efficient photon and lepton isolation at high luminosity.

4. Good missing-transverse-energy and dijet-mass resolution, requiring hadron calorimeters with a large hermetic geometric coverage and with fine lateral segmentation.

The CMS detector [19] is a large, multipurpose apparatus located at one of the beam interaction points at the LHC. It has a size of 21.6 meters in length and 14.6 meters in diameter, with a total weight of 14,000 tons. Installed in an underground cavern near the village of Cessy in France, the detector components are arranged concentrically in a cylindrical shape around the beam pipe.

The main feature of the CMS detector is its capability to achieve excellent identification of the electrons, muons, photons, and hadrons, as well as precise momentum resolution. This is accomplished by the subdetectors illustrated in Figure 2.4. The central component comprises a superconducting solenoid with a 6 m inner diameter and 12.5 m length, generating a magnetic field of 3.8 T that bends the trajectories of the charged particles due to Lorentz force. Within the magnetic volume, the inner part is the tracking system containing the silicon pixel and strip tracker that detects the trajectories and vertices of the charged particles. The Electromagnetic Calorimeter (ECAL), composed of lead tungstate crystals, measures the energy of electromagnetic particles such as electrons and photons, while the Hadron Calorimeter (HCAL), constructed from brass and scintillator plates, measures the energy of hadrons, including protons and neutrons. Both ECAL and HCAL contain a barrel and two end-cap regions. The barrel layers are positioned to cover the lateral surface of the cylinder, while the end-cap layers extend coverage over the flat area of the cylinder. To achieve complete coverage across the entire 4π solid angle, which improves jet detection and transverse energy resolution, a forward calorimeter has been installed. The muon system, outside the solenoid, detects muons with gas-ionization-based detectors that are integrated into the steel flux-return yoke.

The coordinate system and relevant kinematic variables of CMS are detailed in [19]. In the system, the x-axis points towards the center of the LHC ring, while the z-axis aligns with the beamline in the clockwise direction. The corresponding polar coordinates are defined such that r represents the radial distance to the beam pipeline, θ is the polar angle measured with respect to the z-axis, and φ is the azimuthal angle measured from the x-axis. A commonly used quantity in particle physics, pseudorapidity (η), is introduced in this system and is defined as:

$$\eta = -\ln(\tan\frac{\theta}{2})\,. \tag{2.4}$$

Another important notation is p_T, which represents the momentum of the particle that is transverse to the beam.

Given the previously mentioned high instantaneous luminosity, the selection of events of interest is critical due to the data transmission and storage limitation. The CMS trigger system operates using a two-tier level: the first-level (L1) trigger and the high-level trigger (HLT). The L1 trigger uses the information from calorimeters and muon systems to select the events at a rate of 110 kHz, whereas the HLT runs a full event reconstruction optimized for fast processing at a rate of 2 kHz in the latest LHC run [21].

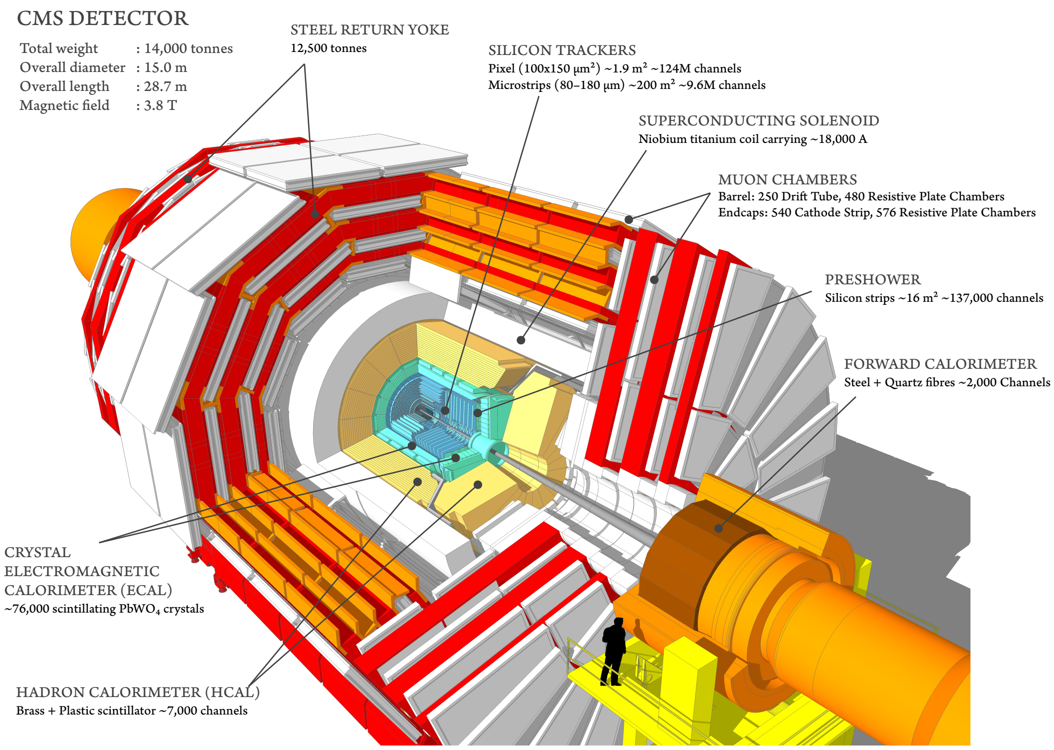

FIGURE 2.4: Cutaway diagrams of the current CMS detector after the upgrade in 2017 [20]. The subdetectors, starting from the center, include the silicon tracker, electromagnetic calorimeter, hadron calorimeter, superconducting solenoid, and the muon system within the steel flux-return yoke.

2.2.1 Tracking Silicon Detectors

The innermost layer of CMS, known as the tracking system or tracker, is responsible for recording particle trajectories, measuring the momentum of charged particles, and reconstructing secondary vertices. The tracker employs all-silicon detectors, which provide fast response, high granularity, and low occupancy [22]. It consists of two types of modules, pixel and strip modules, which are positioned in both the barrel and end-cap layers of the tracker, as depicted in Figure 2.5. The tracker provides coverage up to a pseudorapidity range of $|\eta| < 2.5$ [21].

Starting in 2017, pixel modules are arranged in four barrel layers at radii ranging from 29 mm to 160 mm and three additional layers in the end-cap region. Each pixel module consists of a silicon sensor with 160×416 pixels, each measuring the size of $100 \times 150\,\mu\text{m}^2$, and a sensor thickness of 285 μm. The pixel tracker offers a spatial resolution ranging from 13 μm to 20 μm [22].

Strip modules are distributed across ten barrel layers, extending to radii up to 1100 mm and twelve end-cap layers. The design of the strip sensors varies based on their position within the tracker, resulting in a sensor thickness ranging from 320 μm to 500 μm and a strip pitch between 80 μm and 180 μm. The outer layers have lower granularity and a larger pitch due to the lower hit occupancy. This leads to various spatial resolutions from 23 μm to 52 μm [23]. In Figure 2.5, four layers in the barrel and three rings in the end-caps are depicted in blue segments. In these layers, stereo modules with a second module mounted back-to-back with a stereo angle of 100 mrad are used. The stereo modules offer coarse measurements of an additional coordinate (z in the barrel and r in the end-caps) [21].

With the tracker placed in a magnetic field, the trajectory of a charged particle bends due to the Lorentz force. By equating the centripetal force (p_T/r) to the Lorentz force (qvB), the transverse momentum of the particle can be derived in natural unit form as:

$$p_{\mathrm{T}} = 0.3\,q\,B\,r\,, \tag{2.5}$$

where p_T is the transverse momentum in GeV, q is the charge of the particle in units of the elementary charge e, B is the magnetic field in tesla (T), and r is the radius of the particle's curvature in meters (m) [24]. The CMS tracker is designed to detect and track particles with transverse momentum p_T as low as 50 MeV within the range $|\eta| < 2.5$.

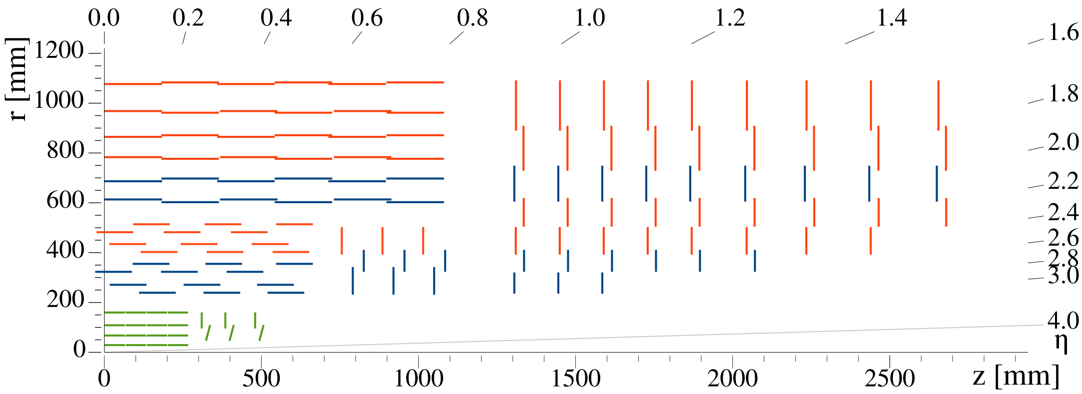

FIGURE 2.5: Schematic view of one quadrant in the r–z view of the CMS tracker. The pixel detector is shown in green segments. The single-sided and double-sided strip modules are depicted as red and blue segments, respectively.

2.2.2 Calorimeters

The calorimeters are typically made of high-density material and are designed to measure the deposited energy of the *particle shower* induced by a traversing particle. While some calorimeters are homogeneous, others, like sampling calorimeters, consist of alternating layers of different materials. The *particle shower*, also known as particle cascade, is a phenomenon where a particle interacts with dense matter and produces a cascade of secondary particles. There are two common types of calorimeter, depending on the nature of the primary particle and the interactions involved, the Electromagnetic Calorimeter (ECAL) and the Hadron Calorimeter (HCAL). In CMS, both ECAL and HCAL are installed between the tracker and the solenoid. To distinguish multiple particles and reconstruct jets with sufficient spatial resolution, calorimeters are segmented.

Electromagnetic Calorimeter

The CMS Electromagnetic Calorimeter (ECAL), shown in Figure 2.6, is a homogeneous calorimeter composed of 75,848 lead tungstate ($PbWO_4$) crystals situated in the barrel ECAL (EB) and end-cap ECAL (EE). Complementing the ECAL is an additional preshower calorimeter (ES), which is positioned in front of the end-cap region. The ES helps identify high-energy photons and electrons by detecting early showers before they reach the main calorimeter. Together, these systems provide a pseudorapidity coverage of $|\eta| < 3$.

The ECAL measures the position and energy of particles that interact through the electromagnetic force with the crystals, where energy loss is predominantly caused by bremsstrahlung for e^+/e^- or by e^+e^- pair production from the photons, leading to the production of additional photons. The scintillation light is subsequently detected by avalanche photodiodes in the barrel detector and vacuum phototriodes in the end-cap detector.

The crystal possesses characteristics, including a small radiation length of $X_0 = 0.89\,\mathrm{cm}$, a Molière radius of 2.2 cm, good radiation hardness, and a fast response time of less than 25 ns. The term X_0 is defined as the mean distance (in cm) into the material over which the energy of an electron is reduced by the factor 1/e. The Molière radius serves as a parameter that characterizes the lateral spread of electromagnetic showers in dense materials. With a depth of 23 cm providing $25.8\,X_0$ of the showering material, the ECAL can confine the entire electromagnetic shower within a compact volume and ensure good energy resolution. The ECAL also provides information on the arrival time of the electrons and photons, which is useful in the study of long-lived particles. More detailed information can be found in [23, 25].

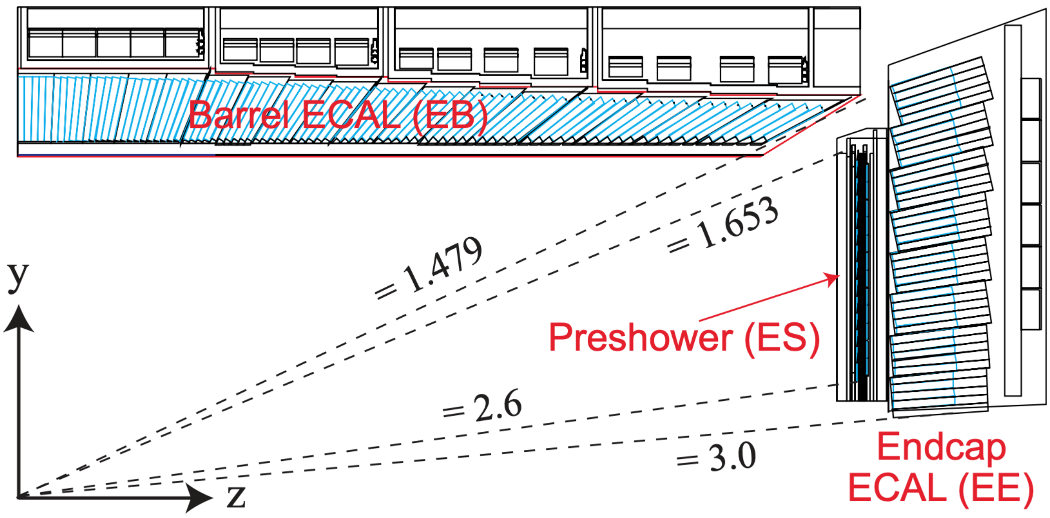

FIGURE 2.6: Geometric view of one-quarter of the electromagnetic calorimeter (ECAL). Presenting the arrangement of the barrel, end-caps, and the preshower in front. [23]

Hadron Calorimeter

The main components of the Hadron Calorimeter are located inside the solenoid and surround the ECAL. The HCAL is a sampling calorimeter made of alternating layers of absorbing material, and scintillation tiles. The HCAL is composed of four subdetectors, as depicted in Figure 2.7. The hadron barrel (HB) and the hadron end-cap (HE), positioned between the ECAL and the solenoid, are made of layers of brass plates interlaced with plastic scintillators. The brass absorber has a nuclear interaction length (λ_I) of 16.42 cm, provides a total depth of approximately $5.8\,\lambda_\mathrm{I}$ at 90° incidence [26]. The hadron forward (HF), situated beyond the end-caps, is made with steel and quartz fibers. The fibers detect the Cherenkov light produced by charged particles in the shower. Lastly, the hadron outer calorimeter (HO) consists of plastic scintillators, located between the solenoid and the muon system. Collectively, these subdetectors provide effective hermeticity, extending coverage up to a pseudorapidity range of $|\eta| < 5.2$.

The HCAL is designed to measure the energy of strongly interacting particles such as charged and neutral hadrons. Hadronic interactions, primarily dominated by strong force, result in the generation of hadronic showers within the brass plates. These showers subsequently interact with the scintillators, and the signal is then detected by the photomultipliers. Figure 2.7 illustrates the segmentation and grouping of layers in the HE, HB, and HO, which are read out by Silicon Photomultipliers (SiPMs), while the HF is read out by Photomultiplier Tubes (PMTs).

The jet energy resolution according to the [21], combining the information from the ECAL and the HCAL, amounts to 15 % to 20 % at 30 GeV, 10 % at 100GeV, and 5 % at 1 TeV.

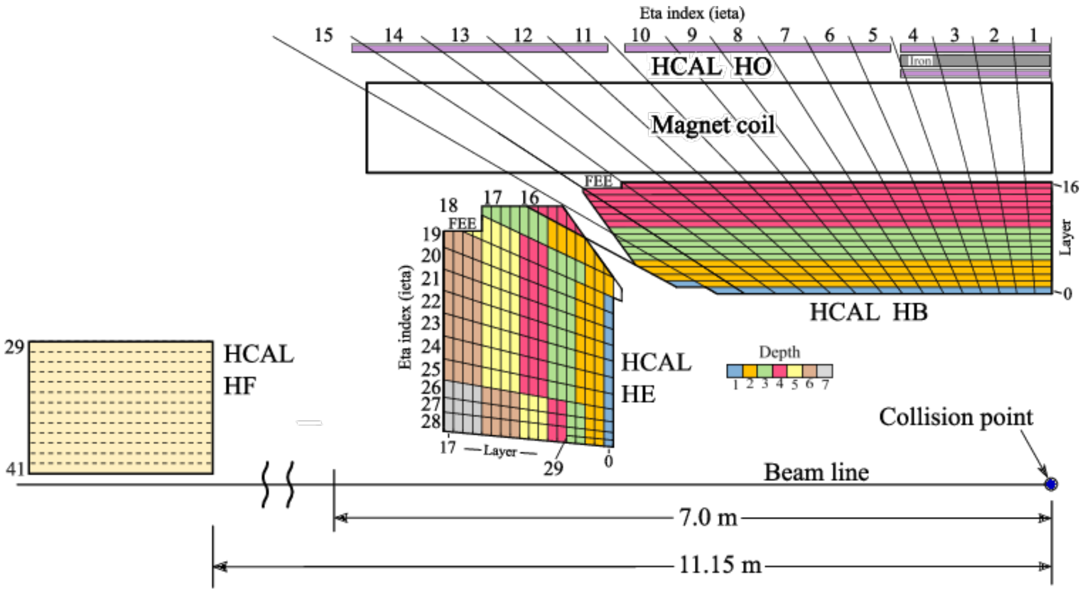

FIGURE 2.7: Geometric view of one-quarter of the hadron calorimeter(HCAL). Showing the arrangement of the four major components: the barrel calorimeter (HB), the end-cap calorimeter (HE), the tail-catching outer calorimeter (HO), and the additional forward calorimeter (HF). [21]

2.2.3 The Superconducting Solenoid

One of the key features of the CMS experiment is its large superconducting solenoid, generating a magnetic field of 3.8 T. A photo of the open detector with a visible solenoid magnet cryostat is shown in Figure 2.8. The solenoid coil is constructed with Niobium-Titanium (Nb_3Ti). It is surrounded by an iron return yoke that confines the magnetic field and only muons and neutrinos escape beyond the solenoid.

The high magnetic field bends the trajectories of the charged particles and enables precise momentum measurement in conjunction with the accurate position measurements provided by the tracker. With a length of 12.5 m and an inner diameter of 6 m, the solenoid effectively encloses the volume occupied by the tracker and calorimeters. This design ensures that the particles do not interact with the solenoid, preventing energy loss.

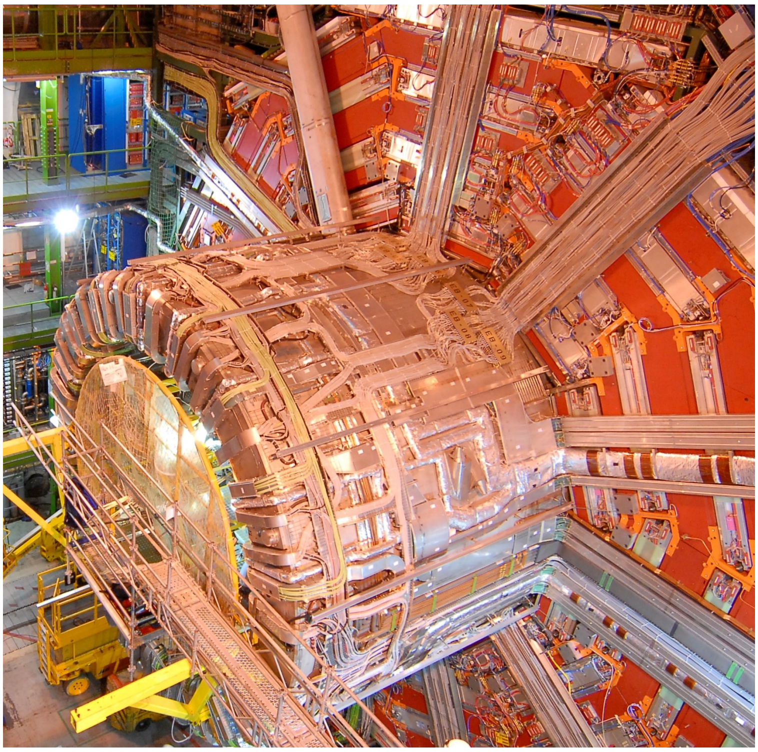

FIGURE 2.8: The solenoid magnet cryostat of the CMS detector. [21]

2.2.4 The Muon System

Another key feature that lends its name to the CMS detector is the muon system. Muons are anticipated to be produced in the decay of heavy particles, showing a signature of interesting physics. With the characteristic of being minimum ionizing particles (MIPs), muons deposit a relatively constant amount of energy as they pass through a material. Thus, they can penetrate the calorimeters and be detected efficiently by the muon system.

The muon system is placed in the outermost part of the CMS detector and is embedded into the flux-return yoke that is mentioned in Section 2.2.3. The objectives include the identification of muons, the precise determination of muon momentum achieved by the 2 T magnetic return field, and the contribution to the trigger system by providing well-identified muon signals. The muon system comprises four gaseous subdetectors, including the drift tubes (DTs), the cathode strip chambers (CSCs), the resistive-plate chambers (RPCs), and the gas electron multiplier (GEM) detector as depicted in Figure 2.9.

The drift tube detector is located in the barrel region, covering a pseudorapidity range up to $|\eta| < 1.2$. Filled with a gas mixture of Ar and CO_2, each tube has an electrode positioned at the center of each tube and cathodes along its borders. Charged particles traversing through the detector induce ionized electrons due to the electric field generated.

The cathode strip chambers (CSCs) are installed in the end-cap region ($0.9 < |\eta| < 2.4$) where the magnetic field and the muon flux are higher than DTs. Filled with a gas mixture of Ar, CO_2, and CF_4, these chambers comprise layers of cathode strips arranged perpendicular to the anode wires, providing a spatial resolution of 50 µm to 140 µm and contributing to the CMS Level-1 Trigger system.

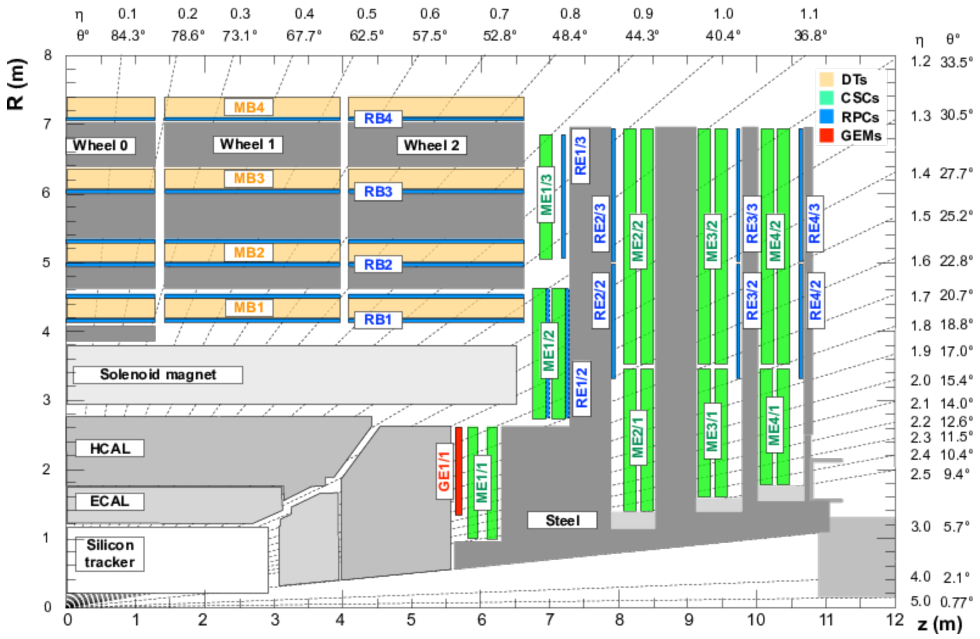

FIGURE 2.9: The schematic view of a CMS detector quadrant. The muon system is shown in color where the drift tubes (DTs) are labeled as MB, cathode strip chambers (CSCs) are marked as ME, resistive plate chambers (RPCs) are labeled RB and RE, and gas electron multipliers (GEMs) captioned with GE. The magnet yoke is represented by the dark gray areas. [21]

The resistive plate chambers (RPCs) are arranged throughout the barrel and end-cap regions, providing coverage within the pseudorapidity range up to $|\eta| < 1.9$. The fundamental structure of RPCs involves two layers, each composed of high-resistivity laminate plates. These plates are separated by a small gas-filled gap containing a mixture of gases such as $C_2H_2F_4$, i-C_4H_{10}, and SF_6. Despite having a coarser spatial resolution compared to the DT and CSC, its superb time resolution of 1.5 ns ensures the contribution to the bunch crossing assignment for muons at the trigger level.

The fourth subdetector that has recently been upgraded in the muon system is the gas electron multipliers (GEMs). The GEMs with better radiation hardness were installed as the first muon layer, covering a pseudorapidity range of $1.55 < |\eta| < 2.18$, to cope with the maximum hit rate in the forward region. It is a foil made of insulating polymer covered by conductors. Operated with a gas mixture of Ar and CO_2, ionized electrons accelerate through the foil holes in the electric field and are subsequently read out by strips with a pitch of 0.6 mm to 1.2 mm. The insertion of the GEM chambers enhances the lever arm traversed by muons by a factor of $2.4 \sim 3.5$, compared to CSC alone. This results in a large reduction in the L1 trigger rate while improving the muon trigger momentum resolution and maintaining high trigger efficiency for low transverse momentum muons [21, 27].

2.2.5 The Trigger and Data Acquisition System

The current LHC delivers proton-proton collision with a center-of-mass energy of 13.6 TeV. It has reached an instantaneous luminosity of $2.1 \times 10^{34}\,\mathrm{cm^{-2}s^{-1}}$ at 40 MHz bunch crossing rate, giving an average pile-up of around 50 interactions per crossing [16, 28]. With the enormous data rate and the number of events, the zero-suppressed data size of one event recorded by the CMS detector is around 1 MB per 25 ns which exceeds the readout and storage capability of the current devices. Therefore, the trigger system accomplishes a reduction in the event rate to a few kHz, selectively triggering the storage of potentially interesting events based on physics motivations. The CMS trigger system achieves the data reduction by a two-level trigger, Level-1 (L1) and High-Level Trigger (HLT) where the data rate are reduced to 110 kHz and 2 kHz, respectively [29, 30]. The trigger algorithms rely on criteria that are applied to one or more objects of a specific category, like muons, hadronic jets, τ leptons, photons, or electrons, as well as quantities such as the scalar sum of transverse energy (H_T) and the energy corresponding to the vector sum of the transverse missing momentum (E_{T}^{miss}). Common criteria involve setting a cut on the transverse component of the object's energy E_{T} (or momentum p_{T}) and on its η. Information on the trigger algorithms and performance are described in [21, 28].

The Level-1 Trigger

The L1 trigger is a hardware-based system using Field Programmable Gate Arrays (FPGA) and high-bandwidth optical data communication links, enabling configurable selection algorithm and fast trigger decisions. It has a fixed latency that allows the data to be buffered in the pipeline memory in the readout electronics. With the limited latency of less than 4 µs, the trigger decisions are only based on coarse information from the calorimeters and the muon detectors. An overview of the current CMS Level-1 trigger system is illustrated in Figure 2.10. Simple regional reconstruction algorithms are processed in each subdetector system where trigger primitives (TP) are generated.

The information from the muon TP is subsequently used to reconstruct muon tracks within the track finder across the three distinct pseudorapidity regions. The reconstructed muon objects are then forwarded to a global muon trigger. In parallel, the calorimeter trigger reconstructs various physics objects, including electrons, photons, τ leptons, jets, and energy sum using the calorimeter TP. A global trigger correlates both muon and calorimeter triggers, targeting specific particle signatures and cuts, and generates an L1 acceptance signal. Upon receiving the L1 acceptance signal at the detector front-end, all subdetectors, including the tracker, ECAL, HCAL, and muon systems, transmit the buffered event data to the second stage of the trigger system, known as the HLT.

The High-Level Trigger

The HLT is a software-based system that runs in parallel on a farm of commercial Central Processing Units (CPUs) and Graphics Processing Units (GPUs). It processes the event data with more detailed reconstructions in real time and refines the event selection based on more complex criteria for offline storage and analysis. The HLT has a workflow of the so-called trigger paths, each corresponding to a dedicated trigger. The path consists of a sequence of algorithm modules performing a well-defined task such as the reconstruction of physics objects and making intermediate decisions based on specific physics requirements. Some generic trigger thresholds and rates in the Run starting in 2022 are reported in [21]. Accepted events by the HLT are forwarded for storage at the CERN computing center and for data quality monitoring.

Due to the limitation of the data acquisition rate, with a bandwidth of the data recorded on a disk at around a few GB/s, HLT data scouting is introduced. It has a reduced trigger threshold and data size containing only the most relevant physics information. In the year 2022, the HLT scouting data were recorded at

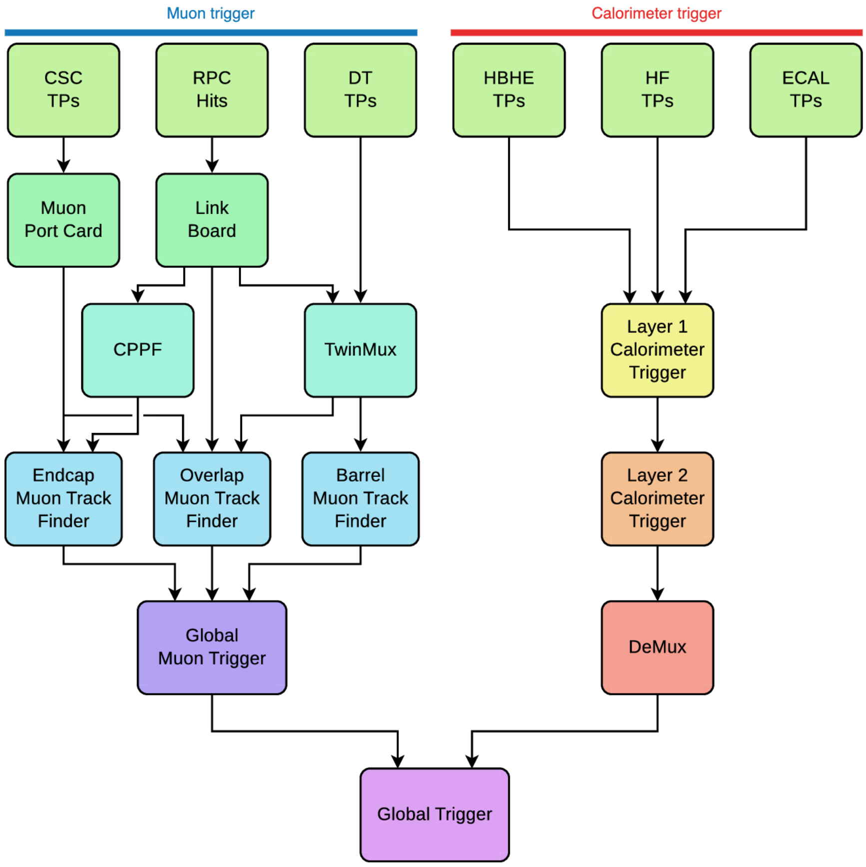

FIGURE 2.10: Overview of the current CMS Level-1 trigger system. Labels in the diagram correspond to trigger primitives (TPs), cathode strip chambers (CSC), drift tubes (DT), resistive plate chambers (RPC), concentration preprocessing and fan-out (CPPF), hadron calorimeter barrel (HB) and end-cap (HE), hadron calorimeter forward (HF), electromagnetic calorimeter (ECAL), demultiplexing card (DeMux). More details on each block are in [28].

a rate of 30 kHz with an event size of 7 kB. HLT scouting is capable of accessing low-momentum or low E_{T} objects with higher data rates and is suitable for studies such as dimuons and diphotons analysis. Another constraint is the bandwidth of the offline event reconstruction. Thus, to increase the storage rate, an extra sample data called the HLT parking data without reconstruction is stored at a rate of around 3 kHz. The parking data will only be reconstructed when the computing resources are available.

2.3 High Luminosity LHC and Upgrades

The LHC and its associated apparatus experiments like CMS and ATLAS, as mentioned in the previous sections, offer the opportunity to investigate the particles predicted in the Standard Model with remarkable precision. However, many questions are still unanswered by the SM. Rare processes demand a substantial accumulation of data, yet the existing detectors have only gathered statistics to a limited extent. This situation poses challenges when attempting to explore new processes beyond the Standard Model. A high-luminosity upgrade of the LHC starting in 2026 will allow the detectors to be exposed to increased data amount by a factor of 10 compared to the current levels and enhance the potential of these experiments for groundbreaking discoveries. In addition to the upcoming High Luminosity Large Hadron Collider (HL-LHC) upgrade, the detectors are necessary to address the challenges posed by increased luminosity and pile-up. These upgrades include the implementation of a new trigger system and subdetectors with enhanced radiation hardness capabilities, and a sufficient data acquisition system to handle the increased data amount.

2.3.1 The High Luminosity Era of the LHC

The current schedule for the physics program and the upgrade plan of the LHC and the HL-LHC is shown in Figure 2.11. The LHC has delivered around 200 fb^{-1} of integrated luminosity and has achieved an instantaneous luminosity of $2 \times 10^{-34}\,\text{cm}^{-2}\text{s}^{-1}$ in the second half of Run 2. An increase in luminosity up to $5 \times 10^{-34}\,\text{cm}^{-2}\text{s}^{-1}$ is anticipated following the long shutdown (LS) and upgrade from 2026 to 2028. The HL-LHC will extend the LHC program into the 2040s, featuring proton-proton collisions at $\sqrt{s} = 14\,\text{TeV}$ and an expected integrated luminosity of 3000 fb^{-1} for both the CMS and ATLAS experiments.

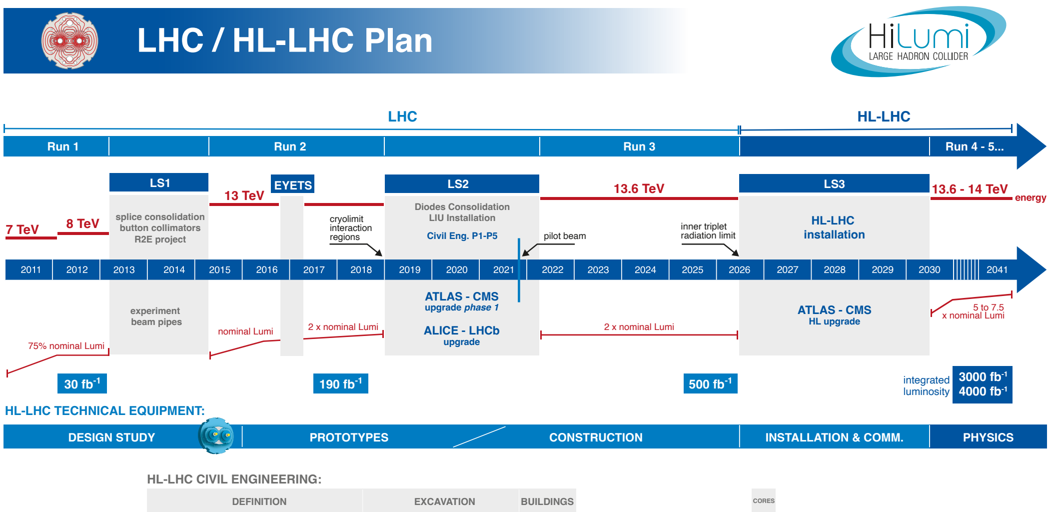

FIGURE 2.11: LHC / HL-LHC Plan (last updated October 2024)[31]. The upgrade of the high luminosity phase is scheduled during LS3 (from 2026 to 2030). Following this upgrade, the HL-LHC is anticipated to boost the instantaneous luminosity by a factor of five beyond the initial design specification and increase the integrated luminosity by a factor of approximately ten throughout the LHC operation period.

The upgrade of the LHC to the high luminosity era depends on crucial technological advancements. This involves advanced superconducting magnets with approximately 12 T to focus and navigate the particle beams with greater precision. Additionally, compact superconducting cavities, known as *crab cavities*, are integrated to tilt and project the beam, enabling better overlap between bunches and significantly increasing the luminosity of the collisions, and new technology for beam collimation and beam cleaning to maintain a clean collision environment. Detailed information on the upgrade technologies and the design of the accelerator for the HL-LHC can be found in the [32].

Several studies have highlighted the significant impact of the HL-LHC on physics research, particularly through enhanced precision in measuring Higgs properties and self-coupling. During HL-LHC, the accumulated data is expected to be 10 times the current dataset. By extrapolating the current data, the expected precision can be extracted. The main production channels of the Higgs boson, the gluon-fusion process (ggH), the vector-boson fusion process (VBF), the production mode associated with a vector boson (WH and ZH), the production mode associated with a pair of top quarks ($t\bar{t}H$), are expected to be observed with a precision range of a few percent. A summary projection of the precision achieved in each Higgs boson channel for both CMS and ATLAS is shown in Figure 2.12, as reported in [33].

To quantify a specific Higgs boson coupling strength, the κ-framework introduces a parameter known as the coupling modifier κ_p for each production or decay mode involving a particular particle p. This modifier scales the computed cross sections (σ), the partial decay width (Γ^f), and the total decay width (Γ_H) based on the corresponding SM predictions [34]. This scaling allows physicists to probe deviations from the SM expectations, where $\kappa_p = 1$ represents the SM expected value. A summary of the anticipated uncertainty in the sensitivity to the κ parameters is shown on the right side of Figure 2.12, displaying an overall uncertainty of less than 2% for bosonic particles, with others falling within a few percentage range. The measurement and evolution of the κ modifier over time are reported in [35], where it is depicted in Figure 2.13. This figure compares the κ value across various datasets: the initial discovery of the Higgs, the complete dataset from LHC Run 1, the dataset from Run 2, and the projected data from the HL-LHC for the CMS experiment. The results reveal that the uncertainty values for each coupling modifier are at the level of a few percent, emphasizing the importance of enhanced precision and deeper insights into physics studies during the upcoming high-luminosity era of the LHC.

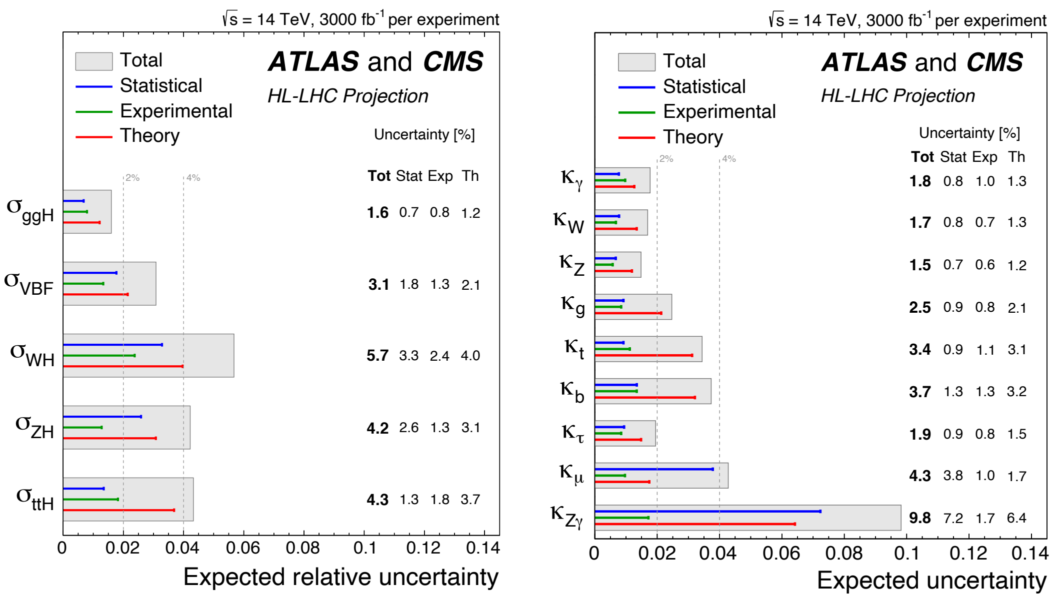

(a) (b)

FIGURE 2.12: Summary plots showing the total expected uncertainties on (a) the cross-sections of each production mode normalized to the SM predictions and (b) the coupling modifier parameters (κ), extrapolated by the combination of ATLAS and CMS measurements. The total uncertainty is represented by a gray box, with the statistical, experimental, and theoretical uncertainties shown by blue, green, and red lines, respectively. The figure was taken from [33].

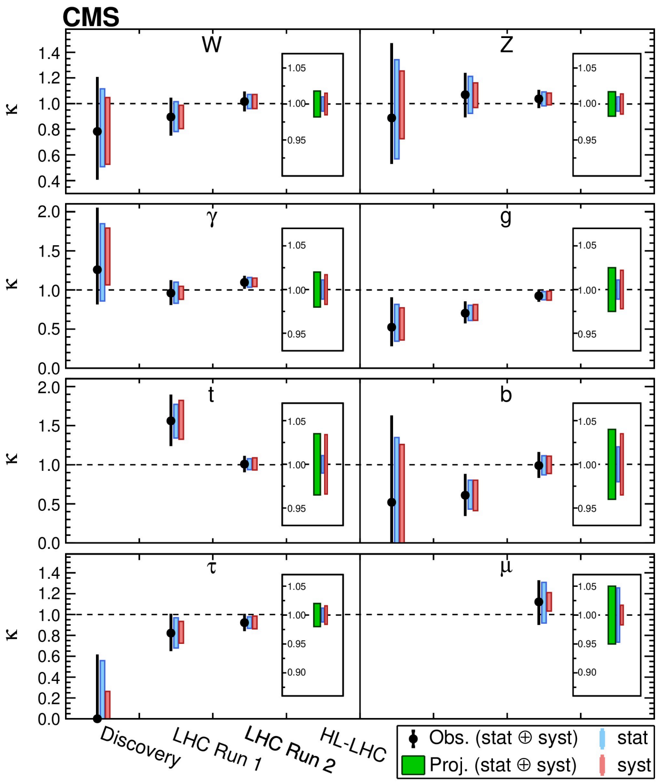

FIGURE 2.13: The analysis in [35] presents observed and projected values derived from the κ-framework fit across various data sets: at the initial discovery of the Higgs boson, using all data from LHC Run 1, within the data set examined in LHC Run 2, and including the projected uncertainty for the HL-LHC at $L = 3000\,\text{fb}^{-1}$. Missing measurements of κ_μ and κ_t are stems from inadequate sensitivity.

2.3.2 The CMS Phase-2 Upgrades

In the operation of the HL-LHC, the increase in luminosity results in a higher occurrence of pile-up, introducing five times more interactions per bunch crossing and a radiation dose impact potentially an order of magnitude greater on the major experiments. To cope with the anticipated challenges and the more demanding operational conditions, the CMS detector is currently undergoing a significant upgrade known as the **Phase-2 Upgrade**.

The increased exposure to radiation results in the deterioration of detector functionality and long-term effectiveness. The silicon tracker and forward calorimeters represent the two subdetectors primarily impacted by these conditions. Upon reaching 1.2 Grad of total ionizing dose and a 1 MeV neutron equivalent fluence of up to $2.3 \times 10^{16}\,\text{n}_\text{eq}/\text{cm}^2$ of the silicon tracker, the radiation induces surface and bulk damage and causes electronic defects. This, in turn, increases the sensor depletion voltage and the leakage current, and traps charge carriers. Consequently, this process increases the leakage current, traps charge carriers, and further affects the charge collection efficiency and detector signal. Performance studies indicate that the current tracker will be rendered unusable due to radiation damage under HL-LHC conditions, necessitating the complete replacement of the tracker. In a high-radiation environment, the calorimeter experiences a decrease in signal efficiency. This occurs as the crystals lose their translucence, preventing the efficient transmission of scintillation photons induced by particle interactions.

The escalated pile-up leads to a higher occurrence of false triggers, impacting track reconstruction performance. Thus the current silicon tracker will be entirely replaced. The new silicon strip and pixel tracker introduced in the Phase-2 upgrade are specifically designed to enhance granularity, minimize material within the tracking volume, provide robust pattern recognition, and extend tracking coverage up to $|\eta| = 3.8$. The existing pixel tracker, located in the innermost part known as the Inner Tracker, will be substituted by new hybrid pixel modules capable of withstanding a hit rate five times greater and a trigger rate 7.5 times higher than the present levels. The pixel sensors, ranging from 100 µm to 150 µm in thickness, are segmented into pixel dimensions of $25 \times 100\,\mu\text{m}^2$ or $50 \times 50\,\mu\text{m}^2$. Such specifications necessitate a low detection threshold within the readout chip. The additional coverage provided by the tracker upgrade is achieved through the disc-like structure in the forward direction. This forward tracker consists of pixel modules that enhance tracking performance in the forward region, improving forward jet reconstruction, missing transverse energy (MET) resolution, and lepton identification. The upgraded Outer Tracker incorporates double-sensor silicon modules equipped with strip and macro-pixel sensors. This design provides an on-module p_T discrimination information to the L1 trigger at 40 MHz and reduces the trigger rate to 750kHz. An overview of the tracker upgrade and the simulation studies for both inner and outer trackers is described in [36].

A new subdetector, MIP Timing Detector (MTD), will also be implemented in-between the tracker and electromagnetic calorimeter during the upgrade to untangle the pile-up, providing the CMS with a novel capability to precisely measure the production time of MIPs. Moreover, the MTD introduces enhanced capabilities for charged hadron identification and facilitates the search for long-lived particles. The addition of track-time information of 50 ps precision from the MTD will significantly improve the event reconstruction.

The end-cap calorimeter with higher granularity (HGCAL) will replace the present ECAL and HCAL end-caps. HGCAL will be based on robust and cost-effective hexagonal silicon sensors and highly segmented plastic scintillators with an on-scintillator SiPM readout. This feature provides a 3D measurement of showers and precise timing measurements.

To maintain a good muon trigger acceptance, enhancements are planned for the muon forward region. This involves an additional large area GEM station and two new generation RPC stations featuring low resistivity electrodes. The upgraded subdetectors will be capable of handling data rates up to a few kHz per cm^2. Furthermore, an extra station of GEM chambers will be installed behind the new forward calorimeter to cover the pseudorapidity region up to $|\eta| = 2.8$.

The upgrades implemented in each subdetector, along with the corresponding improvements in electronics and data acquisition capabilities designed for high luminosity, coupled with a more selective trigger system, allow the CMS detector to maintain optimal performance throughout the HL-LHC era. Figure 2.14 depicts the CMS detector with the subdetector upgrades for HL-LHC. A more detailed overview of the CMS detector upgrades can be found in [36, 37, 38, 39, 40, 41]. The expected performance studies are discussed in [42].

This thesis mainly focused on the upgrade studies of the Outer Tracker. A comprehensive introduction to the Outer Tracker upgrade, including its layout, design concepts, and p_T discrimination functionality, is provided in Chapter 4.

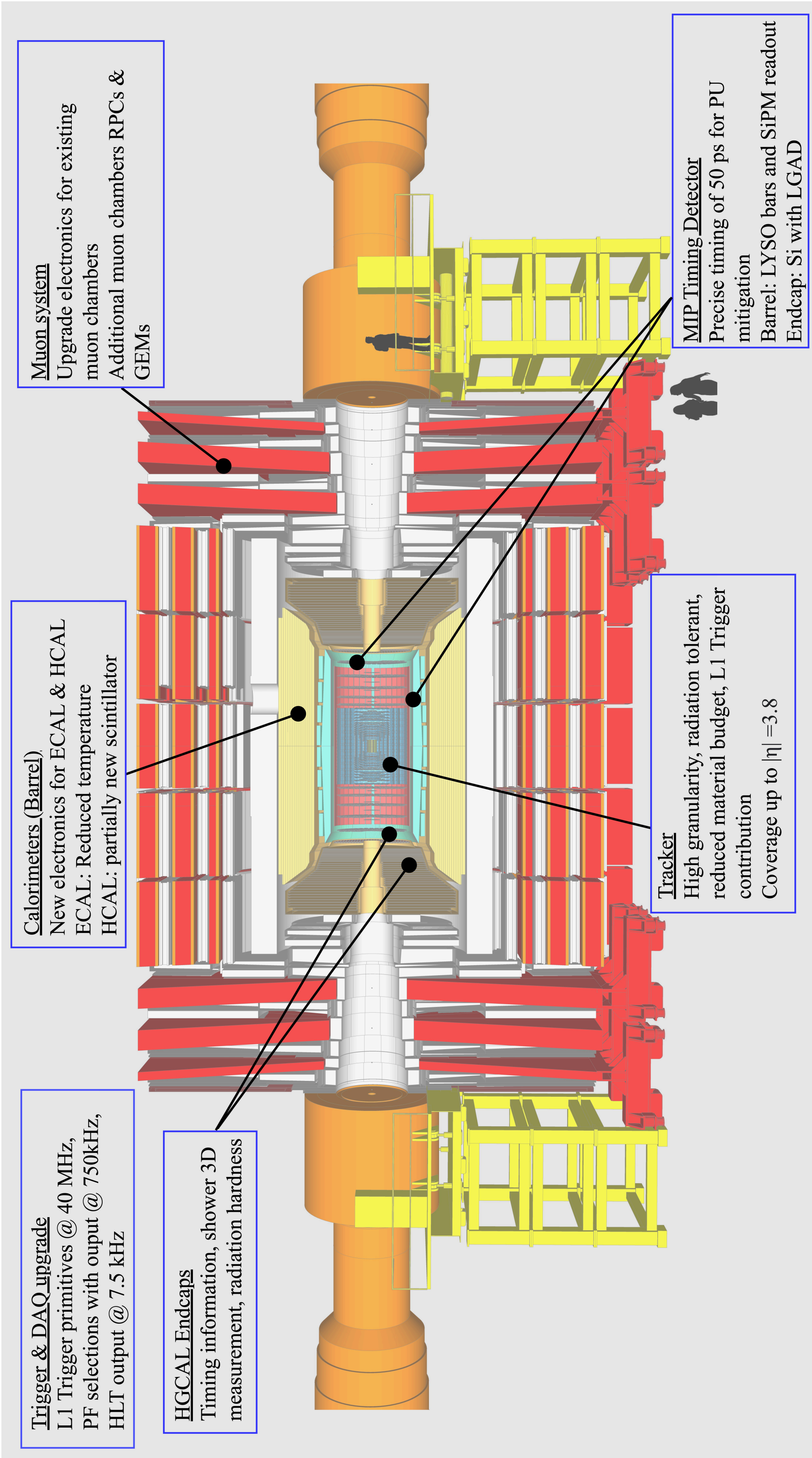

FIGURE 2.14: CMS detector and the subdetectors upgrades for HL-LHC.

Chapter 3

Semiconductor Tracking Detectors

Contents

In the early days of particle physics, devices such as cloud chambers, which visualize particle paths through condensation trails in a supersaturated vapor, and bubble chambers, where superheated liquid boils along ionization paths, were commonly used. Additionally, scintillation counters, which detect particles through light emitted by excited atoms, and spark chambers, which visualize particle paths via electrical discharges in a gas, were used. However, the transition to semiconductor detectors in the late 20th century marked a significant advancement in particle detection technology, especially in trajectory detection.

Semiconductors play a crucial role in particle detection due to their unique properties and advantages. As materials with a band gap significantly smaller than that of insulators, semiconductors are sensitive to the small amount of energy deposited by traversing particles. This sensitivity allows for precise detection, making them invaluable in a wide range of applications from high-energy physics experiments to medical imaging and environmental monitoring.

The primary advantage of using semiconductors as particle detectors lies in their ability to provide high-precision spatial resolution and good energy resolution in calorimeter applications. The segmentation can be small enough to deliver excellent resolution. The fine granularity and robustness enable the construction of large, intricate detector arrays that can accurately track the paths and energies of individual particles or jets. Furthermore, semiconductor detectors have fast response times, which is essential for real-time data acquisition and analysis in dynamic environments such as particle colliders with a bunch crossing rate of 40 MHz.

When a charged particle traverses a semiconductor, it loses energy through ionization, creating electron-hole pairs along its path. The number of these pairs is directly proportional to the energy deposited by the particle. By applying an electric field across the semiconductor, these charge carriers are collected at the electrodes, generating an electric signal. The signal can then be amplified and processed to determine the particle's momentum and trajectory within layers of detectors.

Semiconductors can offer a high signal-to-noise ratio due to their intrinsic properties as well. The purity and crystalline structure of semiconductor materials minimize background noise. The low noise level in semiconductor detectors allows for the detection of weak signals produced by a particle that loses only a small amount of energy. Additionally, semiconductor materials and designs can withstand significant levels of radiation without substantial degradation in performance. Integrated circuit technology can be directly applied to semiconductor detectors, enabling on-chip signal processing and readout, which simplifies the overall detector system design. Compared to other types of detectors, like gas chambers or scintillators, semiconductor detectors are compact.

Overall, with high precision and resolution, good charge collection efficiency and signal-to-noise ratio, radiation hardness, compactness, and versatility, semiconductor detectors are extensively used in the CMS Phase-2 upgrade to enhance performance and meet the demands of the High-Luminosity LHC. These detectors have been primarily used in the current Inner and Outer Tracker and will also be employed in the new Phase-2 upgrade Tracker and High Granularity Calorimeter areas, as shown in Figure 2.14.

3.1 Interaction of Charged Particles and Matter

The detection of particles is a fundamental aspect of experimental high-energy physics. It involves measuring properties such as energy, momentum, and charge of particles produced in interactions or decays. The effectiveness of particle detection hinges on understanding the principles of how charged particles interact with matter. These interactions include excitation, ionization, and radiative processes, which form the basis for the operation of particle detectors.

3.1.1 Interaction Processes

When charged particles traverse a medium, their energy loss is predominantly due to ionization and excitation of atoms in the material. Additional mechanisms, such as scattering and electron-positron annihilation, also contribute to the overall energy dissipation. The energy transferred from the particle to the electrons of the atoms causes excitation which raises electrons to higher energy levels, or ionization that ejects electrons from the atom.

Excitation involves the transfer of energy to bound electrons without liberating them. The bound electrons are elevated to higher energy states which eventually decay back to lower energy levels. This process often emits photons and the detection of these photons is another method used to study the properties of the incident-charged particles. Scintillation detectors, for example, exploit this phenomenon by using materials that emit visible light when excited by ionizing radiation.

Ionization occurs when the energy transferred to an electron is sufficient to overcome the binding energy, resulting in the ejection of the electron from the atom. The ejected electrons, along with the resulting positive ions, create ion pairs that can be detected by various means. The density of ion pairs along the path of the charged particle provides information about the particle's energy loss and its properties such as path length.

Bremsstrahlung radiation becomes the dominant energy loss mechanism over ionization at high energies, especially for electrons and positrons. It occurs when a low-mass charged particle is decelerated or deflected by the electric field of an atomic nucleus or another charged particle, leading to the emission of electromagnetic radiation. The probability and intensity of bremsstrahlung radiation increase with the kinetic energy of the incident particle and the atomic number of the target material. The emitted radiation has a continuous spectrum, with photon energies ranging up to the initial energy of the electron or positron.

3.1.2 Energy Loss

Charged particles, especially heavy charged particles such as protons and alpha particles, interact with matter predominantly through ionization and excitation of atomic electrons. As these particles traverse a material, they lose energy by displacing electrons from atoms (ionization) or raising electrons to higher energy states (excitation). This continuous energy loss allows for tracing the particle's path through the material. The rate of energy loss per unit in a thin layer dx due to ionization and excitation of a particle, known as stopping power, is described by the Bethe-Bloch equation:

$$-\left\langle \frac{dE}{dx} \right\rangle = K\frac{Z}{A}\rho\frac{z^2}{\beta^2}\left[\frac{1}{2}\ln\left(\frac{2m_ec^2\beta^2\gamma^2T_{max}}{I^2}\right) - \beta^2 - \frac{\delta(\beta\gamma)}{2} - \frac{C(\beta\gamma, I)}{Z}\right], \tag{3.1}$$

where $K = 4\pi N_A r_e^2 m_e c^2$ is a constant derived from fundamental physical constants, including Avogadro's number (N_A), the classical electron radius (r_e), and the electron mass (m_e). The density of the material is expressed as ρ. The charge of the incident particle is denoted by z, while Z and A represent the atomic number and atomic mass of the material, respectively. The particle's velocity relative to the speed of light is given by $\beta = \frac{v}{c}$, and the Lorentz factor is $\gamma = \frac{1}{\sqrt{1-\beta^2}}$. The term T_{max} denotes the maximum kinetic energy that can be transferred to a free electron in a single collision, and I is the mean excitation potential of the material. The two correction terms, density effect correction $\delta(\beta\gamma)$ and the shell correction (C/Z), are relevant to high and low energies, respectively.

The behavior of the Bethe-Bloch formula applies to particles with $0.1 \leq \beta\gamma \leq 1000$ and varies across different momentum ranges. At low momentum, the $\frac{1}{\beta^2}$ term dominates, leading to significant energy loss for slower particles. In the intermediate momentum range, the energy loss decreases as β increases. Particles in this range are known as minimum ionizing particles (MIPs) because they experience the least energy loss. At high momentum, the logarithmic term becomes prominent, and the energy loss increases gradually due to the $\ln(\gamma^2)$ dependence. An example of the mean energy loss per unit length for positive muons in copper is illustrated in Figure 3.1.

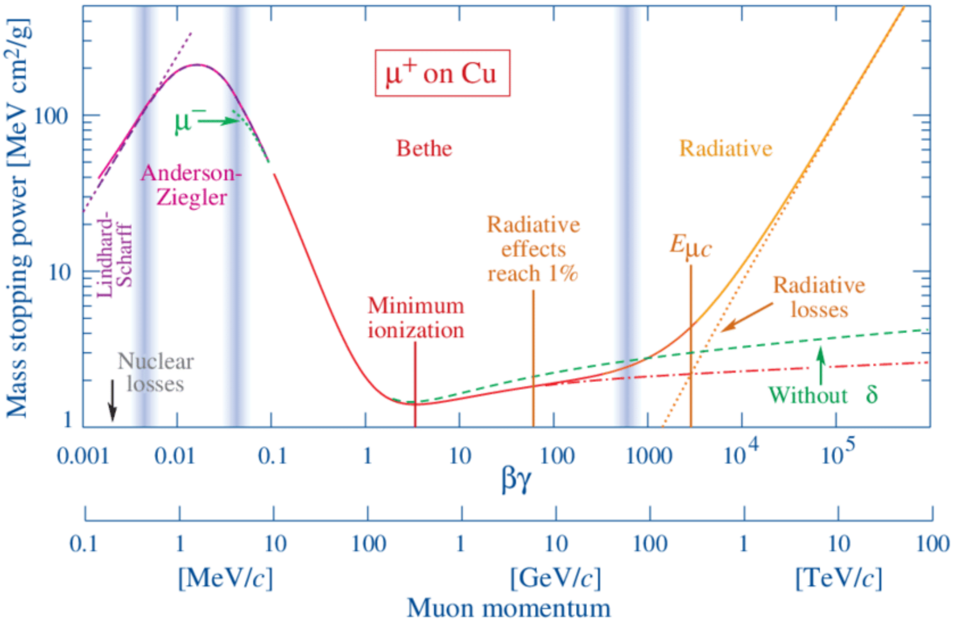

FIGURE 3.1: Mean energy loss per unit length for positive muons in copper as a function of $\beta\gamma = p/Mc$ over nine orders of magnitude in momentum. Solid curves indicate the total stopping power. For particles with $\beta\gamma < 0.1$, nuclear interactions dominate the energy loss. In the region of $0.1 \le \beta\gamma \le 1000$, the energy loss can be described by the Bethe-Bloch formula. At higher particle momentum, radiative processes play a significant role. Figure taken from [43].

The figure includes the stopping power of the positive muon in the regions of $\beta\gamma < 0.1$ and $\beta\gamma > 1000$ which are not covered by the Bethe-Bloch formula. For the low-momentum case, the binding energy of electrons in atoms becomes an important factor. When particles have lower energies, they may not have enough energy to ionize tightly bound inner-shell electrons. Instead, they interact more readily with loosely bound or free electrons. Thus, the energy loss due to ionization is influenced by the atomic structure of the material, specifically the binding energies of the electrons. For the high-momentum case, Bremsstrahlung radiation is a major contributor. The energy loss due to bremsstrahlung is given by the relation:

$$\left(\frac{dE}{dx}\right)_{\text{brems}} \propto \frac{Z(Z+1)\alpha}{m_e c^2} Q^2 E \ln\left(\frac{183}{Z^{1/3}}\right), \tag{3.2}$$

where Z is the atomic number of the matter, α is the fine-structure constant ($\approx \frac{1}{137}$), m_e is the electron mass, c is the speed of light, Q is the charge of the incident particle in units of the elementary charge, E is the energy of the incident particle, and $\ln\left(\frac{183}{Z^{1/3}}\right)$ is a correction factor that accounts for the atomic number dependence and the quantum mechanical nature of the bremsstrahlung process. The energy loss caused by Bremsstrahlung is proportional to the energy of the incident particles and dominates the regime of $\beta\gamma > 1000$. The critical energy $E_{\mu c}$ in the Figure indicates the energy at which ionization and bremsstrahlung contribute equally to the total energy loss.

3.1.3 Energy loss fluctuations

The Bethe-Bloch formula describes the average energy loss per unit length for heavy charged particles. However, the energy loss process is stochastic, meaning that fluctuations in energy loss exist between different particles even if the given initial energy and the traverse distance are the same.

The Landau-Vavilov distribution, often referred to as the Landau distribution, describes the distribution of energy loss fluctuations of charged particles as they pass through different thicknesses of matter. It is a non-Gaussian and asymmetric distribution with a long tail defined as:

$$f(\lambda) = \frac{1}{\pi}\int_0^\infty e^{-t\log t - \lambda t}\sin(\pi t)\,dt\,. \tag{3.3}$$

λ represents the scaled energy loss and obtains the characteristic of a most probable value (MPV) at $\lambda = -0.22278$ and a full width at half maximum (FWHM) of $\Delta\lambda = 4.018$. The tail in the Landau distribution arises from the large energy transfer events during ionizing collisions between the charged particle and atomic shell electrons, creating *delta* electrons and furthermore causing more ionization in the matter.

The shape of the distribution including the MPV and the FWHM, depends on the thickness x of the matter. For the thin layer of silicon detectors of thickness on the order of magnitude of micrometers, the Landau distribution fails to describe the energy loss. The MPV can be adequately evaluated with the Landau distribution, however, their energy loss distributions are wider than Landau's [44]. An example of the distribution in Figure 3.2 shows the energy deposition fluctuations for 500 MeV pions and the variation of the distributions in different thicknesses of silicon.

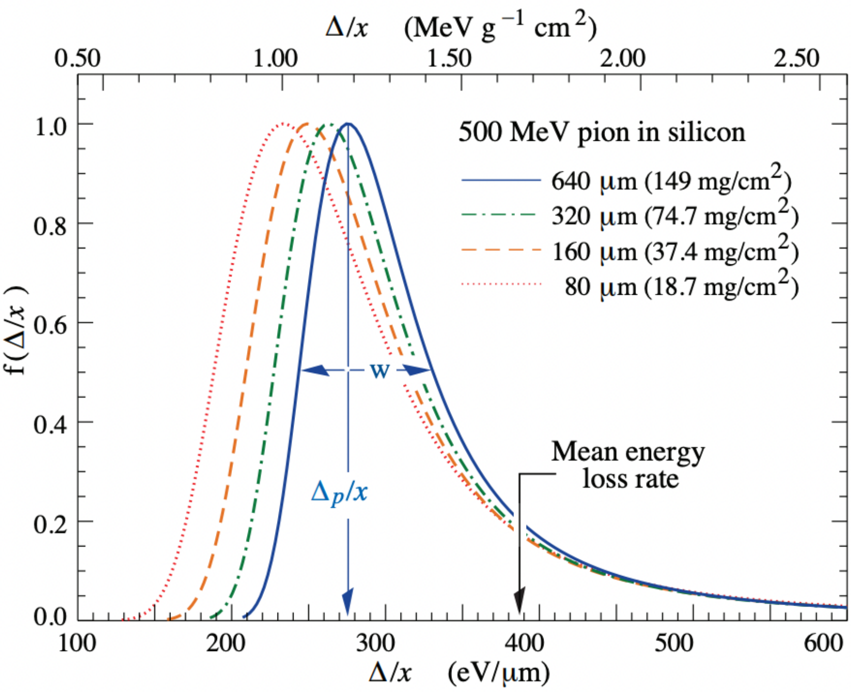

FIGURE 3.2: The energy deposition Δ per unit length x in different thickness of silicon for 500 MeV pions. It is normalized to the most probable value Δ_p/x and w is the full width at half maximum. [45]

The energy lost by ionization and excitation as a charged particle traverses in the medium creates electron-hole pairs. The number of electron-hole pairs created N, can be computed by the mean energy loss ΔE and the average energy needed to generate an electron-hole pair, mean ionization energy ε:

$$N = \frac{\Delta E}{\varepsilon}. \tag{3.4}$$

In the case of silicon, the mean ionization energy ε is 3.62 eV at 300K. The energy loss of a Minimum Ionizing Particles (MIP) in silicon follows a Landau distribution. The most probable value (MPV) of energy loss per micrometer is 280 eV, corresponding to the generation of approximately $78\,\mathrm{e}^-/\mathrm{h}^+$ pairs per micrometer. Silicon, relative to materials like gases and diamond, produces a higher number of electron-hole pairs because of its low ionization energy ε. Additionally, the smaller *Fano factor* in silicon reduces the statistical fluctuations in the number of pairs generated [46]. The Fano factor is a material-dependent parameter that accounts for the reduced variance in electron-hole pair generation compared to a purely Poisson process, due to energy losses in processes like phonon production. This leads to better energy resolution and a stronger detection signal when using silicon as the detection material.

3.2 Silicon Semiconducting Sensors

This thesis focuses on the tracking detector, a vital component of the particle detection apparatus that enables the identification of particle properties such as charge, momentum, and the origin of the interaction vertex. High spatial resolution and efficiency in tracking detectors allow for precise trajectory reconstruction and accurate vertex detection, which are crucial for determining particles' momentum and type, as well as identifying secondary vertices from particle decays in heavy-flavor and τ lepton physics. This precision is essential for separating closely spaced tracks, identifying short-lived particles, and reducing background noise, thereby enhancing the signal-to-noise ratio. Escalated pile-up and radiation in the future HL-LHC era require trackers to have a fast response time, quick readout, and radiation hardness.

After several years of research, silicon has been demonstrated to be the preferred material for particle detectors, particularly trackers, meeting these stringent requirements. Its well-established fabrication processes, cost-effectiveness, and ease of segmentation contribute to its widespread use.

3.2.1 Energy Band Structure

The energy band structure originates from the crystallized structure of silicon as shown in Figure 3.3. In isolated atoms, electrons occupy specific energy levels known as atomic orbitals. When two or more atoms are close enough, such as in the case of a crystal lattice, their atomic orbitals overlap, allowing electrons to tunnel among the atoms. This overlap and tunneling result in the splitting of atomic orbitals into many closely spaced energy levels. The dense packing of the energy levels leads to the formation of energy bands. At 0 K, electrons fill up these energy levels starting from the lowest energy states, obeying the Pauli exclusion principle by not occupying the same state. At 0 K, electrons occupy the energy bands up to Fermi level E_F. For temperatures above 0 K, the probability of an electron occupying an energy level at E_F is 50 %. Due to the Pauli principle, only a finite number of electrons can occupy the energy band. The valence band and the conduction band are the two ranges of electron energy levels that are used to describe the electrical conductivity of matter. The valence band is the highest range of electron energy levels that are fully filled with electrons under normal conditions. The conduction band is the energy band that is higher than the valence band. Electrons in the conduction band are free to move throughout the material because it is only partially filled, allowing them to conduct electric current. The gap between the top of the valence band and the bottom of the conduction band is the energy gap that determines whether a material is a conductor, semiconductor, or insulator. Figure 3.4 shows the band structure of the three categories.

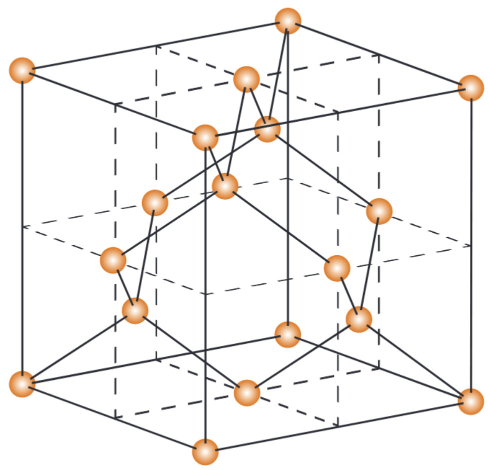

FIGURE 3.3: Cubic face-centered lattice structure of Silicon, a Diamond lattice. [24]

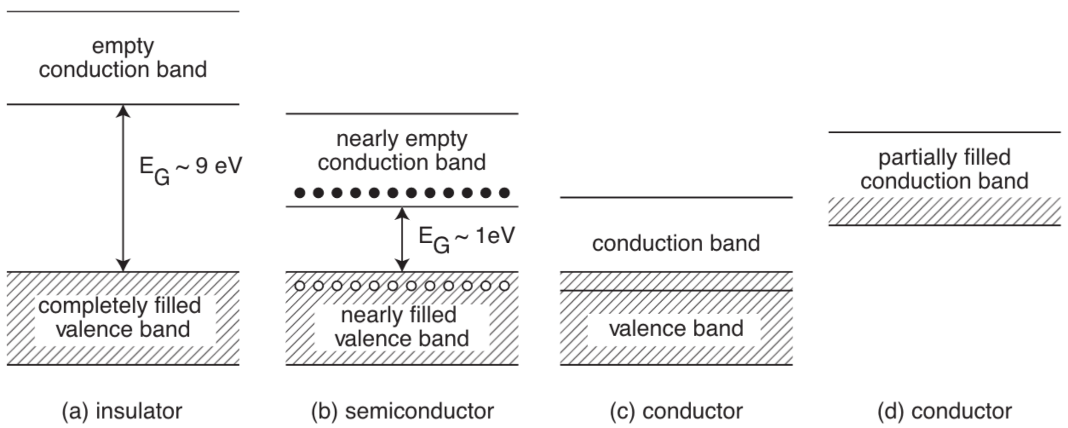

FIGURE 3.4: The energy band structures of an insulator, a semiconductor, and a conductor at temperatures above 0 K. E_G is the band gap between the valence and conduction band. [24]

The band gap depends on the lattice spacing; thus, temperature and pressure influence this gap. As a semiconductor, silicon has a small energy band gap of approximately 1.12 eV at $T = 300$ K. When an external electric field is applied or through thermal excitation, free electrons can be generated in the conduction band, leaving free holes in the valence band. These free holes then act as positive charge carriers. Silicon is one of the *indirect semiconductors*, which means that in the energy-momentum space (E-$\vec{k}$) of its band structure, the electrons in the conduction band and the holes in the valence band have different momentum wave vectors as illustrated in Figure 3.5 [24]. Consequently, an additional momentum transfer is needed for an electronic excitation compared to the *direct semiconductors*, where the peak of the valence band and the trough of the conduction band occur at the same k value. Therefore, the energy required to create an electron-hole pair in silicon is generally around 3.6 eV at $T = 300\,\mathrm{K}$, which is larger than its band gap of 1.12 eV.

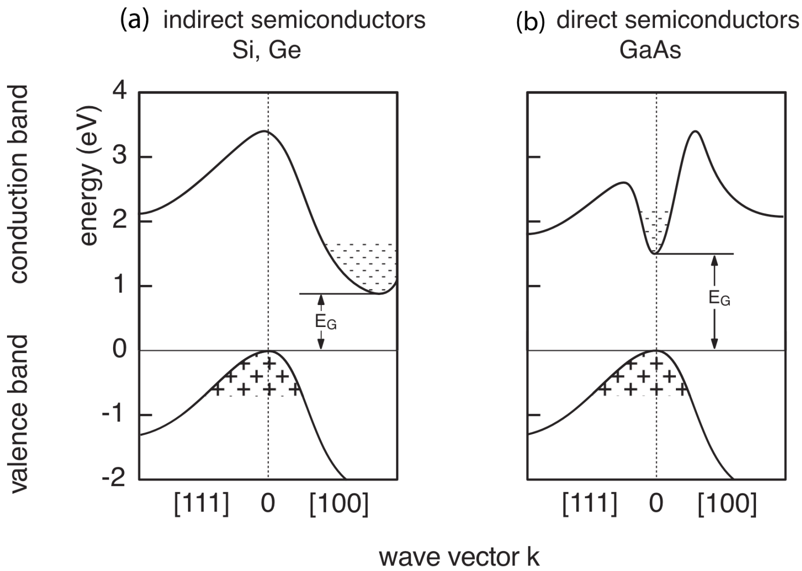

Figure 3.5: The band structure of (a) indirect semiconductor and (b) direct semiconductor. The indices $[klm]$ specify directions within the crystal, defined as $k\vec{a_1} + l\vec{a_2} + m\vec{a_3}$, where $\vec{a_i}$ are the base vectors of the cubic lattice cells. Plus signs and minus signs represent the holes in the valence bands and the electrons in the conduction bands respectively.[24]

3.2.2 Intrinsic and Extrinsic Semiconductors

The pure form of a semiconductor shown in Figure 3.6, free from any impurity atoms, is called an *intrinsic semiconductor*. In materials such as silicon and germanium, the number of free charge carriers is determined solely by the inherent properties of the semiconductor. As discussed in the previous section, electrons can be thermally excited from the valence band to the conduction band, leaving behind holes in the valence band. Both electrons in the conduction band and holes in the valence band act as free charge carriers, resulting in an intrinsic charge carrier density of approximately $n_i \approx 1.01 \times 10^{10}$ cm^{-3} at room temperature for silicon [24]. This intrinsic carrier concentration corresponds to a conductivity of $\sigma_i \simeq 2.8 \times 10^{-4}$ $(\Omega\mathrm{m})^{-1}$, in contrast to the conductivity of copper, which is $\sigma_{\mathrm{Cu}} \approx 10^8$ $(\Omega\mathrm{m})^{-1}$.

To achieve precise control over the conduction properties of semiconductor materials, *extrinsic semiconductors* are created by introducing impurities through a process called *doping*. Doping increases the number of free charge carriers, either electrons or holes, beyond what is naturally available in the pure material. As illustrated in Figure 3.7, specific doping methods can produce two extrinsic semiconductors: n-type and p-type.

In the case of silicon, n-type semiconductors are formed by doping with a group-V element, such as arsenic (As), which replaces some silicon atoms. The doping impurities are known as *donors*, as they introduce additional valence electrons compared to the host material and make electrons the majority carriers. Furthermore, this doping shifts the Fermi level E_F closer to the conduction band.

Conversely, in p-type semiconductors, some silicon atoms are replaced by a group-III element such as boron (B). The impurities are referred to as *acceptors* because they have fewer valence electrons than the host material. This deficiency creates holes in the valence band, which act as positive charge carriers, making holes the majority carriers. As a result, E_F shifts closer to the valence band.

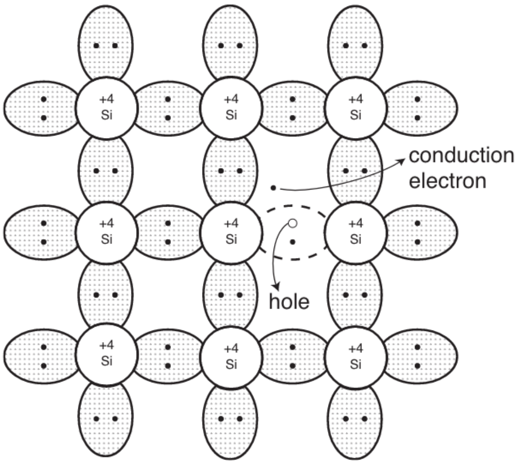

FIGURE 3.6: A schematic bonding drawing of intrinsic semiconductor, where thermal excitation can generate free charge carriers, including both electrons and holes, within the solid.[24]

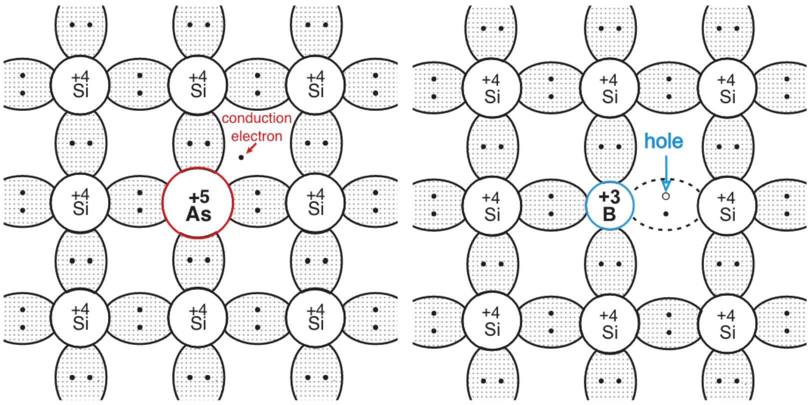

FIGURE 3.7: Schematic bonding diagrams of extrinsic semiconductors. The left diagram represents n-type silicon, and the right diagram shows p-type silicon, where the doping process substitutes one silicon atom with a group-V element in n-type and a group-III element in p-type.[24]

3.2.3 The p-n Junction

As mentioned above, for an intrinsic silicon sensor with a thickness of 300 µm and area of 1 cm^2, the number of free charge carriers is of the order of 10^9, whereas the detection signal from a traversing particle is of the order of 10^4 electron-hole pairs. To achieve a high signal-to-noise ratio, reducing the number of free charge carriers is crucial.

One effective method to achieve this reduction is by incorporating a *p*-*n* junction within the sensor. When *n*-type and *p*-type semiconductors are joined together, they form a *p-n junction*. Figure 3.8 illustrates the Fermi levels in the *p*-type, *n*-type, and *p*-*n* junction regions. In the *p*-type material, the Fermi level E_F is positioned closer to the valence band because the acceptor impurities introduce more holes into the valence band. Conversely, in the *n*-type material, E_F is situated closer to the conduction band due to the presence of donor impurities, which increase the number of electrons in the conduction band.

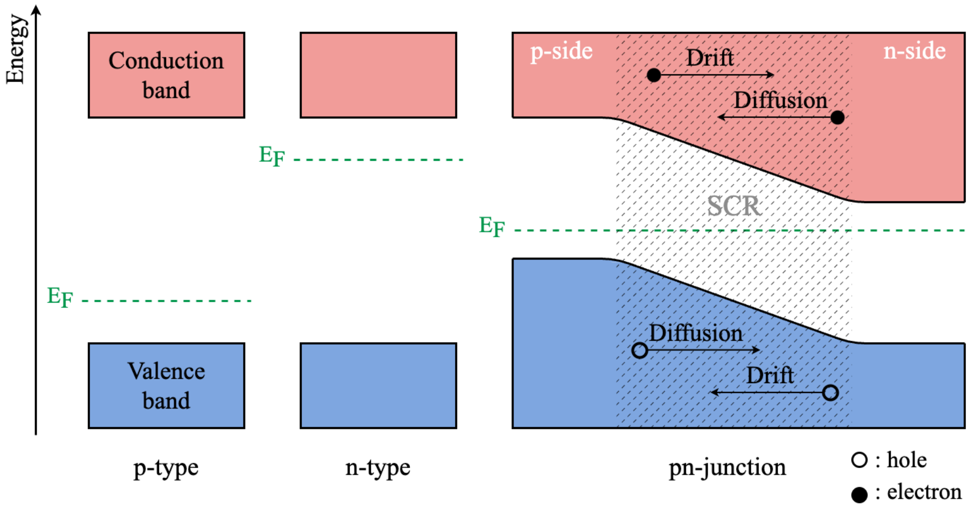

FIGURE 3.8: The band structure of a *p*-*n* junction. Negative charge carriers (electrons) diffuse from the *n*-side to the *p*-side due to the difference in carrier concentration and drift from the *p*-side to the *n*-side under the influence of the built-in potential. Positive charge carriers (holes) exhibit the opposite behavior.

When a *p*-*n* junction is formed, the Fermi levels of the *p*-type and *n*-type regions must align to achieve thermal equilibrium. Before the formation of the junction, the Fermi level in the *n*-type region was higher than in the *p*-type region. Upon the junction's formation, the junction between these two regions creates a boundary where electrons from the *n*-type region begin to diffuse into the *p*-type region due to concentration gradients of the free charge carrier. Simultaneously, holes from the *p*-type region diffuse into the *n*-type region.

The recombination of two carrier types occurs at the boundary of the junction, leading to a zone that is free of charge carriers, referred to as a depletion region. In the depletion region of the semiconductor, the ionized donor and acceptor atoms remain without compensation from the free charge carriers they introduced, resulting in a region depleted of mobile charge carriers. The *p*-side acquires a negative space charge density, while the *n*-side acquires a positive *space charge density*; therefore, this region is also referred to as the space charge region (SCR).

3.2.4 Electrical properties

Depletion Voltage

The electrostatic potential difference across the SCR is known as the *built-in voltage* V_{bi}. The built-in voltage is computed using the one-dimensional Poisson equation, which describes the relationship between the electrostatic potential $\Phi(x)$ and the charge density $\rho(x)$ in a p-n junction. The Poisson equation in one dimension is given by

$$\frac{d^2\Phi(x)}{dx^2} = -\frac{\rho(x)}{\epsilon_{\mathrm{si}}\epsilon_0},$$

where ϵ_0 is the permittivity of free space and ϵ_{si} is the relative permittivity of silicon, which is 11.7. q is the elementary charge. The charge density $\rho(x)$ differs in the p-type and n-type regions. In the p-side, the charge density is $\rho(x) = -qN_A$, where N_A is the acceptor concentration. In the n-side, the charge density is $\rho(x) = qN_D$, where N_D is the donor concentration.

Twofold integration of the Poisson equation yields the electrostatic potential $\Phi(x)$ within the depletion region:

$$\Phi(x) = \begin{cases} -\dfrac{qN_A}{2\epsilon_{\mathrm{si}}\epsilon_0}(x+x_p)^2 & \text{for } -x_p < x < 0 \quad \text{(p-doped region)} \\ 0 & \text{at the junction } x = 0 \\ \dfrac{qN_D}{2\epsilon_{\mathrm{si}}\epsilon_0}(x-x_n)^2 & \text{for } \quad 0 < x < x_n \quad \text{(n-doped region)}. \end{cases} \tag{3.5}$$

Here, x_p and x_n are the widths of the depletion on the p-side and the n-side, respectively. When the doping concentration of the two types is asymmetric in orders of magnitude, the build-in voltage can be simplified by the effective doping concentration N_{eff}, where N_{eff} is the number of donors minus the number of acceptors in the lower doped part. Thus, the built-in voltage is expressed as:

$$V_{\mathrm{bi}} = \frac{q}{2\epsilon_0\epsilon_{\mathrm{si}}} \cdot |N_{\mathrm{eff}}| \cdot w^2, \tag{3.6}$$

where $w = x_p + x_n$ is the width of SCR. The following standard form hence represents the width w:

$$w = \sqrt{\frac{2\epsilon_0\epsilon_{\mathrm{si}}}{q}\frac{V_{\mathrm{bi}}}{|N_{\mathrm{eff}}|}}. \tag{3.7}$$

Typical doping concentrations for silicon detectors are on the order of $N_A = 10^{19}\,\mathrm{cm}^{-3}$ and $N_D = 10^{12}\,\mathrm{cm}^{-3}$. This will result in a built-in voltage of the order of 0.1 V and a depletion thickness of only a few tens of micrometers.

The SCR at thermal equilibrium does not show any net current, as the drift current caused by the V_{bi} and the diffusion current induced by the concentration gradient are in balance. Applying an external voltage V_{ext} to a p-n junction can alter the width of the depletion region depending on the magnitude and polarity of the applied voltage. When a positive voltage is applied to the p-side, referred to as *forward bias*, the V_{bi} decreases, leading to a reduction in the drift current relative to the diffusion current. This results in a narrowing of the SCR. Contrarily, a *reverse bias* condition, where V_{ext} is applied in the same direction as V_{bi}, the effective potential barrier increases.

Applying a reverse bias to the *p-n* junction can widen the depletion region, and the stronger electric field enhances the separation and collection of charge carriers. Ideally, to maximize the detector efficiency, the SCR needs to cover the entire volume of the bulk so that no mobile charge carriers are present. When this condition is met, the minimum bias voltage is called the *depletion voltage* V_{dep}, where $V_{\text{dep}} = V_{\text{bi}} + V_{\text{ext}}$. Since the built-in voltage is comparatively small relative to the applied bias voltage, the depletion voltage can be expressed as

$$V_{\text{dep}} = V_{\text{ext}} = \frac{q}{2\epsilon_0\epsilon_{\text{si}}} \cdot |N_{\text{eff}}| \cdot D^2\,, \tag{3.8}$$

where D represents the full depletion width, which is equal to the thickness of the sensor. For a CMS Outer Tracker silicon sensor with a thickness of 300 µm and standard doping concentrations, full depletion occurs with a bias voltage in the range of 175 V to 350 V. Silicon detectors are often operated at an *over-depletion* voltage, where a higher voltage than the depletion voltage is applied. This results in a stronger electric field, leading to faster charge collection and improved signal formation.

Capacitance

The depletion region behaves like a parallel plate capacitor filled with silicon as a dielectric. The capacitance of the junction is inversely proportional to the depletion width d and is given by the expression:

$$C = \frac{\epsilon_{\text{si}}\epsilon_0 A}{d}\,, \tag{3.9}$$

where A is the cross-sectional area of the junction. Substituting the expression for d, adapted from 3.7, the capacitance becomes

$$C = \begin{cases} A\sqrt{\dfrac{q\epsilon_{\text{si}}\epsilon_0|N_{\text{eff}}|}{2V_{\text{ext}}}} & \text{for } V_{\text{ext}} \leq V_{\text{dep}} \\[2ex] \dfrac{A\epsilon_{\text{si}}\epsilon_0}{D} & \text{for } V_{\text{ext}} > V_{\text{dep}}\,. \end{cases} \tag{3.10}$$

The equations above show the capacitance behavior as a function of external bias voltage. The capacitance remains constant when the junction is over-depleted. In other cases, the capacitance follows the relationship $V \propto 1/C^2$. A common method for determining the depletion voltage of a sensor is to perform a C-V measurement, where the capacitance is measured across different applied external bias voltages. The intersection point of Equation 3.10 indicates V_{dep} as shown in Figure 3.9.

Leakage Current

Ideally, no current due to majority carriers should flow in a reverse-biased silicon sensor. However, a small current is still present, originating from the diffusion of minority carriers from the non-depletion region into the depletion region and the drift of the thermal generation of the electron-hole pairs in the depletion region. This current is called *leakage current*, also known as the reverse current. The leakage current in a

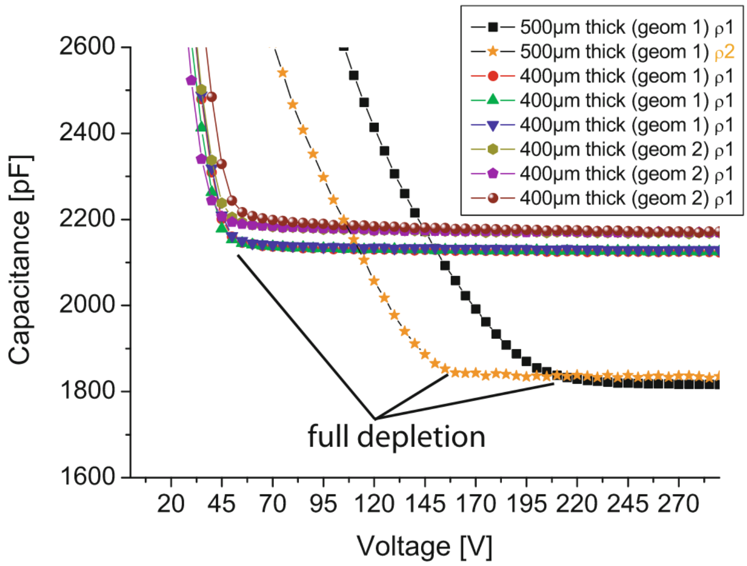

FIGURE 3.9: Capacitance measurement plot for sensors with varying thickness, area, and material resistivity. The transition between the plateau and the linear region with a slope indicates the depletion voltage for each sensor. The capacitance dependence on sensor thickness is also shown. Plot taken from [47].

silicon sensor can influence the noise level and impact the power consumption of the device, which is thus one of the quality factors of the sensor.

The dominant source of the leakage current is the thermally generated charge carriers, and its temperature dependence can be described using the Arrhenius equation,

$$I(T) \propto T^2 \cdot \exp\left(\frac{-E_a}{2k_BT}\right), \tag{3.11}$$

where E_a is the *activation energy* (1.21 eV for silicon [48]), k_B is the Boltzmann's constant, and T is the absolute temperature. The leakage current decreases as the temperature is lowered. At the present LHC, the CMS detector operates at $-10\,^\circ$C, and this will be further decreased to $-20\,^\circ$C during the HL-LHC to compensate for the increased leakage current caused by radiation damage, which leads to higher noise, greater power consumption, and thermal runaway.

3.3 Working principle of a Silicon Tracker

Tracker, the particle tracking detector, commonly employs position-sensitive silicon sensors to identify the trajectories of charged particles. An asymmetric design of the *p*-*n* junction is commonly used in planar sensors, where the bulk material has a thickness ranging from a few tens to a few hundreds of micrometers, and the implant, which is only a few micrometers thick, is located on the surface of the bulk. A reverse bias is applied to the sensor to prevent the ionized charge pairs from recombining shortly after their creation.

3.3.1 Basic Design

To obtain the position measurement of a traversing charged particle, the silicon sensor can be segmented on one or both surfaces with narrow implants. The implants typically have opposite dopant types, forming individual *p*-*n* junctions, and have higher doping concentrations relative to the bulk material. The implants can be segmented in one dimension to create strips on the sensor, or in two dimensions to create pixels. The distance between the center of the segmented implants is called the *pitch*.

The working principle of a silicon strip sensor is illustrated in Figure 3.10. This sensor configuration is referred to as n-in-p sensor where n^+-doped implants are segmented on the surface of the p-doped bulk. When a charged particle passes through a silicon sensor, its energy loss ionizes the silicon atoms along its path. The resulting electron-hole pairs drift in the depleted bulk along the electric field when the depletion bias voltage is applied. Electrons drift toward the nearest n^+ strip implants, while holes move towards the p^{++} backplane. The spatial information of the incident particle is then obtained by collecting these charge carriers. The p^{++} designation indicates that the backplane has a higher doping concentration, which allows for a good ohmic connection with low resistivity, preventing the formation of a Schottky barrier that could arise from the potential difference between the metal and the semiconductor [24]. Furthermore, the backplane and the readout strips are metalized with aluminum for electrical contact.

The charges can be read out by directly connecting the readout chip to the implant through aluminum metallization, a method known as *DC coupling* readout. A more commonly readout method in the current detectors is the *AC coupling* readout. A thin layer of SiO_2 with a thickness of 100 nm to 200 nm is deposited between the implants and aluminum strips. This layer blocks the thermally stimulated leakage current from directly flowing into the readout electronics, while the signal is capacitively coupled from the implants to the aluminum readout strips.

In the case of n-in-p sensor, the positive fixed oxide charge of the SiO_2, arising from imperfections during the oxidation process, can cause the mobile electrons to accumulate around the n^+ implants, potentially leading to shorts between neighboring strips. To prevent this charge leakage and isolate the n^+ implants, two techniques are commonly employed: p-stop and p-spray. The p-stop method involves implanting highly doped p^+ regions between the n^+ strips, creating strong electrical isolation. The p-spray technique uses a uniform, lightly doped p-type layer across the surface, providing continuous isolation without heavily doped regions. In the CMS Phase-2 Outer Tracker, the p-stop technique is used.

Applying a single contact is sufficient to bias a single-sided silicon sensor at the backplane side. However, each read-out electrode needs to be biased to a specific potential. This is achieved by applying a ring structure around the active area, which is called the *bias ring*. The connection should be applied with a high-resistance resistor to prevent the implants from being electrically shorted through the bias ring. Common methods used in the sensors include polysilicon resistors and punch-through biasing. Detailed information is described in [24]. A 3D schematic of the CMS sensor design is sketched in Figure 3.11, where the polysilicon resistors method is implemented. Additional guard ring and edge implants are deposited in the sensor to confine the electric field and avoid conduction damage on the sensor edge. Finally, a passivation layer of SiO_2 covers the top surface of the sensor as protection, leaving only a few

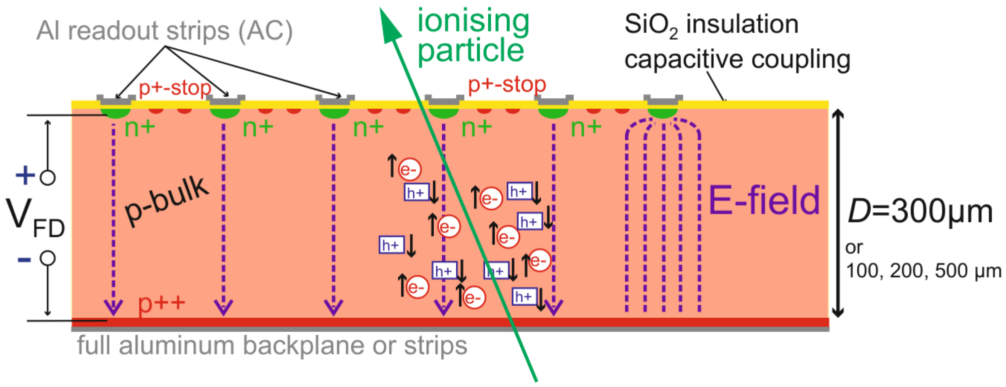

Figure 3.10: Working principle of an n-in-p AC-coupled silicon microstrip detector. Figure taken from [47].

windows for testing and wire bond contact. Each individual strip is read out by wire bonding to front-end readout electronics.

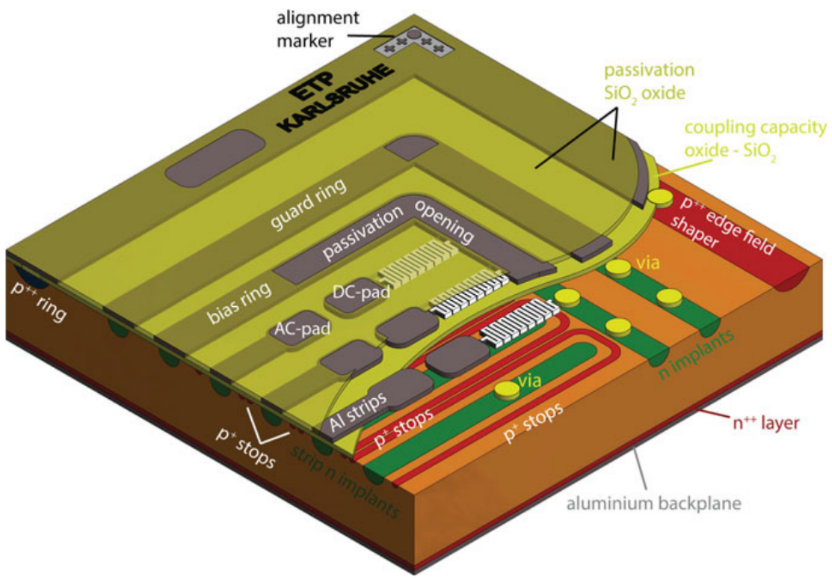

Figure 3.11: A 3D schematic on a n-in-p sensor is shown. This represents the current sensor baseline for the HL-LHC CMS Strip sensor. Adapted from [47].

For hybrid pixel sensors, the segmented implants are arranged in a two-dimensional grid, forming individual pixels. Each pixel implant is bump-bonded to a readout chip that has the same geometry as the pixel and is often referred to as *hybrid pixel*. An example of a pixel detector is shown in Figure 3.12. Small metal bumps, typically made of solder or indium, create direct electrical contacts between the sensor and the readout chip. The individual pixel implants are connected to corresponding channels on the readout chip, allowing for the independent measurement of the charge collected by each pixel.

3.3.2 Signal Formation

The detection signal originates from the energy deposited by the traversing charged particles. The energy loss creates electron-hole pairs with the number of pairs given by Equation 3.4. These charge carriers are separated by the applied electric field in

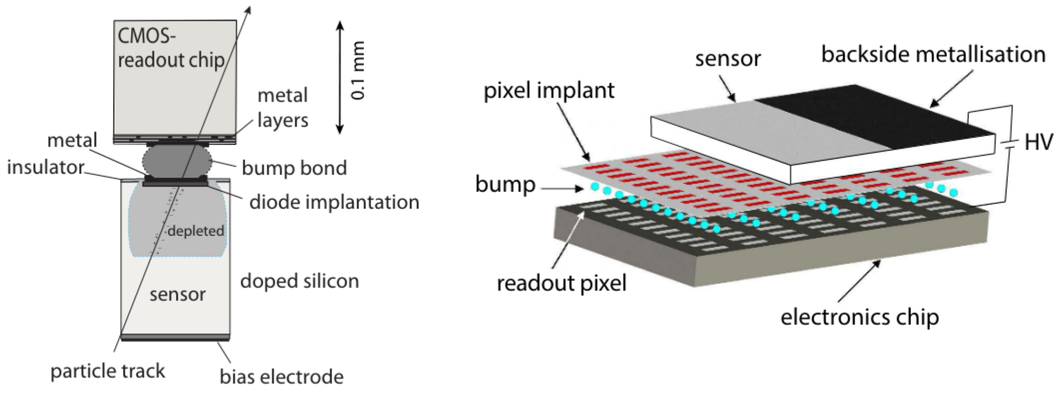

(a) Hybrid pixel cell. (b) Pixel matrix.

FIGURE 3.12: Schematic sketches of the (a) Layout of an individual hybrid pixel cell composed of sensor and electronics cell, (b) hybrid pixel matrix. Sensor and electronics chips connected by bump contacts are subdivided into pixels of the same size. Adapted from [24].

the sensor, causing electrons and holes to drift toward opposite electrodes. At low electric fields, the drift velocity v_d is linearly proportional to the applied field and follows the relation:

$$v_d(x,t) = \mu_0 E_{\text{bias}}(x)\,, \tag{3.12}$$

where μ_0 is the mobility of the charge carriers. The mobility is different for electrons and holes in silicon, with electrons having a higher mobility. At room temperature, the electron mobility μ_e is approximately $1350\,\text{cm}^2/\text{Vs}$, while the hole mobility μ_h is around $450\,\text{cm}^2/\text{Vs}$. As the electric field increases, the drift velocity begins to saturate. For higher electric field regions, the drift velocity approaches a constant value, known as the saturation velocity v_{sat}, which limits the speed of charge collection. More detailed studies on this behavior can be found in [49].

As the charges drift toward their respective electrodes, they induce a current in the readout strips. The induced current can be calculated using the Shockley-Ramo theorem [50][51]. According to the theorem, the instantaneous current I induced on an electrode i by a moving charge q with velocity $\vec{v}$ is given by

$$I_i = q\vec{v}\cdot\vec{\nabla}\Phi_w(\vec{x})\,, \tag{3.13}$$

where Φ_w is the *weighting potential*, a hypothetical scalar potential, that describes the coupling of a charge motion to an electrode [52]. The weighting potential depends solely on the geometry of the sensor and the implant segmentation, assuming full depletion is achieved. It is determined for a particular readout electrode by assigning it a potential of 1, while all other readout electrodes are set to 0.

Several factors can also affect the efficiency of charge collection. One factor is charge carrier trapping, which occurs in the silicon bulk due to defects introduced during manufacturing processes and from radiation-induced damage. Trapping centers, such as vacancies, interstitials, and impurity atoms, capture free charge carriers, therefore reducing the overall signal. Trapped carriers may be released after some time and continue their drift. However, trapping becomes problematic when the carriers remain trapped for a period longer than the readout integration time, as they may be released when the electronics are no longer sensitive to detect the signal.

Another factor that influences charge collection, especially in the case of the CMS detector that operates under a magnetic field, is the Hall effect. The magnetic field causes the charge carriers in the barrel region to experience a deflection in their motion, resulting in a Lorentz angle θ_L between the drift direction under the electric field and the actual trajectory of the charge carriers. The Lorentz angle is given by

$$\tan\theta_L = r_H \mu B\,, \tag{3.14}$$

where B is the magnetic field strength, $r_H = \mu_H/\mu$ is the Hall scattering factor that relates the Hall mobility μ_H and drift mobility μ in the absence of magnetic field [53]. The Hall scattering factor at room temperature is 1.15 for electrons and 0.7 for holes. This drift deflection caused by the Lorentz force contributes to the charge sharing between the neighboring implants.

3.3.3 Front-End Electronics and Readout

The induced signals for a silicon sensor with a thickness of 300 µm are in the range of a few thousand electrons. These current signals are processed by the Front-End (FE) electronics to extract the hit information of traversing particles. A general front-end electronic readout scheme is illustrated in Figure 3.13. The readout scheme begins with a preamplifier which generates a voltage step that is proportional to the input charges. The voltage step is followed by a pulse shaper, which filters the signal. This filtering limits the signal bandwidth, effectively reduces electronic noise, and produces pulses that return to the baseline after a finite time. The shaper also confines the pulse shape such that reducing the shaping time allows the first pulse to return to the baseline before a subsequent pulse arrives.

The discriminator, also known as the comparator, compares the incoming signals to a reference voltage to distinguish valid events from noise. When the signal exceeds this reference voltage, often called the threshold, the signal can be sampled by an ADC to quantify the charge. In a binary readout mode, as used in the CMS outer tracker, the comparator provides the binary information indicating whether or not the signal has exceeded the threshold. A detailed description can be found in [52].

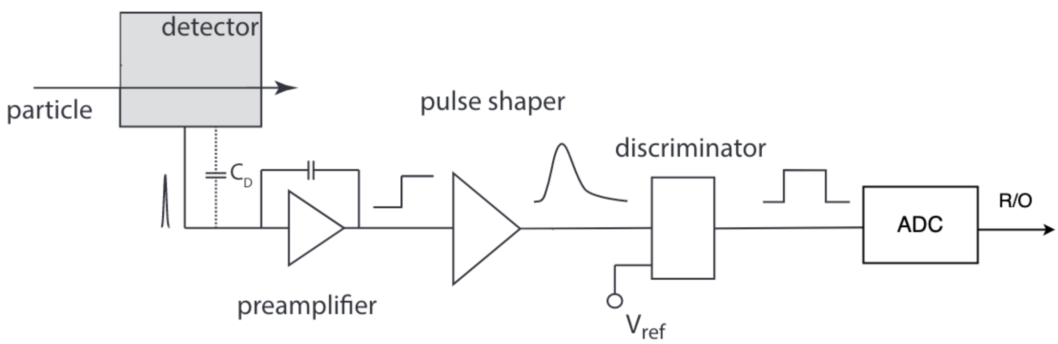

Figure 3.13: General front-end electronic readout components for particle detectors, illustrating stages of signal amplification, shaping, discrimination, and digitization. Modified from [24].

3.3.4 Noise

The noise contribution in a silicon tracker arises from various sources that impact the accuracy of charge collection and the overall performance of the detector. The four main contributions as summarized in [47], are the load capacity C_d, leakage current I_L, parallel and series resistance R_P and R_S, respectively. Noise is typically expressed in terms of the Equivalent Noise Charge (ENC) which quantifies the noise contribution as an equivalent number of charges. By summing the four contributions quadratically, the total ENC is given by

$$\mathrm{ENC} = \sqrt{\mathrm{ENC}_{C_\mathrm{d}}^2 + \mathrm{ENC}_{I_\mathrm{L}}^2 + \mathrm{ENC}_{R_\mathrm{P}}^2 + \mathrm{ENC}_{R_\mathrm{S}}^2}\,. \tag{3.15}$$

The contribution comes from the load capacitance

$$\mathrm{ENC}_{C_\mathrm{d}} = a + b \cdot C_\mathrm{d}\,, \tag{3.16}$$

where a and b are the preamplifier-specific parameters.

The *shot noise* is generated from leakage current

$$\mathrm{ENC}_{I_\mathrm{L}} = \frac{e}{2}\sqrt{\frac{2I_\mathrm{L} \cdot t_\mathrm{p}}{q_e}}\,, \tag{3.17}$$

where e is the Euler number, t_p is signal peaking time of the shaper, q_e denotes the electron charge.

The parallel thermal noise originates from the bias resistance

$$\mathrm{ENC}_{R_\mathrm{P}} = \frac{e}{q_e}\sqrt{\frac{k_B T \cdot t_\mathrm{p}}{2R_\mathrm{P}}}\,, \tag{3.18}$$

where k_B represent the Boltzmann constant and T is the operating temperature.

Finally, the serial thermal noise arises from the series resistance, such as the resistance of the aluminum strips:

$$\mathrm{ENC}_{R_\mathrm{S}} = C_\mathrm{d} \cdot \frac{e}{q_e}\sqrt{\frac{k_B T \cdot R_\mathrm{S}}{6t_\mathrm{p}}}\,. \tag{3.19}$$

Therefore, to minimize the noise in the detector, the sensor should be designed with small load capacitance, low leakage current, high parallel resistance, and small series resistance. Additionally, the readout method must account for the fixed peaking time set by the shaper, ensuring it aligns with the application. In high-frequency environments like the LHC, shorter peaking times prevent signal overlap. Furthermore, temperature directly impacts both shot noise and thermal noise, and operating the detector at lower temperatures helps achieve reduced noise levels.

Chapter 4

The Phase-2 Upgrades of the CMS Outer Tracking Detector

Contents

4.1 Overview of The Phase-2 Tracker Upgrade

The current CMS tracker is designed for operation at an instantaneous luminosity of $1.0 \times 10^{34}\,\mathrm{cm^{-2}s^{-1}}$, corresponding to a pile-up of 20 to 30 collisions with bunch crossing (BX) happening every 25 ns. It is structured to withstand up to $500\,\mathrm{fb^{-1}}$ of integrated luminosity. However, with the LHC now operating at instantaneous luminosity levels exceeding initial design expectations, both strip and pixel detectors in the tracker have already incurred radiation damage, leading to degraded performance. The radiation effects include increased sensor depletion voltage and leakage current, along with reduced charge collection efficiency, which together degrade the spatial resolution and hit efficiency of the tracker. These factors are making continued operations beyond the expected integrated luminosity impossible. Simulation studies on the performance degradation of the tracker are presented in [54].

As a result, the entire tracker will be replaced through the Phase-2 upgrade, which is specifically designed for the High Luminosity Large Hadron Collider (HL-LHC). The HL-LHC will operate at an instantaneous luminosity of 5.0 to $7.5 \times 10^{34}\,\mathrm{cm^{-2}s^{-1}}$, with pile-up reaching up to 140 to 200 collisions per BX, and an integrated luminosity of 3000 to $4000\,\mathrm{fb^{-1}}$ projected by the year 2040.

Several key requirements should be met for the tracker upgrade to operate efficiently. First, excellent radiation hardness is necessary, with the new tracker expected to tolerate radiation exposure up to a 1 MeV neutron equivalent fluence of $2.3 \times 10^{16}\,\mathrm{n_{eq}/cm^2}$

in the inner tracker and $1.1 \times 10^{15}\,\mathrm{neq/cm^2}$ in the outer tracker region throughout its lifetime [36].

Additionally, the tracker requires higher granularity to keep channel occupancy at or below 1%, ensuring high tracking efficiency under increased pile-up. Channel occupancy refers to the fraction of detector channels recording hits. A reduced material budget is also essential, as it minimizes scattering and radiation effects, benefiting overall event reconstruction and calorimeter performance. A detailed description of the tracker layout is provided in Section 4.4, which includes illustrations of the geometry and design considerations.

A key design feature of the Phase-2 tracker is the integration of the Outer Tracker into the Level-1 (L1) trigger system. By incorporating track information into the first trigger stage, the system can optimize event selection, enabling a higher trigger rate while efficiently selecting only the most relevant events. This ensures effective data processing, even under the demanding conditions of the High Luminosity LHC.

The Inner tracker will extend the tracking acceptance up to the pseudorapidity range of $\eta = 3.8$, enhancing the particle detection capability in the forward region. To accommodate the upgraded CMS trigger system with increased latency and output rates, the tracker has been designed to ensure full compatibility with these changes.

Furthermore, improved two-track separation is needed to distinguish high-energy jets, and robust pattern recognition is required to enable fast, efficient track finding, especially at the High-Level Trigger stage.

The Phase-2 tracker comprises an Inner Tracker (IT) region with silicon pixel modules and an Outer Tracker (OT) region utilizing modules featuring strip and macro-pixel silicon sensors. This chapter focuses on the Outer Tracker upgrade and provides an overview of the design concept, including its contribution to the L1 Trigger, the transverse momentum (p_T) discrimination mechanism, the module designs, and the overall detector layout.

4.2 Concept of the Phase-2 Outer Tracker

The increased data rates and pile-up at the HL-LHC will make L1 trigger performance more challenging. As outlined in Chapter 2.2.5, the present L1 trigger relies on coarse information from the calorimeters and muon detectors and must make decisions in a few microseconds. However, the significantly higher rates of muons, electrons, and jets at the HL-LHC will overwhelm the current event selection process. Simply raising the trigger threshold to handle these rates would negatively impact physics performance by discarding valuable events [55]. Therefore, the inclusion of tracking information in the L1 trigger improves the event selection of interesting physics events that involve high-momentum particles. This enhancement allows the trigger to maintain a high output rate while focusing on the most relevant events. With the Phase-2 upgrade, the L1 trigger rate will increase from 100 kHz to 750 kHz, and the latency will expand from 3.2 µs to 12.5 µs, providing more time to analyze data and make complex decisions.

4.2.1 The p_T Module Concept

The outer tracker design is primarily motivated by the L1 trigger concept. Tracking information must be sent to the L1 trigger at the bunch crossing rate of 40 MHz with limited data volume. To achieve this, the selection of high-p_T tracks must occur directly on the individual modules within the detector, which are specifically designed as p_T modules to perform this task at the earliest possible stage. The p_T module consists of two single-sided, closely spaced silicon sensors that share a common set of readout electronics. These readout electronics correlate signals from both sensors and generate *stub* signals when the incident particles are above the chosen p_T threshold. A threshold of approximately 2 GeV achieves a data volume reduction of an order of magnitude [36], enabling transmission of stub information at a rate of 40 MHz. The full event data is temporarily stored in the front-end pipelines and is retrieved upon receiving an L1 trigger-accept signal. Incorporating track information derived from stubs significantly reduces the L1 trigger rate from an unsustainable 4 MHz, observed when tracks are excluded from the trigger decision to 750 kHz [54] while preserving strong physics performance even under high pileup conditions.

When a charged particle traverses a module within the CMS tracker, the magnetic field of 3.8 T induces a curvature in its trajectory. Figure 4.1 illustrates the concept of p_T discrimination. The readout chip defines a programmable acceptance window in the correlation layer, corresponding to the hit position recorded in the seed layer. This setup measures the spatial displacement of the particle as it crosses the two sensors, represented by the red boxes in the figure. If the displacement lies within the acceptance window, the particle is identified as having high transverse momentum and is classified as a *stub*. Particles with displacements exceeding this threshold are rejected as they do not meet the p_T criterion.

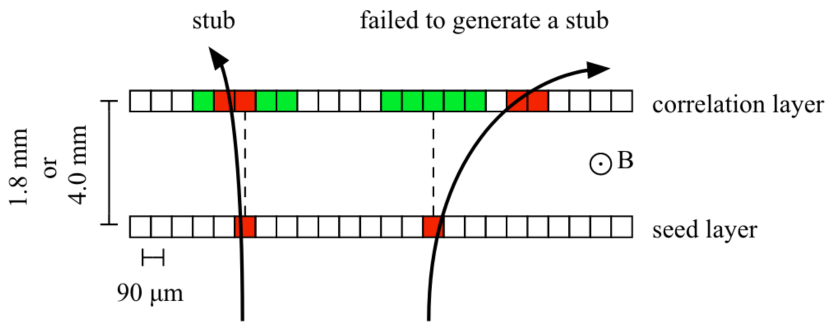

FIGURE 4.1: Sketch of the stub formation inside p_T module under a magnetic field. Silicon strips are arranged along the viewing plane with a pitch of 90 µm. The signal cluster detection is highlighted in red, while the programmable search window is depicted in green. The left arrow indicates a charged particle with high p_T, which successfully forms a stub, and the right arrow shows one with low p_T, which failed to generate a stub. [56].

The separation distance of the two sensors and the size of the acceptance window depend on the radius of the tracker at which the module is located, to achieve a uniform p_T threshold throughout the tracker. Additionally, a programmable offset can be applied to the acceptance window to account for parallax error caused by approximating the cylindrical geometry of the tracker with planar sensors. Further explanation along with the tracker layout is described in Chapter 4.4.

4.2.2 Track finding at Level-1 Trigger

The Level-1 trigger system is designed to identify interesting collision events within a strict latency limit of 12.5 µs. Latency is the time between a collision event and the L1 trigger decision, including signal propagation, data processing, and transmission to the detector's front-end buffers. Figure 4.2 illustrates the data flow from the front-end electronics of the outer tracker modules to the back-end systems and the CMS central data acquisition systems.

The L1 track-finding process begins with stubs, transmitted at a rate of 40 MHz to the back-end electronics, where tracks are reconstructed and correlated with data primitives from other sub-detectors. Timely transmission of stub data is essential to meet the latency requirements for track reconstruction.

To achieve this, the L1 trigger electronics require approximately 3.5 µs to correlate reconstructed tracks with calorimeter and muon data primitives, followed by 1 µs to propagate the trigger decision back to the front-end buffers. A safety margin of 3 µs is included to ensure system reliability. This indicates that with the latency limitation of 12.5 µs, 5 µs is used for track reconstruction, which involves generating, packaging, and transmitting stubs (1 µs) to the Data Trigger and Control (DTC) system, which acts as the interface between the tracker front-end and the central CMS control system, and processing stub data to reconstruct tracks (4 µs) [57].

The Level-1 Track Finder system is responsible for reconstructing particle tracks at the bunch crossing frequency using stub data. These reconstructed tracks are used as inputs for the L1 Trigger decision. Upon receiving an L1 accept trigger, the full buffered data from the front-end pipeline are read out and transmitted to the CMS Data Acquisition system. This readout is performed at a nominal trigger rate of up to 750 kHz, which is a significant increase compared to the CMS Tracker's previous operational rates.

This system architecture efficiently integrates front-end stub generation with back-end data processing, meeting the stringent timing and performance requirements of the L1 trigger.

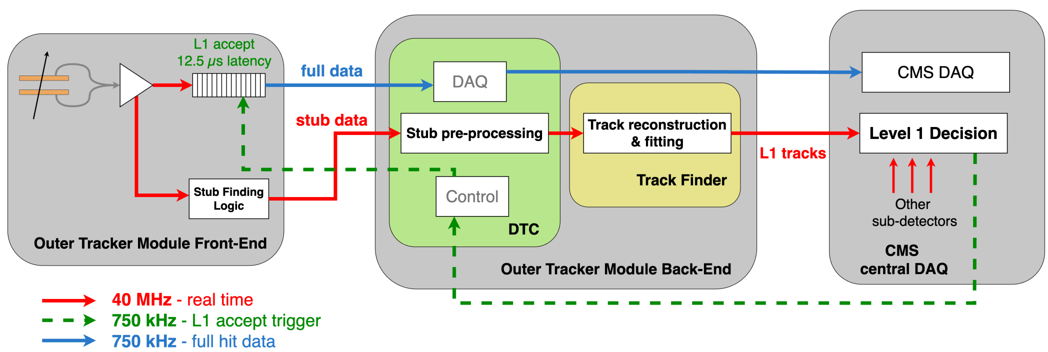

FIGURE 4.2: Schematic diagram of the different data paths of the p_T modules to the back-end electronics for the L1 trigger decision process. The red arrow indicates the stub data path at a rate of 40 MHz, while the green and blue arrows represent the Level-1 accept trigger and trigger data paths, respectively. The accepted trigger and L1 data are limited to 750 kHz.

4.3 The Outer Tracker Modules

Two types of p_T modules are employed in the Phase-2 outer tracker: the Strip-Strip (2S) modules and the Pixel-Strip (PS) modules. The 3D model of the two modules is shown in Figure 4.3. The 2S module features two identical strip sensors, each measuring 10 cm × 10 cm, and consisting of two rows of 1016 strip implants that are 5 cm long, optimized for the outer regions of the outer tracker where particle flux is lower. In contrast, the PS module combines a strip sensor (PS-s) and a macro-pixel sensor (PS-p), each with an area of 5 cm × 10 cm. The PS-s sensor contains two rows of 960 strips, each 2.4 cm long, while the PS-p sensor contains 32 rows of 944 macro-pixels, each 1.5 mm long. The PS module provides higher granularity, which helps mitigate occupancy and is suitable for higher track densities in the inner region of the outer tracker closer to the interaction point.

Sensors used in both of the modules are fabricated on 6-inch high resistivity, thinned float zone silicon wafers, with a physical thickness of 320 µm and an active thickness of 290 µm. Featuring n-in-p polarity, these sensors have n-type implants in a p-type substrate to improve radiation hardness compared to the current tracker. The sensor campaign, including the selection of sensor type and thickness, is discussed in [58, 59], and the sensor specifications and quality control processes are detailed in [60].

The two sensors of both modules are separated by spacers which have a low coefficient of thermal expansion (CTE) of approximately 4 ppm/°C along two axes, closely matching the CTE of silicon sensors (3 ppm/°C) [36]. The different thickness variants are introduced in the spacer design as mentioned in the previous section to perform uniform p_T discrimination in the whole outer tracker. The overall parameters of the 2S and PS modules are summarized in Table 4.1.

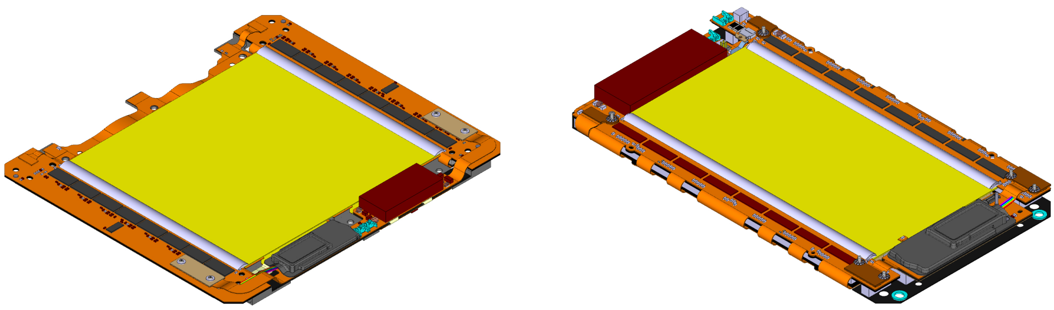

(a) (b)

FIGURE 4.3: The latest approved 3D models of the (a) 2S module and (b) PS module designs as of August 2024 are presented. Both modules feature a stack of two silicon sensors with hybrids surrounding them. The sensors are indicated in yellow, and hybrids are depicted in Orange. The hybrids located on the right and left sides of the sensor stack are the Front-End Hybrids, whereas the hybrid on the remaining side (or two sides in the PS module) is the Service Hybrid.

In Figure 4.3, the sensors of the 2S module are surrounded by three hybrid circuits, whereas four hybrid circuits encompass the PS module. To achieve p_T discrimination through stub finding, the two halves of the sensor are connected to individual readout Application Specific Integrated Circuits (ASIC)s on the Front-End Hybrid (FEH) positioned on two sides of the module. The FEHs are flexible circuits laminated to carbon fiber composite stiffeners and are folded around spacers to facilitate data transmission. For module types with 1.6 mm spacing, the hybrids are folded without

TABLE 4.1: Summary of the 2S and PS module parameters used in the outer tracker.

	2S Module	PS Module
Active Area	$\sim 2 \times 90$ cm^2	2×45 cm^2
Top Sensor	2×1016 strips	2×960 strips
Strip Size	~ 5 cm $\times$ 90 µm	~ 2.4 cm $\times$ 100 µm
Bottom Sensor	2×1016 strips	32×960 macro pixels
Strip/Pixel Size	~ 5 cm $\times$ 90 µm	~ 1.5 mm $\times$ 100 µm
Spacer Variant	1.8 mm, 4.0 mm	1.6 mm, 2.6 mm, 4.0 mm

spacers. Each FEH also hosts a Concentrator Integrated Circuit (CIC) chip, which aggregates and formats the data from all the readout ASICs present on that FEH.

For the 2S module, the other hybrid is the Service Hybrid (SEH), which is also laminated onto CFRP stiffeners. The SEH is responsible for power distribution, data communication, and control functionalities. It is designed to handle the electrical connections between the Front-End Hybrids, and the external Data Acquisition systems. The service hybrid ensures stable power delivery to the different electronics within the tracker module, providing low voltages required by the various sensors and ASICs. Moreover, it plays a role in serializing and transmitting the data aggregated by the CIC from the Front-End Hybrids to the back-end electronics for further processing. This data transmission is done through optical fibers, which are connected to the service hybrid, enabling the high-speed communication necessary to handle the large data volumes generated in high-energy collisions. In the case of the PS module, the functionality of the SEH in the 2S module is divided into two separate hybrids: the Power Hybrid (POH), which is dedicated to power distribution and stable voltage delivery to the sensors and front-end electronics, and the Readout Hybrid (ROH), which handles data communication and control functionalities.

While the 2S and PS modules share similar structures, they are optimized for different regions of the outer tracker and thus have distinct design characteristics and functionalities. The following sections delve into the details of each module, starting with the 2S module, which features identical readout architecture between the two sensors, making it more cost-effective for its designated region. This is followed by the PS module, which is designed for higher occupancy regions closer to the interaction point and offers higher granularity.

4.3.1 The Strip-Strip Module

The design of the 2S module in an exploded view is depicted in Figure 4.4. The module consists of two identical sensors, each with an active area of 9.1×10.0 cm^2. The sensors are AC-coupled, featuring 1016 strips on both the left and right sides, with a strip pitch of 90 µm. A corner of the sensor layout is shown in Figure 4.5. The gray regions represent areas covered by aluminum, while the orange pads indicate the passivation openings necessary for establishing electrical contact. The blue lines depict the polysilicon resistor structures mentioned in Chapter 3.3.1.

The sensors are glued to Carbon Fiber reinforced Aluminium (AlCF) spacers, referred to as *bridges*, with the strip orientation aligned between the top and bottom sensors.

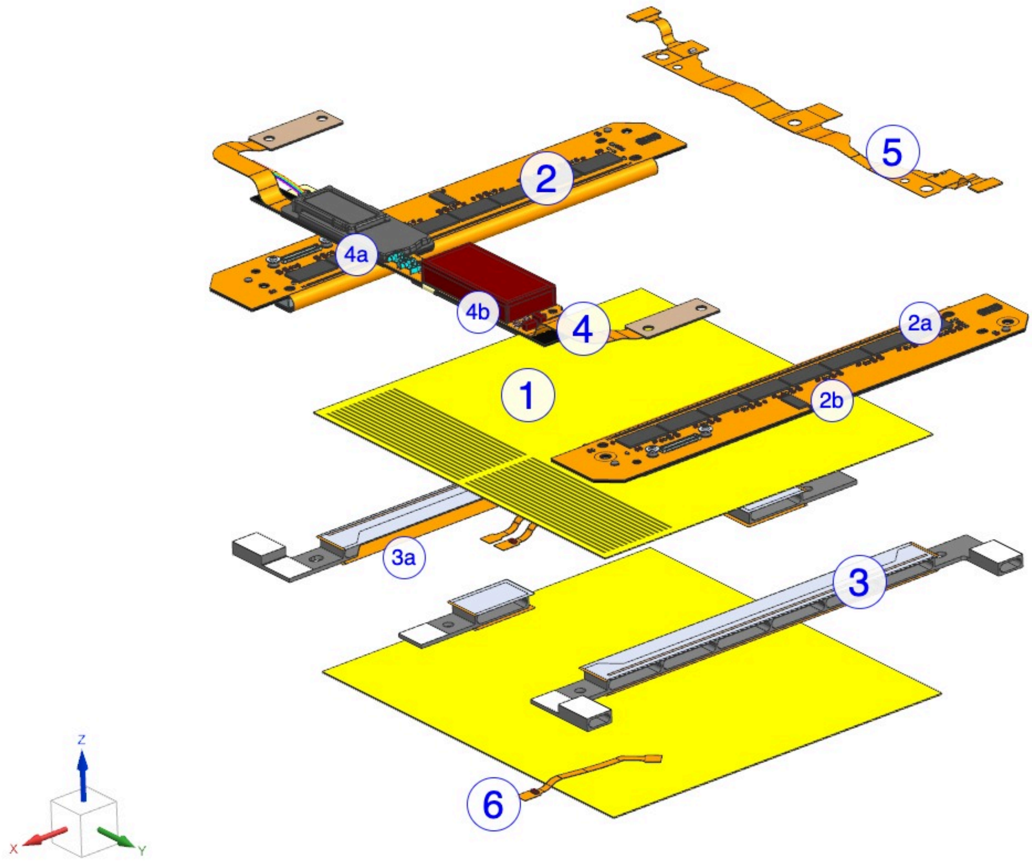

FIGURE 4.4: An exploded view of the 2S module is shown. The components of the module are: (1) two identical sensors with strip orientation indicated by lines, (2) two Front-End Hybrids on either side of the sensor, each containing (2a) eight CMS Binary Chips and (2b) a Concentrator Integrated Circuit chip, (3) Aluminum-Carbon Fiber bridges with Kapton strip isolation, and (4) a Service Hybrid with (4a) a Versatile Link Plus Transceiver, a low-power Gigabit Transceiver, and (4b) low-voltage DC-DC converters, (5) a Ground Balancer that grounds both FEHs to minimize noise, and (6) HV tails glued to the backplane of the top and bottom sensors. An additional tail on the top sensor is used for temperature monitoring.

The spacing bridges shown in the Figure are hollow from the side to reduce the material budget. The material properties of AlCF offer an advantage due to its ease of machining, allowing the formation of hollow structures while ensuring mechanical stability. The spacing structures separate either 1.8 mm or 4 mm between the sensors, serving as the mechanical support and thermal interface for the entire module. The high bias voltage is applied to the back side of the sensors, requiring high voltage tails to be glued to the backside. Kapton isolation materials of 25 µm thickness, however, are placed between the bridges and the sensors to ensure proper electrical insulation and component protection.

The Front-End Hybrid folds around the AlCF bridges, routing signals from the bottom sensor through the fold-over structure of the flexible hybrid. Bond pads are located on both sides of the FEH and are wire-bonded to each individual strip on the sensors. This flexible structure allows the hybrids to read out both sensors simultaneously and correlates the hit information for stub finding. The readout of the sensor is managed by a binary ASIC implemented in 130 nm CMOS technology, known as the CMS

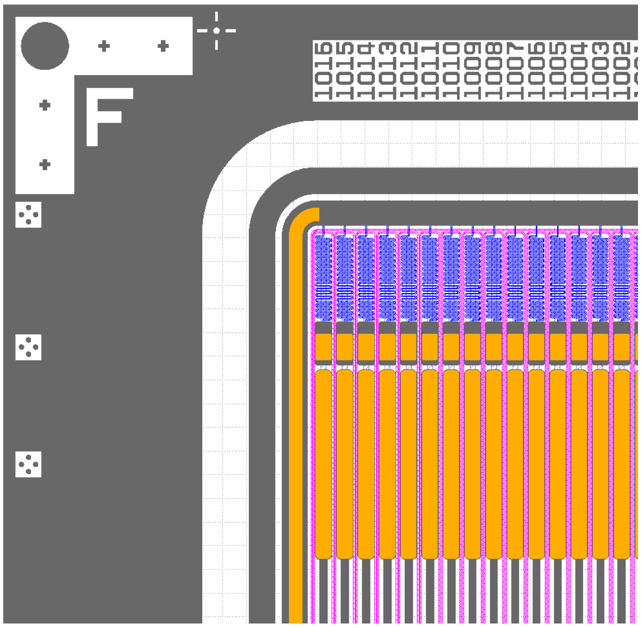

FIGURE 4.5: A corner of the 2S sensor layout showing aluminum strips, passivation windows, and polysilicon resistor structures. The pink regions surrounding the strips, represent p-stop implants

Binary Chip (CBC). Eight CBCs, each featuring 254 input channels that collectively read out signals from the top and bottom sensors, are bump-bonded onto one FEH. To prevent inefficiencies in stub finding at the chip boundaries, the design of the CBC incorporates mechanisms for exchanging hit information between neighboring CBCs.

The analog front-end electronic readout components for a single channel are illustrated in Figure 4.6. The signal input is fed into a preamplifier where it is converted to a voltage pulse, and further amplified by a post-amplifier. An offset adjustment, referred to as *trimming*, can be applied to the output of the post-amplifier to compensate for baseline variations caused by the manufacturing process; this is further detailed in Chapter 5.2.3. The channel noise is designed to be ≤ 1000 electrons, with a leakage current of $\leq 1\,\mu A$ per strip. Finally, a comparator threshold voltage, defined by the internal DAC unit of V_{cth}, is set globally for the chip to provide a binary output to the digital back-end system.

A block circuit diagram of the CBC architecture is shown in Figure 4.7. The chip operates with two clock domains: a 40 MHz domain synchronized with the 25 ns bunch crossing period and a 320 MHz domain dedicated to input and output data transfer, alongside a 1 MHz Inter-Integrated Circuit (I^2C) Slow Control Interface that manages the configuration and programming of various parameters within the chip, such as comparator thresholds, amplifier biases, and programmable delay settings. The Hit Detect circuit, which processes the comparator outputs, is synchronized with the bunch crossing using the Delay Locked Loop (DLL) with a resolution of 1 ns. Subsequent circuit blocks correlate hits between two sensor layers, identifying clusters within a programmable correlation window to detect high-momentum tracks. The Stub Gathering Logic assembles this information, producing a stub position with a resolution of half a strip and bending displacement. The CBC transmits the stub data to the CIC via five scalable low-voltage signaling (SLVS) lines operating at 320 Mbps.

A sixth SLVS line is used to transmit hit information upon detecting a trigger signal. The chip also provides storage for each event's data, accommodating up to 512 bunch crossing intervals (equivalent to 12.8 µs for a 25 ns clock), allowing sufficient time for trigger decisions. Detailed information of CBC can be found in [61].

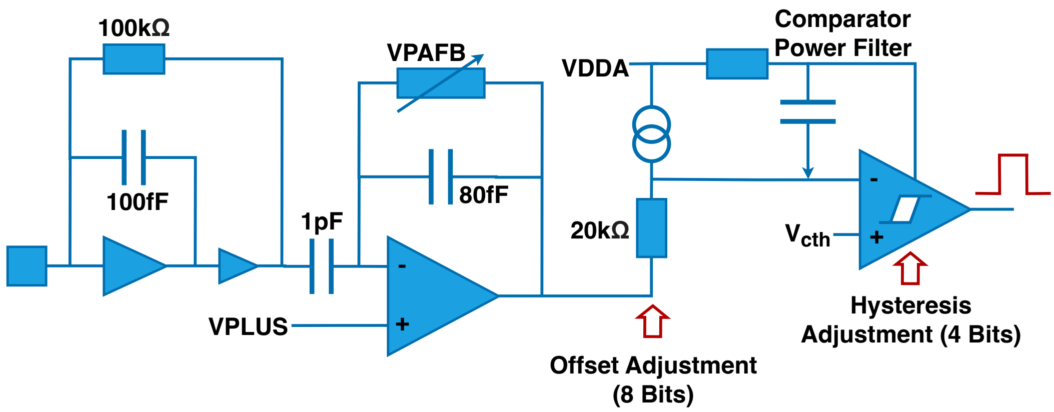

FIGURE 4.6: A sketch of the analog front-end of a channel in the CBC. The most left blue block represents the input bonded to one strip of a sensor. [61].

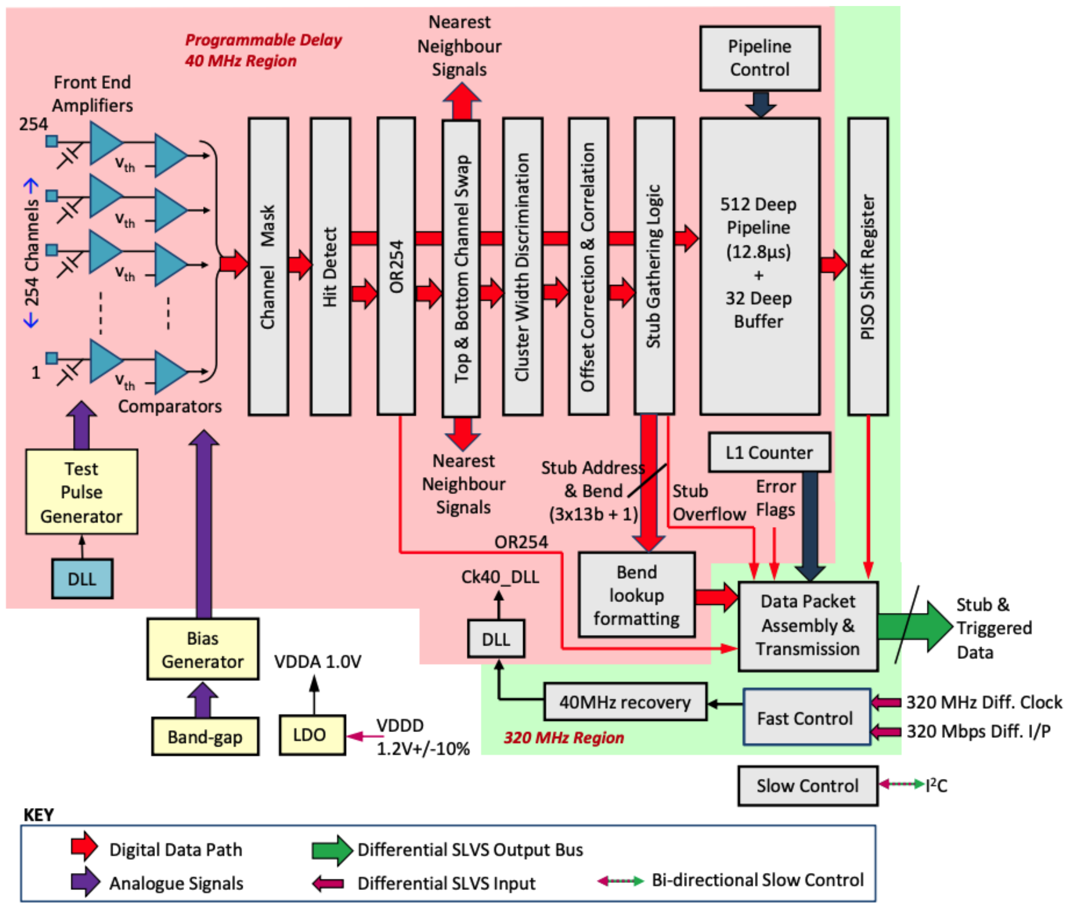

FIGURE 4.7: A block diagram depicts the main circuit blocks of the CBC chip, including the digital and analog signal paths. Color blocks in red and green indicate the two clock domains. [61].

The Front-End Hybrid also utilizes one Concentrator Integrated Circuit (CIC) [62], as illustrated in Figure 4.4 labeled (2b), to aggregate the data generated by eight CBCs.

Within the CIC, the data are sparsified, compressed, and then sent to the Gigabit Transceiver on the service hybrid. The CIC generates two independent data streams for the Back-End, the stub data stream, and the L1 data stream.

To maintain synchronization and minimize data loss, the CIC processes stub data in 8-BX clock. Stub data from eight consecutive bunch crossings are temporarily stored, and sorted according to their bend information. High p_T particles, which produce low bend displacements, are prioritized when the CIC buffer capacity is exceeded during periods of high occupancy. Following serialization, the sorted stub data is transmitted via five SLVS output lines.

Upon receiving an L1 trigger, the CIC processes L1 hit data by clustering hits from neighboring strips to reduce data volume. Only the cluster position and width are serialized and transmitted to the Gigabit Transceiver on the SEH. The L1 data is sent via a single SLVS output line operating at 320 Mbps, with the higher rate allocated to modules in high-occupancy regions.

Additionally, the CIC integrates an I^2C protocol for slow control communication, managed by an internal I^2C slave block, ensuring control and configuration of front-end electronics.

The Service Hybrid shown in Figure 4.4, indicated as (4), hosts a Low Power Gigabit Transceiver (LpGBT) with a Versatile Transceiver Plus (VTRx+) module and DC-DC converters. The LpGBT receives data packets from both CICs, serializes them, and transmits the data to the VTRx+ for optoelectrical conversion. The converted data are then transmitted via optical fiber to the Back-End electronics for track reconstruction. The LpGBT also supports reception control signals for the front-end ASICs via I^2C bus. The DC-DC converter provides low voltage for the front-end electronics and the LpGBT.

4.3.2 The Pixel-Strip Module

The exploded view of the PS module is illustrated in Figure 4.8. Unlike the 2S module, the core of the module is constructed with a Strip Sensor (PS-s) and a Macro Pixel Sensor (PS-p) with an active area of $9.6 \times 4.7\,\mathrm{cm}^2$. The PS-s, shown in 4.9(a), shares a common layout and periphery with the 2S sensor, but differs in overall size, strip length and pitch. It has a strip pitch of $100\,\mu$m and a length of 2.4 cm, and contains 2 rows of 960 strips per sensor. Poly-silicon resistors, shown in blue, are used in the strip sensors to facilitate the necessary biasing for each channel.

The PS-p, in contrast, consists of 960×32 rectangular DC-coupled pixels arranged in a grid with a pitch of 100 µm along the x-axis and approximately 1.5 mm along the y-axis. For biasing, the macro-pixels use punch-through structures to connect each pixel to the bias grid. Both sensors incorporate alignment marks, such as L-shaped, F-shaped, and cross-shaped patterns, to assist with pattern recognition during the automated module assembly process, as precise alignment of the top and bottom sensors is crucial for the p_T measurement. Figure 4.9(b) shows the sensor layout of PS-p. The gray region represents the aluminum metalization, while the orange structure indicates openings in the passivation layer. The pink regions correspond to p-stop implants that provide strip/macro-pixel isolation.

Each PS-p sensor is bump-bonded to 16 Macro-Pixel ASIC (MPA) chips for readout; this sub-assembly is known as the Macro Pixel Sub-Assembly (MaPSA). The macro-pixels of the sensor that are situated at the edge of the corresponding MPA chips

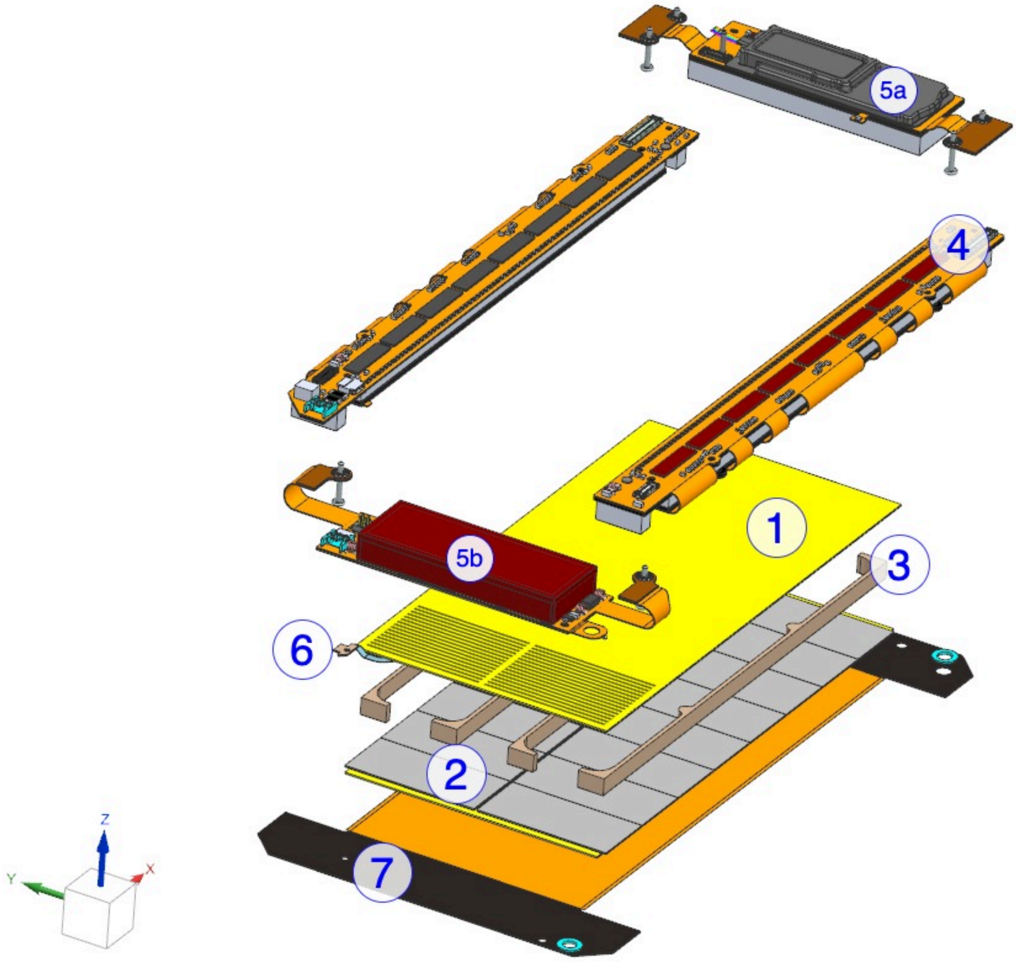

FIGURE 4.8: An exploded view of the PS module is shown, with the following components: (1) a strip sensor with strip orientation indicated by lines, (2) a Macro-Pixel Sub-Assembly, which consists of a macro-pixel sensor and sixteen macro-pixel ASICs, (3) aluminum nitride spacers, (4) two Front-End Hybrids on either side of the sensor stack, each with eight Short Strip ASICs and a CIC on the bottom side of the hybrids, (5a) a Readout Hybrid with an lpGBT ASIC and a VTRx+ module, (5b) a Power Hybrid, (6) a high-voltage tail glued to the backplane of the strip sensor, and (7) a base plate with a Kapton sheet and aluminum inserts that provides structural support for the module.

overlap with the inactive periphery of the chips, leading to a situation where dedicated readout channels cannot be allocated for them. Consequently, the first two and the last two pixel columns on the sensor that correspond to the edges of each MPA chip are merged to form a wider pixel of 200 µm.

The spacing bridges, which provide the separation variants listed in Table 4.1 for the PS module, are made of Aluminum Nitride (Al-N), a material that offers superior electrical insulation compared to AlCF. Since Al-N is an isolator, it can be directly glued between the PS-s and MPA side of the MaPSA. In addition to providing mechanical separation and support, Al-N also serves as a thermal conduction path for the PS-s sensor.

The readout electronics of the PS module rely on ASICs developed using 65 nm CMOS

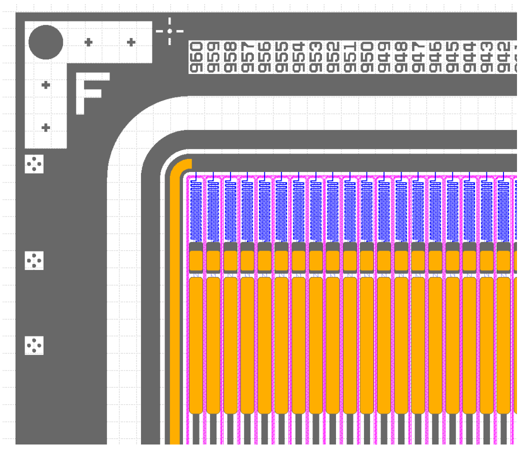

(a)

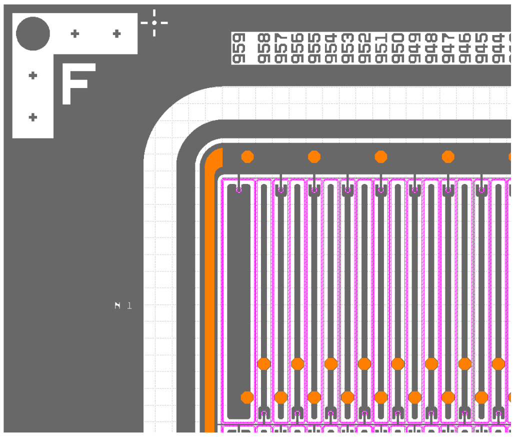

(b)

FIGURE 4.9: A corner layout of the (a) PS-s and (b) PS-p. The PS-s has a similar layout to the 2S sensor, featuring aluminum strips, passivation windows, and polysilicon resistor structures. The PS-p, on the other hand, contains macro-pixels and a bias ring, each with passivation windows, along with a punch-through structure for biasing. Both sensors are equipped with L-shaped and F-shaped alignment patterns to ensure precise alignment during automatic module assembly. The pink regions surrounding the macro-pixels represent p-stop implants.

technology as described in [63]. The two different types of sensors in the PS module utilize dedicated readout ASICs. The Short Strip ASIC (SSA) is designed for the PS-s sensor, while the Macro-Pixel ASIC (MPA) is dedicated to the PS-p sensor.

Two Front-End Hybrids are employed in the PS module, each consisting of 8 SSA chips on the top side and 1 CIC on the bottom side. The fold-over design is implemented on the edge away from the sensors, allowing the MPA chips to be wire-bonded on the bottom side of the FEH and enabling the routing of inputs to the SSAs and outputs from the SSAs in separate areas. The extra surface area allows for the placement of the CIC chip on the bottom side. This fold-over design allows the reduction of the line density on the top side and optimizes signal routing and hybrid performance. Each SSA, bump-bonded onto the FEH, processes signals from 120 channels transmitted via sensor readout pads wire-bonded to the hybrid. The sensor signals are amplified by the SSA front-end followed by a double-threshold discrimination circuitry that differentiates High Ionizing Particles (HIP) from Minimum Ionizing Particles (MIP). The normal threshold is set around a quarter of a MIP, while the second threshold is set to be 1.5 MIP for HIP detection. The SSA then transmits sparsified cluster data to the MPA for the purpose of stub finding at the bunch crossing rate. To mitigate potential inefficiencies arising from gaps in coverage between neighboring chips, the SSA, much like the CBCs in the 2S module, can exchange hit information with adjacent SSA chips. More details can be found in [64].

Each MPA chip features 1888 readout bump connections and employs a single-threshold binary system for data readout, with the threshold set to approximately one-quarter of a MIP. The MPA is responsible for processing and sparsifying hit data from the pixel sensor, integrating strip sensor data from the SSA, and performing p_T discrimination and stub formation. Further details on the MPA can be found in Chapter 6.1.2.

The architecture of the readout ASICs in the PS module is illustrated in Figure 4.10. Two distinct data paths are represented using different colors: the orange arrow represents the stub data path, which corresponds to the trigger-related data flow, while the blue arrow indicates the L1 data path.

In the **stub data path**, the SSA processes the hit data through strip clustering logic that calculates the centroid position of hit clusters while discarding wide clusters exceeding 400 µm. The center positions of the clusters are encoded and transferred from the SSA to the paired MPA at the 40 MHz bunch crossing frequency via eight SLVS lines, each operating at a rate of 320 Mbps. This stub information is then transmitted from the MPA to the CIC via five SLVS lines per MPA, where it is deserialized and decoded. The CIC formats the filtered data into stub data frames, which are subsequently transmitted to the LpGBT over five SLVS output lines.

In the **L1 data path**, strip hits are initially stored in Static RAM (SRAM) within the SSA while waiting for an L1 trigger signal. Once the Level-1 trigger is received, the SSA transmits the L1 data to the MPA over a single SLVS line operating at 320 Mbps. Macro-pixel hits stored in the MPA are processed alongside the strip data, with cluster information including the position and width extracted and encoded. The processed L1 data is then sent to the CIC via a single SLVS line per MPA. The CIC decodes the data and assembles it into a standardized hit frame, which is transmitted to the LpGBT over a single SLVS output as in the 2S module.

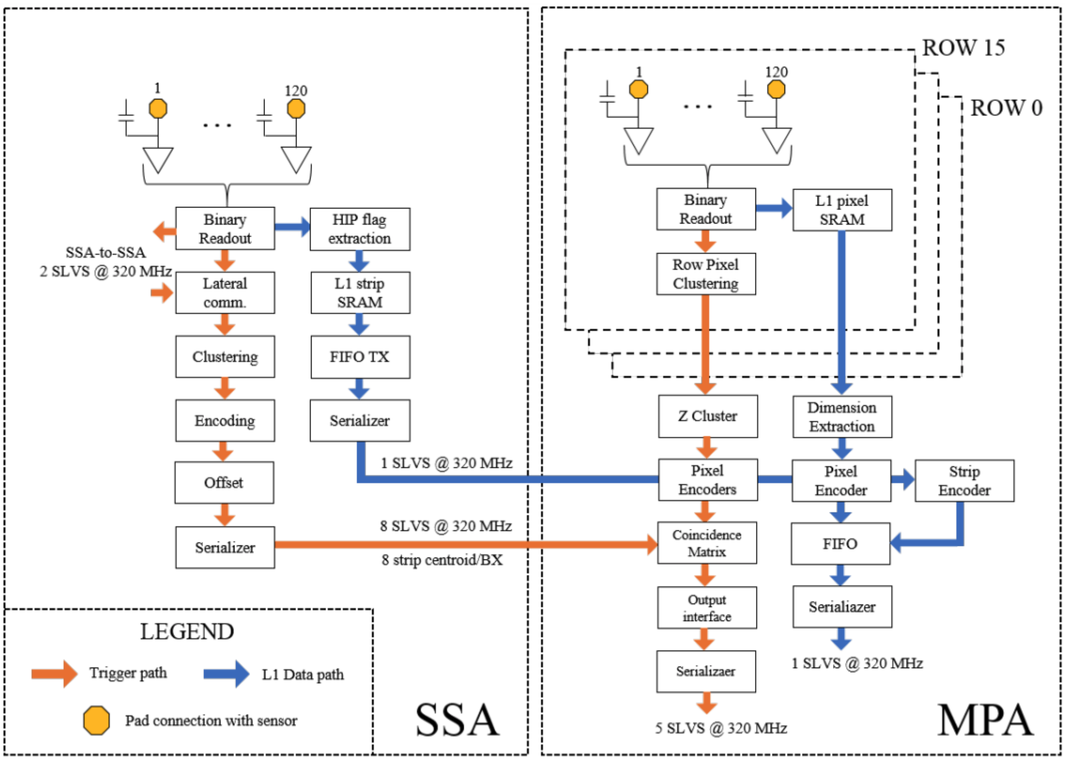

Figure 4.10: The architecture of the PS module readout ASICs is shown. The orange arrow and the blue arrow indicate the trigger path for the stub information and the L1 data path, respectively. Adapted from [64].

While the 2S module features a single Service Hybrid integrating the optical readout and DC-DC converter, the PS module uses two separate hybrids: the Optical Readout Hybrid (ROH) and the Power Hybrid (POH), as shown in Figure 4.8 (5a) and (5b). This separation is necessary due to the smaller geometry of the PS module, which limits the available space for integration.

A baseplate made of Carbon Fiber Reinforced Polymer (CFRP) has been designed for the PS module to facilitate cooling, as shown in (7) in Figure 4.8. This additional cooling solution is necessary because the MPA chips generate significantly more heat compared to the CBC, whose cooling requirements are sufficiently handled through their mounting points in the detector. The CFRP baseplate provides high thermal conductivity, efficiently transferring the heat generated by the MPA chips to the cooling system and ensuring reliable operation.

4.4 The Outer Tracker Layout

The schematic layout of one half of the Phase-2 Tracker in $r-z$ view is shown in Figure 4.11. The structure consists of six cylindrical barrel layers extending up to $|z| < 1200$ mm, along with five end-cap double-discs on either side, extending from $1200 < |z| < 2700$ mm. Covering radial distances from approximately 21 cm to 112 cm from the collision point at (0,0), the Outer Tracker is organized into three primary sub-detectors: the Tracker Barrel with PS modules (TBPS), highlighted in the blue box in the figure; the Tracker Barrel with 2S modules (TB2S), marked in red box; and the Tracker End-cap Double-Discs (TEDD), shown in black box. The short lines shown in the figure represent the p_T modules, with the PS modules depicted as blue lines and the 2S modules as red lines. The number of modules per type and variant installed in each sub-detector are summarized in Table 4.2.

The layout design has been optimized to achieve hermeticity for particles originating within $|z_0| < 70$ mm. This configuration ensures that particles pass through at least six module layers across the pseudorapidity range $|\eta| < 2.4$ as shown in Figure 4.12. A slight reduction in coverage occurs at the interface between the barrel and end-cap sections, around $|\eta| \approx 1$, where particles typically pass through only five layers. Despite this small variation, the six-layer design provides the necessary depth for robust performance in track identification at the Level-1 trigger stage. A simulation performance study is presented in [65].

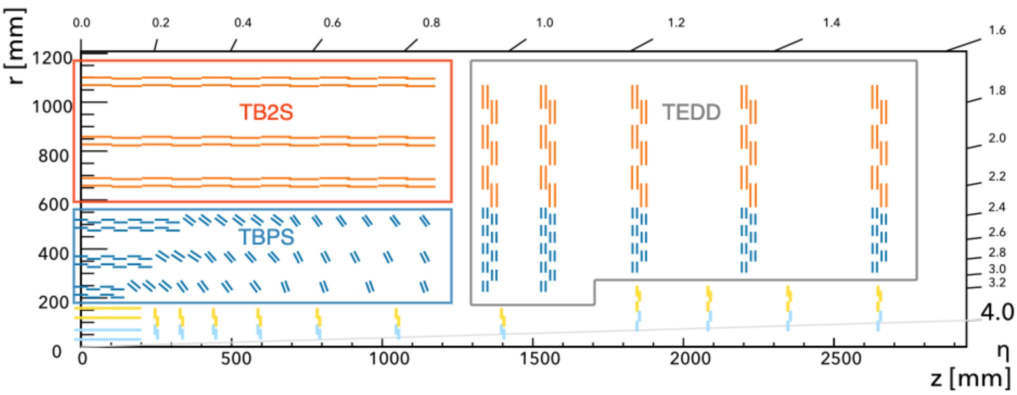

FIGURE 4.11: Sketch of one half of the Phase-2 Outer Tracker in r-z view. In this view, $(0,0)$ represents the interaction point of proton collisions, where r denotes the radial distance from the beamline and z is the coordinate along the beamline. Blue, red, and black boxes indicate the barrel layers with PS modules (TBPS), barrel layers with 2S modules (TB2S), and End-cap Double-Discs (TEDD), respectively. Parallel lines within each sub-detector represent overlapping module layers, positioned at the same r but mounted on opposite sides of the support structure, with PS modules shown in blue and 2S modules in red. The Inner Tracker is also depicted, with its components shown in yellow and light blue.

TABLE 4.2: Number of Outer Tracker modules categorized by module type and spacing variant.

Module Type and Variant		**TBPS**	**TB2S**	**TEDD**	**Total**
2S	1.8 mm	0	4464	2792	7680
	4.0 mm	0	0	424	
PS	1.6 mm	826	0	0	5616
	2.6 mm	1462	0	0	
	4.0 mm	584	0	2744	
Total		2872	4464	5960	13296

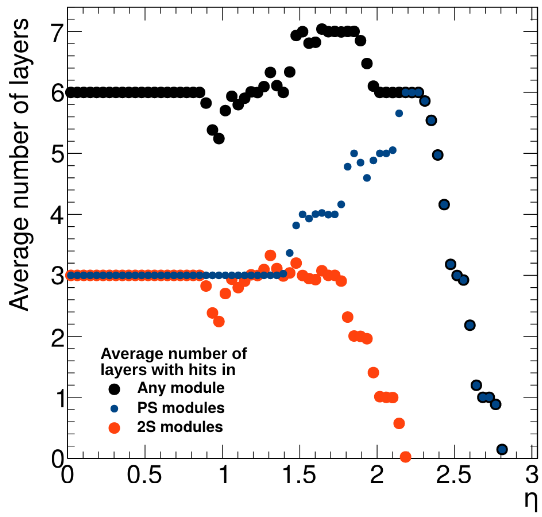

FIGURE 4.12: The average number of module layers crossed by particles as a function of pseudorapidity $|\eta|$ is shown, differentiated for PS modules in blue, 2S modules in red, and the overall total in black. Particles are assumed to originate from a range within $|z_0| < 70\,\mathrm{mm}$, and the trajectories are simplified as straight lines in the simulation, with multiple scattering not considered. Figure taken from [36].

The parallel lines shown in Figure 4.11 represent the modules located on opposite sides of the supporting structure. Front-end and service hybrids are mounted at the module edges, creating inactive regions; therefore, overlapping the modules along all four edges is essential to ensure hermetic coverage in tracking.

Barrel Region, TB2S and TBPS

Figure 4.13 and 4.14 display the 3D model of the module overlaps and a section of the mechanical structure for the TB2S and TBPS, respectively. The 2S modules are mounted onto the ladder structure, with odd-numbered modules on one side and even-numbered modules on the opposite, creating consecutive overlap along the z-axis. Additionally, sequential ladders forming the cylinder are arranged in a zigzag pattern in φ direction. The same configuration appears in TBPS layers with modules installed on the planks.

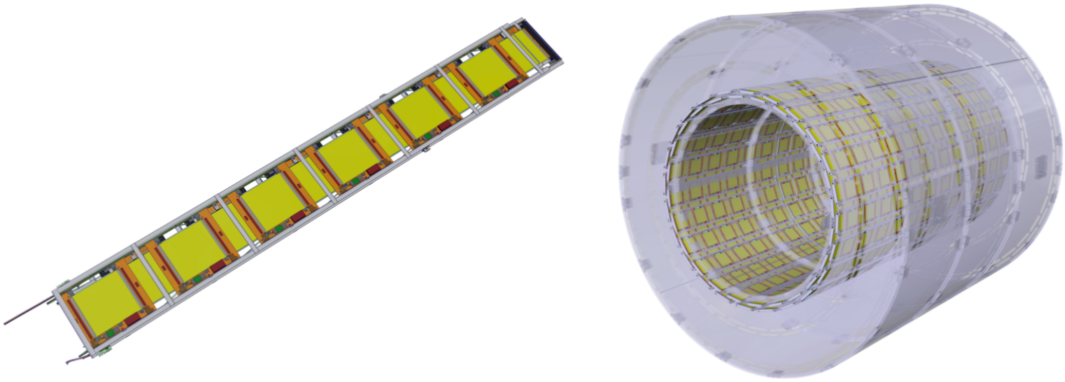

FIGURE 4.13: The 3D model of the TB2S ladder is shown on the left, and the innermost layer of the TB2S inside the support wheel is shown on the right. Adapted from [36].

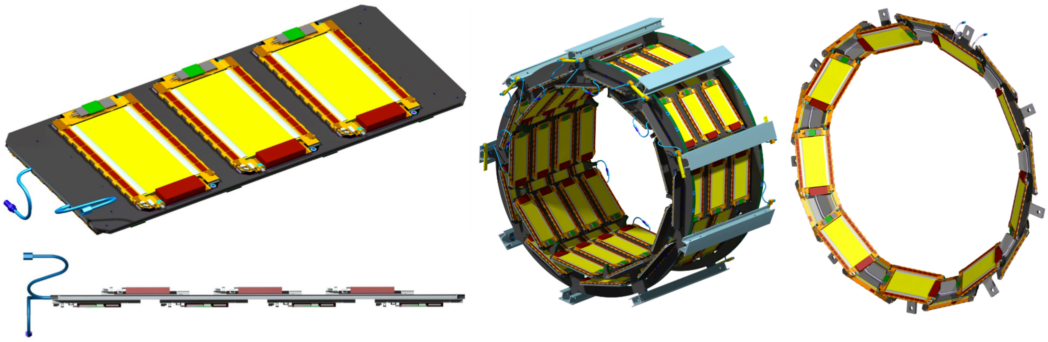

FIGURE 4.14: The left panel shows a 3D model of the TBPS mounted on the flat support structure, along with a side view of the module overlaps. The central figure displays the flat barrel section at the center of the TBPS, while the right panel illustrates a single ring layer in the tilted section. Modified from [36].

At the end of the barrel region, the PS modules are tilted at angles ranging from 35° to 75°. This layout mitigates the stub finding inefficiencies caused by geometric effects, as illustrated in Figure 4.15. Since the two sides of the module are read out by individual Front-End Hybrids, there is a lack of communication between the two halves of the sensor. Without tilting, stub-finding inefficiencies at the edges of the module could be addressed by overlapping a large number of modules; however, inefficiencies at the module center gaps remain uncompensated. Tilting the modules restores stub-finding efficiency with a minimal number of modules in the tracker.

To quantitatively achieve consistent p_{T} discrimination across different module locations in the CMS Outer Tracker, varying module spacings and stub-searching windows are implemented. As a charged particle moves through the CMS magnetic field of $B = 3.8\,\mathrm{T}$, its transverse momentum p_{T} defines the curvature of its path due to the Lorentz force. To effectively identify particle trajectories at different radial positions, modules are optimized with specific spacing and acceptance windows, as shown in Figure 4.16. This configuration is further illustrated in Figure 4.17. In part (a), the formation of a stub within a module is depicted, showing how two hit signals correspond to a particle's curved trajectory based on its transverse momentum. Part (b) demonstrates that modules located in the end-cap require a larger sensor spacing than those in the barrel to achieve equivalent p_{T} discrimination at the same radius. Part (c) highlights that, for a fixed sensor spacing, the distance between two hit signals

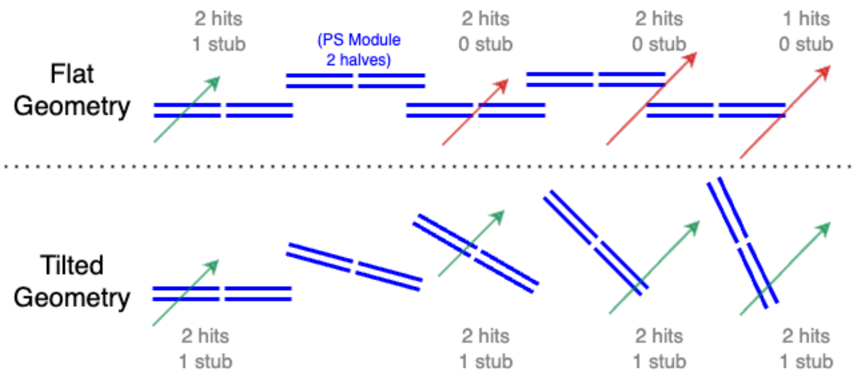

FIGURE 4.15: Illustration of stub-finding inefficiencies without the incorporation of tilted barrel regions. The thick blue lines represent halves of sensor modules. The green traversing lines indicate high-p_T particle trajectories that are successfully recognized by the module and form stubs, while the red traversing lines represent trajectories that fail to produce stubs due to geometric inefficiencies. In the tilted geometry, cases that fail to form stubs in the flat geometry are successfully identified.

increases with the radius for particles with the same p_T, due to the increased path length.

The design concept underlying these diagrams can be expressed by the following equation:

$$p_T \approx \frac{0.57r}{\sin\theta} = 0.57r\sqrt{1+\left(\frac{d}{p\Delta x}\right)^2}, \tag{4.1}$$

where r is the radial position of the module in the detector, d is the module spacing, p is the strip (or pixel) pitch, Δx is the stub acceptance window, and θ is the angle of the particle's trajectory relative to the radial direction. This formulation accounts for both the geometry of the module layout and the particle's trajectory, ensuring consistent p_T discrimination across the Outer Tracker volume.

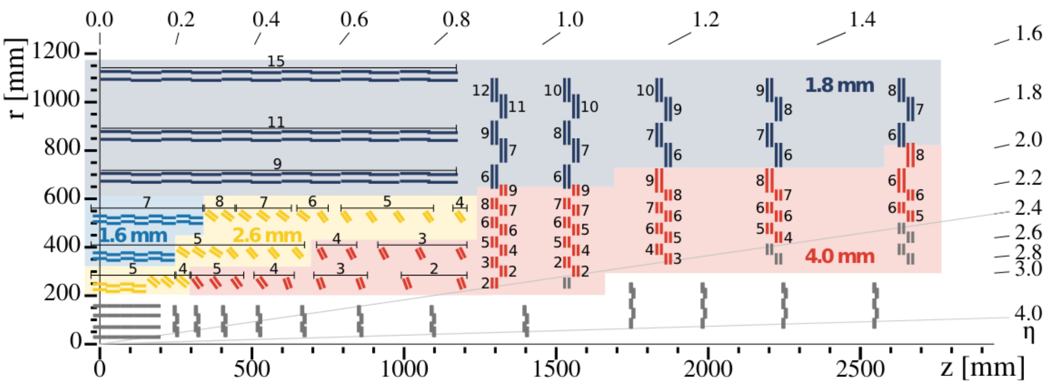

FIGURE 4.16: One half of the tracker in r-z view, showing sensor spacings and stub acceptance windows in strips for Outer Tracker modules. Sensor spacings are represented by colors: 1.6 mm (light blue), 1.8 mm (dark blue), 2.6 mm (yellow), and 4.0 mm (red). Acceptance windows, indicated by black numbers near the modules, are given in channel counts and correspond to a $p_T > 2$ GeV selection cut. Figure taken from [36].

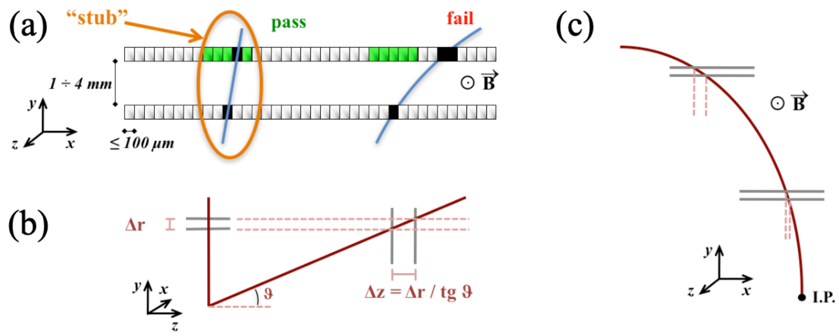

FIGURE 4.17: Simplified illustration of the module spacing and stub acceptance window necessary to achieve the same desired p_T discrimination. (a) Formation of a stub in a module. (b) To achieve equivalent discriminating power in the end-cap discs as in the barrel at the same radius, greater sensor spacing is required. (c) For a given sensor spacing, the same transverse momentum produces a wider separation between two signals at larger radii. Figure taken from [36].

Additionally, an offset correction must be introduced to the acceptance window in the module to address the parallax error resulting from approximating the tracker's cylindrical geometry using flat sensors. This misalignment becomes particularly significant in the inner layers of the tracker, where the sensors cover a larger angular region. In these layers, even high-momentum particles intersect the sensor stack at an angle, due to the flatness of the sensors. By introducing a programmable offset to the centroids in the correlation layer, the acceptance window can be aligned more accurately with the expected trajectory of high-p_T particles. This correction ensures consistent p_T discrimination across the modules and improves the precision of the stub formation process. The impact of this offset is illustrated in Figure 4.18, where the corrected acceptance window compensates for angular deviations and aligns with the actual particle trajectory.

By optimizing module spacing, stub window parameters, and the offset of the acceptance window according to these considerations, the Outer Tracker achieves uniform sensitivity to transverse momentum and effective track discrimination throughout its detection range.

End-cap Region, TEDD

The TEDD structures extend the tracking coverage into the forward regions. On each CFRP disc, PS modules are positioned in the inner regions at radii less than 60 cm, while 2S modules are placed in the outer regions. Hermeticity in the end-cap region is achieved by alternating placement of consecutive modules on opposite sides of the discs, combined with azimuthal overlap to form a continuous ring. In the radial direction, consecutive rings are precisely positioned on the two discs within a pair, ensuring seamless coverage as shown in Figure 4.19. Together, the two discs form the characteristic double-disc structure of the TEDD.

Cooling pipes are integrated within the discs to manage thermal loads effectively. PS modules are directly mounted onto cooled surfaces for optimal heat dissipation, while 2S modules utilize aluminum inserts to transfer heat efficiently to the cooling pipes and to provide precise mechanical mounting. This design ensures both thermal management and structural integrity, preserving high-performance tracking capability under the demanding high-luminosity conditions anticipated at the HL-LHC.

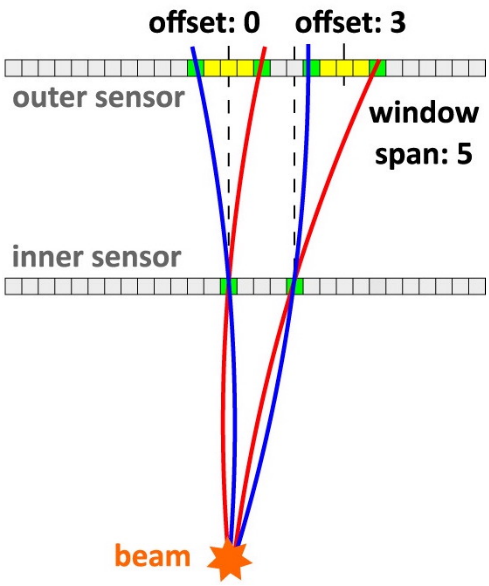

FIGURE 4.18: Illustration of the position-dependent programmable offset applied to the center of the acceptance window in the correlation sensor. This offset corrects the radial projection of a hit from the inner sensor to its corresponding position on the outer sensor, ensuring alignment and accuracy in trajectory reconstruction. Taken from [66].

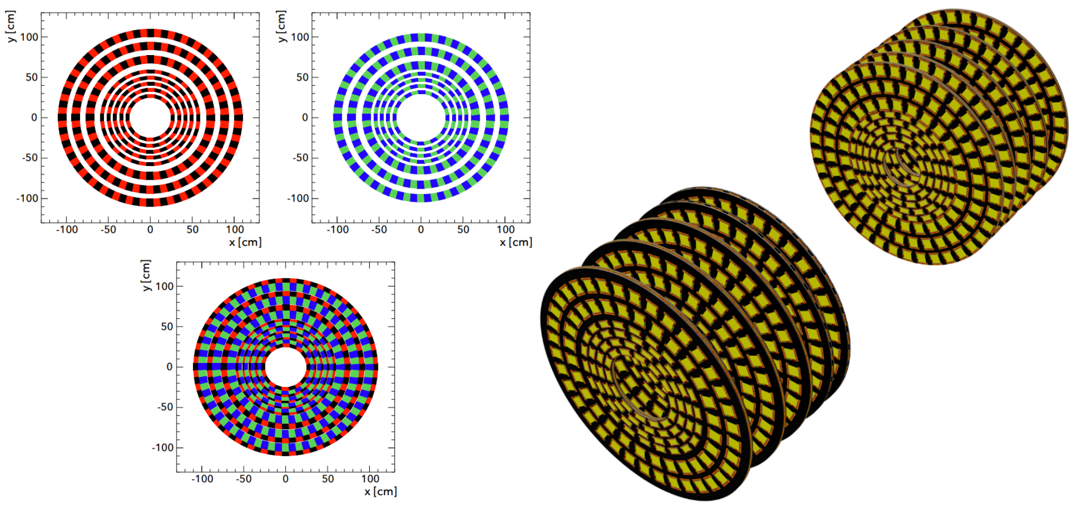

FIGURE 4.19: Schematic layout and 3D model of the TEDD. The left image illustrates the layout, where red and black modules are mounted on the same disc but on opposite sides, while green and blue modules are mounted on the other disc within the same double-disc structure. Together, these modules ensure complete coverage of the end-cap region. The right image shows the 3D model of two identical TEDD units, with five such units used in each end-cap, populated with PS and 2S modules.

4.5 Expected performance

The CMS Phase-2 Upgrade is expected to maintain robust tracking performance and high-resolution event reconstruction even under the challenging conditions of the High Luminosity LHC. This section outlines the anticipated performance of the upgraded tracker based on detailed simulations and analyses presented in [36].

The Outer Tracker is designed with higher granularity to ensure hit occupancy remains low, even under high pile-up conditions. Figure 4.20 based on a simulation of $t\bar{t}$ events with 200 pile-up interactions, shows the occupancy in the Outer Tracker. The exhibit occupancies remain below 3 %, demonstrating acceptable performance. The tilted barrel design significantly reduces occupancy in the $|\eta| \approx 0.5$ region compared to the central flat barrel, particularly for TBPS layer 1. This reduction in occupancy underscores the effectiveness of the tracker layout and the tilted geometry in managing high channel occupancies.

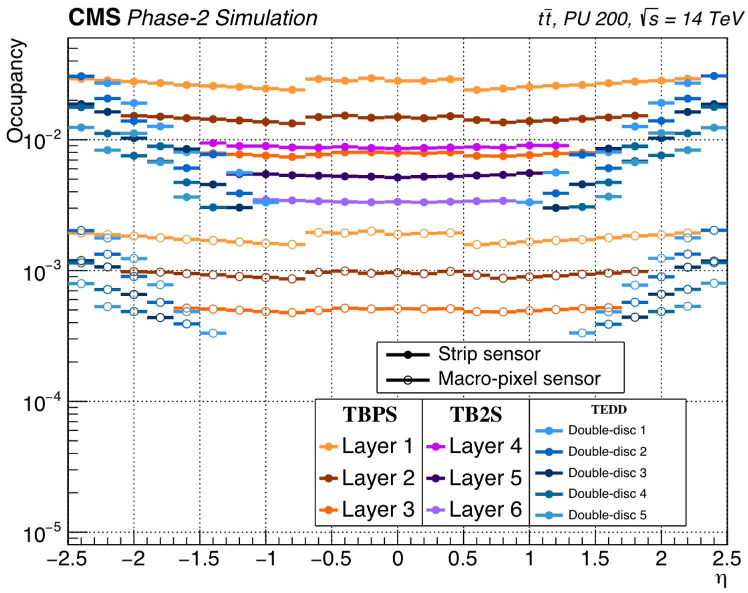

FIGURE 4.20: Simulation of the hit occupancy as a function of pseudorapidity η for all layers and double-discs of the Outer Tracker. The occupancies in strip sensors and macro-pixel sensors are represented by filled and unfilled markers, respectively. Figure adapted from [36].

The tilted barrel geometry enhances stub reconstruction efficiency, achieving values above 90 % across all layers of the tilted barrel as shown in Figure 4.21. Figure 4.22 illustrates the stub reconstruction efficiency for muons as a function of p_{T} across the barrel and end-cap regions. The efficiency exhibits a characteristic turn-on behavior at lower p_{T}, rising at the target threshold of 2 GeV and plateaus near 100 % at higher p_{T}. This performance reflects the optimized design of the stub acceptance windows, ensuring precise and efficient track reconstruction.

Figure 4.23 illustrates the expected tracking performance of the CMS detector under two pile-up(PU) scenarios, a pile-up of 140 and 200. The figure on the left shows the tracking efficiency for single muons with $p_{\mathrm{T}} = 10$ GeV across the pseudorapidity range. The efficiency remains stable and near 100% for both pile-up scenarios, demonstrating robust tracking performance. The figure on the right presents efficiency for tracks from $t\bar{t}$ events, focusing on tracks produced within a radius of 3.5 cm and with $p_{\mathrm{T}} > 0.9$ GeV. The tracking efficiency performance at a high pile-up of 200 for the Phase-2 tracker is comparable to the expected performance of the Phase-1 tracker at a pile-up of 70 events presented in [67].

Details on the Level-1 tracking and overall physics performance can be found in [36, 65, 54].

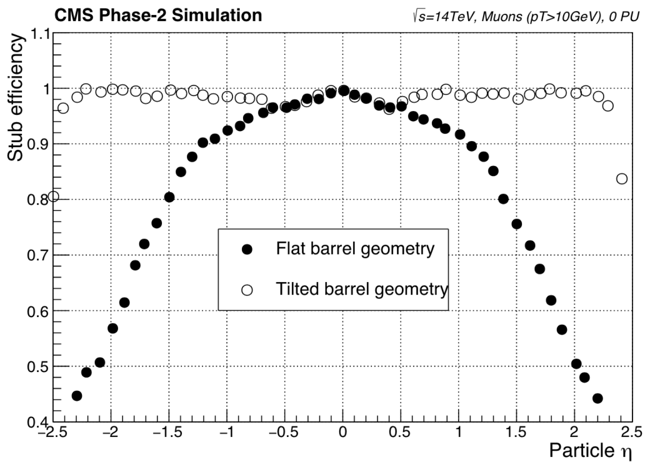

FIGURE 4.21: Simulation of stub reconstruction efficiency as a function of η for stubs with $p_{\mathrm{T}} > 10$ GeV in TBPS layer 1, comparing the flat and tilted tracker barrel geometries. Figure adapted from [36].

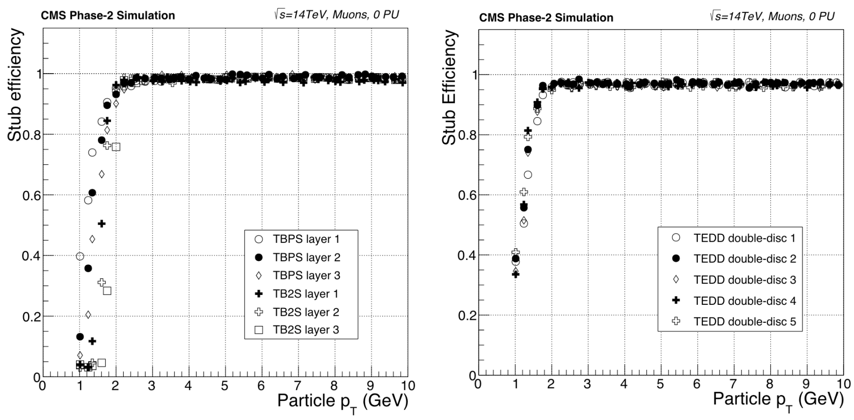

FIGURE 4.22: Simulation of stub reconstruction efficiency as a function of p_{T} for muons in barrel regions on the left, and in end-cap regions on the right. Figure adapted from [36].

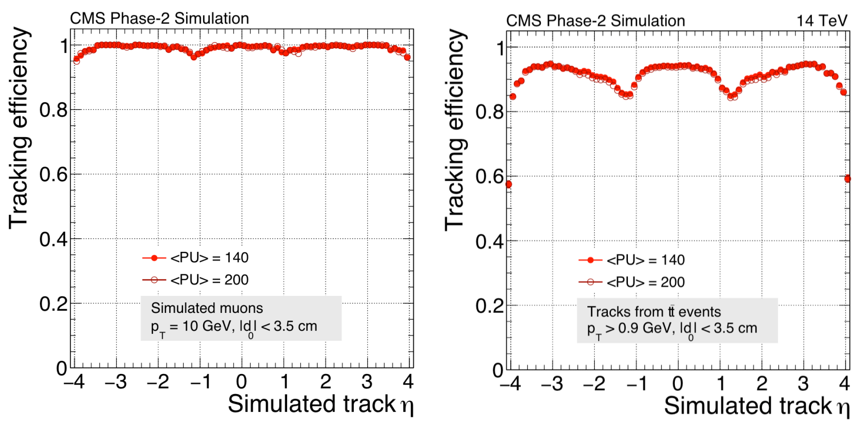

FIGURE 4.23: Tracking efficiency as a function of pseudorapidity under 140 and 200 pile-up conditions for (left) single muons with $p_{\mathrm{T}} = 10$ GeV, and (right) tracks from $t\bar{t}$ events with $p_{\mathrm{T}} > 0.9$ GeV. Only tracks originating within a radius of 3.5 cm from the center of the luminous region are included. Figure adapted from [36].

Chapter 5

Characterization of a Strip-Strip Module

Contents

Before commencing the production phase of the modules, it is essential to perform characterization and functional verification of each prototype module, including p_T discrimination. This step is crucial for evaluating the design and ensuring the achievement of the intended design objectives.

DESY, as one of the PS module assembly institutes, is responsible for assembling modules to demonstrate proficiency in handling and fabricating modules that meet specified requirements, as well as contributing to test beam investigations. The earlier availability of components for a 2S module provided an opportunity to construct and test it in a testbeam at DESY, offering valuable practice and establishing the assembly and analysis framework for the PS modules.

The components described in Section 4.3.1 first underwent electrical tests in a clean-room environment and have been assembled into a module. The module was subsequently characterized under various operating conditions at the DESY II test beam facility, which will be further detailed in Section 5.5. The obtained test beam results were analyzed using the Corryvreckan software [68].

5.1 Pre-Assembly Test

Before assembling the prototype module, all components underwent visual inspection to prevent the assembly of faulty parts. For silicon sensors, it is essential to obtain its depletion voltage. Operating the sensor in a fully depleted state ensures a high electric field across the bulk, enabling efficient charge collection and strong signal generation. Additionally, it is essential to ensure that the sensor does not exhibit current breakdown at the depletion or operation voltage.

5.1.1 Test Setup

Figure 5.1 shows the pre-assembly electrical test setup. The sensors were tested using a probe station equipped with probe needles. The probe station is enclosed by a cover, allowing measurements to be conducted in a dark environment to prevent photon current. The sensor backplane is securely held in place on the chuck using vacuum pressure, while the probe needle establishes contact with the sensor via the bias ring. Figure 5.2 depicts a schematic illustration of the electrical connection between the devices in the setup. An electrometer, which supplies a high bias voltage and measures the leakage current, is directly connected to the chuck through the CV/IV switch box. An LCR meter is connected to a customized CV/IV box, which enables the measurement of capacitance by coupling the LCR meter into the setup. The box also allows switching the connection between I-V and C-V measurements setup.

5.1.2 I-V and C-V Measurements

As mentioned at the beginning of chapter 5.1, it is crucial to find the depletion voltage to maximize the signal and ensure that the Signal-to-Noise ratio is large enough for good data quality. The depletion voltage represents the lowest voltage level at which the bulk of a silicon sensor reaches full depletion and is extracted from capacitance-voltage(C-V) measurement according to Equation 3.10.

During the production phase of module assembly, it is imperative for sensors to achieve minimal leakage current while subjected to a bias voltage of up to 600 V. Although a negative voltage is applied to the backplane of the sensors, all results shown in this chapter are presented as absolute values for simplicity.

In the tracker upgrade campaign, sensors were developed with varying thicknesses: a physical thickness of 320 µm with an active thickness of 290 µm, and a physical and active thickness of 240 µm [58]. However, sensors with a thickness of 240, µm demonstrate vulnerability and sensitivity to scratches on the backplane of the sensor due to a thin implant on the backside, which can result in early breakdown before achieving the desired operational voltage.

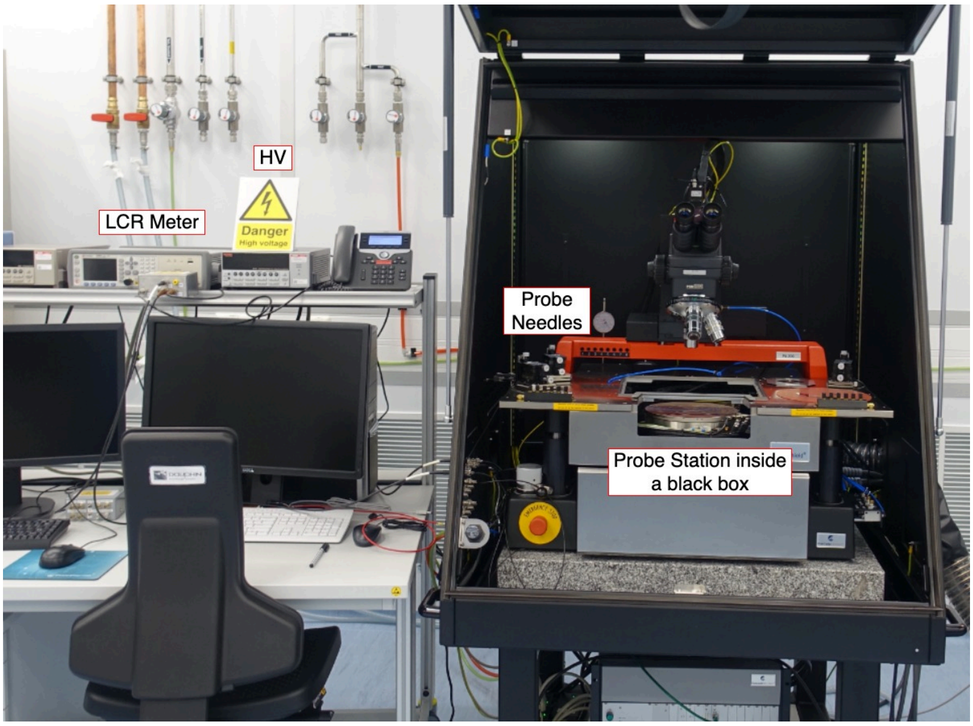

FIGURE 5.1: The probe station setup for pre-assembly electrical tests in the DESY cleanroom.

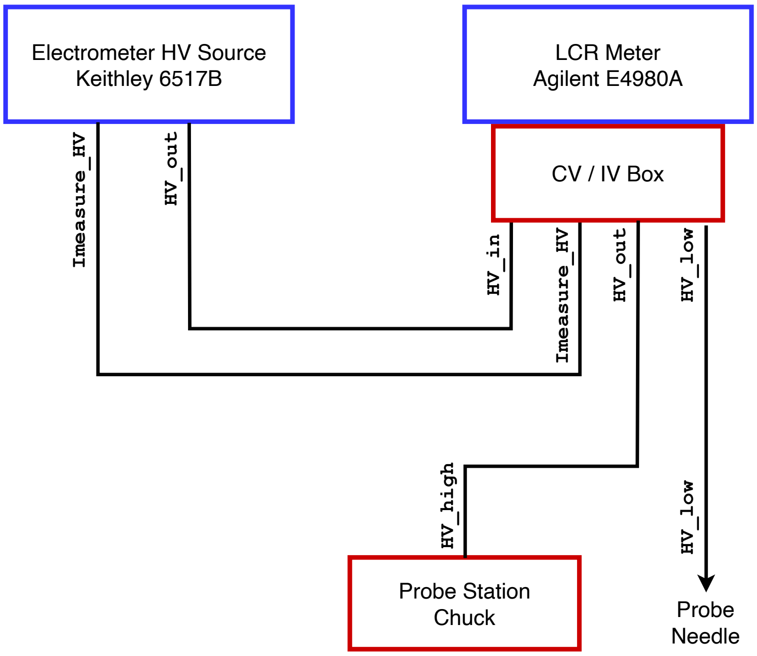

FIGURE 5.2: Sketch of the electrical connections.

The sensors integrated into the 2S module at DESY feature an active thickness of 240 µm, primarily driven by component availability constraints in the collaboration. The *I*-*V* measurement shown in Figure 5.3 demonstrates an early breakdown at approximately 205 V. Consequently, the capacitance measurements were restricted to a maximum of 220 V to safeguard the sensors against potential damage.

The *C*-*V* measurements were conducted in two phases. Initially, an incremental bias

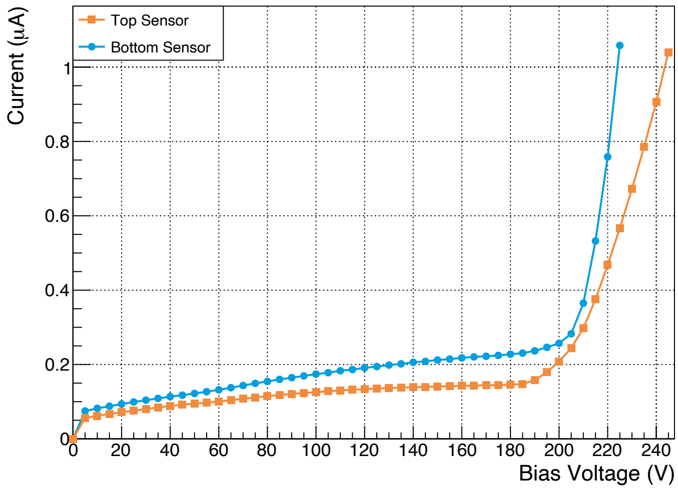

FIGURE 5.3: *I*-*V* measurement of the two silicon sensors.

voltage step of 10 V covering the range from 0 V to 220 V, as depicted in Figure 5.4(a). Subsequently, a finer step size was applied near the depletion voltage to enhance measurement resolution. The depletion voltage was determined by performing a linear fit to two distinct regions of the *C*-*V* measurements shown in Figure 5.4(b): one corresponding to the uprising region before full depletion, where C^{-2} is proportional to the applied voltage, and the other corresponding to the plateau region after full depletion, where C^{-2} remains constant. The intersection of these two fitted lines defines the depletion voltage. The fitting results indicate depletion voltages of 197 V and 209 V for the top and bottom sensors, respectively.

Given that the two available silicon strip sensors were the sole options in this study, and considering that the depletion voltage can still be attained prior to entering the region of elevated leakage current, these sensors were integrated into a 2S module for further investigations.

5.2 Prototype Module Assembly

5.2.1 Prototype Parts

In a similar vein to the components of a 2S module described in Section 4.3.1, the DESY 2S module contains two strip sensors with the size of 10 cm by 10 cm each, two AlCF bridges separating the sensors to achieve a spacing of 1.8 mm, Kapton isolation strips, two Front-End Hybrid (FEH), two Concentrator Integrated Circuit (CIC) mezzanines and a Service Hybrid (SEH).

Since the hybrids were still in development when the module was constructed, the assembly utilized the final version of the readout ASIC, CBC3.1 [69], version 2 of the CIC mezzanines, a VTRx, and a legacy Giga-Bit Transceiver (GBT) chip-set consisting of a GBTx [70] and a Slow Control Adapter ASIC (GBT-SCA) [71].

5.2.2 Assembly Procedures

The ultimate goal of the outer tracker modules, p_{T} discrimination, has high requirements on the alignment of the top and bottom sensor. Additionally, the positioning of

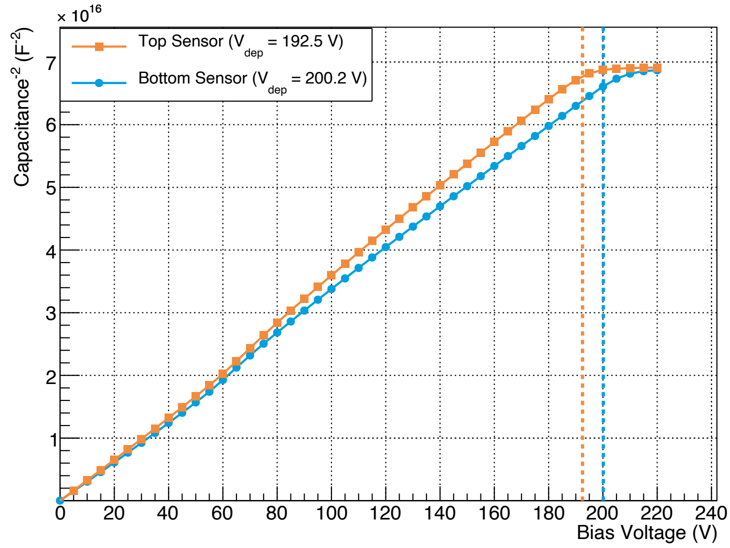

(a)

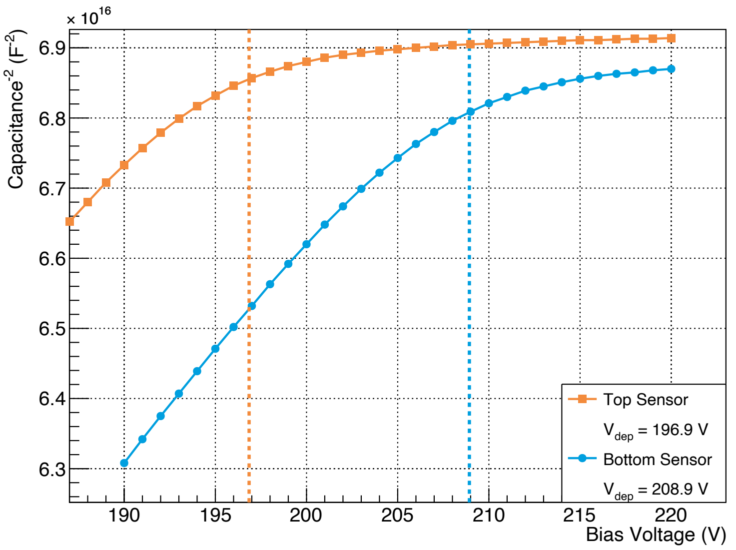

(b)

FIGURE 5.4: (a) C-V measurement of the two silicon sensors. (b) The measurement is taken with a finer increment voltage step around the depletion voltage.

each component must comply with specifications to ensure that the modules meet the required standards during production. Thus, multiple module-assembling jigs with vacuum holes that are shown in Figure 5.5 were designed to achieve precision.

A comprehensive overview of the assembly procedure, as illustrated in Figure 5.6, is outlined below:

1. Kapton isolation strips gluing: Kapton strips were aligned with magnetic stoppers and immobilized by the vacuum provided through positioning jig 1 (in Figure 5.5). Epoxy glue (Polytec EP 601-LV) was applied to the strips. A sensor was placed on jig 2, held in position by the vacuum as well. The positioning jig

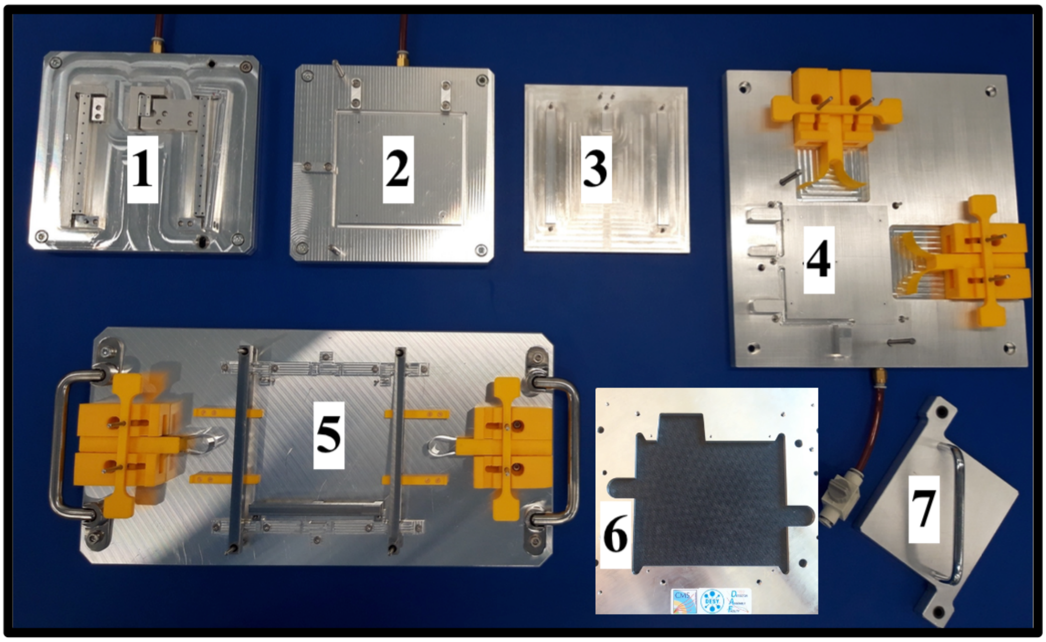

FIGURE 5.5: Specialized assembly jigs are employed for the assembly process of the 2S module, encompassing the following components: 1. Kapton isolation positioning jig, 2. Sensor-holding jig, 3. Glue transfer jig, 4. Sensor gluing jig, 5. Hybrid gluing jig, 6. Module carrier, 7. Weight object for glue curing.

was then inverted and aligned over the sensor-holding jig using guiding pins for precise placement. Once the Kapton strips were properly positioned, the vacuum was released, and the positioning jig was removed.

2. High Voltage (HV) Tails gluing and wire bonding: As shown in Figure 5.6(b), the sensors were positioned within the jig sequentially and HV tails were aligned against the stopper, ensuring secure fixation through vacuum suction. The epoxy adhesive was carefully dispensed onto the tail, followed by the gentle application of slight pressure over the glued region. Subsequently, wires were bonded, establishing a connection from the HV tail pads to the backplane of the sensor, thus facilitating a bias voltage link. Encapsulation was applied. The final step encompassed the application of encapsulation to ensure wire-bond protection.

3. Bare module integration: Using jig 4 as illustrated in Figure 5.5, a bare module was assembled, comprising a stack of two sensors separated by three bridges. The jig is equipped with mechanical pushing arms and aluminum stoppers, strategically designed to achieve sensor alignment, along with position pins to precisely secure spacer positioning. For uniform adhesive distribution, a glue transfer jig 3 was utilized, applying a fine layer of epoxy glue to the spacers.

4. Hybrid gluing: Both FEH and SEH were affixed and precisely aligned through the hybrid gluing jig, which also contains pushing arms to ensure the alignment of the bare module. A higher viscosity epoxy, Polytec TC 437, was applied to

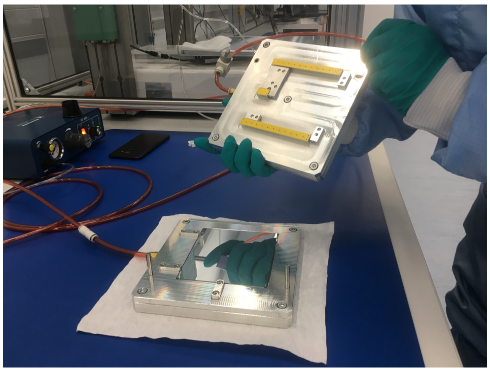

(a) The Kapton strips gluing process

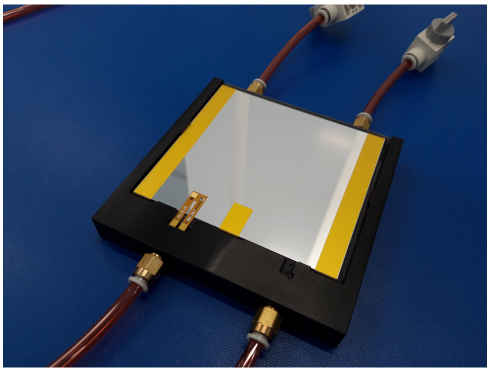

(b) The HV tail gluing process

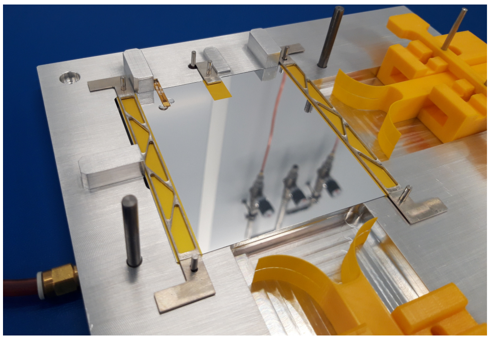

(c) Bare module integration

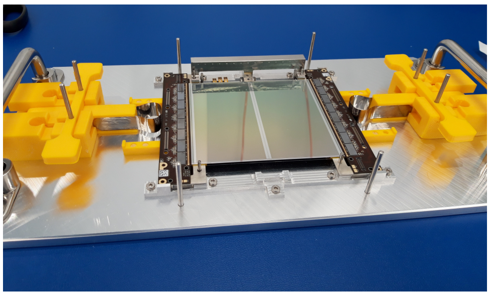

(d) Front-End Hybrids gluing process

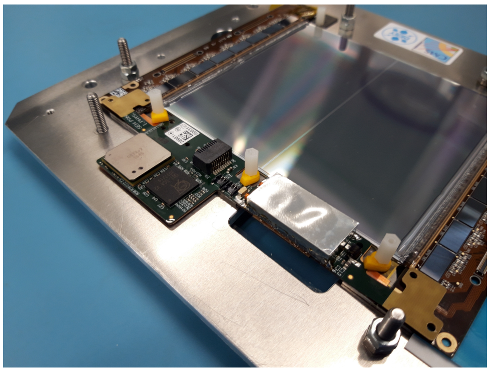

(e) Service hybrids gluing process

(f) Wire bonding process

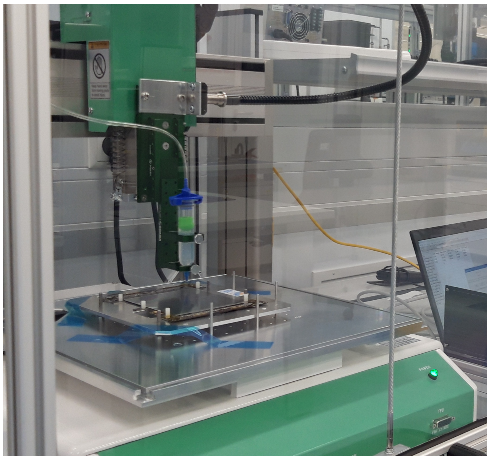

(g) Wire bonds encapsulation process

FIGURE 5.6: Photos of DESY 2S module assembly procedures.

the spacers. Hybrids were placed methodically on the spacers using aluminum pins, depicted in Figure 5.6(d). Concluding the process, a weight bar was placed on the hybrids, allowing a 24-hour curing period. Plastic screws and pins are used for the gluing of the SEH as shown in Figure 5.6(e).

5. Wire bonding and encapsulation: The sensor strips were wire-bonded to the Front-End Hybrids to establish electrical connections. Subsequently, the wire bonds were encapsulated with Sylgard 186 using the three-line method. In this technique, three parallel lines of encapsulant are applied along the direction perpendicular to the wire bonds. The two outer lines are applied first, followed by the central line over the loop of the bonds after a ten-minute interval. This approach ensures uniform coverage over the bonded area while minimizing the risk of air bubbles or glue leakage, providing a clean and secure encapsulation.

In summary, the assembly procedure involves a sequence of meticulously executed steps, each facilitated by specialized jigs and tools. The precision used during each phase contributes to the creation of a robust and high-performing 2S module that is shown in Figure 5.7.

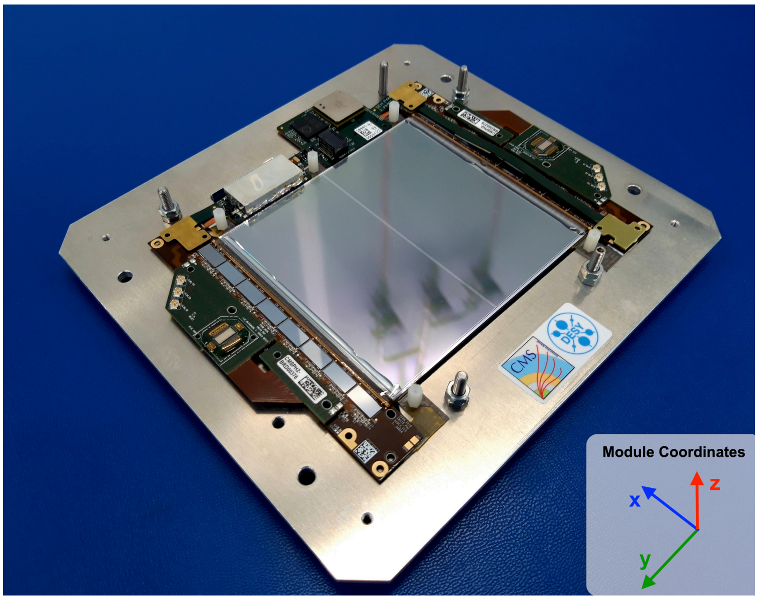

FIGURE 5.7: A photo of the DESY 2S module. The local module coordinates are established as follows: the x-axis aligns with the Front-End Hybrids, the y-axis is set along with the Service hybrid, and the z-axis is perpendicular to the sensor plane.

5.2.3 Post-Assembly Electrical Test

After assembling a module, it undergoes electrical testing, both for noise measurement and to configure it for data acquisition, specifically, the process of threshold equalization known as Trimming. Before commencing data acquisition, a global threshold can be set in each readout chip. However, owing to manufacturing-induced variations in the baseline of amplifier output, an offset adjustment is required for each individual channel to correct the baseline. More comprehensive information regarding threshold equalization is provided in Section 6.2.3, followed by an explanation of the trimming logistics used in the readout chip of the PS module.

The trimming process for a 2S module engaged a different approach compared to that of a PS module. To provide a more comprehensive explanation of the trimming method for a 2S module, it is necessary to introduce the concept of *Hit Occupancy*. Hit Occupancy refers to the average number of hits detected by each channel at a fixed threshold configuration. A predetermined number of triggers is dispatched to all channels, and the objective of the trimming process is to determine the offset adjustment that results in a 50% Hit Occupancy. If the Hit Occupancy exceeds 50 %, the offset is incrementally increased by one bit; conversely, it is reduced until the desired 50 % hit occupancy is achieved for all channels at the same threshold. The setup for the module electrical testing at DESY is described in [72]. Further information regarding the offset configuration is described in the CBC user manual [61].

After completing the trimming procedure, the module will undergo a threshold scan to measure hit occupancy at various threshold settings. As illustrated in Figure 5.8, the results reveal an S-shaped curve characteristic of Gaussian distributed noise. The S-Curve is fitted with an error function, and the standard deviation of this curve serves as a measure of the noise level. The 50 % point of the S-curve is defined as the pedestal.

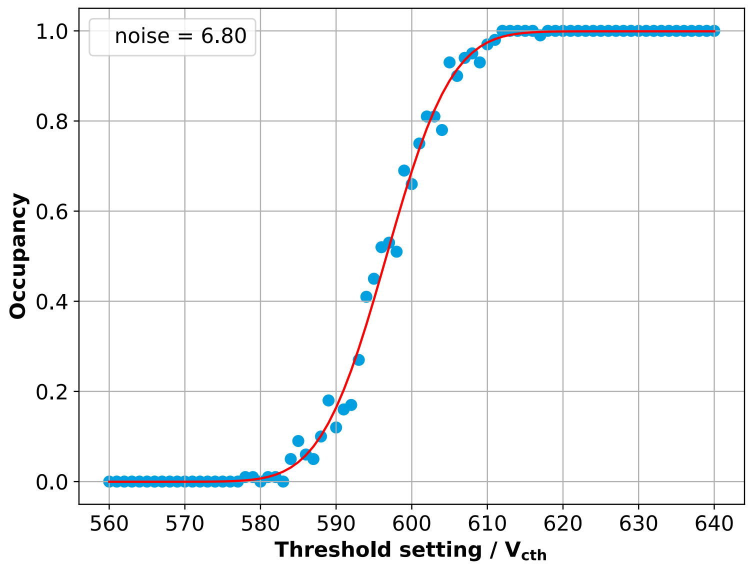

FIGURE 5.8: An example of S-Curve of Bottom sensor strip number 50. The noise unit of 1 V_{cth} equivalent to 156 electrons (e^-). It is important to note that the threshold settings within the CBC are configured inversely, where lower threshold values are associated with higher physical thresholds.

The unit of the threshold Digital-to-Analog Converter (DAC) is defined as V_{cth}, with 1 V_{cth} equivalent to 156 electrons (e^-) [73]. The results obtained from the noise measurement, as illustrated in Figure 5.9, indicate that the top sensor of the 2S module exhibits a noise level of 5.87 V_{cth} (equivalent to 916 e^-), whereas the bottom sensor records a noise level of 6.26 V_{cth} (equivalent to 975 e^-). The elevated noise in the Bottom sensor is attributed to the additional path length created by the folded hybrids.

The noise level from both sensors remains well within acceptable limits for data acquisition. This is because the threshold is typically set at a distance of 4 standard deviations (σ) from the pedestal, and the particle signal is expected to exceed the threshold by at least a factor of 3. Considering that an incident MIP typically generates an average of 76 electron-hole pairs per micron thickness of silicon, as reported in [47], this results in $18,240\,e^-$ being generated in a $240\,\mu m$ thick sensor. Given a noise level of approximately one thousand electrons from the measurements, the 2S module can achieve its optimal efficiency regarding the noise influence.

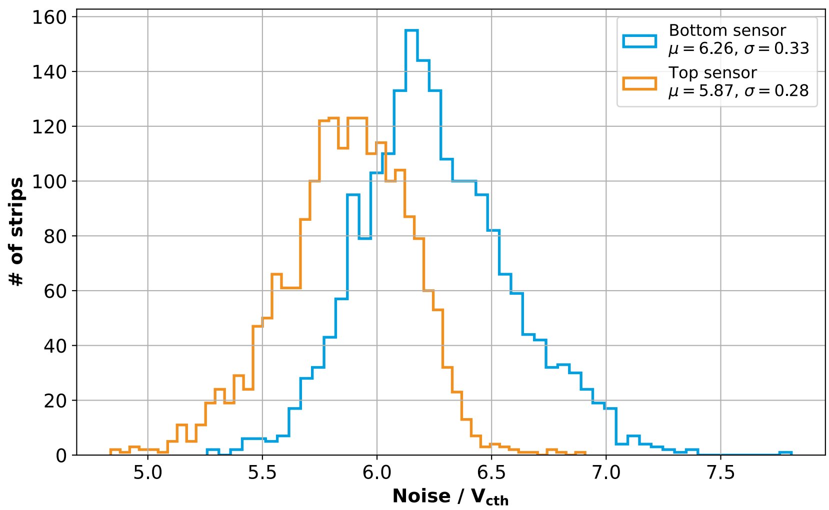

FIGURE 5.9: A module noise measurement of the top and bottom sensors.

5.3 Beam Tests at DESY-II Synchrotron

The 2S module was designed to serve as a tracking detector and contribute to the Level-1 trigger in the CMS Phase-2 detector. To ensure their functionality and efficiency, the modules were tested with particles in what are known as beam tests. Electron beams generated at the DESY-II synchrotron were used to characterize the assembled 2S module. Numerous tests were performed at the test beam facility, evaluating the particle-detection and p_T discrimination efficiency under certain conditions.

5.3.1 The DESY-II Beam lines

The DESY-II test beam facility [74], which operates at DESY-II synchrotron, provides three beam lines for users to conduct various experiments with particle beams. These test beams are created by a double conversion of the primary DESY-II electron beam as illustrated in Figure 5.10. The process involves the creation of bremsstrahlung photons by hitting a primary target positioned along the DESY-II beam orbit. Subsequently, these photons strike a secondary target, leading to the production of electron-positron pairs. By adjusting the polarity and magnetic field strength of the following dipole magnet, the test beams will be tuned to either electrons or positrons with a user-selectable momentum ranging from 1-6 GeV.

In the context of 2S module beam test studies, electron beams ranging from 4-6 GeV were chosen to ensure a consistent data collection process, producing a sufficient

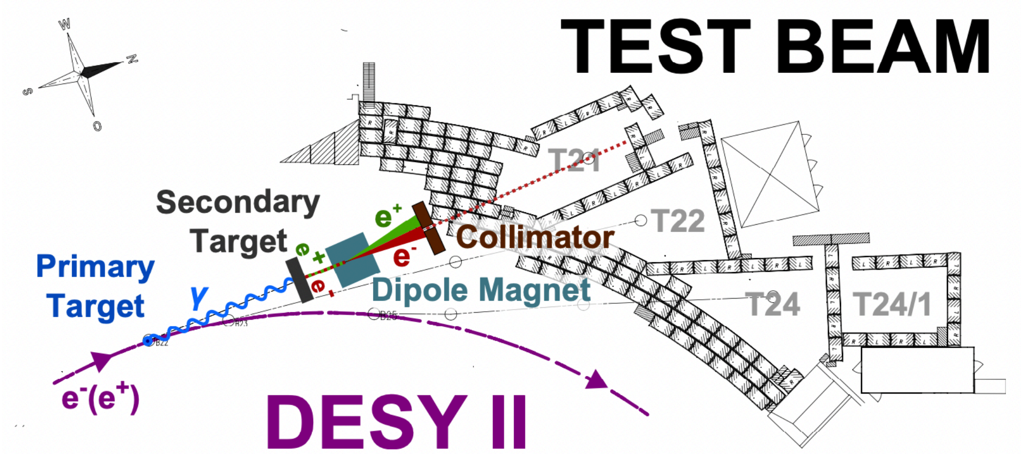

FIGURE 5.10: A schematic view of the test beam generation at DESY-II Test Beam Facility. [74]

number of particle entries necessary for event reconstruction, which will be further elaborated in Section 5.4.

5.3.2 Test Beam Setup

The setup of the DESY 2S test beam campaign, which took place in the testbeam area T21, is depicted in Figure 5.11. The setup contains a movement and rotation stage housing a Device Under Test (DUT) box, a beam telescope with 6 sensor planes, a timing reference plane, two scintillation detectors, and a Trigger Logic Unit (TLU). The DUT box was affixed on the movement and rotation stage providing the capability for displacement in both the x and y directions, as well as rotation around the y-axis. The movement and rotation stage was placed intermediate to the beam telescope arrangement, with three planes positioned in the front and three to the rear along the beam direction (z-axis). To prevent any detrimental scattering effects between the reference plane and the beam from impacting the DUT, the timing reference plane was strategically positioned at the far end point of the z-axis. Two scintillators are situated prior to the telescope plane position along the z-axis. A TLU with a coincidence unit, comprising discriminator boards, is connected to the scintillators and the control hardware of the other devices. The specifics of each of these components are outlined in the following sections:

- **DUT - 2S Module**: The 2S module was installed in a DUT box as shown in Figure 5.12, equipped with a power cable, a data readout link, and an air tube. The latter supplied nitrogen gas to the DC-DC converter, enabling heat dissipation. The position of the DUT within the telescope is controlled by a movement stage with the precision of a micrometer. To validate the functionality of p_{T} discrimination, a rotation stage is added to the movement stage. This arrangement allowed electron beams with fixed directions to intersect the two sensors with a defined offset in strip numbers, effectively simulating charged particles with various curvatures passing through the tracking module under the influence of the magnetic field.
- **EUDET-type Beam Telescope**: In order to distinguish the event of a particle hit from the noise and evaluate the tracking efficiency of the module, a dedicated

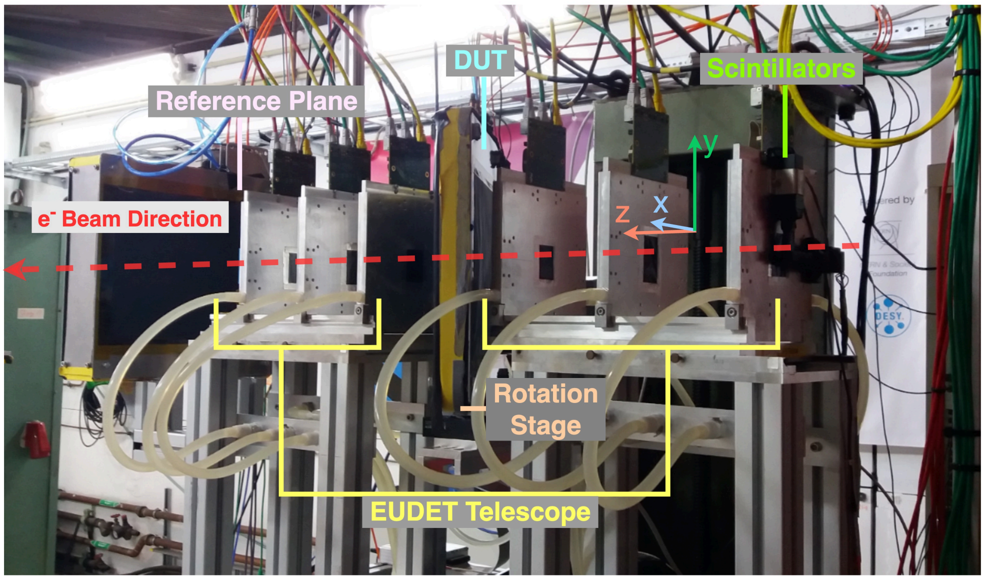

FIGURE 5.11: Test beam setup of the DESY 2S module studies campaign at DESY-II. The global coordinate system is defined with the z-axis aligned in the direction of the beam, orthogonal to the telescope planes. The y-axis is oriented vertically, pointing upwards from the ground, while the x-axis is defined along the sensor's strip arrangement.

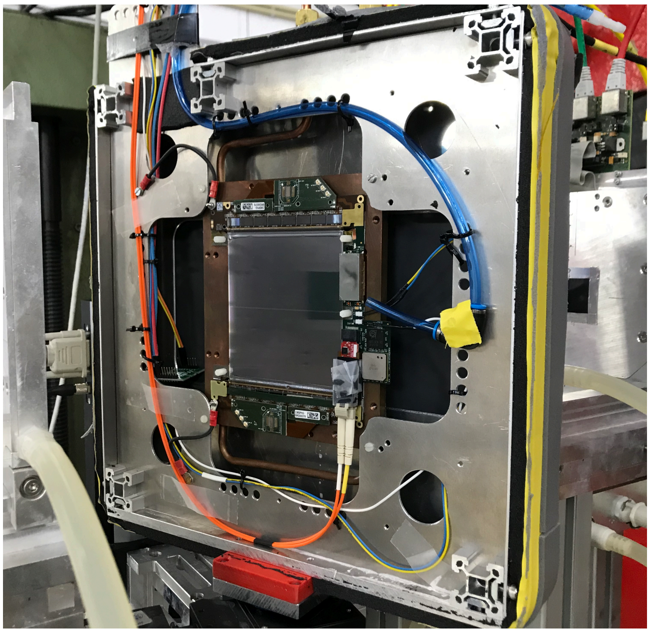

FIGURE 5.12: A photo of the DESY 2S module installed in the DUT box.

tracking telescope was used. The EUDET-type telescope was initially developed within the EUDET[1] project. Three EUDET beam telescopes are provided and installed at the DESY test beam facility, and DATURA[2] was used in the 2S module studies.

The telescope comprises six MIMOSA26, monolithic active silicon pixel sensors,

[1]EUDET: Detector R&D towards the International Linear Collider
[2]The three EUDET telescopes: Azalea, Datura, Duranta.

each manufactured with CMOS technology. The thickness of MIMOSA26 has been measured at $(54.5 \pm 3.5)\,\mu\mathrm{m}$ [75]. A lightproof Kapton foil of 25 µm thickness protects the sensor on each side. Considering these specifications, the total material budget of $x/X_0 = 0.075\%$ [75] for MIMOSA26 is particularly suitable to achieve high track resolution for experiments involving low-energy beams, such as the DESY electron beam and is taken into consideration for the track reconstruction, which will be further discussed in the next Section.

MIMOSA26 pixel sensors offer dimensions of $10.6\,\mathrm{mm} \times 21.1\,\mathrm{mm}$, featuring individual pixels measuring $18.4\,\mu\mathrm{m} \times 18.4\,\mu\mathrm{m}$ arranged in a matrix of 1152 columns and 576 rows. This configuration provides precise spatial measurements, with an average intrinsic resolution of $(3.24 \pm 0.09)\,\mu\mathrm{m}$ [75].

The readout mechanism of the telescope sensors operates using a rolling-shutter technique. This technique permits the simultaneous reading out of parallel data lines in conjunction with 16 cycles of an 80 MHz clock. Furthermore, it also offers zero suppression for the binary data information. The readout yields an integration time of $230.4\,\mu\mathrm{s}$ for the complete sensor to complete the data readout process. This integration time accounts for the need to capture two consecutive data frames ($115.2\,\mu\mathrm{s}$ each), to ensure that all the particle hits are detected regardless of their timing relative to the rolling shutter.

- **Time-reference plane**: The integrated readout time of the telescope is significantly longer than the $25\,ns$ readout interval of the DUT. Consequently, during a single recorded event of the DUT, multiple tracks are accumulated within the readout window of the DATURA telescope, leading to track multiplicity shown in Figure 5.13. The figure illustrates that the track multiplicity within a single event averages around 2.5 for a beam energy of 5.2 GeV. This value is anticipated to rise further as the beam energy decreases to 4 GeV, owing to the increased particle flux of the test beam as discussed in [74].

  To identify the track recorded by the DUT, and considering that the MIMOSA26 sensors lack time information for their pixels, an additional layer of timing data is required. The CMS Phase I pixel module, detailed in [77], was employed during the beam test as a timing reference detector.

  The CMS Phase-I pixel module comprises a planar silicon sensor with a thickness of 285 µm. The sensor possesses an active area of 16.2 mm $\times$ 64.8 mm and is divided into pixels with dimensions of 100 µm $\times$ 150 µm. Notably, the module consists of a total of 2 $\times$ 8 Readout Chip (ROC), with specific placement constraints due to the physical layout. Consequently, the sensor pixels situated along the boundaries of the ROC units have an area twice the size of the regular pixels, and the corner pixels have an area four times larger. This aspect involves careful consideration during the coordinate transformation from local to global frame and track selection within the offline analysis process. Further elaboration on this matter can be found in Section 5.4.4. The timing reference module acquires identical timing characteristics as the 2S module, both operate with a 40 MHz clock. During the offline analysis, the initial step involves selecting telescope tracks by matching them to the reference plane. All the investigations such as efficiency studies of the 2S modules are subsequently conducted using the tracks that have been selected.

- **Scintillation Detector and the Trigger Logic Unit**: Two scintillation detectors with plastic scintillators, each measuring 2 cm $\times$ 1 cm, accompanied

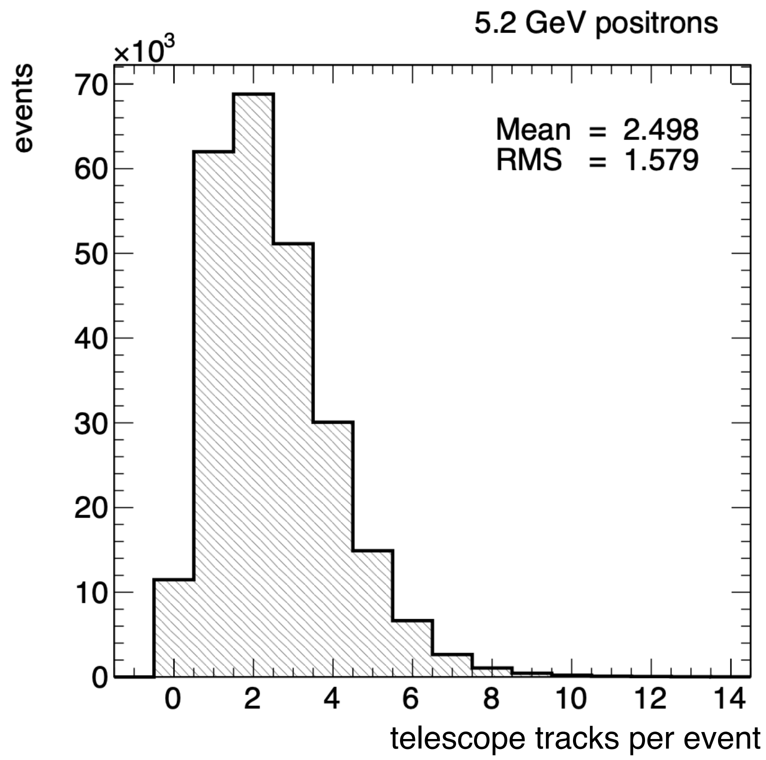

FIGURE 5.13: Track multiplicity in the DATURA beam telescope within one readout frame at particle energy of 5.2 GeV. [76]

by light guides and Hamamatsu PMTs[3], are employed to generate trigger signals corresponding to the incident beam. These scintillators intersect with one another and are positioned in front of the telescope planes along the z-axis within the setup. Their intersection forms an acceptance window of 1 cm $\times$ 1 cm.

Linked to the scintillation detectors is an EUDET trigger logic unit (TLU) [78]. This unit comprises a coincidence module, discriminator boards, and an FPGA board. When a particle passes through the scintillators, the resulting signal pulses are directed into the TLU to implement trigger logic. In this test beam study, the TLU will then generate and distribute common trigger signals for data acquisition across all detector devices solely when both scintillators concurrently provide signals.

Given the diverse response and process times for data readout, to achieve synchronization among all devices, one specific functionality within the TLU, known as the Trigger Handshake mode, remains enabled throughout the tests. In the Handshake mode, depicted in Figure 5.14, when the coincident signal arrives from the scintillators, the TLU generates one common trigger for the devices by asserting the TRIGGER line. Once the devices receive the trigger, they elevate a BUSY line, indicating their processing phase to the TLU. Subsequently, the TRIGGER line transitions to output the contents of a shift register within the TLU. This transition is controlled by 16 clock pulses provided by the DUT, which sequentially clock out the least significant 15 bits of the 32-bit trigger

[3] Photomultiplier Tube

counter onto the TRIGGER line. The data updates on the rising edge of each clock pulse. After the 15 bits are shifted out, the 16th clock pulse ensures the TRIGGER line is reset to a logical low, preventing glitches when the DUT releases the BUSY line.

Throughout the activation of the BUSY state in any device, the Handshake mode prevents the TLU from issuing triggers, allowing subsequent triggers to be issued only after the BUSY state is released from all the devices. This mechanism guarantees synchronization among the devices, ensuring that the collected data in the different detectors correspond to the same particle incident.

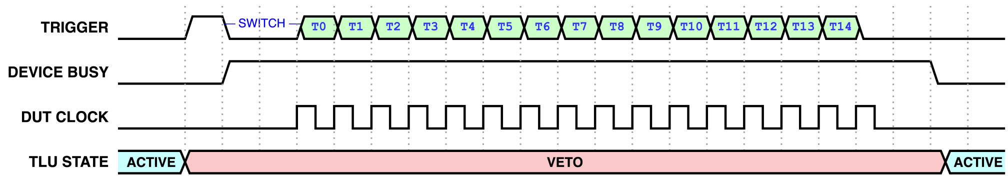

FIGURE 5.14: Signal diagram depicting the EUDET Handshake mode. Upon receiving the BUSY signal, the TLU de-asserts to generate a new TRIGGER signal. Subsequently, the TRIGGER line is switched to the output of a shift register that holds the trigger number. The TLU resumes issuing TRIGGER signals only after the BUSY signal concludes.

5.3.3 Data Acquisition

The hardware and software used for the data acquisition in the testbeam setup are depicted in Figure 5.15. The detectors are connected to their respective data acquisition systems. The beam telescope utilizes a DAQ system based on the National Instrument PXIe crate architecture, with a FlexRIO board [75]. The timing reference module employs the PSI Digital Test Board (DTB), a compact DAQ system with an FPGA and NIOS processor [77]. For the 2S module, the data acquisition system is built around the FC7 FPGA readout board, which is compatible with the µTCA standard. [79]. The FC7, an Advanced Mezzanine Card built around a Xilinx Kintex-7 FPGA, interfaces with the 2S module via optical fibers and supports line rates of up to 10 Gb/s. The board features two FPGA Mezzanine Card (FMC) sockets. One handles the optical fiber interface for the 2S modules, while the other connects to a DIO5 card equipped with LEMO connectors. This socket receives trigger signals from the TLU and passes the BUSY and TRIGGER clock signals back to the TLU.

The detectors are triggered and synchronized by the TLU, while the data acquisition process is managed by the EUDAQ2 framework [80]. EUDAQ2 is a modular data acquisition framework written in C++, specifically designed for test beam experiments. It enables seamless integration of multiple detectors, offering a robust architecture that unifies the collection, synchronization, and monitoring of data streams from diverse hardware systems.

At the core of the framework is the *Run Control*, which serves as the central manager for the entire EUDAQ2 system. It orchestrates the entire data acquisition process, initializing and configuring the system, starting and stopping runs, and monitoring the status of all components. It also provides a Graphical User Interface (GUI) for user interaction.

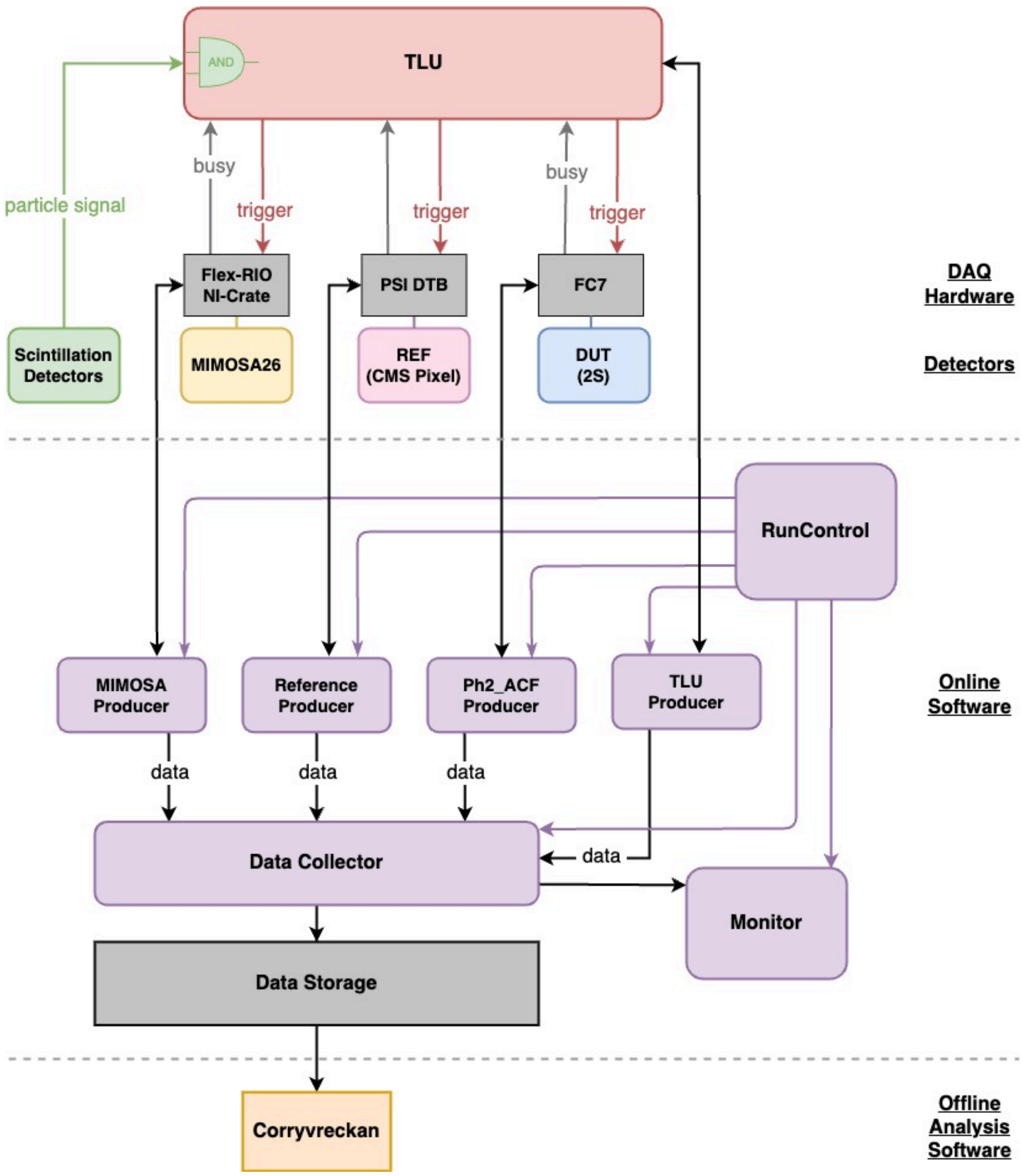

FIGURE 5.15: Data acquisition scheme used in the 2S module test beam. The TLU generates triggers based on coincidences from the scintillators, prompting each detector to be read out by its dedicated DAQ system. The EUDAQ2 framework provides centralized control for the entire process, while offline data analysis is performed using the Corryvreckan software.

Data from each detector system are handled by its sub-processor, referred to as a *Producer*, which is integrated into the EUDAQ2 architecture and linked to the Run Control. Each detector requires a specific Producer to collect raw data and transmit it to the central data handling system. The Producers communicate with the EUDAQ2 framework through a standardized protocol, enabling compatibility and flexibility when integrating different hardware setups. The system includes the MIMOSA Producer for the beam telescope and the CMS Pixel Producer for the timing reference module.

For the Phase-2 CMS tracker, the Phase-2 Acquisition and Control Framework (Ph2ACF) [81] is a software framework developed for the Phase-2 Tracker. It controls the FC7 board for configuration, operation, and data acquisition. To enable integration with EUDAQ2, a specialized Producer is implemented to ensure the data acquired by the Ph2ACF is converted into a format compatible with the EUDAQ2 framework.

Each Producer gathers data from its respective detector and transmits it via the Transmission Control Protocol (TCP) to the *Data Collector* module in the EUDAQ2 framework. The Data Collector combines these detector data streams event by event, using trigger IDs provided by the TLU to ensure proper synchronization of data from the 2S module, reference detector, and beam telescope. The aggregated data is then stored in files for offline analysis.

To ensure data quality during operations, the *Monitor* component provides real-time feedback by analyzing a fraction of the stored data collected by the *Data Collector*. It decodes the data to extract relevant information and generates visual metrics, such as hit maps and correlation plots among the detectors. These plots enable detailed examination of detector performance and interactions, allowing for the immediate identification of potential issues. Figure 5.16 shows the correlation plot of the x-position of hits from one of the sensors in the 2S module, compared with the beam telescope hits (left) and the reference module hits (right). The dense diagonal accumulation of hits indicates strong synchronization between the detectors. Additionally, the *Log Collector* consolidates logs from all components, centralizing system diagnostics and simplifying troubleshooting.

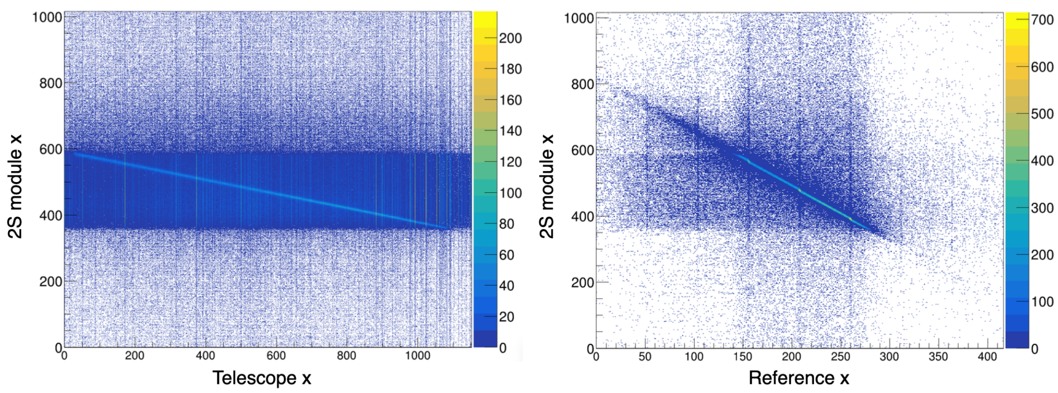

FIGURE 5.16: Online correlation plots of the x-position of the hits from the top sensor in the 2S module relative to the beam telescope (left) and the reference detector (right). The declining trend in the correlation occurs because one of the detectors is flipped, causing its x-axis to be oriented in the opposite direction.

5.4 Offline Event Reconstruction

5.4.1 Corryvreckan Software Framework

The performance study of the 2S module is performed in the Corryvreckan analysis framework [68]. The Corryvreckan framework is a modular and versatile software toolkit designed for reconstructing and analyzing particle tracks and hits during test-beam campaigns. The framework is modular, meaning that each task is implemented as a separate module, allowing users to customize their analysis pipeline based on the specific requirements of their detector setup and experimental goals.

Corryvreckan is compatible with various detectors and data acquisition systems, including the EUDAQ2 framework. Using trigger ID, Corryvreckan reconstructs events from raw data, ensuring that hits recorded across different detectors in a test beam setup correlate accurately. The framework includes independent tools for geometrical alignment among the detector planes, reconstruction of the telescope tracks, track selection, interpolation of the tracks on the device under test, event filtering, and analysis of the selected detectors. The output of the framework is ROOT-compatible, facilitating further analysis using ROOT-based tools.

The workflow that is used in this study is depicted in Figure 5.17, beginning with the input of raw data, formatted using EUDAQ2. Hits are grouped into clusters based on spatial proximity, representing potential particle interactions. Initial alignment is performed using correlation plots to establish spatial relationships between the detectors. Track reconstruction and telescope alignment are then carried out, ensuring precise spatial synchronization across all planes. Clusters from the device under test are associated with selected reconstructed tracks, enabling the alignment of the DUT relative to the telescope. Tracks with hits in the reference plane are subsequently selected to ensure accurate track association. The workflow concludes with event selection and performance analysis to evaluate the detector's efficiency, resolution, and overall behavior. This section provides a detailed overview of the modules and methods employed in the study, highlighting the specific adjustments and contributions made to optimize the framework for 2S module analysis.

5.4.2 Event building and Hit Clustering

The first step in the analysis workflow is event building. This is achieved using the EventLoaderEUDAQ2 module, which reads raw data stored in EUDAQ2 binary files and translates it into a format compatible with the Corryvreckan framework. The module decodes the data and organizes it into discrete events, with each event containing data from all detectors and being identified by a shared trigger number. The Corryvreckan framework retains these events for use throughout the analysis process.

The raw hit data, represented as the pixel (or strip) number that registered a hit, is converted into a physical position within the detector's local coordinate system, with the center of the detector defined as the origin (0,0). This conversion accounts for the geometry of the detector, including the pixel pitch and the total number of pixels. The process allows the hit positions to be further transformed into a global coordinate system shared among all detector planes, enabling proper alignment and track reconstruction.

Since the transformation of the hit position depends on pixel size, sensors with inconsistent pixel sizes must be handled with different conversions. Figure 5.18 shows the hit map of the timing reference module in pixel coordinates. Columns and rows with higher hit entries correspond to enlarged pixels located at the periphery of the readout chips. These enlarged pixels are intentionally designed to eliminate gaps between the readout chips, and are double the standard length in one direction, while corner pixels have quadruple the area of a standard pixel. The coordinate transformation accounts for these large pixels by treating them as two standard pixels along one direction, as illustrated in Figure 5.19. For the hit position at pixel column 6 in the CMS Pixel Module plane, it is first transformed to column 8.5, and then further calculated to correspond to a local position 100 µm. The source code implementing this coordinate transformation is provided in Appendix A.2.

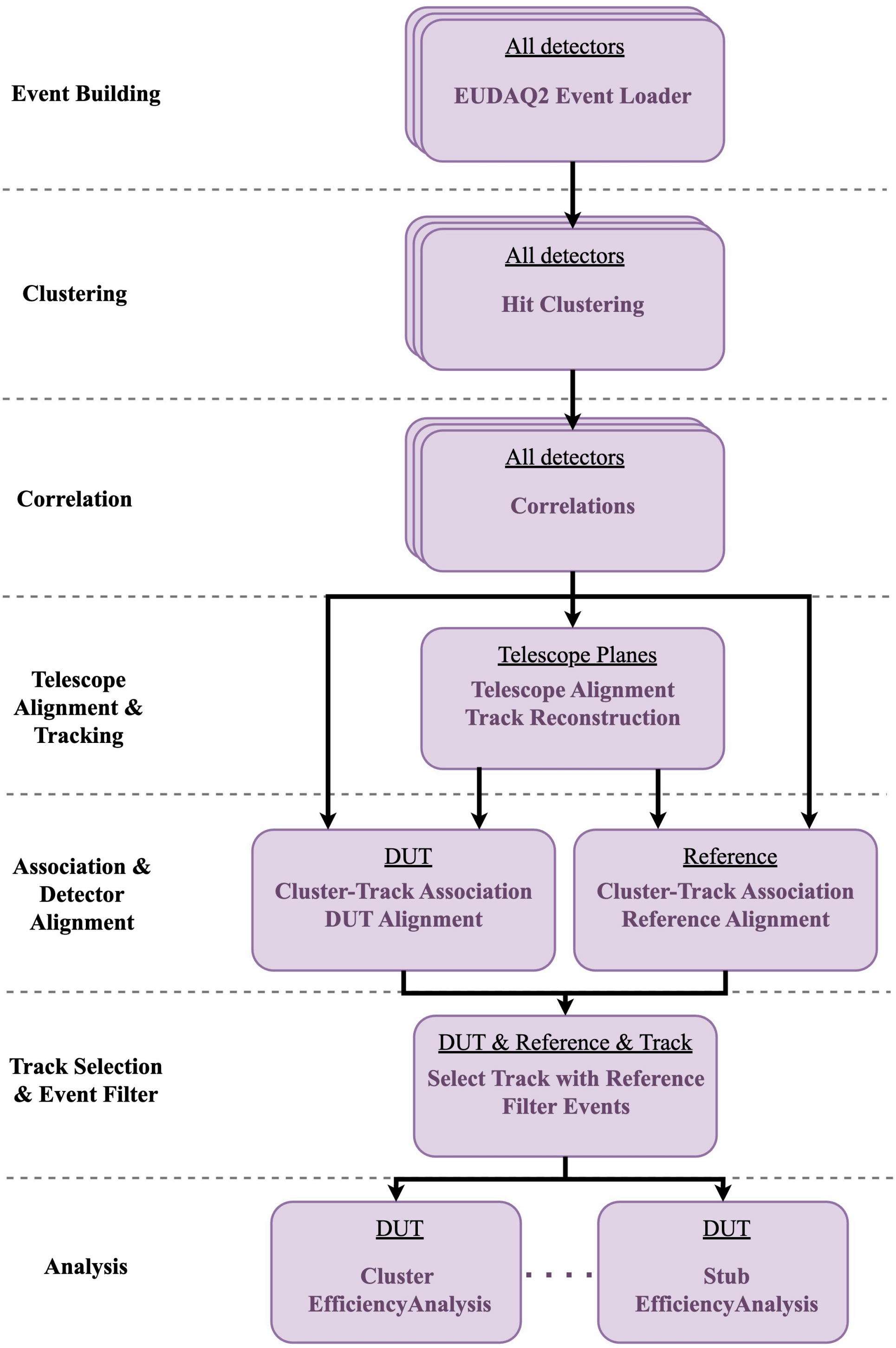

FIGURE 5.17: Flow chart of Corryvreckan used in this testbeam studies.

The hit clustering stage groups individual detector hits into clusters based on their spatial proximity. A cluster is a collection of multiple strips or pixels that are likely generated by the same particle interaction. Before clustering, noisy strips (pixels) are identified and masked to reduce the impact of spurious signals on the analysis. A strip (pixel) is classified as noisy if its hit rate exceeds 50 times the average hit rate of strips (pixels) on the sensor. Typically, the hits within a cluster are neighbors in space. Split clusters are allowed, meaning that hits occurring in consecutive strips are

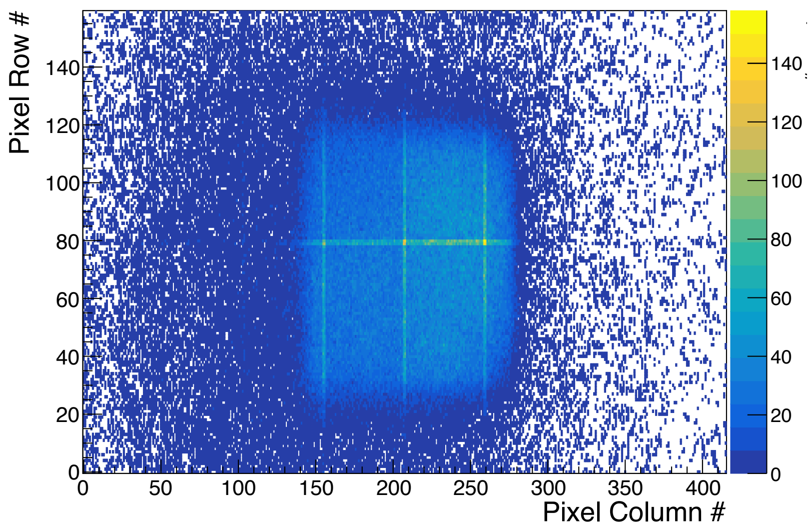

FIGURE 5.18: Hit map of the timing reference (CMS Pixel) module. Pixels at the edges of the readout chips exhibit higher hit entries due to their larger size.

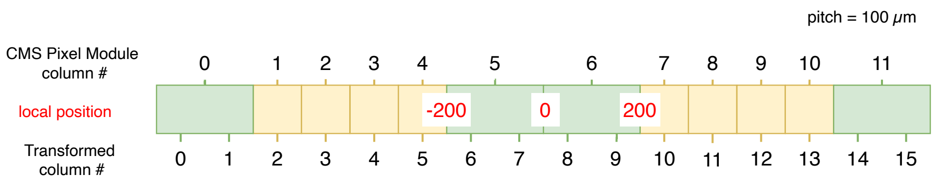

FIGURE 5.19: A simplified sketch of a sensor with enlarged pixels at the periphery of the readout chips. Green blocks represent pixels with double the standard size, while yellow blocks indicate standard-sized pixels.

recognized as part of the same cluster. Each cluster is assigned a center, representing its geometric average position, which is later used for track reconstruction. Since the detectors used in this work have a binary readout system, the *arithmetic mean* of the positions of the hit strips (or pixels) within a cluster is used to calculate the cluster center. The arithmetic mean determines the center of a cluster by averaging the positions of all hits within it and is given by:

$$x_{\text{cluster}} = \frac{\sum_i x_i}{N}, \tag{5.1}$$

where x_i is the position of the i-th strip in the cluster, and N is the total number of strips in the cluster.

5.4.3 Alignment and Tracking

The position of each cluster is initially determined in the local coordinate system of its respective detector plane. To accurately reconstruct particle trajectories across the entire setup, these local positions must be transformed into a common global coordinate system. This transformation accounts for the relative positioning and orientation of each detector within the test beam setup. The physical setup and alignment of the detectors were performed manually by eye, slight offsets from the ideal geometry later used in track reconstruction are inevitable. The offset, such as shifts, rotations, or tilts, can introduce systematic errors and lead to inaccurate track reconstruction. To account for this physical offset, an alignment procedure for the detector planes is required.

The alignment procedure begins with a coarse adjustment using correlation plots between the detector planes. Correlation plots of the global x- and y-positions of hits reveal the relative offsets between detectors, enabling their approximate alignment. For pixel detectors, both x- and y-positions are used, while for strip detectors, only the x-position is considered. By shifting the planes in the reconstruction geometry based on these correlations, a rough alignment is achieved, setting the stage for more precise iterative adjustments.

Following the coarse adjustment, tracks reconstructed from clusters in the beam telescope are used to iteratively refine the alignment parameters. The alignment is achieved by adjusting the position (x, y) and orientation (x-, y- and z-rotation) of the telescope planes with respect to two fixed telescope planes. The two planes are fixed to constrain the degrees of freedom in the alignment process and to avoid systematic misalignments, known as *weak modes* [82]. After each adjustment, the tracks are refitted, and the alignment is optimized by minimizing the overall χ^2 value of the refitted tracks.

Track reconstruction is performed using the Tracking4D module in Corryvreckan, which connects clusters from the first and last detector planes to form initial track candidates. Clusters in intermediate planes are added iteratively if they satisfy spatial cuts. This spatial cut requires clusters to lie within a specified displacement from the track's projected position on the plane. The General Broken Lines (GBL) [83] method is employed during track fitting to account for multiple scattering effects, representing the trajectory as a series of connected straight segments.

These tracks serve as a reference to align the DUT and timing reference module. The alignment process involves iteratively adjusting the translational and rotational corrections of the DUT and the timing reference plane, such that the residuals, defined as the difference between the measured cluster positions on the device and the interpolated positions from the reconstructed tracks, are minimized and centered at zero. The alignment is validated using the plots shown in Figure 5.20(a), where the residual distribution of the clusters is centered at 0.24 µm, indicating good translation alignment of the device. The additional peak in the center arises from 2-cluster events, as such events provide a more precise position located at the midpoint between the two strips. Figure 5.20(b) and 5.20(c) depict the x-residuals plotted as functions of the x- and y-positions of tracks interpolated onto the DUT. These plots demonstrate the rotational alignment quality, with a slope close to zero indicating proper alignment about the y- and z-axes.

By minimizing these residuals and ensuring the fitting slope equal to zero, the clusters on the DUT and timing reference plane can be accurately associated with the correct tracks.

5.4.4 Track Selection

A valid track must have hits on all six telescope planes, ensuring complete trajectory information across the beam telescope. Among all the reconstructed tracks, additional criteria are applied to select the tracks that are used in the analysis.

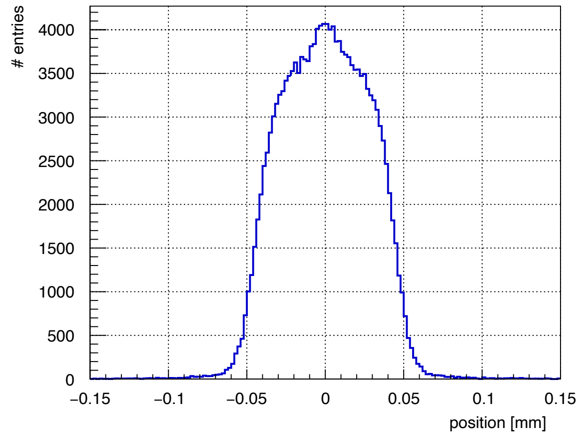

(a) The x-residual distribution of the clusters on the DUT for the testbeam run with zero rotation angle. The x-residual shown here is the difference between the cluster x-position and the selected track interpolated onto the DUT plane. The distribution is centered at zero when good translational alignment is achieved.

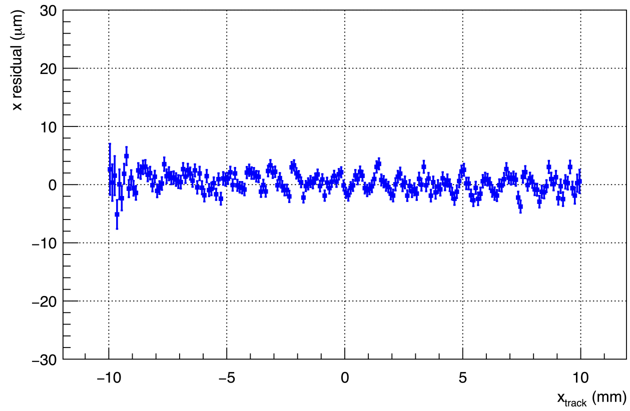

(b) The x-residual as a function of the x-position of tracks interpolated onto the DUT. A slope of approximately zero indicates good rotational alignment around the y-axis.

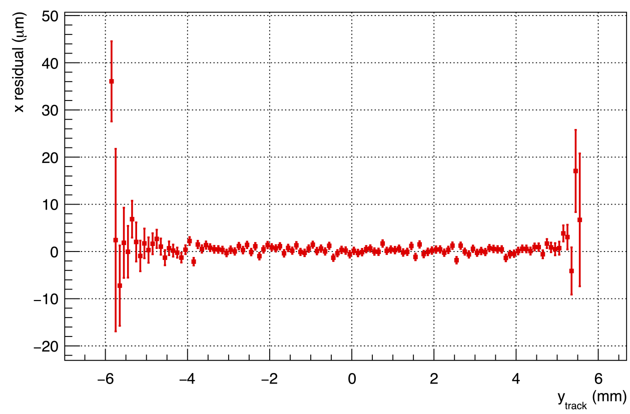

(c) The x-residual plotted against the y-position of tracks interpolated onto the DUT. A slope close to zero signifies proper rotational alignment around the z-axis.

FIGURE 5.20: Validation plots used for the DUT translational and rotational alignment.

The tracks must satisfy the condition $\chi^2/\mathrm{ndof} \leq 3$, where χ^2/ndof quantifies how well the track fits the measured hits. This ensures that the selected tracks align closely with the measured hit positions and are not dominated by deviations. Tracks passing through pixels neighboring a masked pixel are excluded to avoid contamination from noisy or inactive regions of the detector.

Furthermore, tracks are selected based on their association with a cluster on the timing reference plane, which is necessary due to the track multiplicity of the beam telescope, as shown in Figure 5.13. This multiplicity arises from the integrated readout time of 230.4 µs for the beam telescope.

A timing reference with the same integration time is used to identify tracks corresponding to the 2S module's 25 ns readout time frame. Thus, track selection requires an associated cluster on the timing reference plane.

In this testbeam study, the fiducial window that defines the association of clusters on the timing reference plane with interpolated track position is defined using the following spatial cuts:

$$|x^{\mathrm{ref}}_{\mathrm{residual}}| \leq 215\ \mu\mathrm{m} \quad \text{and} \quad |y^{\mathrm{ref}}_{\mathrm{residual}}| \leq 145\ \mu\mathrm{m}\,.$$

The window is selected to be approximately 1.5 times the pixel pitch to account for slight misalignments, residual offsets, and uncertainties in the track interpolation. The residuals are calculated as:

$$x, y\ {}^{\mathrm{ref}}_{\mathrm{residual}} = x, y\ _{\text{cluster in reference plane}} - x, y\ _{\text{interpolated track on reference plane}}\,. \tag{5.2}$$

5.4.5 Tracks on the Strip-Strip Module

The selected tracks, associated with a cluster on the timing reference plane, are further interpolated onto the two sensor planes of the 2S module for efficiency studies. Similar to the spatial cut criteria applied to the hits in the reference plane, clusters on the 2S sensors with an x-residual within a predefined fiducial window are classified as *cluster associated to a track*. The size of the fiducial window is defined as:

$$|x^{\mathrm{2S}}_{\mathrm{residual}}| \leq 150\ \mu\mathrm{m}$$

for both top and bottom sensors. The size of the fiducial window is selected to be approximately 1.6 times the strip pitch. No cut is applied in y-position due to the strip geometry, where the length is 5 cm.

In this testbeam configuration, the bottom sensor serves as the seed layer as it encounters the beam incident prior to the top sensor, which is referred to as the correlation layer for stub formation. Similar to the efficient clusters, the *efficient stubs* are defined as those with stub residuals on the seed layer that satisfy the spatial cut:

$$|x^{\mathrm{stub}}_{\mathrm{residual}}| \leq 150\ \mu\mathrm{m}\,.$$

The efficiency of a cluster or stub is determined by the ratio of the number of clusters or stubs associated with a track on the 2S sensors to the number of selected tracks with associated clusters on the timing reference plane. The efficiency can be expressed as:

$$\epsilon_{\text{cluster/stub}} = \frac{n_{\text{efficient cluster/stub}}}{n_{\text{selected track}}}, \tag{5.3}$$

where $n_{\text{efficient cluster/stub}}$ is the number of clusters or stubs associated with a track, and $n_{\text{selected track}}$ is the total number of selected tracks with associated clusters on the reference plane.

The statistical uncertainty in the cluster and stub efficiency is derived from the standard deviation of the mean of a binomial distribution. For a binomial distribution, where the number of trials is $n_{\text{selected track}}$ and the probability of success is the efficiency ($\epsilon_{\text{cluster/stub}}$), the standard deviation of the mean is expressed as:

$$\sigma_{\epsilon_{\text{cluster/stub}}} = \sqrt{\frac{\epsilon_{\text{cluster/stub}} \cdot (1 - \epsilon_{\text{cluster/stub}})}{n_{\text{selected track}}}}. \tag{5.4}$$

In the Corryvreckan framework, the analysis of cluster efficiency is performed using the *DUTAssociation* module, where spatial cuts are applied, and the *AnalysisEfficiency* module, where efficiency is defined as shown in Equation 5.3. Additionally, the extraction of stub information and the stub efficiency calculation is implemented through a framework module that I contributed to Corryvreckan software. Using these software modules, the resulting efficiency values, along with their statistical uncertainties, are calculated and stored for further analysis.

5.4.6 Event Filtering

At the LHC, a synchronized clock is shared among all detectors, ensuring a fixed phase relationship between the accelerator clock and the data acquisition clock of the 2S module. This synchronization allows the signal pulse to be consistently sampled at its maximum amplitude thereby optimizing detection efficiency. In contrast, during the beam tests operation at DESY II, particle triggers are generated at random times, while the readout system of the 2S module samples incoming signals based on its internal 40 MHz clock cycle. The lack of synchronization means that particle triggers can arrive at any point within the 25 ns clock period of the 2S module, leading to an arbitrary phase difference between the particle trigger and the signal sampling in the CBCs. Consequently, the sampling moment may occur at the lower amplitude of the signal pulse, resulting in signal loss and reduced detection efficiency.

To address the effect of this phase difference, the readout firmware of the 2S module measures the arrival time of each trigger signal relative to the 40 MHz clock using a 320 MHz clock. This provides a time resolution of 3.125 ns and divides the 25 ns clock period into 8 subdivisions. The time difference is encoded by the time-to-digital converter (TDC), and is called the TDC phases. Only certain TDC phases align the sampling moment near the peak of the signal pulse, yielding high detection efficiency. By identifying and analyzing events corresponding to these optimal TDC phases, the analysis compensates for the asynchrony in the testbeam setup.

The TDC phase dependency of the cluster and stub efficiency is illustrated in Figure 5.21. To ensure meaningful studies of the 2S module under LHC operation, only events with TDC phases exhibiting cluster efficiency above 99.9 % on both sensors are selected for further analysis. The selection of TDC phases is performed after the alignment of the detectors to ensure sufficient statistics are available for the alignment process.

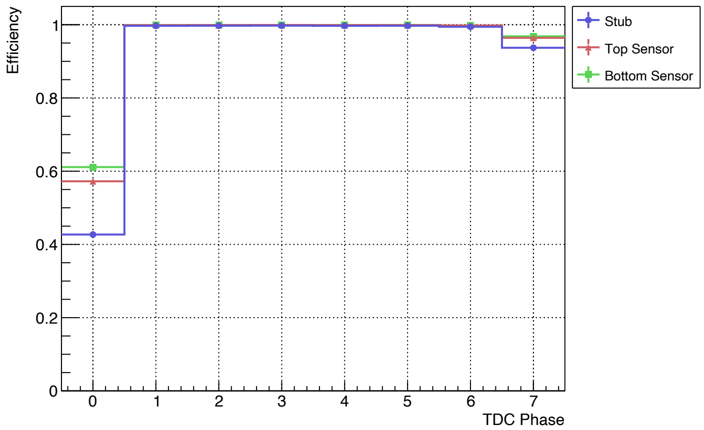

(a)

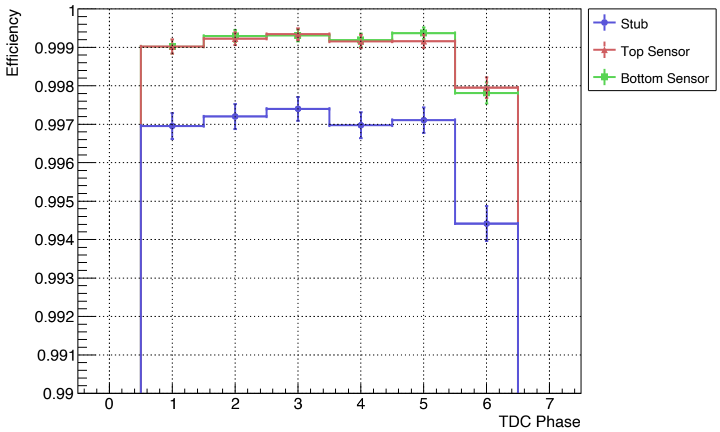

(b)

FIGURE 5.21: Dependency of 2S module hit and stub efficiency on the TDC phase. (a) The asynchronous nature of the accelerator clock and the 2S module data acquisition framework clock during the test beam operation resulted in a dependency of the efficiency on the TDC phase. (b) Zooming into the region where the efficiency exceeds 99 % reveals the statistical uncertainties.

The cluster efficiency is influenced by the operational settings of the 2S module, such as the signal threshold and the bias voltage. The signal threshold defines the minimum charge collected that is required to register a hit, while the bias voltage determines the strength of the electric field within the silicon sensor. If the signal threshold is set too high, small signals from particle interactions may fail to register as hits, leading to a reduction in efficiency. Similarly, if the bias voltage is too low, the electric field may be insufficient to effectively collect charge carriers, resulting in low efficiency across all TDC phases. In situations where the cluster efficiency is below 99.9 % for all TDC phases, it typically indicates non-optimal operational conditions. These conditions may occur during signal threshold or bias voltage dependency studies, particularly when the signal threshold is set too high or the bias voltage is too low.

5.5 Testbeam Performance Studies

This section presents the performance studies of a 2S module built at DESY and tested at the DESY II test beam facility. The module features two 240 µm-thick strip sensors and a module spacing of 1.8 mm. Details of the module components and data readout system can be found in Section 5.2.1. A photo of the DESY 2S module is shown in Figure 5.7.

The performance evaluation of the module was conducted using a 5.2 GeV electron beam at DESY II. The studies included investigations into cluster and stub detection as a function of applied bias voltage, signal thresholds, and performance characterization under varying incident particle angles. Additionally, an angular scan was performed with a module referred to as the 4 mm module, in which the two strip sensors are placed at 4 mm distance. This module is equipped with CIC2, CBC3.1, and lpGBTv0 to verify stub detection capabilities. These comprehensive tests provide insights into the module's performance under particle beam conditions and validate the p_{T} discrimination logic for its application in the CMS Outer Tracker Phase-2 upgrade.

5.5.1 Bias Voltage Dependency

The operational characteristics of the 2S module were investigated under a range of applied bias voltages extending from 25 V to 200 V, in increments of 25 V. These conditions were selected to encompass both the partially depleted and the fully depleted regimes of the sensors, and to determine an optimal operating sensor bias voltage. The scans were performed with the module positioned perpendicular to the electron beam direction, and the stub window configured to be ±4.5 strips with no offset.

The noise distributions of the readout channels, as presented in Section 5.2.3, were used to establish a reliable threshold for the bias voltage dependency study. A common threshold of 5000 e^-, equivalent to five times the average channel noise, was chosen for all the CBCs.

Figure 5.22 illustrates the cluster efficiency curves for the top and bottom sensors, along with the stub efficiency, under varying bias voltages. Both the top and bottom sensors exhibit similar cluster efficiency results, as expected, since the two sensors share the same layout. With an increasing bias voltage, the cluster efficiency rises as the depletion zone in the silicon sensors grows, and the detected charge signal increases.

Starting at 125 V, the cluster efficiency plateaus at 99.7%, which is significantly lower than the depletion voltages determined by the C-V measurements performed during the pre-assembly tests. The depletion voltage was found to be approximately 197 V for top sensor and 209 V for bottom sensor. This transition into the plateau does not indicate a full depletion of the sensors. Rather, it signifies that the electric field in the sensor bulk is sufficiently strong to produce a signal pulse that exceeds the threshold of 5000 e^-, taking Landau fluctuations introduced in Section 3.1.3 and charge sharing into account.

At 200 V, the cluster efficiency improves slightly to 99.9% for both sensors, while the stub efficiency reaches 99.7%, confirming the excellent performance of the 2S module near the depletion voltage. These results highlight the optimal operating conditions for the 2S module.

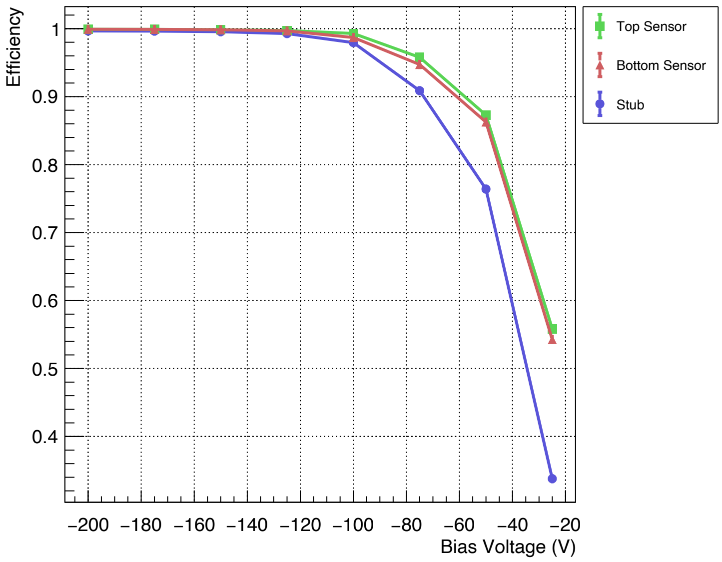

FIGURE 5.22: Efficiency of cluster and stub detection as a function of the bias voltage.

The stub efficiency is inherently coupled to the cluster efficiencies of both sensors, as forming a valid stub requires simultaneous detection of clusters on both the top and bottom sensors. At lower bias voltages, when the cluster efficiency of one or both sensors decreases due to incomplete depletion or suboptimal charge collection, the probability of successfully forming a stub diminishes. This coupled dependency results in the stub efficiency being significantly lower at reduced bias voltages.

5.5.2 Signal Threshold Dependency

A threshold scan was conducted to systematically evaluate the influence of varying signal discrimination thresholds on the efficiency of the 2S module. This study identifies the optimal operational threshold for the 2S module during performance evaluations by focusing on signal efficiency across the range of thresholds and confirming that noise levels remained acceptable throughout the scan.

The bias voltage was fixed at 200 V, a value chosen based on the results from the *C*-*V* measurements and bias voltage dependency study, which indicated this setting as optimal for achieving maximal cluster efficiency.

During the threshold scan, the signal threshold was varied from $27\,\mathrm{V_{cth}}$ relative to the pedestal (corresponds to $4200\,\mathrm{e^-}$) to $177\,\mathrm{V_{cth}}$ (corresponds to $27600\,\mathrm{e^-}$). The results are presented in Figure 5.23(a), showing the efficiency curves for the top and bottom sensors, as well as the stub efficiency. The data highlights a clear dependency of efficiency on the threshold setting, with a sharp decline in efficiency observed at higher threshold values due to the rejection of signals.

Figure 5.23(b) provides a zoomed-in view of the region where efficiency exceeds 94%, illustrating the fine-scale behavior of the sensors and stub efficiency. Within this range, the cluster efficiency for both the top and bottom sensors remains above 99.9% up to a threshold of approximately $5800\,e^-$. Beyond this point, the efficiency gradually decreases, dropping below 99% at around $8000\,e^-$. Notably, at about 5σ ($\sim 4900\,e^-$)

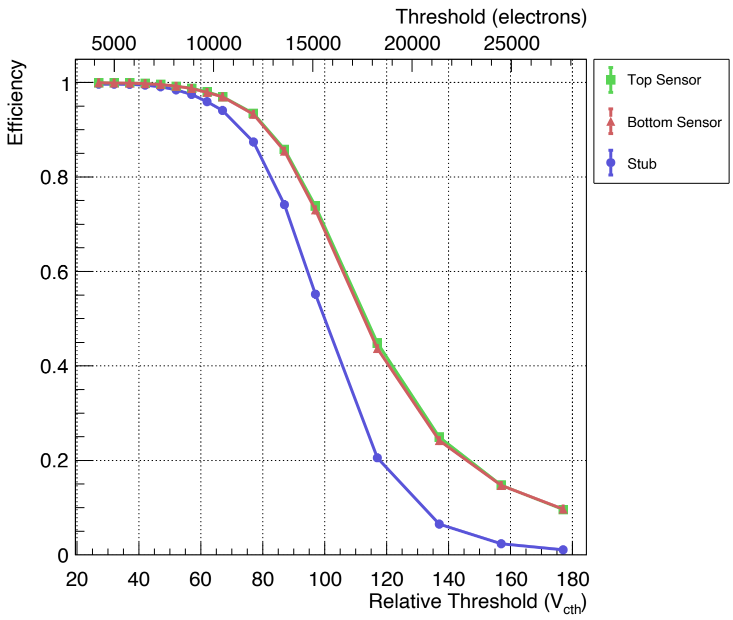

(a)

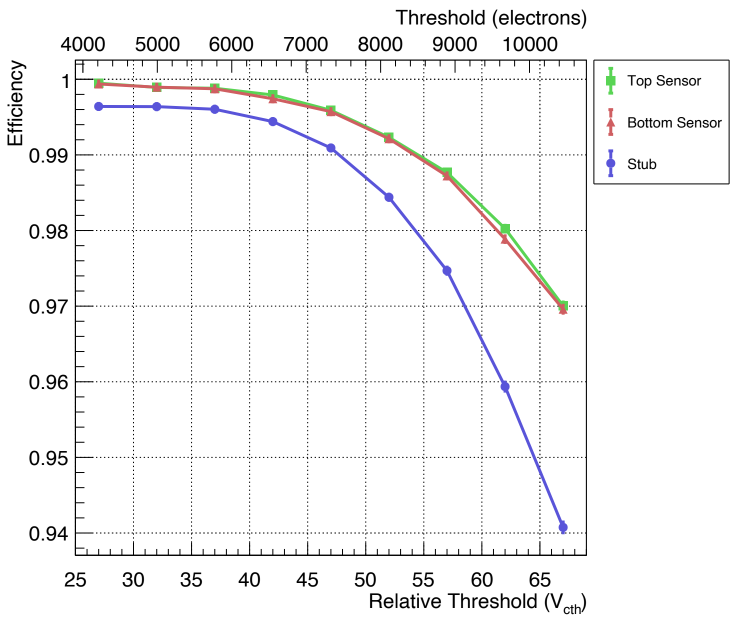

(b)

FIGURE 5.23: Efficiency of cluster and stub detection as a function of the signal threshold. (a) Full range of relative thresholds. (b) Zoomed view for efficiencies above 94%.

above the pedestal, the efficiency still remains high, indicating that this threshold is optimal for module performance studies.

5.5.3 Impact of Angle on Cluster

The following studies were conducted using a test beam configuration in which the DUT was rotated about its y-axis. With the optimal bias voltage set to 200 V and a relative threshold of 32 V_{cth} (approximately 5000 e^-) determined from previous measurements, a scan was performed over a range of rotation angles from $-30°$ to $+30°$.

This study examines how geometric effects influence the size of the detected charge cluster, which increases with the angle of incidence as particle tracks intersect more strips at larger angles. A mathematical model describing the cluster size as a function of the angle of incidence incorporates key parameters like the thickness of the sensor and the strip pitch. The geometric relation is expressed as:

$$s(\theta) = s_0 + \frac{d}{p} \cdot |\tan(\theta - \theta_0)|\,, \tag{5.5}$$

where s is the cluster size, s_0 is the cluster size at zero incidence angle, d is the active thickness of the sensor, p is the pitch of the strips, θ is the incidence angle, and θ_0 is the offset between the rotation stage setting and the actual angle of the module.

However, this simple geometric model does not fully capture the observed behavior, as the cluster size also depends on other factors, such as the threshold setting and the inhomogeneity of the electric field inside the sensor. To account for these additional effects, the parameter d/p is replaced by a scaling factor κ. To further refine the model and account for the smearing introduced by diffusion and angular uncertainties, the functional form is convolved with a Gaussian distribution [81]. This convolution adds an additional parameter, σ_u, representing the angular resolution. The final model is given by:

$$s(\theta) = \frac{1}{\sqrt{2\pi}\sigma_u} \int_{-\infty}^{\infty} [s_0 + \kappa|\tan(\theta' - \theta_0)|] \exp\left(-\frac{(\theta' - \theta)^2}{2\sigma_u^2}\right) d\theta'\,. \tag{5.6}$$

Figure 5.24 illustrates how the mean cluster size varies with the module's rotation angle (track incidence angle) for both top and bottom sensors, including the model fit described above. The parameter s_0, representing the baseline cluster size at zero incidence angle ($\theta = 0°$), was obtained from the fit. The cluster size for the top sensor $s_0 = 0.949 \pm 0.001$ strips, while for the bottom sensor, $s_0 = 0.959 \pm 0.001$ strips.

At perpendicular incidence ($\theta = 0°$), both sensors record a minimum cluster size of 1.08 strips, which is higher than the fitted values of s_0. This difference arises because the fitted s_0 reflects the idealized cluster size in the absence of additional effects, while the observed minimum includes contributions from charge diffusion, threshold settings, and angular smearing. These effects broaden the cluster size distribution, effectively raising the observed minimum beyond the baseline value s_0.

As the angle of incidence increases, the cluster size rises due to charge sharing between adjacent strips, which is governed by the effective path length of the particle track within the sensor. The results align well with the theoretical model, which accurately captures the observed dependence of cluster size on the rotation angle. The distribution offers insight into the rotational misalignment of the module on the rotation stage in the test beam setup. By fitting the cluster size distribution, the rotation angle θ_0 of the module can be extracted, which quantifies the misalignment. For the bottom sensor, the fitted parameter θ_0 is $-0.56° \pm 0.02°$, while for the top sensor, θ_0 is $-0.69° \pm 0.02°$. These values indicate slight rotational deviations of the sensors from their intended alignment, and the uncertainties reflect the precision of the fitting process.

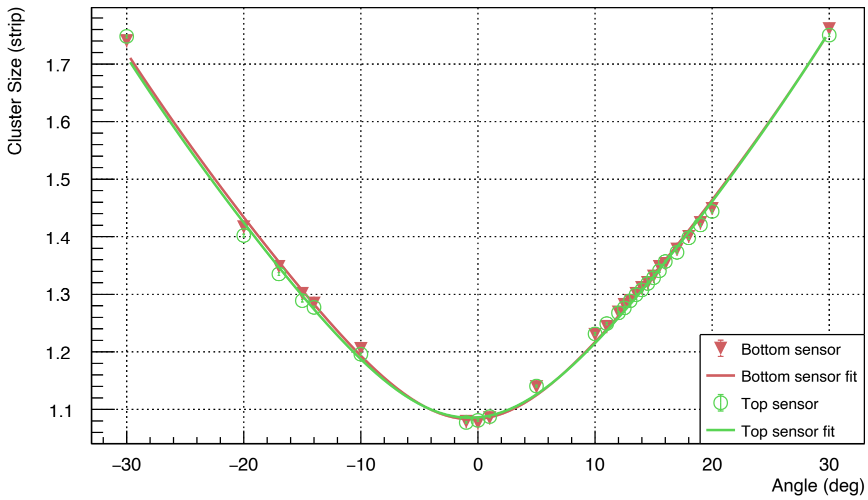

FIGURE 5.24: The cluster size as a function of the rotation angle, along with the corresponding fitting curve.

5.5.4 Resolution

Investigating the position resolution of the sensor is essential for accurate tracking. This resolution quantifies the sensor's ability to determine the particle hit position precisely. It depends on several factors, including the sensor geometry, operational parameters, and intrinsic readout characteristics.

The expected resolution for a strip sensor with a binary readout is determined by its geometry. For perpendicular particle incidence and a single-hit response, the variance from the true entrance point is given by:

$$\sigma_x = \frac{p}{\sqrt{12}}, \tag{5.7}$$

where p is the pitch of the sensor [24]. For the 2S module, which has a sensor pitch of 90 µm, the expected resolution is 25.98 µm.

For the experimental measurement, the resolution is extracted from the distribution of cluster-track residuals. However, this measured resolution is a convolution of the intrinsic resolution of the sensor and the telescope pointing resolution at the DUT. The intrinsic resolution can be calculated as:

$$\sigma_{\text{int}} = \sqrt{\sigma^2_{\text{measured}} - \sigma^2_{\text{telescope}}}. \tag{5.8}$$

The measured resolution is extracted by fitting a generalized error function to the residual distribution. This function arises from the convolution of a box distribution, due to the uniform assignment of hit positions within the strip width, with a Gaussian distribution that accounts for the telescope pointing resolution and other systematic effects. The generalized error function is written as:

$$f(x,\mu,\sigma,\beta,A,C) = A \cdot \frac{\beta}{\sqrt{8}\cdot\sigma\cdot\Gamma\left(\frac{1}{\beta}\right)} \cdot \exp\left(-\left|\frac{x-\mu}{\sqrt{2}\cdot\sigma}\right|^{\beta}\right) + C, \tag{5.9}$$

In this equation, μ corresponds to the central position of the distribution, typically the mean residual. The parameter σ characterizes the width of the distribution and can be interpreted as the resolution of the detector. The parameter β determines the shape of the distribution. For $\beta = 2$, the function reduces to a Gaussian distribution with a smooth, rounded peak and exponentially decaying tails. As β increases beyond 2, the peak becomes flatter near the center, resembling a plateau, while the transition to the tails becomes steeper, leading to faster decay. Conversely, for $\beta < 2$, the peak broadens and the tails become heavier, reflecting increased contributions from larger residuals. The amplitude A scales the overall area under the curve, and C represents a constant background offset.

Figure 5.25 illustrates the effect of the rotation angle on the residual distributions. At 0°, the residual distribution reflects the discrete nature of the binary readout, with broader tails arising from the flat component of the convolution. The generalized error function models this behavior except for the subtle peak in the central region that arises from 2-strip clusters that are generated by charge sharing. These clusters occur when a particle intersects the sensor near the boundary between two strips, leading both strips to register a hit. This results in a precise position assigned to the cluster center, leading to smaller residuals compared to cases where the particle intersects only one strip. Nevertheless, by fitting the data with a generalized error function, a relatively large β of 4.388 ± 0.085 indicates a stronger box-like contribution. In contrast, at 20°, multiple strips record each particle's signal, and the reconstructed cluster position derived from the averaged hits smooths out the discrete binary-readout effects, resulting in a more Gaussian-like distribution. Here, $\beta = 2.175 \pm 0.029$ confirms the closer resemblance to a Gaussian, as the influence of the flat component diminishes.

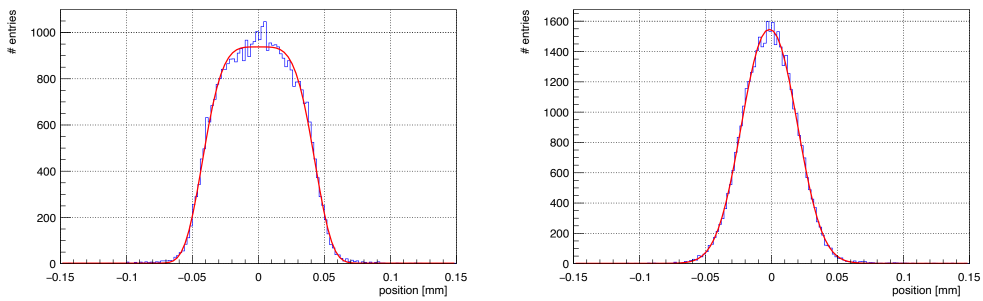

(a) (b)

FIGURE 5.25: Residual distributions at (a) 0° and (b) 20° particle incident. At 0°, the residual distribution is described by a generalized error function. At 20°, the residual distribution exhibits a Gaussian-like shape.

By extracting the resolution for all measurement points, the angular dependency of the resolution can be visualized. The width parameter σ, extracted from the generalized error function fit, provides an interpretation of the resolution, representing the spread of the residual distribution and quantifying the uncertainty in the reconstructed hit position. Figure 5.26 shows the resolution as a function of the rotation angle. The resolution at 0° is relatively poor, measured to be 32.1 µm, due to the binary readout assigning hits to discrete strip positions. As the rotation angle increases, the resolution improves significantly, reaching a minimum value of 20.3 µm at 20°. This improvement is attributed to the larger cluster size at intermediate angles, which allows for the averaging of hit positions across multiple strips, mitigating the effects of the binary readout.

At even larger angles, the resolution starts to degrade as the cluster size approaches two strips. This behavior arises because, at higher angles, the particle trajectory intersects two adjacent strips. While the binary readout assigns positions based on the center of the strips that detect a hit, the ability to further improve resolution is fundamentally limited because the system only knows which strips were hit, not the finer details of the charge distribution. As a result, the resolution of two-strip clusters converges to the intrinsic limitations of single-strip clusters, diminishing the gains previously achieved through position averaging.

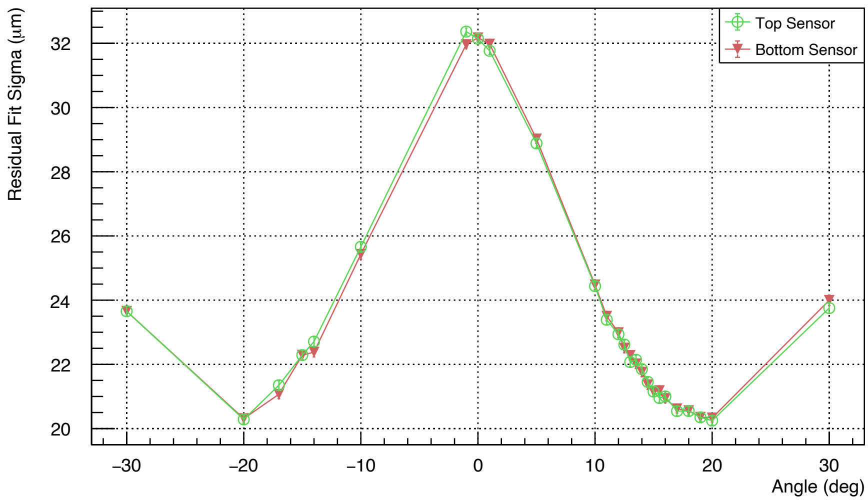

FIGURE 5.26: Spatial resolution extracted from fitting a generalized error function to the residual plot.

By taking the telescope pointing resolution into account, the intrinsic resolution of the detector can be calculated. The telescope pointing resolution, $\sigma_{\mathrm{telescope}}$, is determined using the GBL Track Resolution Calculator [84] and is found to be 6.94 µm. This relatively large telescope pointing resolution arises from widely separated positions of the detectors, which are designed to accommodate the rotation of the DUT, as described in Appendix A.1. As shown in Equation 5.8, the intrinsic resolution is calculated by subtracting the telescope pointing resolution. By taking the telescope pointing resolution into account, the intrinsic resolution at 0° is 31.3 µm.

This intrinsic resolution is larger than the expected resolution of 26.0 µm. The difference between the intrinsic resolution and the expected resolution is not due to the binary readout itself, as the binary readout is already accounted for in the expected resolution calculation. Instead, several other factors contribute to this discrepancy.

First, the generalized error function used for fitting may not fully capture the shape of the residual distribution, particularly in the presence of the 2-strip clusters, systematic effects, or tails. This can lead to an overestimation of the resolution, as the function may inadequately model deviations caused by binary readout effects or noise. Second, delta electrons generated by the ionization of silicon within the sensor can contribute to the resolution degradation. These secondary electrons, while relatively infrequent, can scatter and create additional hits in neighboring strips, broadening the residual distribution and impacting the cluster formation.

The primary contributor to the measured resolution, however, is the generalized error function fit. The fitting procedure, while effective for capturing the general trend of the residuals, does not adequately describe events where clusters are located at the midpoint of two strips. Thus, the extracted resolution may be overestimated. For the 0° run, the RMS value derived from the residual distribution yields an intrinsic resolution of 26.42 µm, which aligns well with expectations for binary readout systems. Several resolution extraction methods are available, and a comparison of the methods can be found in Appendix A.3.

5.5.5 p_{T} Discrimination Performance

The p_{T} discrimination performance of the 2S module was evaluated using a rotation stage to simulate particle incidence at various angles, corresponding to different transverse momenta of particles. This study is crucial for assessing the performance of the 2S module within the CMS Outer Tracker, as the stub detection efficiency directly impacts the Level-1 trigger's ability to discriminate high-p_{T} tracks from low-p_{T} backgrounds.

The stub efficiency, defined by Equation 5.3, was measured across a range of rotation angles. For all measurements, the stub correlation window offsets were programmed to be zero, and the correlation window size was fixed at ±4.5 strips.

Figure 5.27 illustrates the measured stub efficiency as a function of rotation angle. The results indicate that the stub efficiency remains high (99.7%) at smaller angles but drops sharply beyond 12°, eventually reaching zero efficiencies over a narrow transition range. This behavior is attributed to the stub formation logic, which requires the cluster positions in the top and bottom sensors to align within the spatial displacement defined by the correlation window. As the rotation angle increases, the displacement may exceed the defined window, preventing stub formation and resulting in the observed drop in efficiency.

The observed angular dependency of the stub efficiency is described by an error function:

$$f(\theta, p_0, p_1, p_2, p_3) = 1 - \frac{1}{2}\left(p_0 + p_1 \cdot \mathrm{erf}\left(\frac{\theta - p_2}{p_3}\right)\right), \tag{5.10}$$

for $\theta \geq 0°$. In this expression, p_0 represents the baseline efficiency, p_1 denotes the amplitude of the efficiency drop, p_2 is the turn-on threshold angle that corresponds to the angle at which the stub efficiency reaches its half maximum amplitude, and p_3 characterizes the width of the transition region, reflecting the steepness of the efficiency drop.

This error function was fitted separately for angles $\theta \geq 0°$ and $\theta \leq 0°$. The results yielded $p_2^{\geq 0} = 13.89°$ and $p_2^{\leq 0} = -16.02°$. Ideally, the efficiency curves should exhibit symmetry at $\theta = 0°$, since the stub correlation window offset was set to zero and the particle incidence perpendicular to the module plane should correspond to the same efficiency behavior in both angular directions.

The observed asymmetry arises from a misalignment of the DUT on the rotation stage during data collection. The rotation angle 0° was determined visually, introducing a slight rotation around the y-axis. To correct for this misalignment, an offset angle θ_{offset} was calculated as:

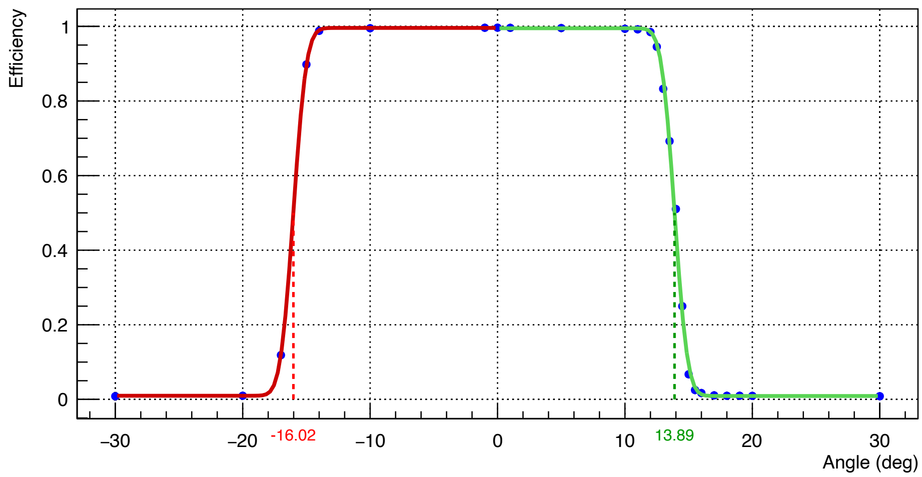

FIGURE 5.27: Stub efficiency as a function of the rotation angle. The efficiency remains high at small angles and drops rapidly beyond 12°. The observed behavior is fitted with an error function, where the red line represents the fit for $\theta \leq 0°$ and the green line corresponds to the fit for $\theta \geq 0°$. The asymmetry between the two fits arises from a slight misalignment of the device under test (DUT) on the rotation stage.

$$\theta_{\text{offset}} = \frac{1}{2}\left(p_2^{\geq 0} + p_2^{\leq 0}\right) = -1.065°\,. \tag{5.11}$$

With this correction applied, the turn-on threshold angle for stub formation is adjusted to 14.96°, providing a more accurate representation of the module's performance.

The rotation angle can be translated into an equivalent transverse momentum (p_T) for different 2S module positions in the CMS detector. Considering the CMS magnetic field strength of $B = 3.8\,\mathrm{T}$, the transverse momentum in GeV is approximated as:

$$p_T \approx \frac{0.57 \cdot R}{\sin(\theta)}\,, \tag{5.12}$$

where R is the radial position of the module in meters, and θ is the rotation angle. For 2S modules located at $R = 715\,\mathrm{mm}$ in the Phase-2 CMS Outer Tracker, the stub correlation window chosen from the simulation in the Figure 4.16 is ±4.5 strips, with a module spacing of 1.8 mm. The stub turn-on angle corresponds to a p_{T} discrimination of 1.58 GeV, with a relative momentum resolution of 7.66%. This resolution is derived from the ratio of the width of the distribution, 0.121 GeV, to the transverse momentum value at the turn-on threshold.

Although the target p_T threshold for the 2S modules is 2 GeV, the calculated value of 1.58 GeV reflects the specific module spacing and the corresponding stub turn-on angle, which influence the stub formation criteria. The discrepancy arising from the module spacing is discussed in the next subsection.

Notably, the primary purpose of the stub correlation window is to reduce the data volume during the Level-1 trigger stage. The exact p_T of the particle for the final analysis will not be determined from the stubs or the track finder in the L1 trigger but will instead be extracted later from the full track reconstruction.

Discussion of stub turn-on threshold and systematic effects

The expected stub turn-on threshold, determined from the module geometry, accounts for the module spacing, strip pitch, and correlation window size. For a correlation window of ±4.5 strips, the turn-on angle, $\theta_{\text{turn-on}}$, is calculated as the average of the angles corresponding to stub offsets of 4.5 strips and 5.0 strips. This averaging is necessary because the stub efficiency transitions from one to zero as the displacement between clusters in the top and bottom sensors exceeds the correlation window. Specifically, for a 4.5-strip window, the stub efficiency is expected to reach one when the cluster displacement equals 4.5 strips, while it drops to zero for a displacement of 5.0 strips. Thus, the turn-on angle is given by:

$$\theta_{\text{turn-on}} = \frac{1}{2}\left[\arctan\left(\frac{4.5\cdot p}{d}\right) + \arctan\left(\frac{5.0\cdot p}{d}\right)\right], \tag{5.13}$$

where $p = 90\,\mu\text{m}$ is the strip pitch and $d = 1.8\,\text{mm}$ is the module spacing. The expected turn-on angle, based on the geometric configuration, is calculated to be 13.36°. However, this differs from the value obtained through the fitting of the data, which yields 14.96°.

The primary source of this discrepancy arises from the spacing of the module, as the finite distance between the midpoint of the sensors introduces systematic effects that influence the stub formation process. The module spacing is achieved by placing the AlCF spacing bridges between the top and bottom sensors. The thickness of these bridges was defined and produced when the sensors were originally designed to have a physical thickness of 320 µm and an active thickness of 200 µm, measured from the top sensor surface. To achieve a module spacing of 1.8 mm, the thickness of the bridges were fabricated to be 1.36 mm. Consequently, the modules in this study are with sensors of a physical thickness of 240 µm, resulting in an effective module spacing of 1.6 mm.

To verify the spacing consistency of the assembled module with design expectations, measurements were performed using a Keyence VHX microscope. The microscope camera was positioned perpendicular to the module sides to ensure precision in the measurements. The results of this verification process indicate a module spacing of 1.57 mm which is consistent with the intended design but slightly reduced due to manufacturing tolerances.

By taking this updated spacing into account, the expected turn-on angle is recalculated to be 15.23°. This difference can be attributed to systematic effects, such as the exact alignment of the sensors and the mechanical tolerances of the module assembly.

Stub performance with a 4 mm module

An additional study has been conducted with a 2S module with a spacing of 4 mm. Due to the larger spacing, the stub efficiency becomes more sensitive to the rotation angles of the module. Figure 5.28 shows the stub efficiency and the fitting results for the two 2S modules.

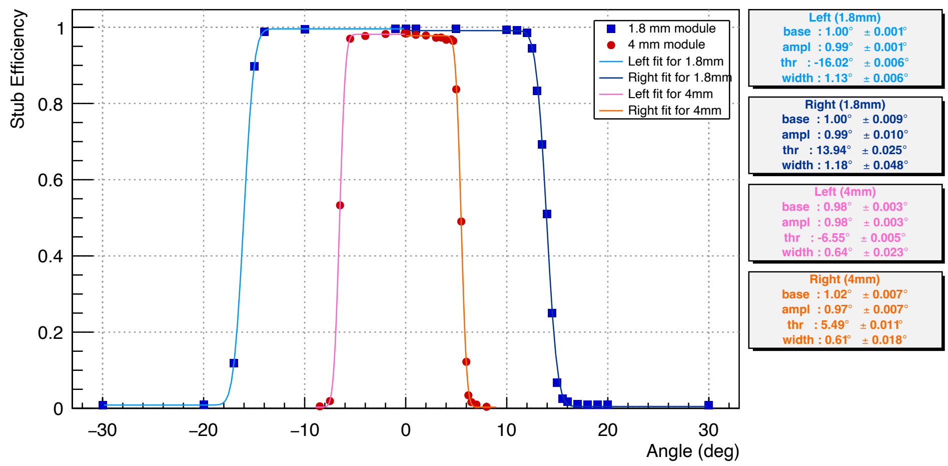

FIGURE 5.28: Stub efficiency as a function of rotation angle for two 2S modules. Blue marks indicate the efficiency results of the 1.8 mm spacing module. Red marks represent the result of the 4.0 mm spacing module. The stub window for both modules is set to be ±4.5 strips.

The 4 mm module exhibits an efficiency above 98.4% at the perpendicular incidence and a sharp drop in efficiency starting at around 5°. The corrected stub turn-on angle is found to be 6.02°, which is in good agreement with the expected value of 6.10° obtained by Equation 5.13 for a module with a 4 mm spacing and a stub window of ±4.5 strips.

The measured stub turn-on angle confirms the expected p_T discrimination performance of the 2S module. At this geometry, the larger module spacing enhances the angular resolution by creating a more distinct correlation between the strip displacements in the top and bottom sensors. This improved resolution allows for a more precise determination of the transverse momentum, particularly for tracks near the turn-on threshold. The agreement between the measured and expected values demonstrates the robustness of the module design and its capability to efficiently identify tracks with low transverse momentum, a critical requirement for the Level-1 trigger system of the CMS Outer Tracker.

5.6 Summary and Outlook

This chapter presented a detailed characterization of a 2S module prototype assembled and tested at DESY, with a focus on validating its key performance parameters, including cluster efficiency, spatial resolution, and p_T discrimination capabilities.

Before the assembly phase, thorough pre-assembly tests, including I-V and C-V measurements, were performed to ensure the integrity of the silicon strip sensors. These tests determined the depletion voltages of the sensors, ensuring their functionality within operational bias ranges. Post-assembly electrical tests confirmed the module's readiness for beam tests, with noise levels remaining well within acceptable limits.

Assembly procedures for the 2S modules were established, ensuring the consistency and reliability of the production process. Specialized jigs and tools were developed to achieve high mechanical precision, which is critical for p_T discrimination performance.

The module was characterized in beam tests using electron beams at the DESY-II synchrotron. High-efficiency particle detection and accurate cluster formation were observed across a range of operating conditions. Bias voltage and threshold scans demonstrated optimal module performance at 200 V bias and a relative signal threshold of approximately 5000 e^-, achieving cluster efficiencies exceeding 99.9% and stub efficiencies near 99.7%.

A comprehensive angular scan highlighted the impact of particle incidence angles on cluster size and position resolution. The spatial resolution at perpendicular incidence was measured to be 31.3 µm, which is larger than the expected intrinsic resolution. This discrepancy arises from limitations of the generalized error function fit, which overestimates the resolution by not fully accounting for events where particles intersect the sensor near the boundary between two strips. By contrast, using the RMS of the residual distribution at perpendicular incidence yields a resolution of 26.42 µm, which aligns well with the expected intrinsic resolution. At intermediate angles, the resolution improved significantly, reaching a minimum of 20.3 µm due to the averaging effect of larger clusters. At larger angles, where two-strip clusters dominate, the resolution degrades due to the binary readout system's inherent limitation in assigning cluster positions, converging back to the intrinsic limitations of single-strip clusters.

The module's p_T discrimination performance was studied by evaluating stub efficiency as a function of rotation angle. The results demonstrated a good agreement with theoretical expectations, with a stub turn-on angle of 14.96° corresponding to a p_T threshold of 1.58 GeV. A relative momentum resolution of 7.66% was extracted from the angular transition width, showcasing the module's sensitivity to discriminating low-p_T tracks. Systematic effects, such as slight module misalignments and mechanical tolerances, were identified and considered, further improving the precision of the turn-on measurement.

A comparative study with a 4 mm module further validated the p_T discrimination capabilities of the design. The larger module spacing increased angular sensitivity, resulting in a lower turn-on angle of 6.02°, consistent with the expected value of 6.11°. These results confirm the robustness of the module design and its ability to efficiently identify low-p_T tracks under realistic conditions.

Significant contributions were made to the test beam analysis software, including improving its compatibility with CMS test beam studies. These developments improved the software's integration with ongoing experiments, facilitating precise alignment, track reconstruction, and performance analysis of the DUT.

Outlook

The detailed characterization of the 2S module at DESY represents an important step in the development and validation process of the CMS Phase-2 Outer Tracker. The results presented in this chapter validate the performance of the module in experimental conditions of using particle beams and highlight its readiness for integration into the CMS experiment. Future studies will focus on:

- Extending the studies on module performance under operational conditions, including radiation damage effects and long-term stability, as outlined in the most recent 2S performance studies [56].

- Evaluating module performance within larger systems to ensure seamless integration into the CMS Outer Tracker.
- Optimizing assembly procedures for the mass production phase, ensuring reliability and consistency in module fabrication.

The results obtained in this chapter provide confidence that the 2S module design meets its intended performance objectives and will contribute to the successful upgrade of the CMS Outer Tracker for the HL-LHC era.

Chapter 6

Testing of Macro Pixel Sub-Assembly

Contents

The Pixel-Strip (PS) module, one of the two types of Outer Tracker modules for the CMS Phase II Upgrade, will be assembled at DESY. Before assembly, rigorous testing of the PS module components is essential to ensure their quality and reliability for the CMS operation. The DESY working group will produce 1,250 PS modules and has established a comprehensive testing infrastructure to achieve this objective.

This chapter presents the testing infrastructure established at DESY, outlining the MaPSA qualification procedures, the testing workflows, and the probing system used for quality assurance. Key topics include the hardware and software used in MaPSA testing, detailed testing results, and contributions from this thesis to the CMS collaboration by refining testing procedures and optimizing quality assurance processes for the production phase.

6.1 Macro Pixel Sub-Assembly

A PS module, as described in Section 4.3.2, is a module located in the inner layers of the Outer Tracker. It comprises one strip sensor and one macro-pixel sensor. The readout ASIC for the strip sensor is referred to as Short Strip ASIC (SSA), while the ASIC for the macro-pixel sensor is known as Macro-Pixel ASIC (MPA). Figure 6.1 shows a side view drawing of a MaPSA integrated into a PS module, with the MaPSA highlighted in a red box.

The MaPSA comprises two rows of eight MPA chips bump-bonded to the Macro Pixel Sensor (PS-p) sensor. Figure 6.2 shows photos of a MaPSA from two different views: one with the backplane of the PS-p sensor on top and another with the MPA chips on top. The PS-p sensor in general serves as the seed layer for the p_{T} module, while the MPA chips perform front-end data processing, correlation of strip and pixel data received from the SSA, and generation of stub information for the Level-1 (L1) trigger. Additionally, the MPA chips store full event information for transmission upon receiving a L1 trigger decision.

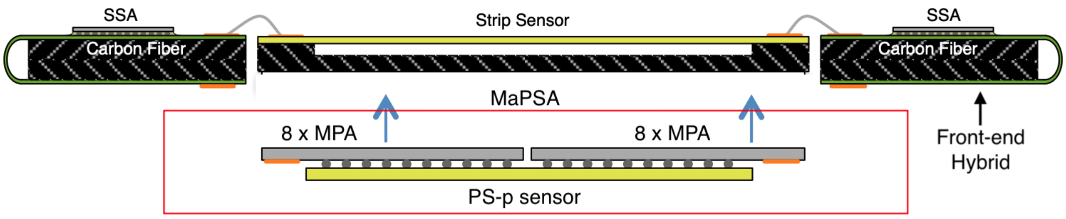

FIGURE 6.1: Side view schematic drawing of a MaPSA in a PS module. The red box highlights the MaPSA.

6.1.1 Macro Pixel Sensor

The PS-p sensor is an n-in-p silicon sensor featuring highly n-doped pixels embedded in a p-doped bulk material with p-stop isolation to minimize inter-pixel interference. It has an active thickness of 290 µm and a total thickness of 320 µm, covering a total surface area of 98.74 mm × 49.16 mm.

The sensor is segmented into 32 × 944 macro-pixels, each with a length of 1.467 mm, a pitch of 100 µm, and a width-to-pitch ratio of 0.25. The pixels are directly connected to the readout electronics through a DC coupling configuration. Pixel biasing to the global bias grid is achieved through a punch-through bias structure, which can achieve a more compact layout design compared to other biasing methods and allows the sensor to be tested without a readout chip.

6.1.2 The Macro Pixel ASIC

The dedicated readout chip, Macro Pixel ASIC, is designed using 65 nm CMOS technology. It has a dimension of 25.2 mm × 11.9 mm, integrates a matrix of 16 rows and 118 columns, resulting in 1888 front-end readout channels.

The floor plan of the MPA chip is illustrated in Figure 6.3. The pixel region, occupying an area of 11.9 mm × 23.16 mm, is segmented to align with the sensor pixel size, meeting the granularity requirements of the CMS upgrade. The digital periphery logic, along with the bump bonding pads for common ground connections and wire bonding

(a)

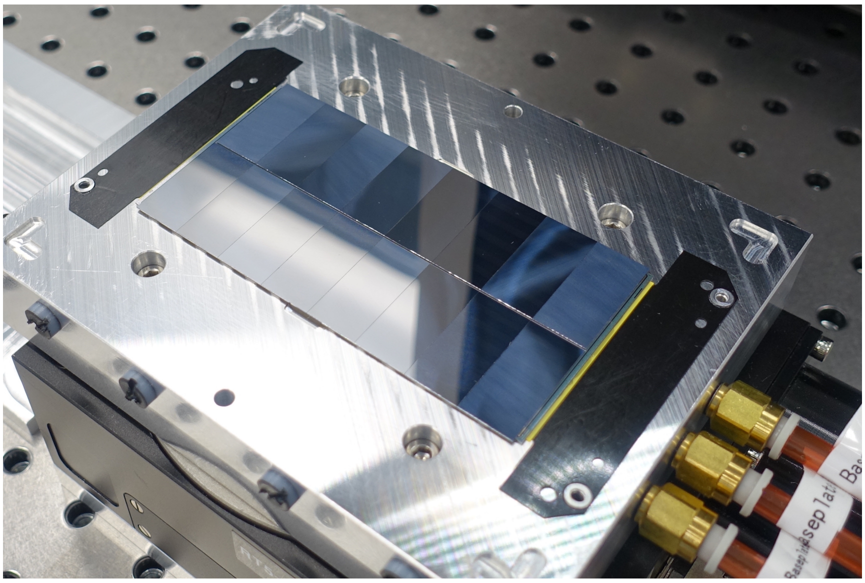

(b)

FIGURE 6.2: Photos of a MaPSA from different views: (a) backplane of the sensor visible on top, and (b) MaPSA placed on the PS module baseplate with MPA chips visible on top.

pads for readout, is located in a region approximately 2 mm wide at the edge of the chip.

Figure 6.4 shows the top-level block diagram of a single MPA chip, where the L1 trigger path (stub data path) and the L1 data path are highlighted in orange and cyan, respectively. The pixel array is responsible for binary readout, clustering, and initial signal processing. The periphery receives strip data from the SSA, forms stub information, transmits stub data for the L1 trigger decision, and formats and outputs the requested event data upon the arrival of a L1 trigger. The chip is capable of reading out complete event data at a maximum trigger rate of 1 MHz, with a latency of up to 12.8 µs.

While the top-level block diagram illustrates the overall data flow and functionality of the MPA chip, the detection of particles starts at the level of individual MPA channels.

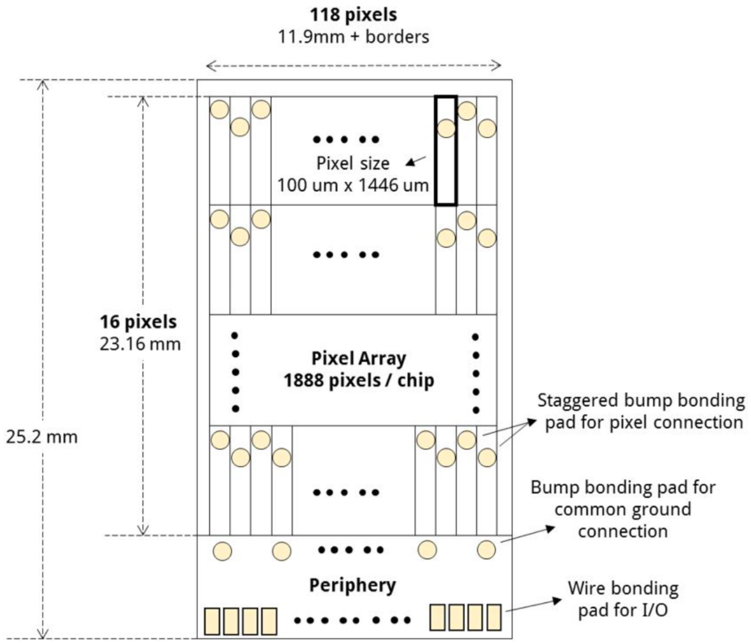

FIGURE 6.3: The floor plan of a MPA chip. [85]

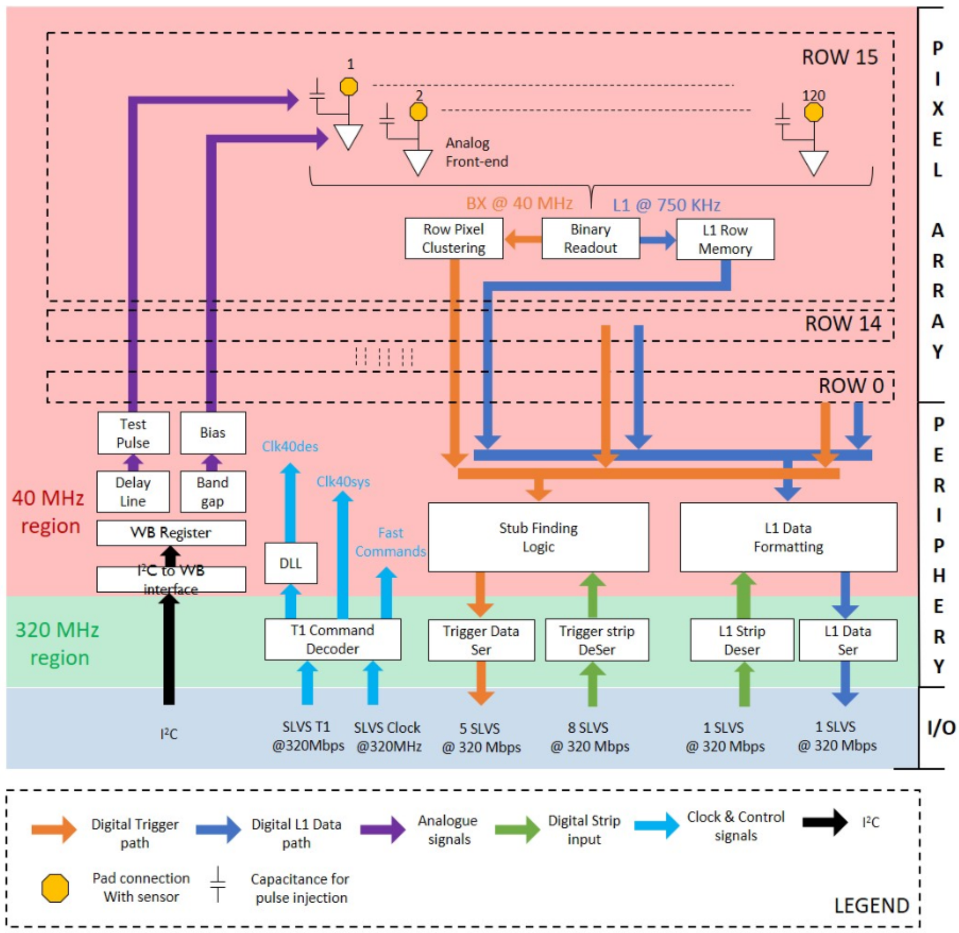

FIGURE 6.4: Top-level block diagram of the MPA design. Adapted from [85].

Each of the 1888 channels is dedicated to processing signals from its corresponding pixel, converting the raw charge generated by particle interactions in the sensor into digital data. This process starts in the analog front-end circuitry and proceeds through the digital back-end, as shown in Figure 6.5.

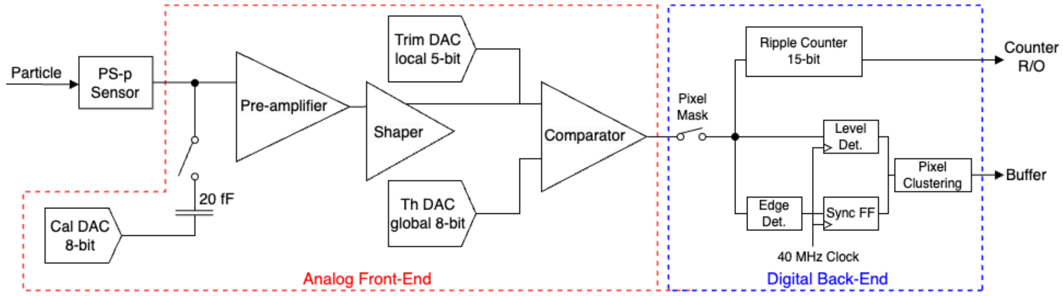

FIGURE 6.5: A simplified electronics schematic for a single MPA channel. The red dash-line indicates the analog front-end electronics whereas the blue dash-line specifies the digital pixel back-end.

The analog front-end circuitry begins with a charge-sensitive pre-amplifier that integrates and amplifies the current pulse signal, which can originate either from the pixel implant due to particle interactions or from the discharge of a capacitor in the calibration circuit. The amplified signal is then passed through a shaper, which refines the waveform by filtering out low-frequency baseline noise and high-frequency random noise. This shaping process improves the signal-to-noise ratio [52].

After shaping, the signal enters the comparator, where it is digitized and discriminated. The comparator compares the incoming signal pulse against a DC threshold voltage provided by a dedicated 8-bit Threshold DAC (ThDAC). This threshold voltage is globally applied to all pixel channels, but individual adjustments are necessary to account for variations in the pixel circuitry. To address these variations, each pixel is equipped with a local 5-bit Trimming DAC (TrimDAC) that adjusts for offset corrections to the threshold voltage. This process ensures that all front-end channels exhibit uniform response characteristics to identical incoming pulses, as further detailed in Section 6.2.3.

Once the signal is digitized, it is directed to the digital back-end for further processing. In the digital back-end of the MPA pixel channel, three distinct acquisition methods for the readout illustrated in Figure 6.6 are provided:

1. Synchronous Readout Modes: Two of the acquisition modes operate synchronously with the 40 MHz system clock. These modes sample and align the output level of the comparator with the clock cycles.

    - The Level-Sensitive mode: In this mode, the input pulse from the comparator is sampled on the rising edge of the system clock. The output pulse depends on the duration of the signal pulse and remains high as long as the input from the comparator stays high. A key advantage of the level-sensitive mode is its reduced sensitivity to the precise clock cycle of signal arrival. For long pulses, it is easier to detect hits spread over varying latencies. However, for short pulses, as depicted in the Figure, the pulse signals might be missed if they occur entirely between two rising edges of the clock.

    - The Edge-Sensitive mode: This mode detects the transitions of the comparator output as the input signal pulse crosses the threshold. The output of the comparator is connected to a D Flip-flop (FF) that acts as an edge-sensitive detector. This detector generates a pulse on the rising edge of the comparator output and is reset on the falling edge of the system clock to prepare for the next transition. A second FF, referred to as the Sample FF samples the output of the edge-sensitive detector on the rising edge of the system clock, producing a synchronized pulse with a duration of one clock cycle. This means that regardless of the input pulse duration, the output is always a one-clock-cycle digital pulse. Unlike the level-sensitive mode, this method is particularly effective for detecting short-duration pulses, and will be used in the CMS operation.

2. Asynchronous Mode: The third acquisition method employs a 15-bit ripple counter and a shutter mechanism, operating independently of the system clock. The shutter is controlled by fast commands, defining the start and end of the acquisition period. While the shutter is open, the counter records the number of threshold crossings detected by the comparator. Once the shutter is closed, the accumulated data is read out. The asynchronous mode is primarily designed for calibration and testing purposes, offering a straightforward way to monitor pixel activity and validate detector performance. Further details on its implementation and use are provided later in this chapter.

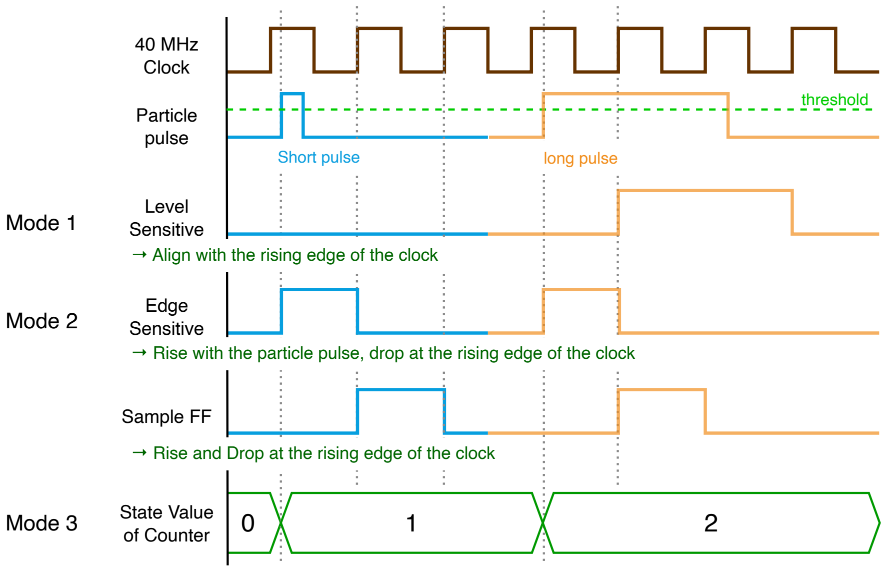

FIGURE 6.6: The three acquisition methods in the digital back-end of an MPA channel.

6.1.3 Assembly of the MaPSA

The assembly of the MaPSA utilizes a flip-chip process where individual MPA chips are bump bonded to the PS-p sensor using a standard Controlled Collapse Chip Connection (C4) process due to the relatively large bump pitch compared to other pixelated detectors. This process interconnects the chips to the sensor with solder bumps deposited onto the chip pads.

Figure 6.7 shows that the bump bonding process involves several critical steps. Both the sensor and MPA bonding pads are prepared with a 5 µm layer of Under Bump Metallization (UBM) consisting of Al/NiV/Cu to ensure compatibility with the soldering material and to establish stable electrical contact. Lead-free SnAg solder spheres are deposited onto the UBM pads. During the bonding process, the components are aligned, and the assembly is heated in a reflow oven. The solder bumps melt, forming robust electrical connections between the MPA and sensor, while the MPA chips settle into their final positions.

To protect the silicon wafer during the C4 process, a passivation layer is applied to avoid structural damage caused by environmental factors. Openings are made only at locations where the aluminum pads are present. Additionally, on the MPA side, a polyimide layer is deposited on top of the passivation layer. This ensures the passivation layer's quality and thickness, as well as the integrity of the silicon substrate, remain unaffected during the high-temperature bonding process.

Finally, for breakdown protection along the long edge of the MaPSA, a Kapton strip measuring 25 µm × 1.2 mm × 10 cm is inserted and glued with epoxy between the PS-p sensor and the MPAs. This protection is necessary because the sensor operates at high voltage, and the close proximity of the MPA and sensor along their long edges creates a region of high electric field. Without proper insulation, this could lead to dielectric breakdown or surface discharges, potentially damaging the components. An overview of the fabrication, assembly process, and quality control flow is shown in Figure 6.8.

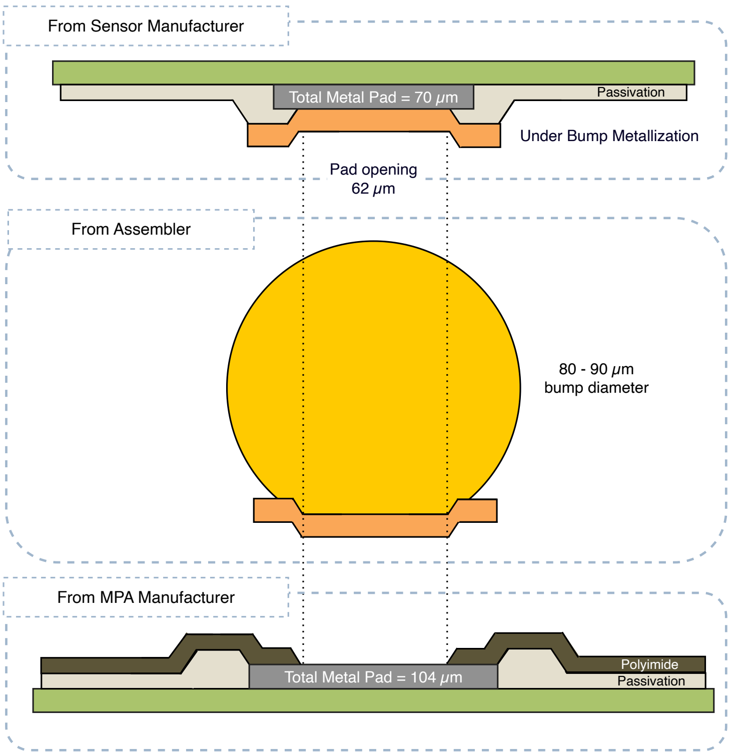

FIGURE 6.7: Bump bonding diagram. Adapted from [86].

After the assembly, the completed MaPSA consists of two rows of eight MPA chips bump-bonded to a PS-p sensor, as shown in Figure 6.9. The edge pixels on the leftmost and rightmost columns of each MPA chip must be separated by approximately 100 µm from the adjacent MPA chips [85]. This separation is necessary for two reasons: first, the MPA chip has a dicing target overhang of 20 µm on the edges to accommodate the laser dicing groove, which prevents chipping on the backside of the chip. Second, the

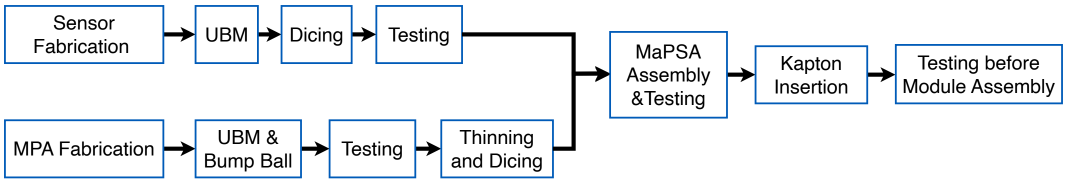

Figure 6.8: MaPSA production and quality control flow diagram.

edges correspond to the inactive periphery of the chips, where no readout channels can be allocated. The separation ensures proper alignment of the readout channels of the MPA chips with the pixel electrodes of the sensor. Comparatively, the pixels on the sensor corresponding to the edge pixels on the MPA chips are twice the size of the other pixels, as shown in Figure 6.10.

The readout pads of the MPA chips are located at the edges of the chip. To connect these pads to the FEH, wire bonding is used. Consequently, the edge of the MPA chips extends beyond the edge of the sensor after the MaPSA is assembled, as shown in Figure 6.9. This extended section, which contains aluminum wire bond pads, facilitates the connection to the FEH for signal transfer and chip operation.

These wire bond pads also serve an additional purpose during probe testing, which ensures the quality of the MaPSA after manufacturing and assembly. During this process, a probe card with 118 probe needles is used to test each MPA chip. However, probe testing leaves permanent marks on the wire bond pads, potentially complicating the wire bonding process during module production. To mitigate this, only one-third of the area of each bond pad is designated for probe testing, while the remaining area is preserved exclusively for wire bonding. This division ensures that the wire bonding process remains unaffected, as illustrated in the right diagram of Figure 6.9.

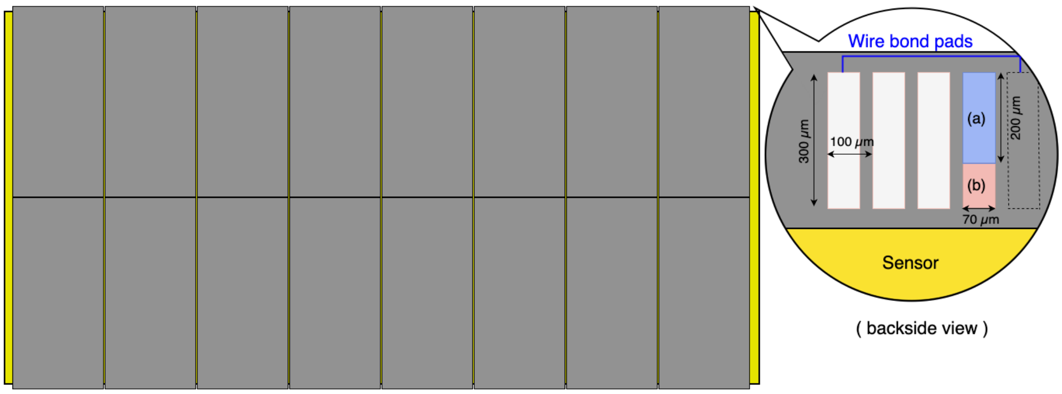

Figure 6.9: A diagram of a MaPSA, top view from MPA side. The yellow part indicates the shape of a PS-p sensor. In the backside view drawing, section (a) of the Aluminum pads are conserved for wire bonding, and section (b) is dedicated to probe test purposes.

6.2 Quality Assurance of MaPSAs

6.2.1 Overview of the Quality Assurance of MaPSAs

To construct a detector on the scale of an LHC particle detector, which includes multiple sub-detectors as mentioned in Section 2.2, each individual particle detection

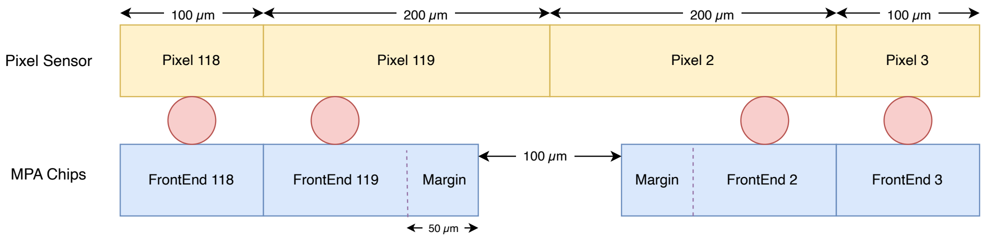

FIGURE 6.10: Edge pixel connection of MPA chips.

module must exhibit high manufacturing quality, precise assembly alignment within and between modules, adherence to the designed readout performance, and tolerance to irradiation. Consequently, a comprehensive Quality Control (QC) plan has been developed to address the aforementioned criteria.

During the production of the CMS Phase-II Outer Tracker, all module components undergo visual inspection. Dedicated procedures are implemented to mechanically and electrically assess these components. For example, 5 % to 10 % of the 2S and PS-s sensors will go through Sensor Quality Control (SQC) that characterizes the actual sensors. 10 % to 20 % of the test structures from the sensor wafer will undergo Process Quality Control (PQC) providing an insight into production stability. And 1 % of the sensors and test structures will be irradiated, annealed, and tested to ensure the radiation hardness.

The hybrids undergo functional tests, which involve testing the hybrid circuits without any attached sensors. They are mounted onto specially designed test cards and plugged into a test crate capable of testing up to 10 hybrids simultaneously, enabling automated testing of the same type of hybrid without manual intervention. These tests include power verification, I^2C communication validation, ASIC configuration, data communication analysis, threshold and noise measurements, and assessment of hybrid connectivity. Test procedures are detailed in [72].

Regarding MaPSA, since it is a sub-assembly component that contains both sensor and readout chips, it has a slightly different quality control process than the QC plan described above. PS-p sensors will undergo simple *I*-*V* and *C*-*V* characterization at the foundry, and only the sensors that comply with the specification will be shipped to the MaPSA assembly vendor. MPA chips will also be tested at the wafer level before being sent to the dicing and assembly vendors.

After the assembly of the MaPSAs, all units will undergo testing at the designated testing sites. Those MaPSAs demonstrating good quality will then be distributed to the PS module assembly sites. The quality control process is shown in Figure 6.8. DESY also contributes to the MaPSA quality control to ensure that MaPSA which are received at DESY are not damaged during shipment in the production phase. For 1250 PS modules that will be assembled at DESY, it is foreseen that all the MaPSAs will be tested in the pre-production phase, and 50 % of the MaPSAs will be tested on-site before module assembly during the production phase. During the R&D phase, where testing software and hardware were developed, the results presented in this chapter made a significant contribution to the establishment of quality assurance guidelines and procedures for the MaPSA.

The quality control of a MaPSA, ensuring both mechanical and electrical integrity, includes several tests executed at the testing sites:

1. Visual inspection to confirm the flatness of the MaPSA, alignment between the MPA chips and PS-p sensor, and the quality of Kapton strip insertion.
2. Electrical tests including sensor characterization such as IV measurement, pixel characterization and masking ability, bump bonding quality, noise measurement, and threshold equalization among all the pixels.

The preliminary electrical test criteria for assessing the quality of a MaPSA are summarized in Table 6.1. The definition of a faulty pixel is detailed in Section 6.4. This section also outlines the testing procedures and presents the corresponding results, offering a comprehensive overview of the quality evaluation process.

The grading criteria, as shown in Table 6.1, categorize MaPSAs into three grades: Grade A, Grade B, and Grade C. Grade A MaPSAs are designated for installation into the CMS detector. Grade B devices are kept as spares in case an insufficient number of Grade A MaPSAs are available for assembly. Grade C devices do not meet the required performance criteria and should not be installed in the CMS detector. The grade of a MaPSA is assigned as the lowest grade among its 16 MPA chips and the leakage current performance.

TABLE 6.1: Summary of MaPSA grading criteria [87]

MaPSA Grade	Operational Pixels (per MPA)	Faulty Pixels (per MPA)	Leakage Current at $V_{\text{bias}} = 600\,\text{V}$
Grade A	$> 99\%$	< 19	$< 1\ \mu$A
Grade B	95–99%	19–94	1–10 μA
Grade C	$< 95\%$	> 94	$> 10\ \mu$A

6.2.2 S-Curve and Noise

The MPA employs a binary readout system, where only signals exceeding a predefined threshold are registered. Hence, it is crucial to determine an optimal threshold to effectively suppress noise. As part of the MaPSA quality control process, electrical tests include evaluating pixel noise levels and analyzing pixel responses to uniform input signals at the chosen threshold.

To extract noise levels and evaluate the response of pixels to signal pulses, test pulses generated by the calibration circuitry in the MPA chip are used. For a single channel, the test pulse is produced by discharging a 20 fF calibration capacitor through a CMOS switch into the pixel front-end circuitry. The amplitude of the pulse is determined by an internal 8-bit Calibration DAC (CalDAC). The global threshold, as described in Section 6.1.2, is set by a dedicated 8-bit ThDAC, which provides a uniform DC threshold voltage to all pixels. In the scope of this chapter, the Least Significant Bit (LSB) is used as the unit for both the CalDAC and ThDAC, representing the numerical value configured in the DAC. A single unit of ThDAC corresponds to $94\,e^-$, while a single unit of CalDAC corresponds to $181\,e^-$.

A threshold scan is performed on each pixel while a number of fixed-amplitude test pulses are sent. During the scan, the threshold is incrementally increased across its full range of 256 discrete levels, and the response of a pixel to the test pulses is recorded at each setting.

The MPA operates in counter mode during this procedure, where a hit is registered by the counter each time the amplitude of the comparator's input pulse exceeds the current threshold. By recording the number of hits at each threshold setting, the resulting data generates the output shown in Figure 6.11.

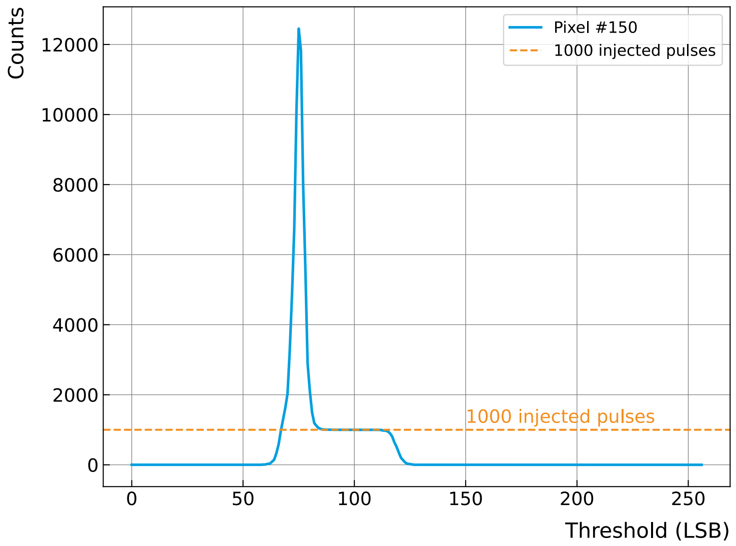

FIGURE 6.11: Threshold scan for a single pixel, showing the response to 1000 injected pulses.

The output of a threshold scan contains information about the pixel, including the baseline of the amplifier, the intrinsic noise of the pixel, the amplitude of the test pulses, and the pixel's response at varying threshold levels. These key concepts can be interpreted as follows:

- At the beginning of the threshold scan where the threshold level is smaller than the baseline of the comparator's input pulse, the counter returns always with a count of 1 since the pulse crosses above the threshold once when the chip is powered.
- The number of registered hits increases rapidly as the threshold approaches the baseline of the input pulse. This is due to the intrinsic noise of the pixel, which causes small fluctuations in the pulse to frequently exceed the threshold. These fluctuations result in multiple hits being registered by the counter, forming a characteristic noise peak.
- At a threshold level above the baseline of the input pulse, the counter registers exactly one hit per injected pulse. This behavior creates a plateau in the recorded data, where the number of counts corresponds directly to the number of injected test pulses. The width of the plateau reflects the amplitude of the test pulses.
- As the threshold approaches the amplitude of the input pulse, a transition region emerges, producing an S-shaped curve (S-Curve). This transition is caused by noise in the pixel, which dominates the number of pulses crossing the threshold. The S-Curve can be modeled using an error function:

$$f(x) = \frac{1}{2} n \times \operatorname{erfc}\left(\frac{x-\mu}{\sqrt{2}\sigma}\right), \tag{6.1}$$

where n is the number of injected pulses, σ represents the noise level of the pixel. Pixels with higher noise will lead to a longer transition phase. The midpoint (μ)

of the S-Curve, referred to as the turn-on threshold, is a critical parameter in the threshold equalization procedure that is described in the next section.

- Once the threshold exceeds the amplitude of the input pulses, no further counts are registered, leaving the counter at 0.

An alternative method for characterizing pixel performance is the calibration pulse scan, which increments the amplitude of the injected test pulses while keeping the threshold at a fixed, reasonable value. The amplitude of the test pulses is determined by the CalDAC, an internal 8-bit DAC, where each CalDAC step corresponds to a voltage increment of 1.456 mV. Similar to a threshold scan, a set of pulses is injected into the chip, and the counter registers the number of hits for each CalDAC step at a fixed threshold.

Ideally, once the pulse amplitude exceeds the threshold, the number of hits sharply reaches the number of injected pulses. However, due to noise in the chip, a transition region resembling an S-Curve, similar to that observed in the threshold scan, appears. When the amplitude is consistently above the threshold, a plateau is formed, corresponding to the number of injected pulses, and this remains until the end of the scan, as shown in Figure 6.12.

The S-Curve can be modeled using the following function:

$$f(x) = \frac{1}{2} n \times \left(1 + \operatorname{erf}\left(\frac{x-\mu}{\sqrt{2}\sigma}\right)\right), \tag{6.2}$$

where n represents the number of injected pulses, μ is the midpoint of the S-Curve, and σ denotes the noise level of the pixel.

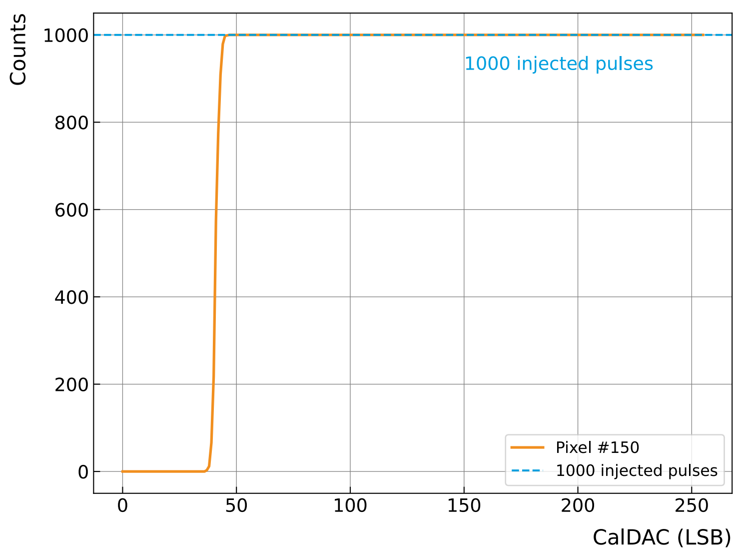

FIGURE 6.12: Calibration pulse scan for a single pixel, showing the transition of an S-Curve as the pulse amplitude increases relative to a fixed threshold.

6.2.3 Threshold Equalization (Trimming)

For the proper operation of the detector, the response of the electronics to identical particle interactions should be uniform for each pixel. When a global threshold is applied to the MPA chip, all readout channels are expected to produce a consistent response to the same charge signal. However, achieving this consistency is challenging due to the variations in the signal baseline and comparator offset of the front-end channels, which arise naturally from the manufacturing process of the readout chip. These variations may result in certain channels failing to detect charge signals that should be recorded, while others might falsely trigger on noise.

To address these variations, a fine-tuning process called threshold equalization, known as *Trimming*, is applied. Trimming utilizes a TrimDAC to adjust the comparator offset of each channel, compensating for the pixel-to-pixel differences caused by the manufacturing process. The TrimDAC provides a per-pixel adjustment range of 0 to 120 mV [85], implemented with a 5-bit resolution. This configuration enables 32 discrete adjustment steps, allowing precise shifts to the baseline of each channel as needed. By aligning the baselines across all channels, the global threshold can be applied effectively, ensuring uniform responses to identical charge signals.

To determine the needed baseline adjustment for each pixel, threshold scans as mentioned in Section 6.2.2 are conducted. In the threshold scan, 1000 test pulses with a fixed amplitude are injected into the pixels.

Since the baseline of the front-end output varies from pixel to pixel, the resulting S-Curves for all the pixels on an MPA chip are scattered throughout the threshold settings, as shown in Figure 6.13(a).

By applying the TrimDAC adjustments to each pixel individually, the baseline differences are redressed. The TrimDAC adjustment for each pixel is determined by fitting the S-Curve with an error function, as described in Eq. 6.1. The mean value of the fitted curve is extracted and compared to the desired turn-on threshold target. The difference between the mean of the S-Curve and the target threshold indicates the adjustment needed to shift the baseline.

Figure 6.13(b) illustrates a 2D map of the trimDAC values applied to each pixel, represented in units of LSB. These values indicate the adjustments made to align the baselines across the MPA chip. The trimming process shifts the baseline of each pixel, aligning the S-Curves to ensure they have a similar turn-on threshold. The outcome of this trimming procedure is illustrated in Figure 6.13(c)

Pixels with S-Curves that cannot be shifted to align with the others, even after applying the correction voltages, are classified as *untrimmable pixels* which is an important criterion for the quality assessment of the MPA chip. The trimming process depends on several factors, including the trimming threshold target, amplitude of the test pulse, trimming range, step size, and the ability to fit the S-Curve accurately. To prevent any deception of identifying untrimmable pixels, the procedure and strategy of selecting the TrimDAC value for each pixel is implemented as follows:

1. Select a **trimming target**: The trimming target is defined as the desired turn-on threshold value that the mean of the pixel S-Curve should achieve after trimming. Ideally, this target can be any threshold value within the operating range provided by the ThDAC. However, two main constraints must be considered when selecting the target in the MPA chips: the limitation of the TrimDAC and the distribution of the turn-on threshold of all the pixels before trimming.

   The TrimDAC is a 5-bit DAC with a selectable range of 0 to 120 mV, meaning that any target requiring adjustments beyond this range will not be achievable. To determine an achievable target, the smallest and largest TrimDAC settings (corresponding to values 0 and 31) are applied to all the pixels, and the resulting

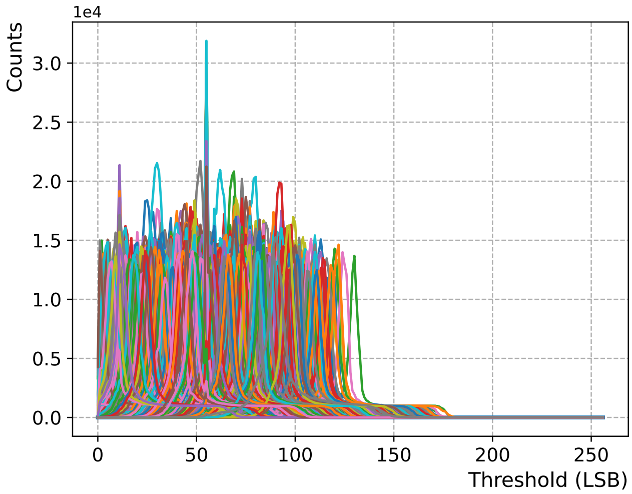

(a) S-Curve before threshold equalization.

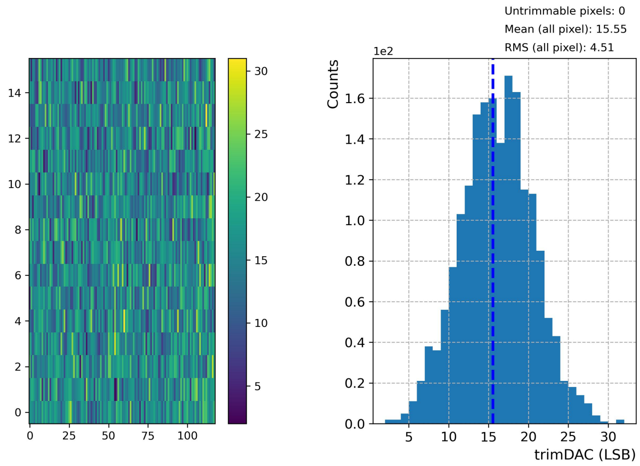

(b) The 2D map and distribution of the comparator offset applied to the pixels on an MPA chip.

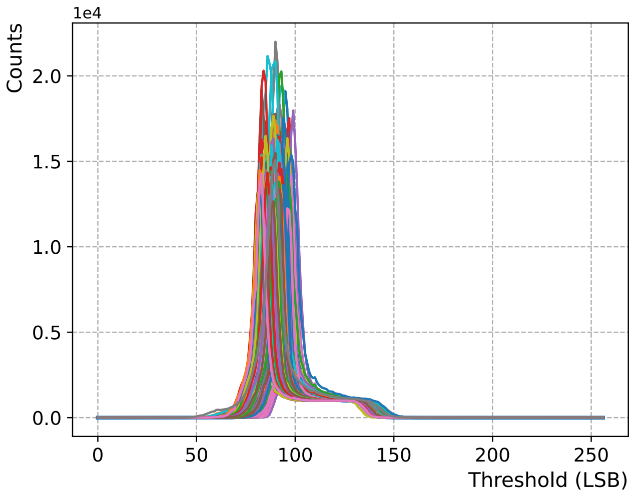

(c) S-Curve after threshold equalization.

FIGURE 6.13: Example S-Curve plots of threshold scans on all the pixels on a single MPA chip, showing pre-trimming and post trimming distribution of the registered hits by the counter, along with the trimDAC values applied for the trimming procedure.

distributions of the S-Curve mean values are analyzed. These distributions represent the minimum and maximum achievable turn-on thresholds for the given TrimDAC range, providing the basis for selecting a feasible trimming target within these limits.

Figure 6.14 illustrates the two distributions of the S-Curve mean values. The cyan distribution corresponds to the smallest TrimDAC setting, while the orange distribution corresponds to the largest setting. For the first distribution (cyan), where the smallest TrimDAC setting is applied to all pixels, it is not possible to shift the S-Curves any further downward, as the minimum adjustment has already been reached. Similarly, for the second distribution (orange), where the largest TrimDAC setting is applied, no further upward adjustment can be made, as the maximum adjustment of the TrimDAC has already been applied.

Therefore, the trimming target should be selected to maximize the number of pixels whose S-Curves can still be adjusted to align with the target value. An optimal choice for the trimming target is the midpoint of the two distributions, as it balances the range of adjustments available to align the maximum number of pixels with the target threshold.

In the figure, the midpoint of the two distributions is at 102 (ThDAC LSB), as highlighted by the green vertical line. Pixels within the cyan distribution to the right of the target line and those within the orange distribution to the left of the target line are classified as non-trimmable pixels, as their S-Curves cannot be adjusted to align with the target.

Additionally, the peak at a mean value of 180 (ThDAC LSB) corresponds to pixels that failed to produce a well-fitted S-Curve. These pixels and their implications will be further discussed in Section 6.2.4.

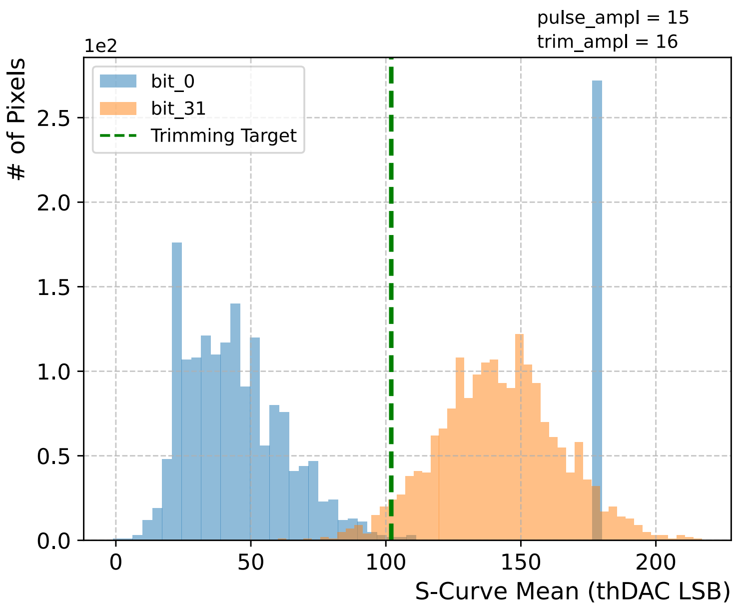

FIGURE 6.14: An example of the S-Curve mean value distributions with the minimum and maximum TrimDAC settings applied to all the pixels on an MPA chip. The green vertical line indicates the trimming target.

2. Find an optimal **calibration pulse amplitude** (`pulse_ampl`): As mentioned in the first bullet point, the trimming target is derived from the fitted S-Curve,

making the fitting performance a critical factor in this procedure. To ensure accurate determination of the turn-on threshold and avoid errors from poor fitting results, the S-Curve shape in the threshold scan must be distinct. This is achieved by selecting an appropriate amplitude for the injected calibration pulse such that the S-Curve is well-separated from the noise peak, and the plateau corresponding to the number of injected pulses is clearly visible. These conditions are necessary to ensure that the S-Curve behavior is well-described by Equation 6.1, as insufficient distinction may lead to fitting failures.

If the amplitude is too small, the S-Curve may overlap with the noise peak, leading to indistinct rising edges and fitting failures. While a larger amplitude improves visibility, it must remain within the operating range of the ThDAC used in the threshold scan. Therefore, the pulse amplitude is carefully chosen to balance these factors, ensuring an accurate S-Curve model fit.

3. Determine a reasonable **trimming range** (`trim_ampl`): The correction applied to a pixel depends not only on the TrimDAC settings but also on the step size provided by each setting. The range of the TrimDAC is controlled by another global 5-bit DAC, which defines the gain of each TrimDAC step for all pixel front-ends. A larger trimming range allows pixels with turn-on thresholds further from the target to be trimmed within the 5-bit setting of the TrimDAC. However, this comes at the cost of precision, as a larger step size prevents fine adjustments for pixels requiring smaller corrections.

   To achieve a balance between trimming range and precision, the goal is to select a range that maximizes the number of trimmable pixels while maintaining sufficient precision for accurate alignment. This optimization process is further described in Section 6.2.4.

4. Calculate the **trimDAC**: For each pixel, threshold scans should ideally be performed with all 32 TrimDAC settings applied to determine the optimal TrimDAC value that corresponds to the S-Curve with the trimming target. However, to improve efficiency during the MaPSA test in production, the trimming step that one TrimDAC can provide is calculated using only two TrimDAC settings, based on the linear relationship between the mean value of the S-Curve (μ) and the TrimDAC value.

   Figure 6.15 demonstrates this linear relation between the μ and the applied TrimDAC settings. The trimming step, representing the change in the mean S-Curve per TrimDAC step, is determined by:

$$\text{trimDAC step} = \frac{\mu \text{ of a higher trimDAC} - \mu \text{ of a lower trimDAC}}{\text{trimDAC LSB difference}}. \tag{6.3}$$

   In the figure, the μ for a higher TrimDAC is indicated in red, while that for a lower TrimDAC is highlighted in cyan. The TrimDAC LSB difference corresponds to the x-axis separation between these two points.

   Using this trimming step, the required TrimDAC setting to achieve the trimming target is given by:

$$\text{required trimDAC} = \text{initial trimDAC} + \text{correction trimDAC}, \tag{6.4}$$

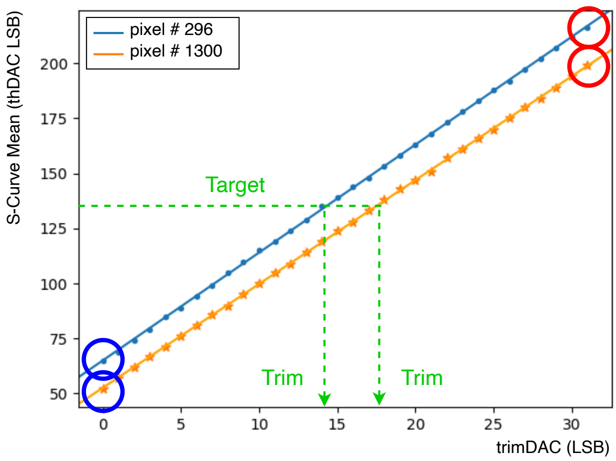

FIGURE 6.15: An example of a linear relation in the mean value of S-Curves with 32 trimDAC settings applied.

where the correction TrimDAC is defined as:

$$\text{correction trimDAC} = \frac{\mu_{\text{target}} - \mu \text{ of a lower trimDAC}}{\text{trimDAC step}}. \tag{6.5}$$

In this context, the initial TrimDAC refers to the current TrimDAC setting applied to the pixel, while the μ_{target} represents the desired turn-on threshold, corresponding to the μ after adjustment. The μ of lower TrimDAC is the mean value of the S-Curve obtained using a lower TrimDAC setting, as illustrated in Figure 6.15. The TrimDAC step, calculated earlier, represents the change in the mean S-Curve value per TrimDAC increment.

If the required TrimDAC falls outside the range of $0 \leq \text{trimDAC} \leq 31$, the pixel is classified as a nontrimmable pixel since the required adjustment cannot be achieved within the limits of the 5-bit TrimDAC. Nontrimmable pixels are defined as faulty pixels, as they fail to meet the trimming requirements necessary for uniform detector operation.

This approach provides an efficient method to determine the appropriate TrimDAC value for each pixel. Instead of measuring the S-Curve mean values across all 32 TrimDAC settings, this method requires measurements at only two TrimDAC settings to calculate the necessary parameters, significantly reducing the time required for the trimming procedure.

In addition to performing a threshold scan, a calibration pulse scan can also be employed for pixel trimming. Within the MaPSA testing procedure, the calibration pulse scan serves as a cross-check to validate the accuracy of the trimming performance.

A trimming procedure is required for each MPA chip and must be determined at least once before detector operation. The TrimDAC settings applied to each pixel can be saved to a file and re-applied whenever the chip is power cycled.

6.2.4 Trimming optimization

In the MaPSA trimming procedure mentioned in the previous section, the trimming target and the resulting number of untrimmable pixels heavily depend on the S-Curve fitting results. To achieve reliable trimming, the two initial TrimDAC configurations used to define the trimming target should be selected to produce well-fitted S-Curves. These configurations require optimal parameters as described in the trimming strategy above.

As shown in Figure 6.16, the minimum TrimDAC setting and the maximum TrimDAC setting were applied to an MPA chip with a trimming range of 20 LSB. This range is determined by a global 5-bit DAC that defines the gain of one TrimDAC step. In this configuration, the two distributions overlap, resulting in the misclassification of some pixels as untrimmable. Regardless, an optimal trimming target is still selected within the overlapping region to minimize the impact of this limitation. By increasing the trimming range to 31 LSB, the distributions are clearly separated, as illustrated in Figure 6.16(b).

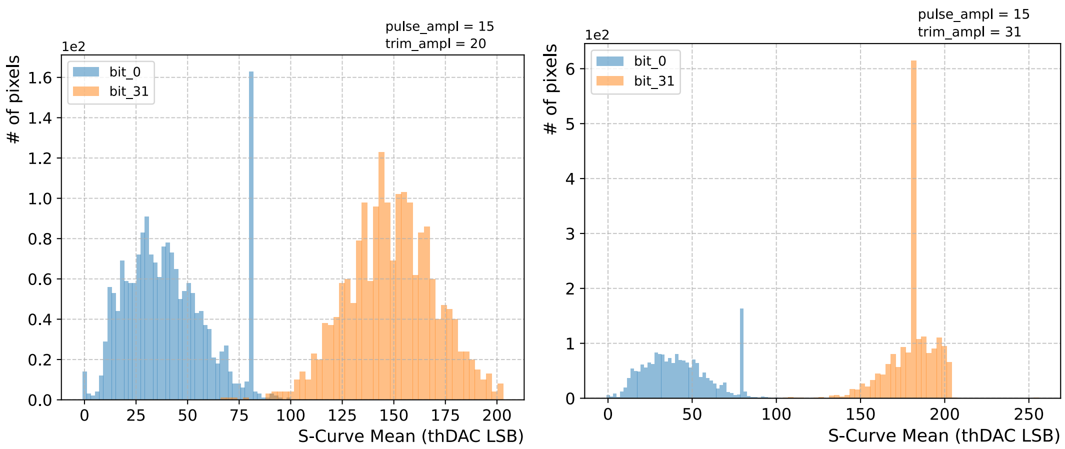

(a) Trimming range of 20 LSB. (b) Trimming range of 31 LSB.

FIGURE 6.16: Distributions of the mean of the S-Curves for the pixels on a single MPA chip with the trimming range of 20 LSB in the left Figure and 31 LSB in the right Figure. The trimDAC configuration with a value of 0 LSB is depicted in cyan, whereas the configuration with the maximum trimDAC value (31 LSB) is depicted in orange.

In Figure 6.16(b), the distributions are widely separated, allowing the trimming target to be chosen without intersecting any of the distributions. However, some abnormal peaks were observed due to fitting failures of the S-Curve. The S-Curve is fitted by an error function, with the fit range starting 20 LSB in ThDAC away from the noise peak in the S-Curve. For noisy pixels, the transition region of the S-Curve can merge into the noise peak if the injected pulse amplitude is too small, resulting in a fitting failure, as shown in Figure 6.17.

In this figure, one pixel with a noise peak merges with the S-Curve, which results in the fitting failure peak observed in the orange distribution of Figure 6.16(b). The plateau of the S-Curve is not well-defined, and the transition region is indistinct, making it challenging for the error function to provide a reliable fit. To address this, the pulse amplitude should be increased to separate the S-Curve from the noise peak, ensuring a clear transition region and a visible plateau for accurate fitting.

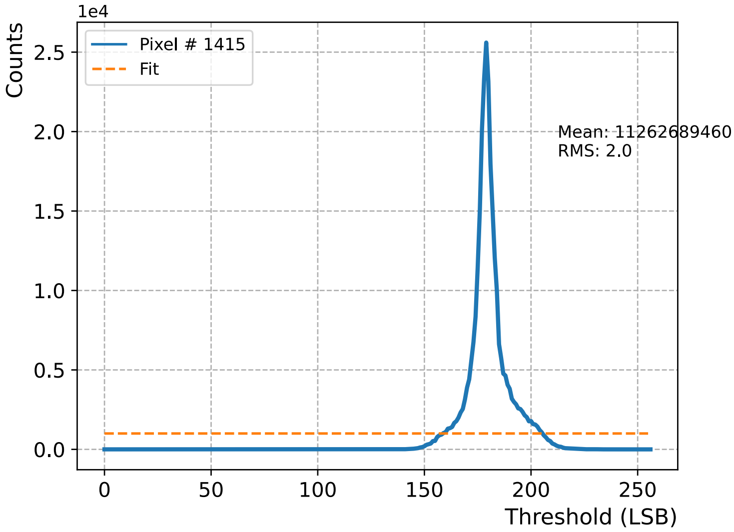

FIGURE 6.17: The S-Curve of a noisy pixel with a trimming range of 31 LSB and a pulse amplitude of 15 LSB. The indistinct transition and merging with the noise peak result in fitting failure.

By increasing the pulse amplitude from a CalDAC value of 15, LSB to 25, LSB, the plateau and transition shape of the S-Curve become more noticeable, as shown in Figure 6.18(a). However, the fitting still fails because the S-Curve transition is close to the end of the threshold scan range, leading to a fitting failure. To address this issue, another factor in the trimming process must be optimized.

When the S-Curve is out of range in the threshold scan, it results in a cutoff that prevents accurate fitting. This issue is illustrated in Figure 6.18(a) for the TrimDAC configuration with a value of 31 LSB, where the S-Curve transition occurs near the upper limit of the scan range. Similarly, Figure 6.18(b) shows the S-Curve cutoff for the TrimDAC configuration with a value of 0 LSB, where the transition occurs near the lower limit of the scan range. These out-of-range scenarios contribute to the fitting failure peaks observed in the orange and cyan distributions, respectively, in Figure 6.16(b).

To resolve these issues, alternative TrimDAC configurations must be selected to ensure the S-Curve is fully visible within the threshold scan range. As discussed in the previous section and shown in Figure 6.15, the linear relationship between the 32 TrimDAC values enables flexibility in achieving the same trimming step with different configurations. Therefore, instead of using TrimDAC values of 0 and TrimDAC 31 LSB, configurations with TrimDAC settings of 10 and 21 LSB are employed.

Using these alternative configurations, along with a pulse amplitude of 25 LSB and a trimming range of 31 LSB, the distributions of the S-Curve mean values are shown in Figure 6.19. No abnormal peaks are observed, and the distributions are well-separated, ensuring reliable trimming. The trimming target is determined as the average of the two distribution means as highlighted in a green vertical line. These optimized parameters have been implemented in the MaPSA testing procedure, as discussed in Section 6.4.

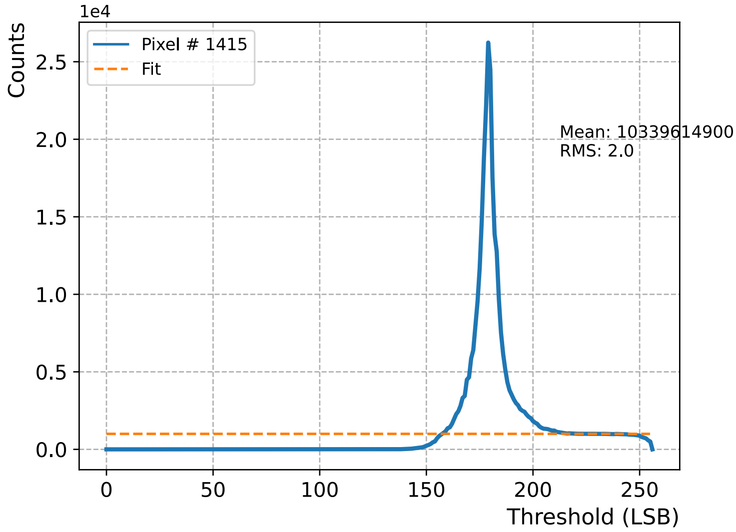

(a) The S-Curve of a noisy pixel with a trimming range of 31 LSB and a pulse amplitude of 25 LSB. The clearer plateau and transition region improve the fitting, but the S-Curve transition remains close to the end of the threshold scan range, leading to fitting failure.

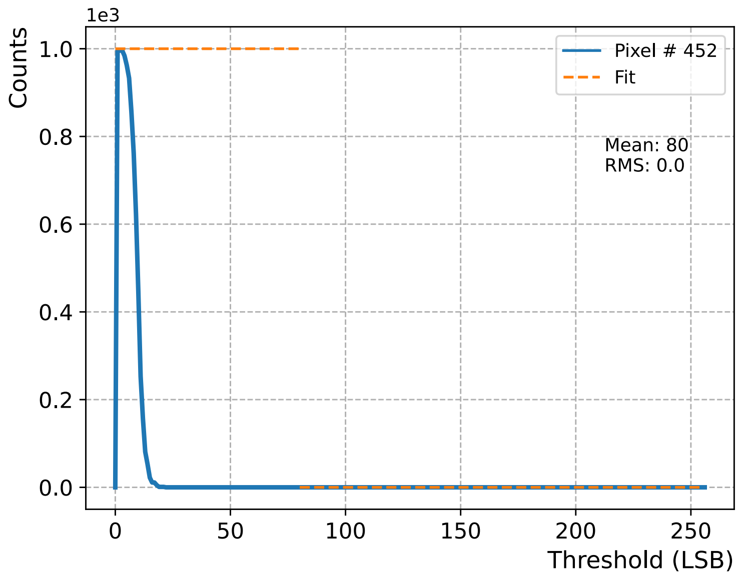

(b) An example of an S-Curve that appears out of range in the trimDAC configuration with a value of 0 LSB. The fitting failed, returning a value of $\mu = 80,$LSB, which corresponds to the fitting failure peak in the cyan distribution of Figure 6.16(b).

FIGURE 6.18: Issues in S-Curve fitting due to pulse amplitude and threshold scan range contribute to fitting failure peaks of (a) the orange distribution and (b) the cyan distribution in Figure 6.16(b).

6.3 MaPSA Probing System

The probe testing system for a MaPSA builds on the foundation of the wafer test system initially developed at CERN for MPA chips. Fermilab subsequently adapted this framework to create a dedicated testing system for MaPSA. Five testing sites across US and European institutes have implemented the system with local modifications to suit their specific setups and requirements.

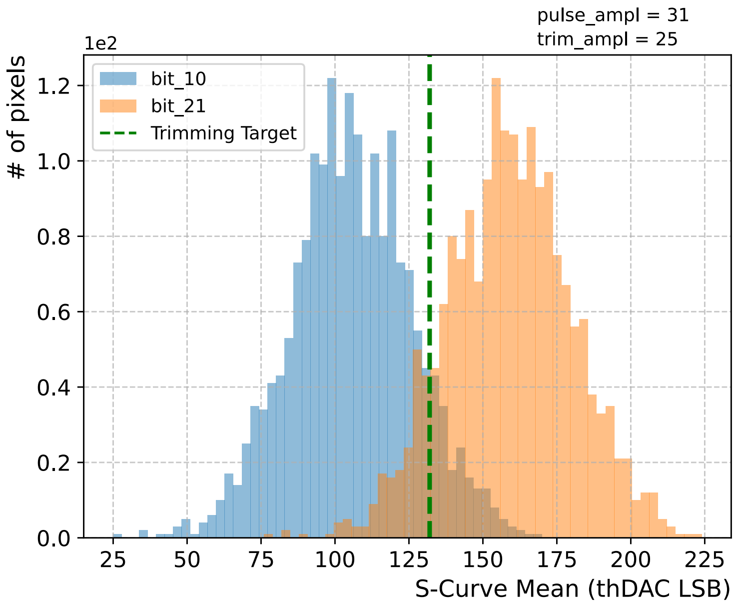

FIGURE 6.19: S-Curve distributions for trimDAC configurations 10 and 21 LSB with a pulse amplitude of 25 LSB and a trimming range of 31 LSB. These configurations ensure well-separated distributions and a reliable trimming process, and are implemented in the MaPSA test.

6.3.1 Probe Test Setup

The test setup at DESY is established in a cleanroom environment and includes a probe station equipped with a probe card, two computers, and an FPGA system. The FPGA system is responsible for controlling the testing software and the precise movement of the probe chuck. The probe card, which contains 119 probe needles, is mounted onto the station. Of these, 118 needles are dedicated to the readout channels of a single MPA chip, while an additional probe needle provides the high-voltage connection.

The MaPSA under test is securely held in place by vacuum onto the movable probe chuck. A microscope is installed to facilitate the visual inspection of the probe pads and ensure proper alignment of the needles with the pads. An overview of the MaPSA test setup is shown in Figure 6.20.

The detailed components of the setup are listed in Table 6.2. Two computers are responsible for commanding the probe station and the data acquisition system. One computer, equipped with VELOX software, manages the movement of the probe station chuck and microscope. It features semi-automated functions such as two-point alignment of the probe needles and pads, as well as probe contact positioning.

The other computer, running the testing software, communicates with an FPGA-based Advanced Mezzanine Card (AMC), called FC7. The FC7 board serves as the primary readout system for the prototyping phase of the CMS Outer Tracker. Attached to the FC7 is an L12 FPGA Mezzanine Card (FMC) that provides access to high-speed serial lines. This FMC is connected to an interface board using a 68-pin LVD SCSI cable. The interface board, developed at Rutgers University, is powered by a Low Voltage (LV) supply and performs data level shifting, communication handling, and voltage regulation for the MPA readout chips. Lastly, a probe card with 119 Tungsten-Rhenium needles is connected to the interface board at a tilted angle which is shown

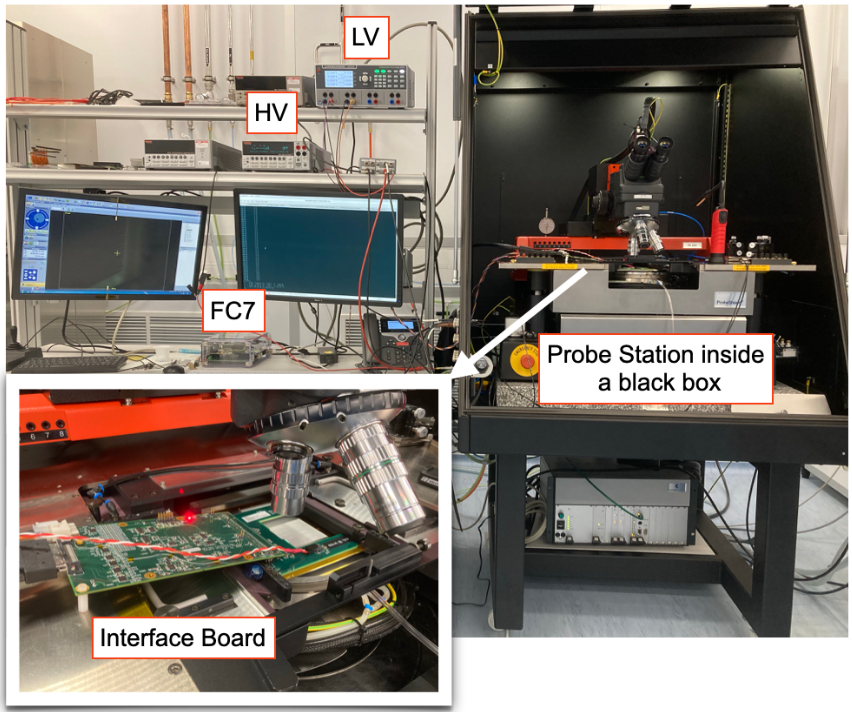

(a) DESY MaPSA probe test setup

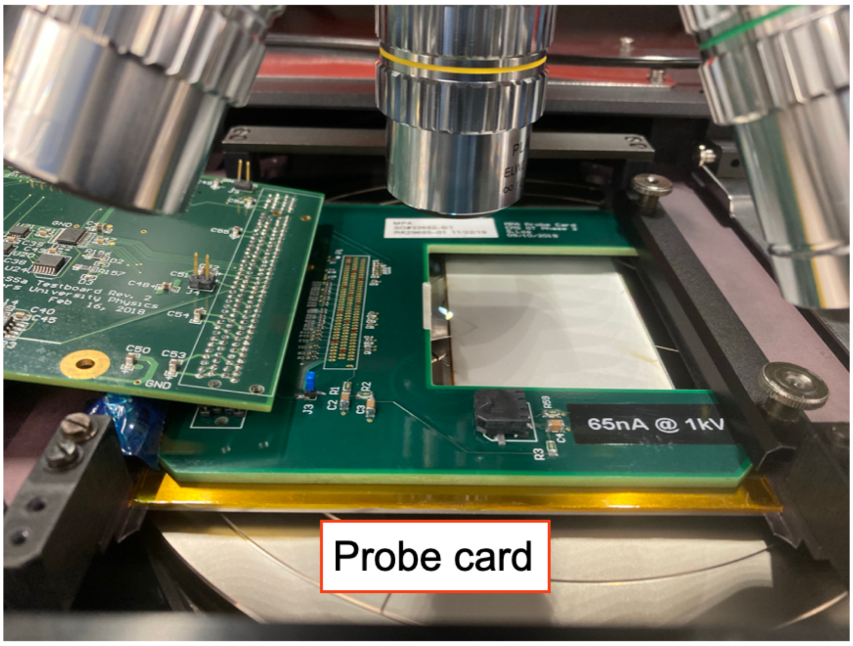

(b) Probe card in the station

FIGURE 6.20: DESY MaPSA probe test setup overview.

in Figure 6.20(b).

The tilted angle of the probe card initially posed a concern, specifically regarding the electrical connection stability due to the mechanical limitations of the probe station. To address this issue, a flexible cable card was designed and developed at DESY, as shown in Figure 6.21(a). This custom cable provided additional flexibility in the connection arrangement.

However, it was discovered that the flexible cable card was unable to effectively transmit commands and data through the high-speed data line, potentially due to its excessive length. Consequently, the idea of using the flexible cable card was abandoned. To overcome the height difference and ensure data transmission without relying on the additional placement freedom provided by the flexible card, an additional pin layer was introduced between the probe card and the interface board, as shown in Figure 6.21(b). This figure provides a side view of the connection, illustrating how the additional pin layer bridges the gap and ensures a stable electrical connection.

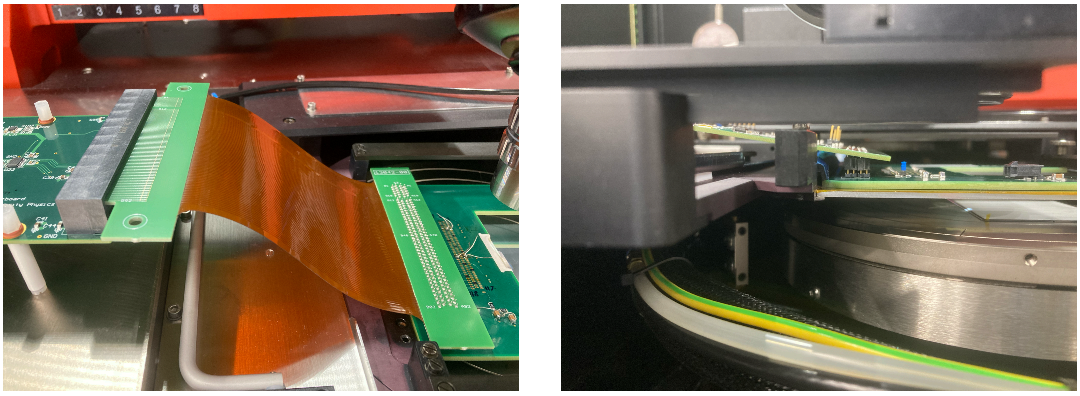

(a) Flexible cable card developed at DESY to address the tilted angle of the probe card and provide additional placement flexibility.

(b) Side view of the additional pin layer introduced between the interface board and the probe card to compensate for the height difference and ensure stable data transmission.

FIGURE 6.21: The connection between the interface board and the probe card, addressing the height difference between the two components in the probe station setup.

Additionally, an aluminum plate, covered with Kapton tape to avoid electrical conductivity, was placed in the probe card holder as shown in Figure 6.20(b). These measures were taken to compensate for the height difference and achieve reliable data transmission.

During the probe testing process, the MaPSA is securely held in place by a custom-designed chuck. The chuck incorporates several dedicated vacuum holes to firmly secure the MaPSA in position. A total of 118 probe needles from the probe card are carefully aligned over the MPA wire-bond pads. The custom-made chuck, attached to the probe station chuck, is then elevated to a contact height where the probing pads come into contact with the probe needles. To ensure good electrical contact, a slight over-driving contact of 100 µm to 125 µm, meaning pushing the chips further towards the needles, is necessary. Additionally, a bias voltage is supplied to the backplane of the PS-p sensor via a long needle on the probe card, which is connected to a HV Keithley 2410.

6.3.2 Testing Software

The testing software is a Python-based application designed for conducting comprehensive evaluations on MPA chips. Various test functions have been integrated into the software to facilitate thorough testing of the MaPSA. Its features encompass performing basic IV scans, detecting faulty bump bonds, detecting non-functional pixels, and identifying pixels that cannot achieve threshold equalization. Additionally, MPA-level tests are included, such as memory tests, which validate the Level-1 (L1)

TABLE 6.2: Summary of devices used in the MaPSA probe station setup and their respective purposes.

Devices	Type	Purpose
Linux PC	CentOS 7	PC with testing software. Sends commands to FC7 and reads back the data.
HV Supply	Keithley 2410	Provides High Voltage Source up to -1100 V.
LV Supply	R&S HMP 4040	Provides Low Voltage to the Interface board.
FC7	Xilinx Kintex-7 FPGA	To control and readout MPA.
L12	FMC	Provides access to all high-speed serial lines and SCSI connection for the interface board.
Interface Board	Version 3	Level shifting, communication, and voltage regulation of the MPA chip.
Probe Station	PA200 and Windows 10 PC	Includes a semi-automation moving chuck and a microscope. Allows probe pads auto alignment, controls the microscope and chuck movement.
Vacuum Chuck	7.5 mm thickness	Holds MaPSA with vacuum holes within the dimension of a single MaPSA. The chuck is also vacuum-hold to the probe station chuck.

memory by injecting charge into each pixel, sending a trigger, and reading back the stored contents, and register tests, which verify the functionality of the I^2C-configured registers by writing and reading specific values.

6.4 Probe Testing Results

6.4.1 I-V Measurements

During the HL-LHC run, the tracker will be operated at a temperature of $-20°$ C and will eventually operate at a bias voltage of -600 V. To guarantee higher voltage endurance and prevent sensor damage during testing, IV measurements are conducted to characterize the sensors before any additional electrical tests.

The current is measured at bias voltages ranging from 0 V to -800 V in 10 V intervals at room temperature. Each measurement is separated by a delay time of at least 0.5 s. For these tests, the high-voltage connection to the PS-p sensor backplane is made via a probe card needle, and the current is monitored using a Keithley 2410 Power Supply.

A good-quality MaPSA is required to have a leakage current below 10 µA at -600 V. The depletion voltage of the PS-p sensor, typically starting at around -180 V, can increase to as much as -350 V due to intrinsic variations in the material properties and doping profiles of the silicon.

In the results shown in Figure 6.22(a), the sensor exhibits sensitivity to humidity. High humidity causes positive surface charges to accumulate on the passivation layer of the silicon sensor, particularly near the edges and guard ring regions [88]. This accumulation alters the electric field distribution, creating localized high-field regions that lower the breakdown voltage and increase leakage current. By purging the MaPSA with dry air, the surface charge accumulation is reduced, restoring stable IV characteristics and enabling further electrical testing.

The IV measurements of four prototype MaPSAs are shown in Figure 6.22(b). Three of the four samples demonstrate good IV characteristics, with the current remaining consistently low and stable up to $-800\,\mathrm{V}$. While one sample exhibited a slightly higher leakage current at lower bias voltages, it remained within an acceptable range, ensuring no risk of sensor damage. Sensor damage typically occurs only when exposed to higher currents, exceeding those observed in these tests.

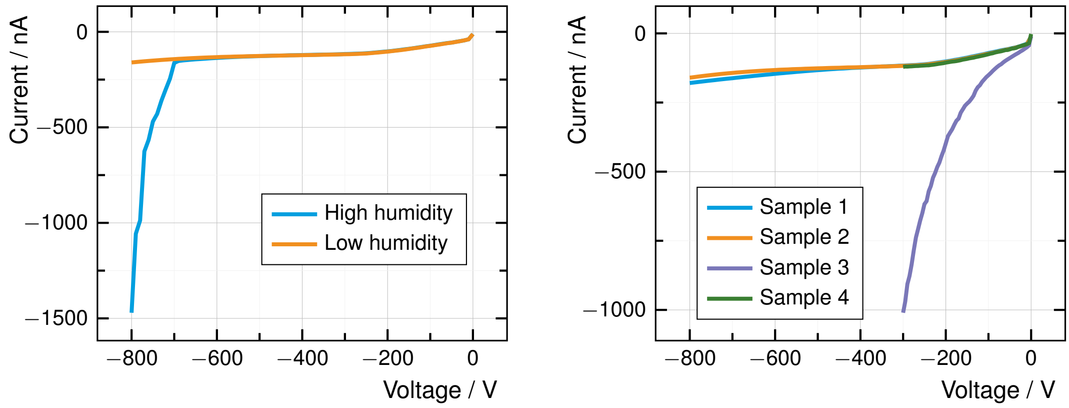

(a) An example of observing a breakdown phenomenon in Sample 2 when exposed to a high humidity environment.

(b) IV measurement of four prototype MaPSAs.

FIGURE 6.22: The result of IV measurements.

6.4.2 Single Pixel Qualification

To ensure the tracking detector achieves its maximum performance, certain tests are conducted for each MPA chip. Any dead, inefficient, or noisy pixels can produce unreliable or erroneous signals, which can negatively impact the quality of the data collected by the detector. Dead pixels, which fail to respond to injected test signals, are classified as faulty pixels. If a large area of dead pixels is observed in a single MPA chip, the chip will be graded as bad. Furthermore, every pixel must be maskable in the CMS detector; therefore, any MaPSA containing an MPA chip with an unmaskable pixel is also marked as bad. The following tests aim to verify that there are no dead areas in the sensor, that the readout chips can mask noisy pixels, and that the chips meet the operational criteria for detector integration.

- **Pixel Alive** test: To evaluate the efficiency of all pixels within a MaPSA, a test is conducted where 100 pulses with large amplitudes are injected into each pixel across the 16 chips. The counter records the number of counts for each pixel, enabling the identification of inefficient or dead pixels. To minimize the influence of noise, the test is performed with a relatively high threshold configured in the comparator. The results of the pixel alive test for the entire MaPSA are presented in Figure 6.23. The data reveals that all pixels consistently register 100 hit counts, indicating the absence of any dead or inefficient pixels across the 16 chips.

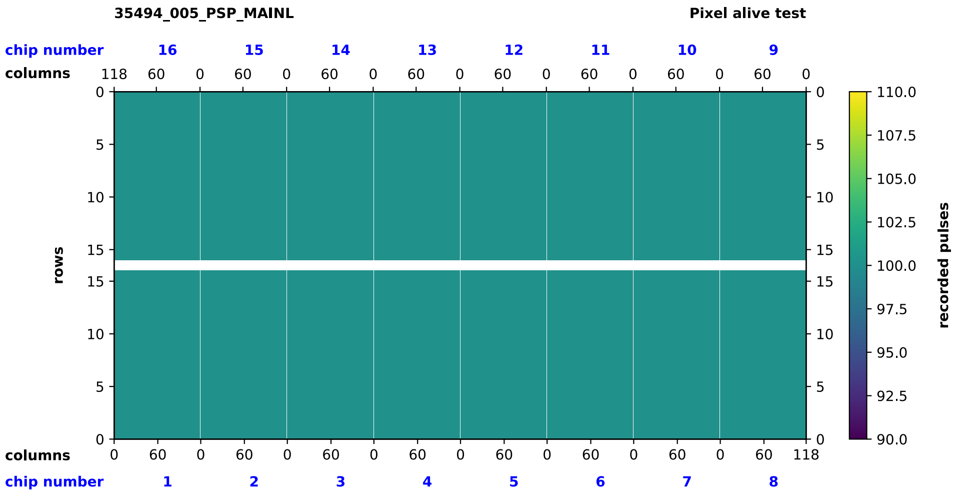

FIGURE 6.23: Pixel alive test results for a full MaPSA. The 2D plot represents the recorded pulse counts for all pixels across the 16 chips, arranged by their row and column positions. The chip numbers are labeled along the horizontal axis, with individual rows corresponding to the 118 pixels of each chip. All pixels exhibit consistent counts of 100, indicating no dead or inefficient pixels.

- **Pixel Masking** test: To assess the masking capability of all pixels across the MaPSA, a test pulse was applied to each pixel while its masking function was activated. This test verifies the ability of each pixel to disconnect from the pixel Back-End, ensuring noisy pixels can be suppressed as needed. When the masking function is active, the expected outcome is 0 counts for all pixels.

  The results of the Pixel Masking test for the entire MaPSA are shown in Figure 6.24. The color-coded 2D plot confirms that all pixels across the 16 chips exhibit 0 counts, demonstrating that no pixels are unmaskable, and the masking functionality operates as intended.

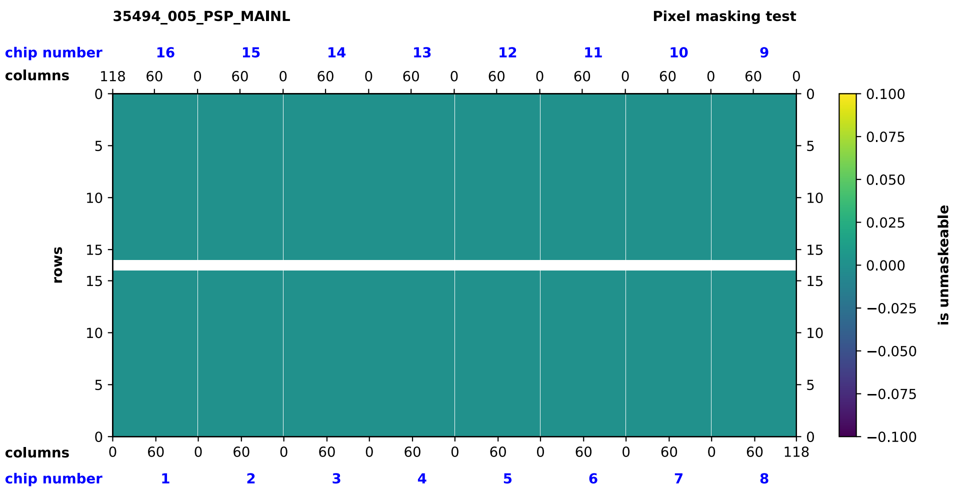

FIGURE 6.24: Pixel Masking test results for a full MaPSA. The 2D plot represents the recorded pulse counts for all pixels across 16 chips, arranged by their row and column positions. The chip numbers are labeled along the horizontal axis, with individual rows corresponding to the 118 pixels of each chip. The consistent color-coded value of 0 confirms that all pixels are maskable, validating the proper functionality of the masking feature.

6.4.3 Bad Bump Bonding Identification

Each pixel on an MPA chip is bump-bonded to the bonding pads of a pixel on the PS-p sensor through the C4 process as discussed in Section 6.1.3. This bonding technique ensures a dependable electrical connection between the pixels on the MPA chip and the bonding pads of the PS-p sensor. The bump bonds play a crucial role in facilitating the data readout processes. Thus, any bad bumps created through the manufacturing process or shipment should be identified.

The test to identify faulty bump bonds involves applying a low bias voltage of $-2\,\mathrm{V}$ to the sensor and injecting 1000 test pulses into each individual channel on the MPA chip. A low bias voltage is used because unconnected pixels exhibit lower noise levels due to the absence of capacitance from the sensor, making it easier to distinguish faulty bumps. For unconnected pixels, the pixel capacitance is 0, and the noise level remains low in comparison to properly connected pixels.

Pixel noise was assessed through a calibration pulse scan, as elaborated in Section 6.2.2. The noise level for each pixel on the MPA chip was extracted and analyzed. The resulting noise distribution of all pixels is shown in Figure 6.25(a). Pixels with noise levels below 3 calDAC LSB were classified as having faulty bumps, as these low noise values indicate a lack of electrical connection due to defective bump bonds. The testing software generates a file that provides a Boolean value for each pixel, indicating whether it has faulty bumps. It is visually represented in Figure 6.25(b), confirming the classification of faulty bumps.

6.4.4 Trimming Results

The trimming procedure was conducted according to the guidelines outlined in Section 6.2.3, where 1000 test pulses were injected into the MaPSA while applying a nominal bias voltage of -300 V to the PS-p sensor. The threshold scans using a pulse amplitude of 25 LSB of the CalDAC and a trimming range of 31 LSB of a 5-bit DAC were performed to determine the trimming target. The trimming target was derived from the mean of the fitted S-Curve of two trimDAC configurations: trimDAC values of 10 LSB and 21 LSB, which provided the necessary trimming steps.

During the operation of the detector, a global threshold is applied to all pixels within each MPA chip. It is important to note that the trimming target is determined on a per-chip basis, ensuring individual optimization for each chip. Pixels that cannot be trimmed to the desired target due to insufficient adjustment capabilities are classified as untrimmable pixels, which are then categorized as faulty pixels.

To provide a comprehensive overview of the testing results, the mean value of the fitted S-Curve is shown in Figure 6.26. The turn-on threshold of the MaPSA samples after the trimming procedure was found to average 135.36 ThDAC LSB with a standard deviation of 2.53 for Sample 1, and 133.51 ThDAC LSB with a standard deviation of 2.74 for Sample 2.

Notably, Sample 1 and Sample 2 exhibit slight variations in the trimming target across different chips. However, as long as the S-Curve mean value demonstrates uniformity among the pixels within the same chip, the trimmed pixels will exhibit consistent responses to identical pulses when subjected to the same global threshold.

The noise measurement was obtained by analyzing the σ of the fitted S-Curve, to identify noisy pixels exhibiting higher noise levels. The unit of the threshold value, expressed in terms of ThDAC, corresponds to 94 electrons for each MaPSA chip.

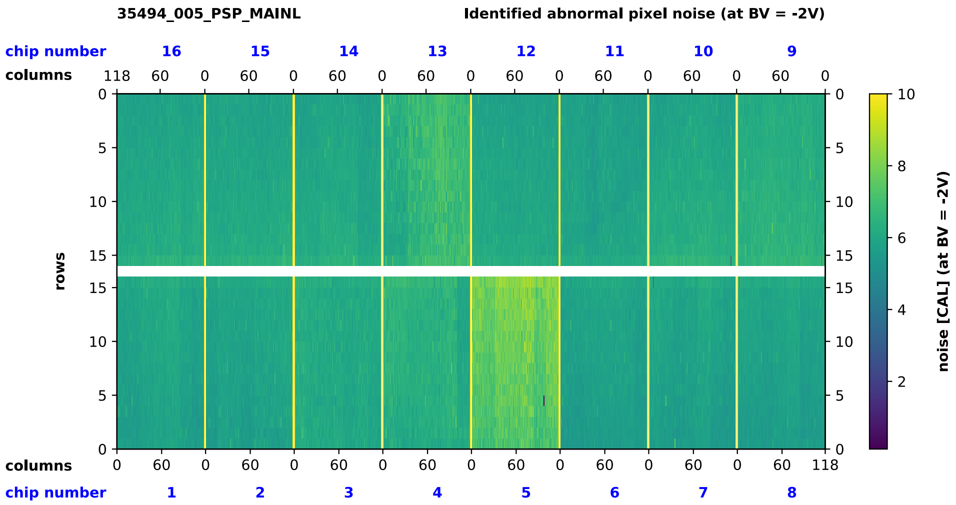

(a) Noise measurement results of all pixels on the MaPSA during the bump bonding test. The plot shows the noise levels across all 16 MPA chips, with pixels having noise levels below 3 CalDAC LSB classified as faulty bumps.

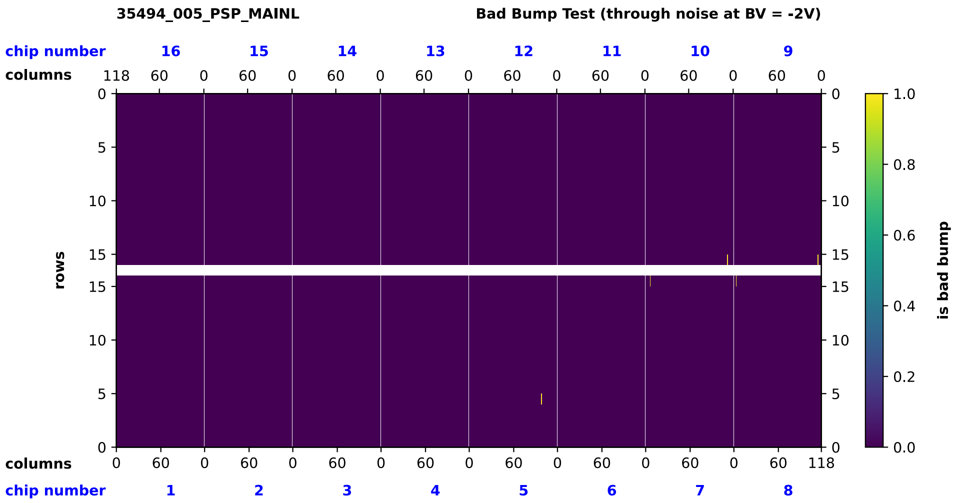

(b) Final results of the bump bonding test. The binary map indicates faulty bump identification across the entire MaPSA.

FIGURE 6.25: Overview of the bump bonding test results, showing noise levels and faulty bump identification across the MaPSA.

Therefore, the noise measurements presented in Figure 6.27 indicate comparable noise levels of 2.69 ThDAC LSB (253 e^-) for MaPSA Sample 1 and 2.72 ThDAC LSB (256 e^-) for MaPSA Sample 2. These values are within the expected range for MaPSA assemblies, which, according to the CMS Outer Tracker group specifications, is between 2 and 4 ThDAC [89]. Pixels exhibiting noise levels greater than 4 ThDAC are considered noisy pixels. Both MaPSA samples exhibit good noise levels.

Pixels at the edges of the MPA chip typically exhibit higher capacitance than the central pixels due to their wider size. This increased capacitance results in higher noise levels, as seen in the noise distribution shown in the figure. Even with the higher noise in the edge pixels, the trimming results demonstrate excellent performance. The edge pixels are successfully trimmed and show consistent behavior with the rest of the pixels during the trimming procedure.

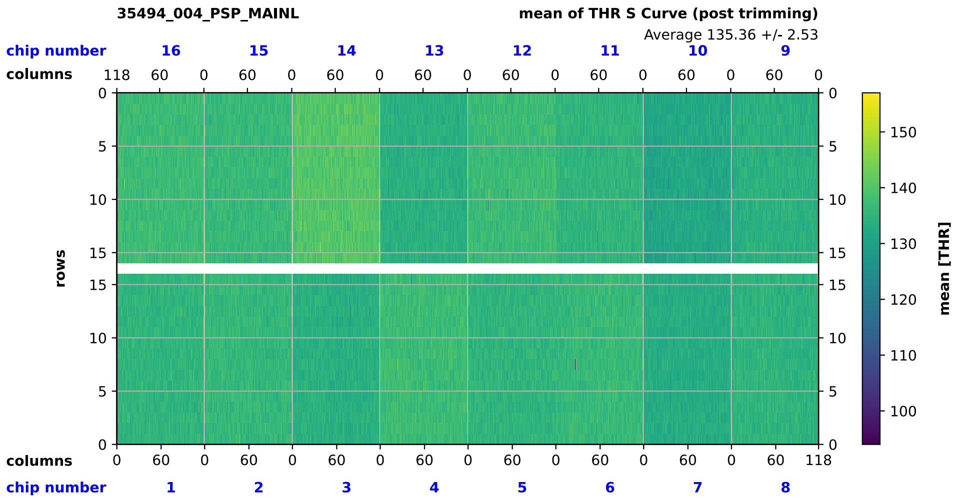

(a)

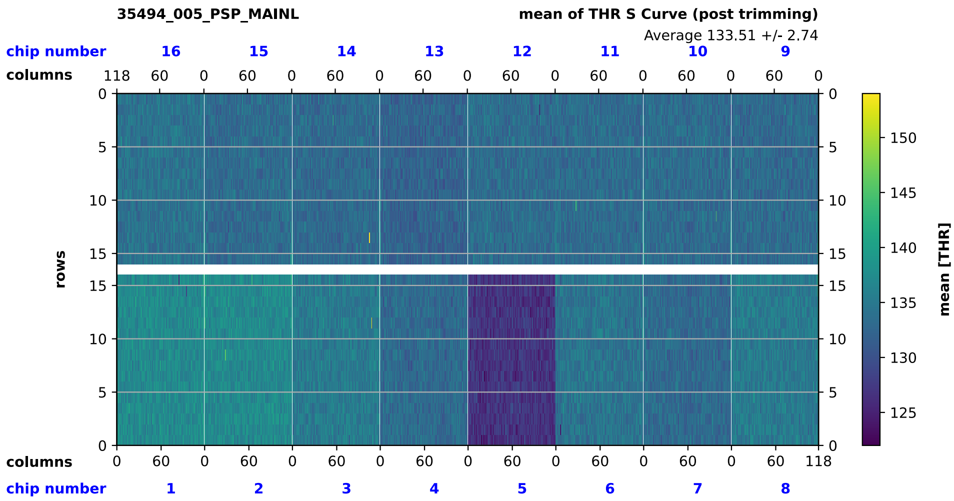

(b)

FIGURE 6.26: The mean value of the S-Curve of the 16 chips of MaPSA Sample 1 (a) and Sample 2 (b) after the trimming procedure was performed.

The demonstrated performance confirms that both MaPSA samples exhibit excellent electrical characterization with the expected noise levels. These results validate their suitability for integration into a PS module, paving the way for further studies and investigations.

6.5 Summary and Outlook

This chapter presented the testing process of the Macro Pixel Sub-Assembly (MaPSA) used in the CMS Phase-2 Upgrade, specifically focusing on the testing infrastructure, quality assurance, and the significant contributions from this work to optimize testing procedures.

The MaPSA, composed of the PS-p sensor and MPA chips, is a key component in the CMS Outer Tracker. Prior to the assembly of a tracking detector module, it is essential to ensure the quality and reliability of the components over their

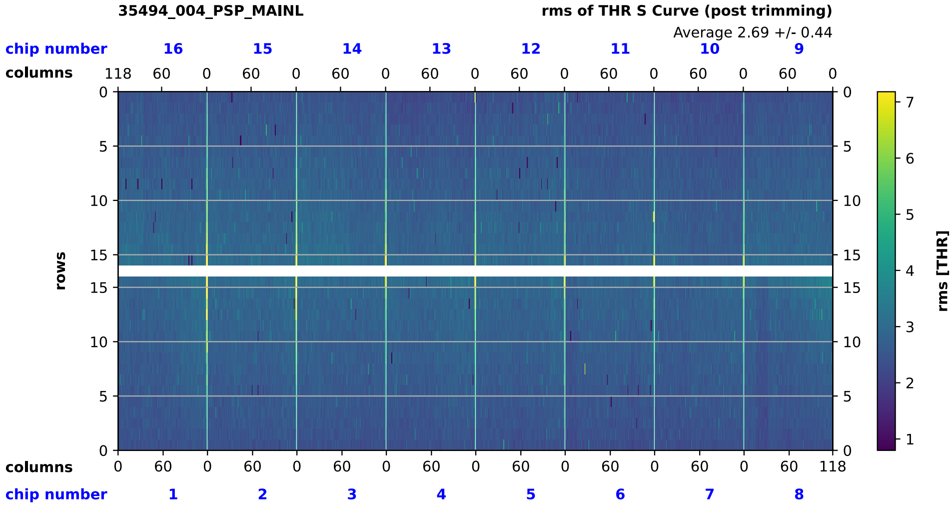

(a)

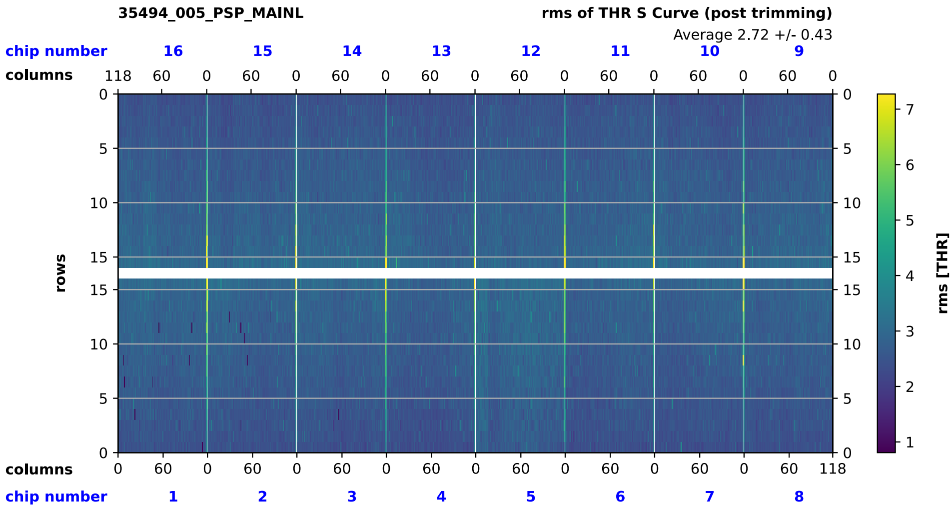

(b)

FIGURE 6.27: The noise measurement of the 16 chips of MaPSA Sample 1 (a) and Sample 2 (b).

operational lifetime. A comprehensive set of electrical testing procedures has been developed and refined specifically for MaPSA as part of the CMS Outer Tracker development. These procedures focus on verifying the MaPSA's robust performance and adherence to quality standards, including characterizing the current at high bias voltages, evaluating the electrical performance of individual pixels, assessing the threshold equalization capability of the MPAs, and identifying any faulty bump bonding. The optimization and refinement of these procedures have ensured reliable and consistent results. Moreover, the optimized threshold equalization procedure has been contributed to the testing development working group and is implemented for the production phase.

The presented results demonstrated that the MaPSA samples exhibited excellent electrical characteristics, with noise levels of 2.69 ThDAC LSB (253 e^-) for MaPSA Sample 1 and 2.72 ThDAC LSB (256 e^-) for MaPSA Sample 2, both within the expected range.

Regarding trimming performance, the turn-on threshold of the MaPSA samples after the trimming procedure gave an average of 135.36 ThDAC LSB with a standard deviation of 2.53 for Sample 1, and 133.51 ThDAC LSB with a standard deviation of 2.74 for Sample 2. The close alignment of these turn-on thresholds, with minimal variation within each MPA chip, confirms that the trimming process successfully aligned the pixel responses.

Following the trimming procedure, the quality assurance tests confirmed that the MaPSA samples meet critical performance thresholds: the leakage current was below 10 µA at −600 V, no dead pixels or unmaskable pixels were found, and only a few degraded bump bonds, no more than five, were observed. Furthermore, no untrimmable pixels were identified during the trimming process. These results confirm that the MaPSA samples are well-suited for integration into the CMS Phase-2 Outer Tracker, with all key parameters meeting the performance standards necessary for the detector's operation.

The optimization of the trimming process has been a key focus of this study. In particular, the careful selection of trimming targets and pulse amplitudes was critical for achieving consistent and accurate alignment of the S-Curves baseline across the pixels. This work has ensured that the trimming procedure is now well-optimized, providing a solid foundation for ongoing and future testing during the production phase.

The test stand has been successfully developed and adapted at DESY, and prototype MaPSAs have been tested. It is now ready to be seamlessly integrated into the quality assurance workflow for the assembly of the 1,250 PS modules at DESY for the CMS Phase-2 production.

Chapter 7

Summary and Conclusion

The Large Hadron Collider (LHC), located at CERN, is the most powerful particle accelerator in the world, designed to explore fundamental physics by accelerating particle beams in opposite directions and colliding them at unprecedented energy levels. Currently, it achieves a center-of-mass energy of 13.6 TeV in proton-proton collisions, allowing for measurements of particles and forces in the Standard Model. In 2026, the LHC is scheduled to undergo a significant upgrade, transitioning to a High-Luminosity LHC (HL-LHC) operation by 2030. This enhancement aims to increase the nominal luminosity to $5 \times 10^{34}\,\mathrm{cm}^{-2}\,\mathrm{s}^{-1}$, with potential peak luminosities reaching up to $7.5 \times 10^{34}\,\mathrm{cm}^{-2}\,\mathrm{s}^{-1}$ under optimal conditions. This upgrade will expose detectors to significantly higher radiation doses and pile-up, posing new challenges for the detectors, such as managing increased data throughput and maintaining accurate tracking and event selection under more extreme conditions.

The Compact Muon Solenoid (CMS) detector is one of the four major apparatus located at CERN. In preparation for the High-Luminosity LHC (HL-LHC) operation, the CMS detector will undergo a Phase-2 upgrade, which includes the replacement of the entire silicon tracker. The new tracker will provide enhanced radiation tolerance and higher granularity, meeting the challenges posed by the HL-LHC environment. As part of this upgrade, the Outer Tracker introduces a new module concept, the p_T module. This module consists of two closely separated silicon sensors, and by comparing the detection positions of charged particles on both sensors, the transverse momentum (p_T) of the particle can be calculated. Particles with high p_T exhibit smaller curvatures in the CMS magnetic field, and by defining a correlation window in the sensor, based on the incident position of the other sensor, particles with high, will pass within the window and be marked as a *stub*. The stub information is then used in the Level-1 Trigger decision to significantly reduce the data rate to manageable levels for the detector's capability. Two types of modules have been designed, with varying module spacing and correlation window sizes, to achieve the same p_T discrimination threshold throughout the Outer Tracker volume. These two modules are the 2S strip-strip sensor module, which consists of two strip sensors, and the PS module, which combines a macro-pixel sensor with a strip sensor. The PS module, positioned closer to the particle interaction point, provides higher granularity, making it suitable for the inner regions of the Outer Tracker.

In the workflow of the CMS Phase-2 Tracker Upgrade, after the design stage, prototype modules were built to validate the p_T module concept and refine the assembly process. A 2S module was constructed at DESY, where the module assembly procedures were established, optimized, and verified during the prototyping process. The module underwent comprehensive electrical testing and beam testing at the DESY II test beam facility, demonstrating a particle detection efficiency exceeding 99.9 % and a stub detection efficiency above 99.7 %. During the beam tests, the prototype modules were rotated to study the stub turn-on threshold behavior. The results aligned with theoretical expectations, confirming the module's design principles. Specifically, modules with larger spacing exhibited a smaller turn-on threshold angle, consistent with their geometry. These tests demonstrated the good sensor performance and effective p_T discrimination capability of the module. Additionally, contributions to the CMS collaboration included the development of dedicated test beam analysis software tailored for the CMS module concept and testbeam operation condition. This software, incorporating specialized functions for the p_T modules, has been adopted by the collaboration for similar analyses.

As the CMS collaboration progresses to the production phase, all components to be assembled into modules must undergo a rigorous quality assessment to ensure reliable performance. DESY is responsible for producing 1,250 PS modules during this phase. A critical component of the PS module is the Macro Pixel Sub-Assembly (MaPSA), which consists of a macro-pixel sensor bump-bonded to 16 dedicated readout chips. To prevent defective components from degrading the detector's performance, each MaPSA undergoes thorough inspections and is graded based on quality before being assembled into a module. The electrical grading includes current measurements, single-pixel qualification, bump bonding verification, noise measurement, and pixel threshold equalization.

A test stand has been established on a probe station in a cleanroom environment at DESY, and several MaPSAs have already been tested with this setup. Threshold equalization (Trimming), a crucial step in ensuring uniform response across all pixels to a fixed threshold, involves adjusting the comparator offset of individual pixels to compensate for variations caused by manufacturing processes. An optimized threshold equalization procedure was developed to prevent the misidentification of untrimmable pixels and to achieve precise alignment of signal pulse baselines at the comparator stage. The tested MaPSAs demonstrated excellent quality, and the established quality control and testing procedures have been fine-tuned for stability and consistency. The test stand is now fully prepared for the production phase, supporting the reliable assembly of PS modules.

The CMS Phase-2 Outer Tracker Upgrade is a cornerstone of the preparation for the High-Luminosity LHC era, addressing the unprecedented challenges of radiation, pile-up, and data throughput. The efforts detailed in this thesis, from validating the p_T module concept with 2S prototypes to establishing a robust quality assurance workflow for MaPSA testing, represent significant contributions to this endeavor. The successful development and optimization of module assembly, testing procedures, and analysis software have ensured that both the 2S and PS modules meet the stringent performance standards required for the upgraded tracker. With a comprehensive understanding of module performance and the readiness of testing infrastructure, the CMS collaboration is well-prepared to deliver an Outer Tracker capable of supporting the ambitious physics program of the LHC in its high-luminosity phase.

Appendix A

Supplemental Materials

A.1 DESY 2S Testbeam Setup

The 2S module testbeam setup during the angular scan is illustrated in Figure A.1, where the z-position of each detector is specified. The MIMOSA telescope consists of six planes, with the first three and last three planes widely separated to allow the Device Under Test (DUT) to be rotated. This rotation is essential to assess the p_T-discrimination capability of the 2S module.

A manual measurement of the z-position is required during beam tests, as it directly affects track alignment and reconstruction. Furthermore, it is utilized in the GBL (General Broken Lines) Track Resolution Calculator to estimate the telescope's pointing resolution.

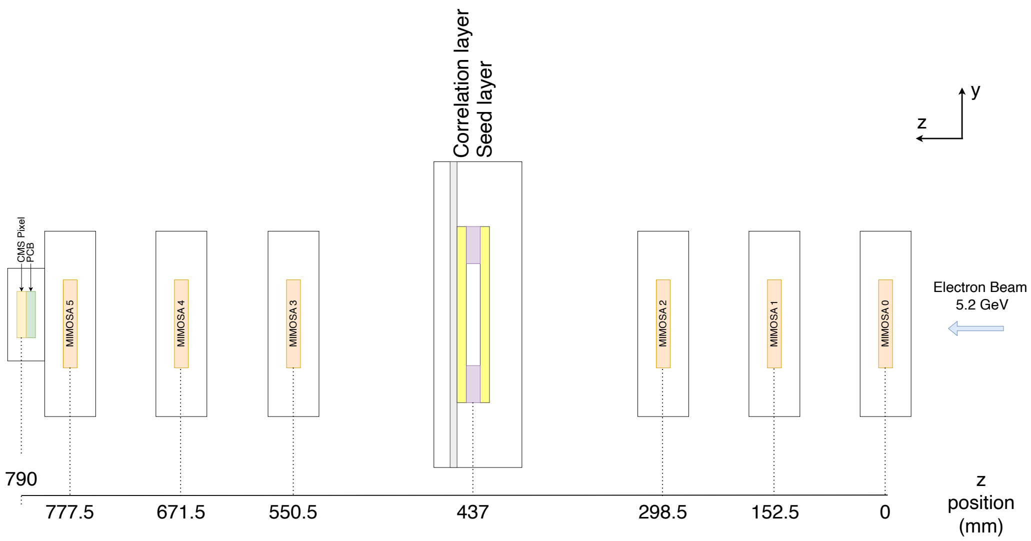

FIGURE A.1: The z position of the detectors in the testbeam setup during the angular scan.

During the bias scan and threshold scan, the distances between the telescope and the DUT are reduced, with the detectors positioned at $z_{\mathrm{DUT}} = 345\,\mathrm{mm}$ and $z_{\mathrm{MIMOSA\ 3}} = 383\,\mathrm{mm}$. The spacing between MIMOSA planes 3, 4, and 5 remains unchanged.

A.2 Coordinate Transformation Source Code

The source code of coordinate transformation for the detector with larger pixels implementation in C++.

```cpp
#include "BigPixelDetector.hpp"
#include "core/utils/log.h"
#include "exceptions.h"

using namespace ROOT::Math;
using namespace corryvreckan;

BigPixelDetector::BigPixelDetector(const Configuration& config) : PixelDetector(config) {

    // Auxiliary devices don't have: number_of_pixels, pixel_pitch, spatial_resolution, mask_file, region-of-interest
    if(!isAuxiliary()) {
        config_bigpixel(config);
        build_axes(config);
    }
}

void BigPixelDetector::config_bigpixel(const Configuration& config) {

    m_big_pixel = config.getMatrix<int>("big_pixel");
    big_pixel_x.assign(m_big_pixel.at(0).begin(), m_big_pixel.at(0).end());
    big_pixel_y.assign(m_big_pixel.at(1).begin(), m_big_pixel.at(1).end());

    m_big_pixel_spatial_resolution = config.get<ROOT::Math::XYVector>("big_pixel_spatial_resolution", 2.*m_spatial_resolution);

    LOG(INFO) << "Numbers of Big Pixels in X : " << big_pixel_x.size();
    LOG(INFO) << "Numbers of Big Pixels in Y : " << big_pixel_y.size();

    // sort big_pixel
    sort(big_pixel_x.begin(), big_pixel_x.end());
    sort(big_pixel_y.begin(), big_pixel_y.end());

    // transformed big pixel : treating big pixel as 2 regular pixels
    for(unsigned int i = 0; i < big_pixel_x.size(); i++) {
        transformed_big_pixel_x.push_back(big_pixel_x[i] + i);
        transformed_big_pixel_x.push_back(big_pixel_x[i] + i + 1);
    }
    for(unsigned int i = 0; i < big_pixel_y.size(); i++) {
        transformed_big_pixel_y.push_back(big_pixel_y[i] + i);
        transformed_big_pixel_y.push_back(big_pixel_y[i] + i + 1);
    }
    LOG(DEBUG) << "Numbers of transformed Big Pixels in X : " << transformed_big_pixel_x.size();
    LOG(DEBUG) << "Numbers of transformed Big Pixels in Y : " << transformed_big_pixel_y.size();

    for(auto i = transformed_big_pixel_x.begin(); i != transformed_big_pixel_x.end(); ++i) {
        LOG(DEBUG) << "Transform big pixel vector in X : " << *i;
    }

    for(auto i = transformed_big_pixel_y.begin(); i != transformed_big_pixel_y.end(); ++i) {
        LOG(DEBUG) << "Transform big pixel vector in Y : " << *i;
    }
}

// Functions to get row and column from local position// FIXME: Replace with new coordinate transformation
double BigPixelDetector::getRow(const PositionVector3D<Cartesian3D<double>> localPosition) const {

    int n_big_y_left = 0;
    bool is_big_y_pixel = 0;
    double row = 0;

    double tempPosition = ((localPosition.Y() + getSize().Y() / 2.) / m_pitch.Y()) - 0.5;

    for(unsigned int i = 0; i < transformed_big_pixel_y.size(); i++) {
        if(transformed_big_pixel_y[i] <= tempPosition) {
            n_big_y_left += 1;
            if(fabs(tempPosition - static_cast<double>(transformed_big_pixel_y[i])) < 0.5) {
                is_big_y_pixel = true;
            }
        } else {
            if(fabs(tempPosition - static_cast<double>(transformed_big_pixel_y[i])) < 0.5) {
                is_big_y_pixel = true;
            }
            break;
        }
    }

    if(is_big_y_pixel == true) {
        for(unsigned int i = 0; i < transformed_big_pixel_y.size(); i = i + 2) {
            if(fabs(tempPosition - transformed_big_pixel_y[i]) <= 2) {
                row = (tempPosition - transformed_big_pixel_y[i]) / 2. + big_pixel_y[i / 2] - 0.25;
            }
        }
    } else {
        row = tempPosition - n_big_y_left / 2.;
    }

    return row;
}

```

```
double BigPixelDetector::getColumn(const PositionVector3D<Cartesian3D<double>> localPosition) const {

    int n_big_x_left = 0;
    bool is_big_x_pixel = 0;
    double column = 0;

    double tempPosition = ((localPosition.X() + getSize().X() / 2.) / m_pitch.X()) - 0.5;

    for(unsigned int i = 0; i < transformed_big_pixel_x.size(); i++) {
        if(transformed_big_pixel_x[i] <= tempPosition) {
            n_big_x_left += 1;
            if(fabs(tempPosition - static_cast<double>(transformed_big_pixel_x[i])) < 0.5) {
                is_big_x_pixel = true;
            }
        } else {
            if(fabs(tempPosition - static_cast<double>(transformed_big_pixel_x[i])) < 0.5) {
                is_big_x_pixel = true;
            }
            break;
        }
    }

    if(is_big_x_pixel == true) {
        for(unsigned int i = 0; i < transformed_big_pixel_x.size(); i = i + 2) {
            if(abs(tempPosition - transformed_big_pixel_x[i] - 0.5) <= 2) {
                column = (tempPosition - transformed_big_pixel_x[i]) / 2. + big_pixel_x[i / 2] - 0.25;
            }
        }
    } else {
        column = tempPosition - n_big_x_left / 2.;
    }

    return column;
}

// Function to get local position from row and column
PositionVector3D<Cartesian3D<double>> BigPixelDetector::getLocalPosition(double column, double row)
     const {

    int n_big_x_left = 0;
    bool is_big_x_pixel = 0;
    int n_big_y_left = 0;
    bool is_big_y_pixel = 0;
    double col_integer, row_integer;

    for(unsigned int i = 0; i < big_pixel_x.size(); i++) {
        if(big_pixel_x[i] <= column - 0.5) {
            n_big_x_left += 1;
            if(fabs(column - big_pixel_x[i]) < 0.5) {
                is_big_x_pixel = true;
            }
        } else {
            if(fabs(column - big_pixel_x[i]) < 0.5) {
                is_big_x_pixel = true;
            }
            break;
        }
    }

    for(unsigned int i = 0; i < big_pixel_y.size(); i++) {
        if(big_pixel_y[i] <= row - 0.5) {
            n_big_y_left += 1;
            if(fabs(row - big_pixel_y[i]) < 0.5) {
                is_big_y_pixel = true;
            }
        } else {
            if(fabs(row - big_pixel_y[i]) < 0.5) {
                is_big_y_pixel = true;
            }
            break;
        }
    }

    return PositionVector3D<Cartesian3D<double>>(
        m_pitch.X() * (column + 0.5 + n_big_x_left + (is_big_x_pixel ? std::modf((column + 0.5), &
             col_integer) : 0)) -
            getSize().X() / 2.,
        m_pitch.Y() * (row + 0.5 + n_big_y_left + (is_big_y_pixel ? std::modf((row + 0.5), &row_integer
             ) : 0)) -
            getSize().Y() / 2.,
        0.);
}

XYVector BigPixelDetector::getSize() const {
    return XYVector(m_pitch.X() * (m_nPixels.X() + static_cast<double>(big_pixel_x.size())),
                    m_pitch.Y() * (m_nPixels.Y() + static_cast<double>(big_pixel_y.size())));
}

XYVector BigPixelDetector::getSpatialResolution(double column = 0, double row = 0) const {
    bool is_big_x_pixel = 0;
    bool is_big_y_pixel = 0;

    for(unsigned int i = 0; i < big_pixel_x.size(); i++) {
        if(fabs(column - big_pixel_x[i]) < 0.5) {
            is_big_x_pixel = true;
            break;
        }
    }
```

```cpp

    for(unsigned int i = 0; i < big_pixel_y.size(); i++) {
        if(fabs(row - big_pixel_y[i]) < 0.5) {
            is_big_y_pixel = true;
            break;
        }
    }

    double resolution_x = is_big_x_pixel ? m_big_pixel_spatial_resolution.x() : m_spatial_resolution.x();
    double resolution_y = is_big_y_pixel ? m_big_pixel_spatial_resolution.y() : m_spatial_resolution.y();
    return XYVector(resolution_x, resolution_y);
}

TMatrixD BigPixelDetector::getSpatialResolutionMatrixGlobal(double column = 0, double row = 0) const {
    TMatrixD errorMatrix(3, 3);
    TMatrixD locToGlob(3, 3), globToLoc(3, 3);
    auto spatial_resolution = getSpatialResolution(column, row);
    errorMatrix(0, 0) = spatial_resolution.x() * spatial_resolution.x();
    errorMatrix(1, 1) = spatial_resolution.y() * spatial_resolution.y();
    alignment_->local2global().Rotation().GetRotationMatrix(locToGlob);
    alignment_->global2local().Rotation().GetRotationMatrix(globToLoc);
    return (locToGlob * errorMatrix * globToLoc);
}

Configuration BigPixelDetector::getConfiguration() const {
    auto config = PixelDetector::getConfiguration();

    config.setMatrix("big_pixel", m_big_pixel);
    config.set<XYVector>("big_pixel_spatial_resolution", m_big_pixel_spatial_resolution);

    return config;
}
```

Listing A.1: BigPixelDetector Implementation in C++

A.3 Residual Analysis Methods for Resolution Extraction

In the context of a residual distribution, three common approaches to extract the resolution are the root mean square (RMS) method, quantile-based methods, and fitting-based methods. Each provides a different perspective on the distribution's shape and varies in its sensitivity to outliers or tails.

The **RMS method** computes the standard deviation of the entire residual distribution, capturing both the central spread and the contribution from the tails:

$$\mathrm{RMS} = \sqrt{\frac{1}{N}\sum_{i=1}^{N}(x_i - \overline{x})^2},$$

where x_i are the residuals, $\overline{x}$ is the mean of those residuals, and N is the total number of entries. The RMS offers a quick and comprehensive measure of the overall spread but is sensitive to outliers and heavy tails, which can inflate the resolution value.

The **quantile-based methods** estimate the resolution by restricting the calculation of the standard deviation to a central fraction of the distribution, such as 98%, 99%, or 99.5%. By excluding outliers in the tails, these methods produce a robust measure of the spread in the core of the distribution. For a quantile range $[q_1, q_2]$, the standard deviation is computed only within these bounds:

$$\sigma_{\text{quantile}} = \sqrt{\frac{1}{N_{\text{quantile}}}\sum_{x_i \in [q_1, q_2]}\left(x_i - \overline{x}_{\text{quantile}}\right)^2},$$

where N_{quantile} is the number of entries in $[q_1, q_2]$. Although this approach mitigates the effects of outliers, the chosen quantile range can introduce subjectivity and complicate comparisons across datasets.

Fitting-based methods employ a functional form, such as a Gaussian or the generalized error function, to model the entire residual distribution, including its peak and tails. The generalized error function can be written as:

$$f(x,\mu,\sigma,\beta,A,C) = A \cdot \frac{\beta}{\sqrt{8}\sigma\Gamma(\frac{1}{\beta})} \exp\left(-\left|\frac{x-\mu}{\sqrt{2}\sigma}\right|^{\beta}\right) + C,$$

where μ represents the mean, σ indicates the spread of the distribution, β is the shape parameter, A denotes the amplitude, and C is the constant offset. The parameter σ, extracted from the fit, is the resolution. While this approach effectively models the box distribution, it fails to account for the two-strip cluster events, which produce a peak around $x = 0$.

Figure A.2 shows the residual distributions of the 2S module at rotation angles of $-1°$ and $30°$, fitted with both Gaussian functions and generalized error functions. The standard deviation of each distribution is indicated in the plot as Std Dev. Figure A.2(e) compares the resolution extraction methods described above.

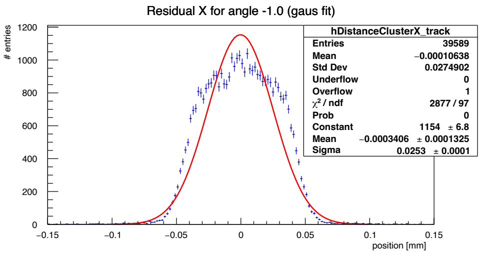

(a)

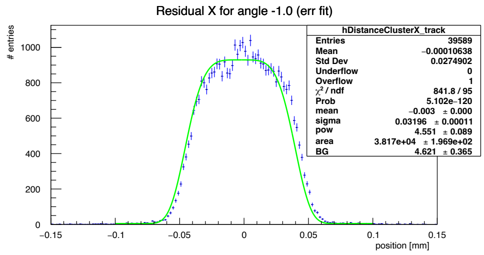

(b)

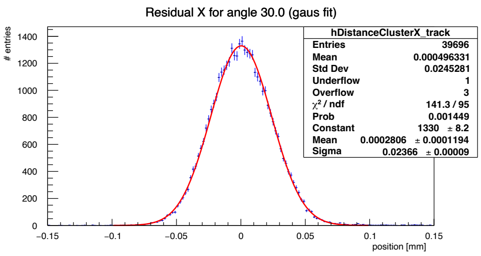

(c)

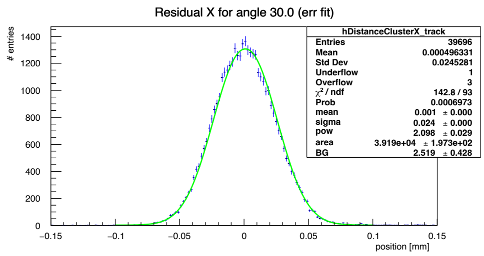

(d)

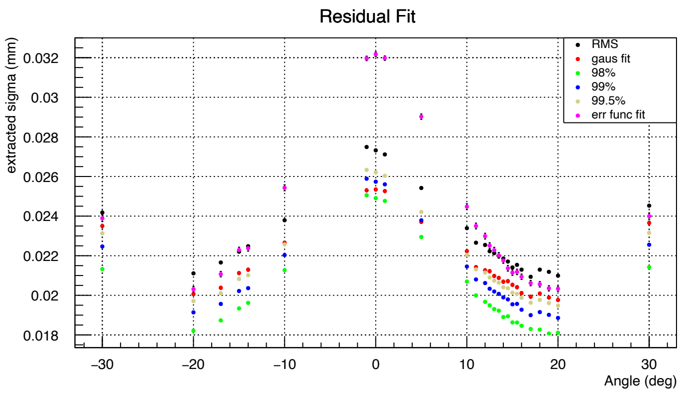

(e)

Figure A.2: Residual distributions at (a) $-1°$ particle incident fitted with Gaussian function and (b) $-1°$ particle incident fitted with Generalized Error function. (c) $30°$ particle incident fitted with Gaussian function and (d) $30°$ particle incident fitted with Generalized Error function. (e) The extracted measured resolution with various methods: root mean square (RMS), quantile-based, and fitting-based approaches, including Gaussian and Generalized Error functions.

List of Figures

List of Tables

List of Acronyms and Abbreviations

2S Strip-Strip. 45, 50, 52, 53, 64–66, 70–75, 109

AlCF Carbon Fiber reinforced Aluminium. 46, 47, 51, 66, 97

Al-N Aluminum Nitride. 51

AMC Advanced Mezzanine Card. 121

ASIC Application Specific Integrated Circuits. 45–47

BX bunch crossing. 41

C4 Controlled Collapse Chip Connection. 106, 107

CalDAC 8-bit Calibration DAC. 110, 112, 119, 127

CBC CMS Binary Chip. 47–49, 52, 54, 71, 88

CIC Concentrator Integrated Circuit. 46, 48–50, 52, 53, 66

CMS Compact Muon Solenoid. 8–11, 13–16, 19–21, 35, 36, 39, 43, 44

DAC Digital-to-Analog Converter. 71, 110

DTC Data Trigger and Control. 44

DUT Device Under Test. 73, 75–77

ECAL Electromagnetic Calorimeter. 9, 11–13, 16

ENC Equivalent Noise Charge. 40

FEH Front-End Hybrid. 45–48, 52, 66, 68, 108

FF D Flip-flop. 106

FMC FPGA Mezzanine Card. 121, 124

FPGA Field Programmable Gate Arrays. 16

GBT Giga-Bit Transceiver. 66

HCAL Hadron Calorimeter. 9, 11–13, 16

HIP High Ionizing Particles. 52

HL-LHC High Luminosity Large Hadron Collider. 18–21, 35, 41, 42, 124

HLT High-Level Trigger. 16

HV High Voltage. 68, 123

I^{2}C Inter-Integrated Circuit. 48, 50

IT Inner Tracker. 42

L1 Level-1. 16, 42–44, 50, 53, 102, 103, 123

LHC Large Hadron Collider. 5–9, 15, 17–19

LpGBT Low Power Gigabit Transceiver. 50, 53

LSB Least Significant Bit. 110

LV Low Voltage. 121

MaPSA Macro Pixel Sub-Assembly. 50, 51, 106–110, 116, 118–121, 123–129

MIP Minimum Ionizing Particles. 28, 52, 72

MPA Macro-Pixel ASIC. 50–54, 102, 103, 105–110, 112, 113, 115, 117, 118, 120, 121, 123–125, 127, 128, 143

MPV most probable value. 27

OT Outer Tracker. 42

POH Power Hybrid. 46

PS Pixel-Strip. 45, 50–52, 63, 64, 70, 71, 101, 109, 129

PS-p Macro Pixel Sensor. 50, 102, 106–108, 110, 123, 124, 127

PS-s Strip Sensor. 50, 109

QC Quality Control. 109

ROC Readout Chip. 75

ROH Readout Hybrid. 46

SCR space charge region. 32–34

SEH Service Hybrid. 46, 50, 66, 68, 70

SLVS scalable low-voltage signaling. 48–50, 53

SSA Short Strip ASIC. 52, 53, 102

SUSY Supersymmetry. 5, 8

ThDAC 8-bit Threshold DAC. 105, 110, 113, 115, 116, 118, 127, 128

TLU Trigger Logic Unit. 73, 76, 77, 79

TrimDAC 5-bit Trimming DAC. 105, 113, 115–119

UBM Under Bump Metallization. 106, 107

VTRx+ Versatile Transceiver Plus. 50, 51

Bibliography

[1] L. Hoddeson, L. Brown, M. Riordan, and M. Dresden, *The Rise of the Standard Model: A History of Particle Physics from 1964 to 1979*. Cambridge University Press, 1997, ISBN: 9780511471094.

[2] L. Di Lella and C. Rubbia, "The Discovery of the W and Z Particles," *Adv. Ser. Dir. High Energy Phys.*, vol. 23, pp. 137–163, 2015. DOI: 10.1142/9789814644150_0006.

[3] H. D. Politzer, "Reliable Perturbative Results for Strong Interactions?" *Phys. Rev. Lett.*, vol. 30, pp. 1346–1349, 26 Jun. 1973. DOI: 10.1103/PhysRevLett.30.1346.

[4] S. Bethke, "Experimental Tests of Asymptotic Freedom," *Progress in Particle and Nuclear Physics*, vol. 58, no. 2, pp. 351–386, Apr. 2007, ISSN: 0146-6410. DOI: 10.1016/j.ppnp.2006.06.001.

[5] The CMS Collaboration, "Observation of a New Boson at a Mass of 125 GeV with the CMS Experiment at the LHC," *Physics Letters B*, vol. 716, no. 1, 2012, ISSN: 0370-2693. DOI: 10.1016/j.physletb.2012.08.021.

[6] C. Burgard and D. Galbraith, *The Standard Model of Physics*, https://texample.net/tikz/examples/model-physics/, Accessed: 05.01.2024.

[7] V. Barger, D. Marfatia, and K. Whisnant, *The Physics of Neutrinos*. Princeton University Press, 2012, ISBN: 9780691128535. [Online]. Available: https://books.google.de/books?id=qso8NEr3XY8C.

[8] M. Mulders and G. Perez, Eds., *2013 European School of High-Energy Physics: Paradfurdo, Hungary 5 - 18 Jun 2013*, CERN, 2015. DOI: 10.5170/CERN-2015-004.

[9] M. Dine, *Supersymmetry and String Theory: Beyond the Standard Model*, 2nd ed. Cambridge University Press, 2023, ISBN: 978-1-009-29092-0.

[10] L. Evans and P. Bryant, "LHC Machine," *Journal of Instrumentation*, vol. 3, no. 08, S08001, Aug. 2008. DOI: 10.1088/1748-0221/3/08/S08001.

[11] L. Arnaudon *et al.*, "Linac4 Technical Design Report," CERN, Geneva, Tech. Rep., 2006. [Online]. Available: https://cds.cern.ch/record/1004186.

[12] M. Benedikt, P. Collier, V. Mertens, J. Poole, and K. Schindl, *LHC Design Report*, ser. CERN Yellow Reports: Monographs. Geneva: CERN, 2004. DOI: 10.5170/CERN-2004-003-V-3.

[13] E. Lopienska, *The CERN Accelerator Complex, layout in 2022*, https://cds.cern.ch/images/CERN-GRAPHICS-2022-001-1, Accessed: 21.01.2024.

[14] W. Herr and B. Muratori, "Concept of Luminosity," 2006. DOI: 10.5170/CERN-2006-002.361.

[15] C. Pralavorio, "Record luminosity: well done LHC," 2017. [Online]. Available: https://cds.cern.ch/record/2295027.

[16] The CMS Collaboration, *Public CMS Luminosity Information*, https://twiki.cern.ch/twiki/bin/view/CMSPublic/LumiPublicResults, Accessed: 23.01.2024.

[17] D. Bertolini, P. Harris, M. Low, and N. Tran, "Pileup per particle identification," *Journal of High Energy Physics*, vol. 2014, no. 10, Oct. 2014, ISSN: 1029-8479. DOI: 10.1007/jhep10(2014)059.

[18] The CMS Collaboration, "Observation of a new boson at a mass of 125 gev with the cms experiment at the lhc," *Physics Letters B*, vol. 716, no. 1, pp. 30–61, 2012, ISSN: 0370-2693. DOI: https://doi.org/10.1016/j.physletb.2012.08.021.

[19] The CMS Collaboration, "The CMS experiment at the CERN LHC," *Journal of Instrumentation*, vol. 3, no. 08, S08004, Aug. 2008. DOI: 10.1088/1748-0221/3/08/S08004.

[20] T. Sakuma, "Cutaway diagrams of CMS detector," 2019. [Online]. Available: https://cds.cern.ch/record/2665537.

[21] The CMS Collaboration, *Development of the CMS detector for the CERN LHC Run 3*, 2023. arXiv: 2309.05466 [physics.ins-det].

[22] A. Dominguez *et al.*, "CMS Technical Design Report for the Pixel Detector Upgrade," Tech. Rep., 2012. [Online]. Available: https://cds.cern.ch/record/1481838.

[23] The CMS Collaboration, *CMS Physics: Technical Design Report Volume 1: Detector Performance and Software*, ser. Technical design report. CMS. Geneva: CERN, 2006. [Online]. Available: https://cds.cern.ch/record/922757.

[24] H. Kolanoski and N. Wermes, *Particle Detectors*. Oxford University Press, Jun. 2020, ISBN: 978-0-19-885836-2.

[25] The CMS Collaboration, *The CMS electromagnetic calorimeter project: Technical Design Report*, ser. Technical design report. CMS. Geneva: CERN, 1997. [Online]. Available: https://cds.cern.ch/record/349375.

[26] S. Abdullin *et al.*, "Design, performance, and calibration of CMS hadron-barrel calorimeter wedges," *European Physical Journal C*, vol. 55, pp. 159–171, 2008. DOI: 10.1140/epjc/s10052-008-0573-y.

[27] C. Battilana, "Upgrades of the CMS muon detectors: from Run 3 towards HL-LHC," in *Proceedings of European Physical Society Conference on High Energy Physics — PoS(EPS-HEP2019)*, vol. 364, 2020, p. 156. DOI: 10.22323/1.364.0156.

[28] A. Sirunyan *et al.*, "Performance of the CMS Level-1 trigger in proton-proton collisions at $\sqrt{s} = 13$ TeV," *Journal of Instrumentation*, vol. 15, no. 10, P10017, Oct. 2020. DOI: 10.1088/1748-0221/15/10/P10017. [Online]. Available: https://dx.doi.org/10.1088/1748-0221/15/10/P10017.

[29] G. L. Bayatyan, N. Grigorian, V. G. Khachatrian, A. T. Margarian, and A. M. Sirunyan, *CMS TriDAS project: Technical Design Report, Volume 1: The Trigger Systems*, ser. Technical design report. CMS. [Online]. Available: https://cds.cern.ch/record/706847.

[30] V. Khachatryan *et al.*, "The CMS trigger system," *Journal of Instrumentation*, vol. 12, no. 01, P01020, Jan. 2017. DOI: 10.1088/1748-0221/12/01/P01020.

[31] The HL-LHC Collaboration, *LHC/ HL-LHC Plan (last update October 2024)*, https://hilumilhc.web.cern.ch/content/hl-lhc-project, Accessed: 27.11.2024.

[32] G. Apollinari *et al.*, "High-Luminosity Large Hadron Collider (HL-LHC): Technical Design Report V. 0.1," CERN, Geneva, Tech. Rep., 2017. [Online]. Available: https://doi.org/10.23731/CYRM-2017-004.

[33] The CMS Collaboration, "Snowmass White Paper Contribution: Physics with the Phase-2 ATLAS and CMS Detectors," CERN, Geneva, Tech. Rep., 2022. [Online]. Available: https://cds.cern.ch/record/2806962.

[34] S. Heinemeyer *et al.*, *Handbook of LHC Higgs Cross Sections: 3. Higgs Properties: Report of the LHC Higgs Cross Section Working Group*, S. Heinemeyer, Ed., ser. CERN Yellow Reports: Monographs. 2013. DOI: 10.5170/CERN-2013-004.

[35] The CMS Collaboration, "A portrait of the higgs boson by the cms experiment ten years after the discovery," *Nature*, vol. 607, no. 7917, pp. 60–68, Jul. 2022, ISSN: 1476-4687. DOI: 10.1038/s41586-022-04892-x. [Online]. Available: http://dx.doi.org/10.1038/s41586-022-04892-x.

[36] The CMS Collaboration, "The Phase-2 Upgrade of the CMS Tracker," CERN, Geneva, Tech. Rep., 2017. DOI: 10.17181/CERN.QZ28.FLHW.

[37] The CMS Collaboration, "A MIP Timing Detector for the CMS Phase-2 Upgrade," CERN, Geneva, Tech. Rep., 2019. [Online]. Available: https://cds.cern.ch/record/2667167.

[38] The CMS Collaboration, "The Phase-2 Upgrade of the CMS Level-1 Trigger," CERN, Geneva, Tech. Rep., 2020, Final version. [Online]. Available: https://cds.cern.ch/record/2714892.

[39] The CMS Collaboration, "The Phase-2 Upgrade of the CMS Muon Detectors," CERN, Geneva, Tech. Rep., 2017. [Online]. Available: https://cds.cern.ch/record/2283189.

[40] The CMS Collaboration, "The Phase-2 Upgrade of the CMS Endcap Calorimeter," CERN, Geneva, Tech. Rep., 2017. DOI: 10.17181/CERN.IV8M.1JY2.

[41] The CMS Collaboration, "The Phase-2 Upgrade of the CMS Barrel Calorimeters," CERN, Geneva, Tech. Rep., 2017, This is the final version, approved by the LHCC. [Online]. Available: https://cds.cern.ch/record/2283187.

[42] The CMS Collaboration, "Expected performance of the physics objects with the upgraded CMS detector at the HL-LHC," CERN, Geneva, Tech. Rep., 2018. [Online]. Available: https://cds.cern.ch/record/2650976.

[43] K. Olive, "Review of particle physics," *Chinese Physics C*, vol. 38, no. 9, p. 090 001, Aug. 2014.

[44] H. Bichsel, "Straggling in thin silicon detectors," *Rev. Mod. Phys.*, vol. 60, pp. 663–699, 3 Jul. 1988. DOI: 10.1103/RevModPhys.60.663.

[45] R. L. Workman *et al.*, "Review of Particle Physics," *PTEP*, vol. 2022, p. 083C01, 2022. DOI: 10.1093/ptep/ptac097.

[46] Knoll, Glenn F., *Radiation Detection and Measurement*, 4th. Wiley, 2010, ISBN: 978-0-470-13148-0.

[47] F. Hartmann, *Evolution of Silicon Sensor Technology in Particle Physics*, ser. Springer Tracts in Modern Physics, 275. Springer Cham, 2017, ISBN: 978-3319644349. DOI: 10.1007/978-3-319-64436-3.

[48] M. A. Green, "Intrinsic concentration, effective densities of states, and effective mass in silicon," *Journal of Applied Physics*, vol. 67, no. 6, pp. 2944–2954, 1990. DOI: 10.1063/1.345414.

[49] S. M. Sze and M.-K. Lee, *Semiconductor Devices: Physics and Technology*, 3rd. John Wiley & Sons, 2016, ISBN: 978-0-470-53794-7.

[50] W. Shockley, "Currents to conductors induced by a moving point charge," *Journal of Applied Physics*, vol. 9, no. 10, pp. 635–636, Oct. 1938. DOI: 10.1063/1.1710367.

[51] S. Ramo, "Currents induced by electron motion," *Proceedings of the IRE*, vol. 27, no. 9, pp. 584–585, 1939. DOI: 10.1109/JRPROC.1939.228757.

[52] Spieler, Helmuth, *Semiconductor Detector Systems.* Oxford University Press, 2005, ISBN: 978-0198527848.

[53] J. Ruger, R. Hübel, and M. Schikorr, "Analysis of the hall mobility and the hall scattering factor in semiconductors," *Nuclear Instruments and Methods*

in Physics Research Section A: Accelerators, Spectrometers, Detectors and Associated Equipment, vol. 454, no. 1, pp. 148–153, 2000. DOI: 10.1016/S0168-9002(00)01206-7.

[54] D. Contardo, M. Klute, J. Mans, L. Silvestris, and J. Butler, "Technical Proposal for the Phase-II Upgrade of the CMS Detector," CERN, Geneva, Tech. Rep., 2015. DOI: 10.17181/CERN.VU8I.D59J.

[55] G. Hall, "Design of a trigger module for the CMS Tracker at SLHC," *Topical Workshop on Electronics for Particle Physics*, 2009. DOI: 10.5170/CERN-2009-006.243.

[56] The Tracker Group of the CMS Collaboration, *Beam Test Performance Studies of CMS Phase-2 Outer Tracker Module Prototypes*, 2024. arXiv: 2404.08794.

[57] R. Aggleton *et al.*, "An FPGA based track finder for the L1 trigger of the CMS experiment at the High Luminosity LHC," *Journal of Instrumentation*, vol. 12, no. 12, P12019, 2017. DOI: 10.1088/1748-0221/12/12/P12019.

[58] CMS Tracker Group, "Selection of the silicon sensor thickness for the Phase-2 upgrade of the CMS Outer Tracker," CERN, Geneva, Tech. Rep. 11, 2021. DOI: 10.1088/1748-0221/16/11/P11028.

[59] W. Adam *et al.*, "Experimental study of different silicon sensor options for the upgrade of the cms outer tracker," *Journal of Instrumentation*, vol. 15, no. 04, P04017, Apr. 2020. DOI: 10.1088/1748-0221/15/04/P04017.

[60] K. Damanakis, "Silicon sensors for the Phase-2 upgrade of the CMS Outer Tracker; status and early results from the production phase," *Nuclear Instruments and Methods in Physics Research Section A: Accelerators, Spectrometers, Detectors and Associated Equipment*, vol. 1040, p. 167 034, 2022, ISSN: 0168-9002. DOI: https://doi.org/10.1016/j.nima.2022.167034.

[61] M. Prydderch, "CBC3.1 User Manual," Jul. 2019. [Online]. Available: http://www.hep.ph.ic.ac.uk/ASIC/CBC_documentation/CBC3p1_User_Manual_V1p4.pdf.

[62] G. Bergamin *et al.*, "CIC2.1 Technical Specification," Internal Document, version 1.4, 2024.

[63] D. Ceresa, J. Kaplon, R. Francisco, A. Caratelli, K. Kloukinas, and A. Marchioro, "A 65 Nm Pixel Readout ASIC With Quick Transverse Momentum Discrimination Capabilities For The CMS Tracker At HL-LHC," *Journal of Instrumentation*, vol. 11, no. 01, p. C01054, Jan. 2016. DOI: 10.1088/1748-0221/11/01/C01054.

[64] A. Caratelli, D. Ceresa, J. Murdzek, J. Kaplon, K. Kloukinas, and S. Scarfi, *Short Strip ASIC User Manual v0.1*, 2017.

[65] J. Butler, D. Contardo, M. Klute, J. Mans, and L. Silvestris, "CMS Phase II Upgrade Scope Document," CERN, Geneva, Tech. Rep., 2015. [Online]. Available: https://cds.cern.ch/record/2055167.

[66] N. Pozzobon, "Development of a Level 1 Track Trigger for the CMS experiment at the high-luminosity LHC," *Nuclear Instruments and Methods in Physics Research Section A: Accelerators, Spectrometers, Detectors and Associated Equipment*, vol. 732, pp. 151–155, 2013, Vienna Conference on Instrumentation 2013, ISSN: 0168-9002. DOI: https://doi.org/10.1016/j.nima.2013.06.010.

[67] The CMS Collaboration, "2017 Tracking Performance Plots," 2017. [Online]. Available: https://cds.cern.ch/record/2290524.

[68] D. Dannheim *et al.*, "Corryvreckan: a modular 4D track reconstruction and analysis software for test beam data," *Journal of Instrumentation*, vol. 16, no. 03, P03008, Mar. 2021. DOI: 10.1088/1748-0221/16/03/p03008.

[69] K. Uchida *et al.*, "The CBC3 Readout ASIC for CMS 2S-Modules," CERN, Geneva, Tech. Rep., 2018. [Online]. Available: `http://cds.cern.ch/record/2312215`.

[70] P. Moreira *et al.*, *GBTX manual; V0.18 draft*. 2021. [Online]. Available: `https://cds.cern.ch/record/2809057`.

[71] A. Caratelli *et al.*, "The GBT-SCA, a radiation tolerant ASIC for detector control and monitoring applications in HEP experiments," *JINST*, vol. 10, no. 03, p. C03034, 2015. DOI: `10.1088/1748-0221/10/03/C03034`.

[72] Y. Otarid, "Pixel-Strip Modules for the CMS Tracker Phase-2 Upgrade: From DAQ test system development to module assembly and qualification," Presented 15 Jun 2023, Hamburg University, 2023. [Online]. Available: `https://cds.cern.ch/record/2876414`.

[73] S. Maier, "Assembly and qualification procedures of 2S modules and high rate tests of the CMS Binary Chip for the Phase 2 Upgrade of the CMS Outer Tracker," Ph.D. dissertation, Karlsruhe Institute of Technology (KIT), 2019.

[74] R. Diener *et al.*, "The DESY II test beam facility," *Nuclear Instruments and Methods in Physics Research Section A: Accelerators, Spectrometers, Detectors and Associated Equipment*, vol. 922, pp. 265–286, 2019, ISSN: 0168-9002. DOI: `https://doi.org/10.1016/j.nima.2018.11.133`.

[75] H. Jansen *et al.*, "Performance of the EUDET-type beam telescopes," *EPJ Techniques and Instrumentation*, vol. 3, no. 1, Oct. 2016. DOI: `10.1140/epjti/s40485-016-0033-2`.

[76] S. Spannagel, "Test Beam Measurements for the Upgrade of the CMS Pixel Detector and Measurement of the Top Quark Mass from Differential Cross Sections," 2016. [Online]. Available: `https://cds.cern.ch/record/2162902`.

[77] W. Adam *et al.*, "The cms phase-1 pixel detector upgrade," *Journal of Instrumentation*, vol. 16, no. 02, P02027, Feb. 2021. DOI: `10.1088/1748-0221/16/02/P02027`.

[78] D. Cussans, "Description of the JRA1 Trigger Logic Unit (TLU), v0.2c," *EUDET-MEMO-2009-4*, 2009. [Online]. Available: `https://www.eudet.org/e26/e28/e42441/e57298/EUDET-MEMO-2009-04.pdf`.

[79] M. Pesaresi *et al.*, "The FC7 AMC for generic DAQ &; control applications in CMS," *Journal of Instrumentation*, vol. 10, no. 03, p. C03036, Mar. 2015. DOI: `10.1088/1748-0221/10/03/C03036`.

[80] Y. Liu *et al.*, "EUDAQ2—A Flexible Data Acquisition Software Framework for Common Test Beams," *Journal of Instrumentation*, vol. 14, no. 10, P10033–P10033, Oct. 2019, ISSN: 1748-0221. DOI: `10.1088/1748-0221/14/10/p10033`.

[81] M. Haranko, "Development of a Test DAQ System for the CMS Phase-2 Outer Tracker Upgrade," Hamburg U., 2019. [Online]. Available: `https://cds.cern.ch/record/2711873`.

[82] J. Roskes, "Alignment and Calibration of the CMS Tracker," in *A Boson Learned from its Context, and a Boson Learned from its End*. Cham: Springer International Publishing, 2020, pp. 21–46, ISBN: 978-3-030-58011-7. DOI: `10.1007/978-3-030-58011-7_3`.

[83] C. Kleinwort, "General broken lines as advanced track fitting method," *Nuclear Instruments and Methods in Physics Research Section A: Accelerators, Spectrometers, Detectors and Associated Equipment*, vol. 673, pp. 107–110, 2012, ISSN: 0168-9002. DOI: `https://doi.org/10.1016/j.nima.2012.01.024`.

[84] S. Spannagel and H. Jansen, *Gbl track resolution calculator v2.0*, version v2.0, Apr. 2016. DOI: `10.5281/zenodo.48795`.

[85] D. Ceresa, J. Kaplon, and G. Bergamin, *MPA2 User Manual v0.1*, Apr. 2022. [Online]. Available: `https://twiki.cern.ch/twiki/pub/Sandbox/FNALOuterTracker/mpa2_user_manual_v01.pdf`.

[86] D. Berry and R. Lipton, “MaPSA Assembly Specification,” CMS Collaboration, Internal Document, 2016, Original date: 10/22/2016, Last Revised date: 02/06/2023.

[87] D. Berry, J. Dickinson, and Fermilab, “CMS Macro Pixel Sub-Assemblies (MaPSAs) Round 2 Note,” CMS Tracker Group, Internal Document, 2021, Original date: 06/13/2021, Last Revised date: 18/08/2022.

[88] I.-S. Ninca *et al.*, “TCAD simulations of humidity-induced breakdown of silicon sensors,” *Nuclear Instruments and Methods in Physics Research Section A: Accelerators, Spectrometers, Detectors and Associated Equipment*, vol. 1067, p. 169 729, 2024, ISSN: 0168-9002. DOI: `https://doi.org/10.1016/j.nima.2024.169729`.

[89] U. Heintz, A. Dierlamm, and O. Pooth, “QC Document for Preproduction and Production Modules (v1),” CMS Collaboration, Internal Document, Oct. 2024.